universität wien

MASTERARBEIT / MASTER'S THESIS

Titel der Masterarbeit / Title of the Master's Thesis

„Internal color gradients and distributions of stellar populations of early-type galaxies in z ~ 0.4 CLASH clusters"

verfasst von / submitted by

Victor Marian Bakk. rer. nat.

angestrebter akademischer Grad / in partial fulfilment of the requirements for the degree of

Master of Science (MSc)

Wien, 2016 / Vienna 2016

Studienkennzahl lt. Studienblatt / degree programme code as it appears on the student record sheet:	A 066 861
Studienrichtung lt. Studienblatt / degree programme as it appears on the student record sheet:	Masterstudium Astronomie
Betreut von / Supervisor:	Univ.-Prof. Dipl.-Phys. Dr. Bodo Ziegler

The history of astronomy
is a history of receding horizons.

EDWIN POWELL HUBBLE,
THE REALM OF THE NEBULÆ

Abstract english:

To better understand the processes involved in the formation and evolution of elliptical galaxies, 2D models were created in the course of this thesis, which offer the possibilities to constrain the probabilities of various scenarios. The galaxies are members of the clusters MACS J1206.2-0847 and MACS J0416.1-2403 at an average redshift of $z \sim 0.4$. Utilizing the, by the models determined structural parameters Sérsic index n and effective radius r_e, as well as the total integrated magnitude, radial surface brightness profiles were derived for each of the observed galaxies in each of the twelve bands along with radial profiles for the four colors $g_{475} - I_{814}$, $r_{625} - Y_{105}$, $I_{814} - H_{160}$ and $Y_{105} - H_{160}$. Thereupon the logarithmic slopes of these color profiles were determined, as well as the influence on them from the ages and metallicities of the underlying stellar populations. It became apparent that the sizes of the stellar structures on average decrease with increasing wavelength, while n remains constant. Already this observation indicates on average negative color gradients, which are indeed also found. As a consequence one can conclude that the stars are redder in the centers of the galaxies than in the exterior regions. Whether this is the result of radial variations in age and/or metallicity should be answered with the help of models of stellar populations. To that end for the mentioned colors a variety of values were simulated at the redshifts of the galaxy clusters, being based on differing formation redshifts and metallicities. A comparison of the simulated against the measured values yields that both a radial difference in ages and especially a metallicity gradient are the reasons for the observed color gradients. The magnitudes of these gradients favour a scenario, which predicts with progression in time a passive evolution combined with minor dry mergers with mass-poor systems, which are relaxing mainly into a more extended structure than the initial one for very distant ($z \sim 2$), compact, but mass-rich elliptical galaxies, which means that the galaxies undergo an inside-out-growth.

Abstract deutsch:

Um die Vorgänge bezüglich der Entstehung und Entwicklung von elliptischen Galaxien besser zu verstehen, wurden im Zuge dieser Arbeit 2D-Modelle dieser Objekte erstellt, die es ermöglichten, die Wahrscheinlichkeit diverser Szenarios einzuschränken. Die Galaxien sind Mitglieder der Haufen MACS J1206.2-0847 und MACS J0416.1-2403 bei einer mittleren Rotverschiebung von $z \sim 0.4$. Mithilfe der von den Modellen ausgegebenen strukturellen Parametern Sérsic Index n und Effektiv Radius r_e, sowie der integrierten, totalen Helligkeit wurden für die Beobachtungen in zwölf verschiedenen Filtern für jede Galaxie jeweils ein radiales Oberflächenhelligkeitsprofil, als auch anschließend die radialen Profile für die vier Farben $g_{475}-I_{814}$, $r_{625}-Y_{105}$, $I_{814}-H_{160}$ und $Y_{105}-H_{160}$ erstellt. Daraufhin wurden die logarithmischen Steigungen dieser Farbprofile bestimmt, ebenso wie der Einfluss von Alter und Metallizität der zugrunde liegenden stellaren Populationen auf diese. Es stellte sich heraus, dass die Durchmesser der stellaren Strukturen im Mittel mit zunehmender Wellenlänge kleiner werden, während n konstant bleibt. Bereits dies deutet im Durchschnitt gesehen auf negative Farbgradienten hin, die auch tatsächlich gefunden wurden. Als Konsequenz daraus lässt sich schließen, dass die Sterne in den Zentren der Galaxien röter sind als in den äußeren Bereichen. Ob dies nun ein Resultat aus radialen Variationen im Alter und/oder der Metallizität sei, sollte mithilfe der Modellierung von stellaren Populationen ermittelt werden. Zu diesem Zweck wurde eine Vielzahl an Werten für die bereits erwähnten Farben bei der Rotverschiebung der Galaxiehaufen erstellt, variierend aufgrund verschiedener „Entstehungs-rotverschiebungen “, sowie Metallizitäten. Ein Abgleich der simulierten mit den gemessenen Werten ergab, dass sowohl eine radiale Differenz des Alters, als auch insbesondere ein Metallizitätsgradient die Gründe für die beobachteten Farbgradienten sind. Die Größenordnungen dieser Gradienten bevorzugen ein Szenario, das für weit entfernte ($z \sim 2$), kompakte, aber massereiche elliptische Galaxien mit Verlauf der Zeit nur noch eine passive Evolution vorhersagt, kombiniert mit gasarmen Verschmelzungen mit masseärmeren Systemen, die hauptsächlich eine ausgedehntere Struktur bilden als die ursprüngliche und die Galaxien somit von innen nach außen hin wachsen.

Contents

Introduction **1**

1. Theory & observations **5**
1.1. Classification of galaxies 5
1.2. Formation and evolution of galaxies 8
1.3. Light profiles and color gradients 10
1.3.1. Sérsic profile 10
1.3.2. Surface brightness profile 13
1.3.3. Colors of galaxies 14
1.4. Stellar population synthesis 18

2. Tools & Software **21**
2.1. Parametric fitting: Source Extractor, GALFIT and Megamorph . . . 21
2.1.1. Source Extractor 21
2.1.2. GALFIT 22
2.1.3. Megamorph 24
2.2. Stellar population modeling: EzGal 26

3. Data **29**
3.1. CLASH 29
3.2. CLASH-VLT 32
3.3. MACS 1206 33
3.3.1. Selection 34
3.4. MACS 0416 36
3.4.1. Selection 36

4. Modelling of galaxies **39**

5. Comparison with SSP models **49**

6. Results **51**
6.1. Wavelength-dependence of parameters 51
6.2. Color gradients 59
6.3. Determination of age and metallicity 67

7. Conclusions **83**

8. Summary **87**

Acknowledgements **89**

Appendix **103**
A. Source Extractor input file 103
B. MegaMorph setup file 107
C. MegaMorph results 113
D. Gradient results 145
E. SSP results 149

Introduction

Already in 1755 Immanuel Kant coined the term 'Welteninseln' ('island universes') for diffuse nebula-like objects observed in the night sky and assumed the universe consisting and containing numerous of those objects. But it was only in the twenties of the 20th century, that the nature of those structures became a matter of debate.

By this time several observations and measurements of those 'nebulae' took place, for example the creation of the *General Catalogue of Nebulae* by William and John Herschel containing survey results of the Northern and Southern hemisphere, the additions to this catalogue by John Dreyer, who consolidates these results into the *New General Catalogue*, which is still very much in use, or Vesto Melvin Slipher's measurements revealing the spectral lines of those objects being redshifted.

All these new insights lead to more questions than answers and on the 26th April 1920 in the Baird auditorium of the Smithsonian Museum of Natural History, Harlow Shapley and Heber Curtis were the two opponents of a debate, which was titled 'The scale of the universe'. The main question was whether these nebulae were relatively small and therefore part of our Milky Way or independent systems, making them exceedingly large and especially distant objects. Shapley favoured a scenario, in which the Milky Way is in fact the whole visible universe, while Curtis believed in those nebulae just being independent systems, much like the Milky Way itself.

Only a few years later Edwin Hubble (Hubble, 1926) was able to resolve this issue using Cepheid variables as distance indicators. As this class of stars has a pulsation period, which is precisely proportional to their luminosities, measuring their apparent magnitude can be directly used to calculate the distances, which makes them so-called standard candles. Hubble was therefore able to eventually establish those faint nebulae as distant, large and independent objects we nowadays know as galaxies, planting the seed of extragalactic research.

Our knowledge about these structures has grown enormously over the last decades, not only, but also thanks to the technological advances. Not even mentioning the emergence of powerful computers, which enable theoreticians to create complex simulations ranging from the formation of single stars to the whole universe, also obser-

vations became more precise, efficient and numerous, be it, among other things, due to the introduction of Charged Coupled Devices (CCDs), the possibilities to detect objects not only in the visible range of the spectrum, but also for example in the UV, IR or X-ray regimes thanks to satellites or last but not least the construction of monumental observatories, like the Mauna-Kea Observatories or the Paranal ESO Observatory.

Nonetheless there are still countless questions, which desire an answer. It is well known, that the nowadays estimated up to a total of 100 - 200 billion galaxies in the universe, come in all shapes, sizes, colors and environments. Thus they can be found in the field as single objects with no gravitational interaction with any other galaxy right up to clusters containing hundreds, if not thousands of galaxies, or even superclusters, representing presumably the largest gravitational bound structures in the universe.

Still almost all galaxies can be described by a bimodal distribution, segregating them into blue spirals with young stellar populations in a prominent disk component and red, old elliptical galaxies. How those two populations of galaxies form and evolve over time is an ongoing topic of research and due to the finite speed of light and the launch of the *Hubble Space Telescope* (HST) and other extraordinary telescopes, we are also in the lucky position to be able to take a look into the past and therefore shed some light on the different formation and evolution scenarios of galaxies, by observing at different redshifts and also galaxies in different environments (e.g. Silk & Mamon (2012); Conselice (2014)).

An important part plays the usage of the observed structures of the galaxies to defer properties directly related to the formation and evolution. One well established option is to examine the light profiles of the galaxies as a function of radius. Applying this method to different wavelengths and consequently exploring how the light distribution changes with different passbands (i.e. filters), opens up the possibility to derive the colors in dependence of radius. These colors, respectively their change with radius, i.e. the color-gradients, are directly correlated to the underlying spatial distribution of the stellar population of a galaxy, therefore making it possible if not to decipher, but to constrain possible formation scenarios of galaxies.

The first two chapters intend to give an overview of the theoretical framework of this thesis, as well as describing the tools applied to facilitate this study. The third chapter depicts the data, while the fourth and fifth outline the modelling of the sample galaxies and the comparison of the derived color-gradients with Simple

Stellar Population (SSP) models. In the sixth and seventh chapter results and an analysis are given, as well as a comparison to other publications and studies. Finally in the eighth and last chapter a summary of this thesis is presented.

1. Theory & observations

This chapter intends to give insights on the needed background without going into too many details. The first three sections focus on observational results, the last part on the rather numerical element of simulating galaxy populations. It also gives an overview of the current status regarding the formation and evolution of galaxies to put the results presented in this thesis in up to date context.

1.1. Classification of galaxies

Galaxies come in a wide variety, consisting of stars formed possibly at different times and are maybe even still in the process of creating new stars. They possess different amount of gas and dust and are embedded into different environments. Galaxies therefore occur in all kinds of appearances and in order to make comparisons among diverse galaxies easier, one tries to classify them into different categories.

Edwin Hubble did not only resolve the issue of whether the observed nebulae are independent objects or not and in addition formulated his famous law correlating the recession velocity of an extragalactical object with its distance, but he also developed his notable tuning fork scheme (Hubble, 1926) for classifying galaxies solely based on their observed appearances and segregating them into elliptical early-type galaxies and late-type spiral galaxies. The former population is further distinguished by the parameter n in regard to their projected ellipticity $e = 1 - b/a$ with $n = 10 \times e$. The spiral population in turn is divided by taking their disk/bulge ratio into account and also the possible presence of a bar, marked by the extra 'B', ranging from Sa (SBa), describing a spiral galaxy with tightly wound smooth spiral arms and a large, bright bulge to Sc (SBc), a galaxy showing very loose, fragmented spiral arms and a small, faint bulge.

With today's knowledge about galaxies this classification scheme seems far too superficial, but nevertheless aside from minor modifications, like the addition of a few more galaxy types to be able to classify for example the lenticular S0 galaxies, in this thesis counted as early-type galaxies, or irregular galaxies, which are showing no

distinctive features, (e.g. Sandage (1961); Kormendy & Bender (2012)), it is still in use (Fig. 1.1). Therefore we nonetheless exploit mainly these two categories, early and late-type, to classify observed galaxies.

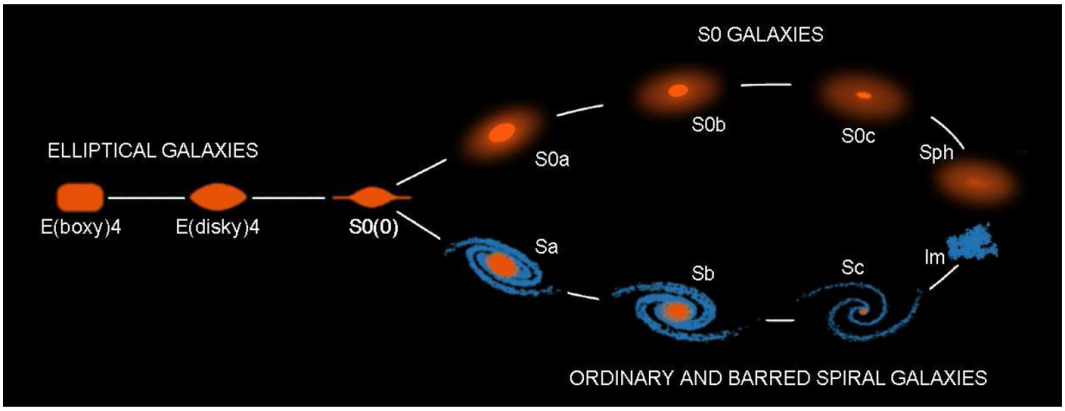

Figure 1.1.: A modern version of the conventional Hubble tuning fork to classify galaxies. Taken from Kormendy & Bender (2012).

The validity of this approach is supported by the fact, that numerous physical properties of galaxies correlate with their morphologies and show also a bimodal distribution. It has been well known for more than four decades that early-type galaxies are more massive and redder (Fig. 1.2), with these galaxies occupying a tight region in the color-magnitude-space (the so-called red sequence) out to $z \sim 2$ (Kodama & Arimoto, 1997) and also showing little to no star formation in comparison to late-type galaxies, which leaves them passively evolving (Holmberg, 1958). But this bimodality does not only concern mass, color and star formation, but also for example metallicity Z, gas content, mass-to-light ratio (M/L) and the bulge fraction (Conselice, 2006). So early-type galaxies possess a higher metallicity, low or almost no gas content, a large M/L and a very high bulge fraction in the form of those galaxies being pure bulges.

Considering all these correlations one can conclude, that the morphology of a galaxy is the product of the formation and especially its evolution over time, including, amongst other factors, possible interactions with their environment or other galaxies in the form of mergers or internal perturbations (Buta, 2011).

Nevertheless it must be considered, that although distant galaxies seem to exhibit same morphologies as local galaxies, they do not possess the same properties like sizes, colors or star formation rate. Consequently the conventional Hubble sequence is not completely established at higher redshifts, is not present to the full extent at

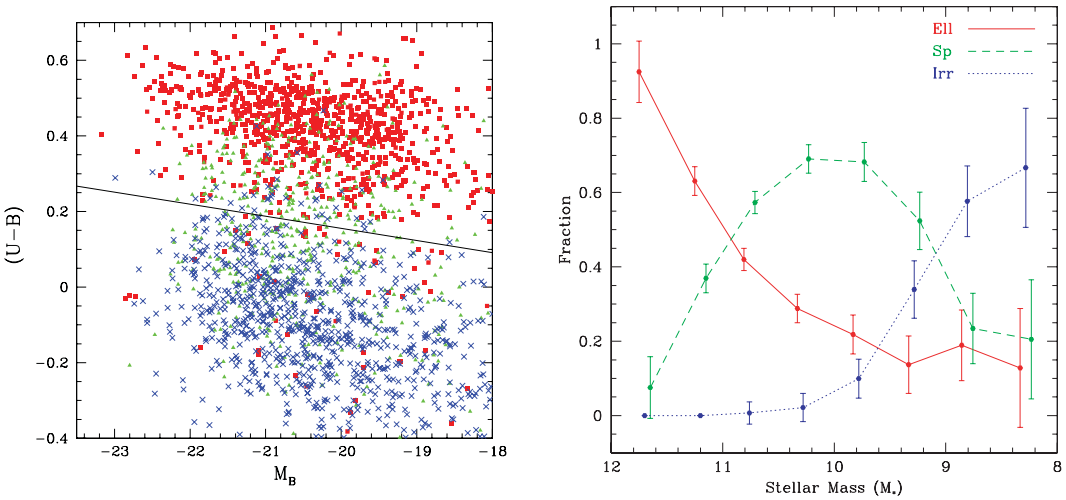

Figure 1.2.: Left side: Color-magnitude diagram depicting the red sequence of early-type galaxies, shown as red squares. Later-types are displayed as blue crosses and intermediates as green triangles. Right side: Fractions of different morphological types at different stellar masses. The solid, red line represents early-types, the dashed green line spirals and the blue dotted line irregular galaxies. Diagrams taken from (Conselice, 2006).

$z \gtrsim 1$ (van den Bergh et al., 1996) and entirely vanishes at $z \gtrsim 2$. Hence spiral and elliptical galaxies in the classical sense following Hubble's classification only appear at $z \sim 1.5$ with the fraction of early-type galaxies increasing from $\sim$ 20 - 30 percent at $z \sim 3$ to $\sim$ 70 percent at $z \sim 0$ with elliptical galaxies being the dominating morphological type for massive galaxies since only $z \sim 1$ (Buitrago et al., 2013). However this trend seems to show a dependency on mass as the transition redshift, where the combined fraction of early- and late-type galaxies equal that of peculiars, shifts from higher redshifts ($z \sim 2.22 \pm 0.82$) for higher mass galaxies ($\log M_* > 10.5$) to lower redshifts ($z \sim 1.73 \pm 0.57$) for lower mass galaxies ($\log M_* < 10.25$) (Mortlock et al., 2013).

Yet in the local universe the distinction between early- and late-type galaxies is an important indication for the understanding of the physical processes involved in the formation of galaxies. As spheroidal galaxies (ellipticals and S0) contain $\sim$ 60 percent of all stellar mass (Hogg et al. (2002b);Driver et al. (2006)) and the highest numbers of early-type galaxies can be found in highest density regimes (Dressler (1980);Dressler (1984)), i.e. the center of clusters, elliptical galaxies are the targets of this analysis. Furthermore at the redshifts examined in this thesis they represent the majority of galaxies and an understanding of their evolution is an important part to explain the general development of galaxies.

1.2. Formation and evolution of galaxies

One way to gain insights into the formation and evolution of galaxies is to examine the structure of galaxies, which links directly to galaxy properties from which the evolution for single galaxies can be derived. Hence it is naturally a complex issue to describe the formation and evolution of all galaxies in its entirety, due to their wide variety in numerous properties, e.g. star formation history, formation epoch, sizes, mass. Nevertheless the extragalactic research made great strides in the last decades and the knowledge regarding this manifold topic increased significantly. As early-type galaxies are the topic of this thesis the focus lies on the description of the formation and evolution of spheroidal galaxies, although of course the general conclusions are also applicable to late-type galaxies, all the more, as spiral galaxies can also play an important role in the progression of elliptical galaxies, due to interactions.

Historically two main frameworks for the formation of galaxies exist: The (revised) monolithic or top-down model and the hierarchical or bottom-up scenario. The former predicts a formation of spheroids at a very early epoch of the universe resulting from a global starburst followed by a passive evolution to the present day. Subsequently spheroids may form a disk component by accreting gas from the surrounding environment causing limited incidents of star formation, thus making spheroids preceding disks. The latter scheme envisions big spheroids as the result of a gas-rich, 'wet', merging event of two disk galaxies, thus making disks preceding spheroids, leading to an intense burst of star formation, forming the bulk of the newly created elliptical galaxy (Renzini, 2006). Another possibility would be a 'dry' merger scenario with passive galaxies forming a brighter more massive early-type galaxy.

Unfortunately both models are found to have shortcomings in comparison to simulations and also cannot completely explain observations, such as the down-sizing problem describing more massive galaxies being older, thus contradicting the hierarchical scheme. In the wake of these complications a new scheme arose and became widely accepted, termed 'inside-out-growth', one might say an adaption of the hierarchical scheme. Supported by observations and simulations early-type galaxies still form at high redshifts ($z \sim 4-5$), but in contrast to the monolithic model as compact spheroids resulting from gas-rich mergers. This would also clarify the down-sizing phenomena, as the star formation starts first in the regions of highest densities, which will develop into the most massive ($\gtrsim 10^{11}$ $M_\odot$) galaxies.

With time those compact early-type galaxies are taking part in subsequent 'dry', minor mergers increasing the galaxy in size, but hardly in mass. This picture is consistent with the findings of Driver et al. (2013), describing a turning point of the cosmic star formation history for the Universe at $z \sim 1.7$ shifting from a 'hot mode evolution' - spheroid formation and growth via mergers and/or collapse - to a 'cold mode evolution', characterizing a disk formation or growth by gas infall and minor mergers.

Indeed this scenario can also be described successfully by hydrodynamical cosmological simulations (Naab et al., 2009) and by using the Virial theorem one can demonstrate why minor mergers should increase the size of a galaxy, but not the mass to the same extent (Bezanson et al., 2009). Denoting the kinetic energy of the remnant after the merger as the sum of the kinetic energies of the progenitor galaxies

$$K_R = K_1 + K_2 = \frac{1}{2} M_R v_R^2 = \frac{1}{2} M_1 v_1^2 + \frac{1}{2} M_2 v_2^2 \tag{1.1}$$

and considering that $M_R = M_1 + M_2$ with $M_1 \gg M_2$, which leads to

$$\frac{M_R}{M_1} \approx \frac{v_1^2}{v_R^2} \tag{1.2}$$

as well as $v^2 \propto \frac{GM}{r}$ one arrives at

$$\frac{r_R}{r_1} \approx \frac{M_R}{M_1} \frac{v_1^2}{v_R^2} \approx \left(\frac{M_R}{M_1} \right)^2 . \tag{1.3}$$

Thus the radius grows by the square of the mass, rather than just linearly, which would be the case for a merger of equal mass galaxies ($M_1 = M_2$).

Numerous observations exist to confirm both parts of this theory, one being the early formation of the core of early-type galaxies, the other the growth in size. So it is meanwhile well established, that the majority of stars of spheroids were formed at high redshifts ($z \approx$ 3-5) and on short timescales ($\tau \sim 1$ Gyr) (Thomas et al., 2005, 2009). This notion is supported by several correlations between global properties of early-type galaxies, such as color-magnitude, the fundamental plane (Bender et al., 1992) or the Mg-σ-relation (Ziegler & Bender, 1997).

The case of small sized, massive galaxies at high redshifts ($z \sim$ 1.5 - 2) is likewise well observed, requiring a growth in size, but not in mass, which is most likely achieved by means of minor mergers (Daddi et al., 2005; Trujillo et al., 2007, 2011;

van Dokkum et al., 2008, 2010). As a consequence this would result in an evolution of the effective radius by a factor of ~ 1.5 from $z \sim 1.5$ to $z = 0$ (Buitrago et al., 2008; Longhetti et al., 2007) and a factor of ~ 4 since $z \sim 2$ (Chan et al., 2016), which relates to $r \propto (1+z)^{-1.48}$ (van der Wel et al., 2014). Furthermore such small, but massive galaxies have no local counterpart, endorsing that those galaxies are the progenitors of the local massive early-type galaxies.

However recent studies show that this inside-out-growth scenario is only valid for high-mass early-type galaxies. For galaxies in the mass range like our Milky Way ($\sim 10^{10}$ $M_\odot$) and also containing disks, the mass growth appears at all radii (van Dokkum et al., 2013).

1.3. Light profiles and color gradients

1.3.1. Sérsic profile

A simple and common way to measure magnitudes and light distributions is aperture photometry, in which one measures the intensities at certain radii and ends one's measurements at a chosen radius, where the flux does not seem to increase significantly any more. Ideally this radius corresponds to an aperture large enough to encompass all the flux of the object. However due to the noise from the background and maybe also from interfering neighbours the choice of finding the right aperture is a complex task and in most cases the way in which the radius is chosen leads to a loss of flux. Furthermore multiple images and therefore also varying signal to noise (S/N) values, various light distributions and also different wavelengths can impede such efforts. Especially observing galaxies at different wavelengths implicates disparate results, as the diverse fluxes in differing wavelengths result in different apertures leading to wrong estimates.

One approach to evade such problems is to describe the intensity progression with radius and in the course of that also the structure of galaxies with integrated light profiles, which is one of the earliest, but nevertheless still commonly used methods. Simply spoken, one measures the average intensity of a galaxy at a certain radius and determines from that how the intensity changes with centric distance.

The first one to apply this method on a large sample was Gérard de Vaucouleurs, who demonstrated that practically all early-type galaxies show the same smooth light distribution, following the de Vaucouleurs' $R^{1/4}$law (de Vaucouleurs, 1948). Almost a decade later José Luis Sérsic started his work at the 1.54m-telescope at the

Astrophysical Station at Bosque Alegre in Argentina, with his groundbreaking work being summarized in his galaxy atlas 'Galaxias Australes' (Sérsic, 1968). Already a few years before publishing his famous work he deduced a generalised version of the de Vaucouleurs' law to describe not only early-type but all types of galaxies (Sérsic, 1963). Applying his Sérsic's $R^{1/n}$ law to all sufficiently large galaxies in his atlas, he was in the position to derive total magnitudes and structural parameters of those objects, which eventually showed a high correlation with the visually observed morphologies.

The Sérsic profile is best known in the version of an intensity profile (Graham & Driver, 2005), which outlines as

$$I(R) = I_e \exp\left\{-b_n\left[\left(\frac{R}{r_e}\right)^{1/n} - 1\right]\right\}. \tag{1.4}$$

I_e is the intensity at the effective radius r_e, which describes the radius at which half of the total emitted light of the galaxy is encompassed, which is ensured by the dimensionless constant b_n. The last parameter n, also called Sérsic index is responsible for the curvature of the profile and it hence provides information about the morphology of the scrutinized galaxy (Fig. 1.3).

So indicates an $n = 4$ a light distribution related to an early-type galaxy as the Sérsic profiles turns into the known de Vaucouleurs' $R^{1/4}$ law for spheroidal galaxies, whereas an $n = 1$ converts the Sérsic profile into an exponential profile, best fitting for disks (Fig. 1.3). Therefore an early-type galaxy can be easily described by a simple one component Sérsic profile, unlike spiral galaxies, which require usually a combination of two profiles with different n, due to their spheroid galaxy resembling bulge component and additional disk element, a circumstance first described by Freeman (1970). Of course the presence of further features like bars may demand even more sophisticated model combinations. As a result a particular n was introduced to separate the early- and late-type populations. Most commonly used and also adapted in this thesis is $n = 2.5$ (Shen et al., 2003), as this distinction also marks the exact average between the exponential and de Vaucouleurs form of the Sérsic profile.

Fig. 1.3 shows the Sérsic profiles for fixed I_e and r_e and also the, with different n correlating characteristics. The decreasing central concentration of the light distribution is evident, as well as the steepening slope of the profile at larger radii with smaller n. Hence early-type galaxies with usually a larger n, show a high density

core, but a significant outer wing, extending outwards to large radii, making it difficult to find the edge of a galaxy, as its light blurs into the sky background noise. For an $n = 4$ profile, 84.7 percent of the flux are within $4r_e$, for $5r_e$ the contained flux amounts to 88.4 percent (Graham & Driver, 2005).

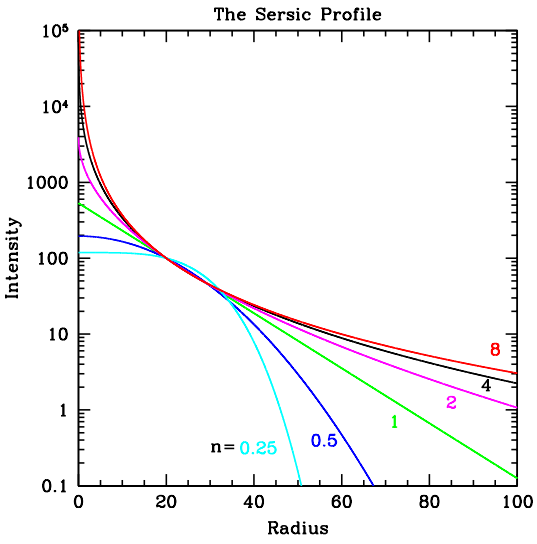

Figure 1.3.: Different Sérsic profiles with same I_e and r_e. The distinctions in the center and large radii depending on n can easily be seen. Diagram from (Peng et al., 2010).

To acquire the luminosity L within a certain radius R, one can integrate Equation (1.4) over the area of a disk, $A = \pi R^2$:

$$L(< R) = \int_0^R I(R')2\pi R' dR'. \quad (1.5)$$

After substituting $x = b_n \left(\frac{R}{r_e}\right)^{1/n}$ this results into

$$L(< R) = I_e r_e^2 2\pi n \frac{e^{b_n}}{(b_n)^{2n}} \gamma(2n, x), \quad (1.6)$$

with $\gamma(2n, x)$ being the incomplete gamma function. Replacing $\gamma(2n, x)$ with the complete gamma function $\Gamma(2n) = \gamma(2n, \infty)$ equation (1.6) yields the value for the total luminosity L_{tot} (Ciotti, 1991).

Thus considering the definition of r_e, b_n is the solution of the equation

$$\gamma(2n, b_n) = \frac{\Gamma(2n)}{2}, \quad (1.7)$$

which can only be solved numerically. Ciotti & Bertin (1999) did an asymptotic expansion for b_n and concluded that even a truncation after the first four terms shows better results than previous solutions, with errors being smaller than $\sim 10^{-6}$. Therefore their equation for b_n

$$b_n(n) = 2n - \frac{1}{3} + \frac{4}{405n} + \frac{46}{25525n^2} \quad (1.8)$$

is used throughout this thesis.

1.3.2. Surface brightness profile

Taking the negative logarithm of equation (1.4) and multiplying the result with 2.5 the result is the surface brightness profile

$$\mu(R) = \mu_e + \frac{2.5 b_n}{\ln(10)} \left[\left(\frac{R}{r_e} \right)^{1/n} - 1 \right], \tag{1.9}$$

where μ_e is the surface brightness at r_e, i.e. the 'mean effective surface brightness'. Letting $R = 0$ yields then the central surface brightness μ_0

$$\mu(R = 0) = \mu_0 = \mu_e - \frac{2.5 b_n}{\ln(10)}. \tag{1.10}$$

To obtain the mean surface brightness $\langle \mu \rangle_e$, defining the surface brightness within r_e one has to consider the average intensity, $\langle I \rangle_e$, which is acquired by integrating the intensity over the area $A = \pi r_e^2$, such that

$$\langle I \rangle_e = \frac{\int I \mathrm{d}A}{A} = \frac{I_e \mathrm{e}^{b_n} \int_0^{r_e} \mathrm{e}^{-b_n (R/r_e)^{1/n}} 2\pi R \mathrm{d}R}{\pi r_e^2}. \tag{1.11}$$

Applying again the same substitution $x = b_n \left(\frac{R}{r_e} \right)^{1/n}$, $\langle I \rangle_e$ can be written as

$$\langle I \rangle_e = I_e \frac{2n \mathrm{e}^{b_n}}{b_n^{2n}} \int_0^{b_n} \mathrm{e}^{-x} x^{2n-1} \mathrm{d}x = I_e f(n). \tag{1.12}$$

Reminding that b_n ensures that r_e is indeed the radius at which half of the total light is contained, one obtains

$$f(n) = \frac{n \mathrm{e}_n^b}{b_n^{2n}} \int_0^{\infty} \mathrm{e}^{-x} x^{2n-1} \mathrm{d}x = \frac{n \mathrm{e}^{b_n}}{b_n^{2n}} \Gamma(2n), \tag{1.13}$$

which finally leads to

$$\langle \mu \rangle_e = \mu_e - 2.5 \log(f(n)) = \mu_e - 2.5 \log \left(\frac{n \mathrm{e}^{b_n}}{b_n^{2n}} \Gamma(2n) \right). \tag{1.14}$$

Now considering again equation (1.6) and multiplying the negative logarithmic equivalent of this equation with 2.5, one obtains the enclosed magnitude within a radius R

$$m(< R) = \mu_e - 5 \log(r_e) - 2.5 \log \left[2\pi n \frac{\mathrm{e}^{b_n}}{(b_n)^{2n}} \gamma(2n, x) \right] \tag{1.15}$$

This provides the opportunity to substitute equation (1.14) into equation (1.15), which yields at $R = r_e$

$$m(< r_e) = \langle\mu\rangle_e - 2.5\log(\pi r_e^2) \tag{1.16}$$

or for the total apparent magnitude m_{tot}

$$m_{tot} = \langle\mu\rangle_e - 2.5\log(2\pi r_e^2). \tag{1.17}$$

1.3.3. Colors of galaxies

The *HST* and also the emerging of other powerful telescopes in the last two decades, be it in space or on the ground, opened up new chances to resolve more and also even more distant galaxies, not only in the optical, but also other wavelength ranges like UV or IR.

By using these multi-band images and fitting a Sérsic profile (see section 2.1) to the galaxies one has now the possibility to derive the fundamental structural parameters n and r_e at different wavelengths and is therefore capable to trace different stellar populations of the galaxy. Shorter, bluer wavelengths are an indicator for the distribution of recently formed young stars, optical wavelengths, which are on the redder side of the Balmer break ($\sim$ 4000 Ångström), detect a mixture of stars at different ages and at longer wavelengths only old, red and long-living stars are pinpointed. Thus it is also possible to reconstruct the evolutionary path the galaxy has taken over its lifespan and its internal components.

Indeed there have been many recent studies describing variations in n and r_e with wavelength at all redshifts suggesting the existence of different stellar populations in one galaxy, supporting the hierarchical scenario. So La Barbera et al. (2002) found for example that r_e in NIR is $\sim$ 40 percent smaller than in the optical wavelength regime for cluster early-type galaxies with $n \gtrsim 4$ at intermediate redshift ($z = 0.31$). Subsequently this has been confirmed by using a larger sample at different intermediate redshifts (z = 0.21-0.64) (La Barbera et al., 2003), showing that on average early-type galaxies are more concentrated at longer wavelengths, which reveals r_e becoming smaller moving from UV to NIR, while n increases.

The same r_e evolution can be observed from local, low-redshift early-type galaxies, with r_e decreasing $\sim$ 40 percent going from g to K band (La Barbera et al., 2010; Kelvin et al., 2012), while n shows no dependence on wavelength (Kennedy et al.,

2015; Vulcani et al., 2014), which confirms the assumption that spheroids can be described by a single Sérsic profile in all wavelengths.

Finally also at high redshifts ($z \sim 1.5$) a decrease in size by approximately 20 percent going from the i to the H band can be observed (Chan et al., 2016).

However in addition to structural parameter measurements, a more thorough inspection of galaxies can be achieved by examining the colors respectively the color profiles and the change of these profiles with radius, i.e. the color gradients, disentangling the underlying physical processes associated with the evolution of passive galaxies, represented by age and metallicity gradients.

The colors of a galaxy are simply defined as the differences of the surface brightness in two different wavelengths at a certain radius, being the result of different structural parameters for the two passbands. The color profile is therefore the radial trend in color of a galaxy. Following equation (1.9) the color profile $(\mu_{\lambda_1} - \mu_{\lambda_2})(R)$, with λ_1 being the bluer band results in

$$\begin{aligned}(\mu_{\lambda_1} - \mu_{\lambda_2})(R) = \mu_{e,\lambda_1} + \frac{2.5 b_{n,\lambda_1}}{\ln 10}\left[\left(\frac{R}{r_{e,\lambda_1}}\right)^{1/n_{\lambda_1}} - 1\right] \\ -\mu_{e,\lambda_2} + \frac{2.5 b_{n,\lambda_2}}{\ln 10}\left[\left(\frac{R}{r_{e,\lambda_2}}\right)^{1/n_{\lambda_2}} - 1\right].\end{aligned} \tag{1.18}$$

The color gradient is then the slope of the color profile between a chosen radius interval, commonly scaled logarithmically.

$$\nabla_{\lambda_1 - \lambda_2} = \frac{\Delta\left((\mu_{\lambda_1} - \mu_{\lambda_2})(R)\right)}{\Delta \log R} \tag{1.19}$$

One common way to derive the slope is to fit a least squares fit onto the color profile with the slope of the fit being an estimate for the gradient or one of the alternative options is to do this 'analytically' following La Barbera et al. (2002), where the parameters r_m and r_M are the inner and outer boundaries in units of r_e of the chosen radius interval to calculate the color gradient in.:

$$\nabla_{\lambda_1-\lambda_2} = \frac{2.5\log(\mathrm{e})}{\log(r_M) - \log(r_m)} \times \left\{ b_{n,\lambda_2} \left[\left(\frac{r_m}{r_{e,\lambda_2}} \right)^{1/n_{\lambda_2}} - \left(\frac{r_M}{r_{e,\lambda_2}} \right)^{1/n_{\lambda_2}} \right] + b_{n,\lambda_1} \left[\left(\frac{r_M}{r_{e,\lambda_1}} \right)^{1/n_{\lambda_1}} - \left(\frac{r_m}{r_{e,\lambda_1}} \right)^{1/n_{\lambda_1}} \right] \right\}. \tag{1.20}$$

Using now simulated models describing the formation and developmental history of galaxies (see section 1.4), one is in the position to decipher, which processes and formation scenarios are responsible for and matching the observed colors and color gradients best, as the assembly history is imprinted in its stellar populations, with colors reflecting the time and conditions of the star formation, whereas the spatial distribution gives insights into the structures in which those stars were formed or accreted.

Considering the two major formation scenarios, the monolithic model and the hierarchical scheme, it becomes clear, that both models prognosticate different color gradients.

So the monolithic dissipative model predicts steep metallicity and constant or mildly positive age gradients, with stars in the center of a galaxy being younger and therefore bluer than the average population in the outskirts. The reason for those appearances lies in the underlying physics of the scenario itself. During the gravitational collapse, so the formation of the galaxy, gas flows towards the center, which leads to a more metal-rich population in the center than in the external regions, characterized by a negative metallicity gradient. Additionally this condition is enhanced due to the central deeper gravitational potential well, causing gas to keep flowing inwards, triggering a star formation and hence chemical enrichment, which is lasting longer in the center than in the outer regions, which is the reason for a null or positive age gradients, but a steep negative metallicity gradient. Thus the latter should dominate the color profile revealing a strong negative color gradient with values greater than -1 mag dex^{-1} in radius for the classical and -0.5 to -0.3 mag dex^{-1} for the revised monolithic model (Montes et al., 2014, and references therein).

Applying the hierarchical dry merger and also the inside-out-growth scenarios on the other hand will result in much shallower gradients, due to a dilution of pre-

existing gradients as a result of the merger(s). The end result would depend on whether the stellar populations were mixed, according to the hierarchical model or the accreted stellar content just being added as an envelope to the existing galaxy, following the preferred inside-out-scheme.

Color gradients have been measured already almost 30 years ago (e.g. Vader et al., 1988), even then supporting negative color gradients, which are corresponding to a decrease in metallicity with radius for local, early-type galaxies (Peletier et al., 1990a,b). Using data from the extensive *SDSS* survey (La Barbera & de Carvalho, 2009) substantiated this picture of negative, metallicity-driven gradients, but also found a small positive age gradient implying early-type galaxies having smaller r_e at higher redshifts (Montes et al., 2014; Wu et al., 2005).

With the advancement in technology newer studies followed allowing to expand the color gradient measurements to more distant galaxies. Those investigations confirmed metallicity as the dominant driver for color gradients for passive galaxies in the field, as well as in clusters, with the origin of the color gradients being independent of the respective galaxy environment (Saglia et al., 2000; Smail et al., 2001; Tamura & Ohta, 2000; Tamura et al., 2000). La Barbera et al. (2003) found a mean UV-optical color gradient of -0.18 $\pm$ 0.04 mag dex^{-1}, respectively a mean optical-NIR color gradient of -0.4 $\pm$ 0.1 mag dex^{-1} for passive galaxies at intermediate redshifts ($z \sim$ 0.21 - 0.64).

At high redshifts ($z \sim$ 1-2) the color gradients of elliptical galaxies appear significantly steeper with the values reaching twice the local values (Gargiulo et al., 2011, 2012; Guo et al., 2011), implying an important contribution by an age gradient at such high redshifts (Chan et al., 2016). The reason for that behaviour may be justified with the galaxies just reaching the phase of passive evolution (De Propris et al., 2015). In the following $\sim$ 8-9 Gyrs the galaxies evolve and the age gradient tends to null, as the young, blue stars vanish and only the old, red, long-living stars remain in every region of the galaxies, with the metallicity gradient prevailing to be the reason for the color gradients at $z \sim 0$.

All these results regarding the evolution of the color gradients over cosmic time in combination with the size evolution and dependency on wavelength give reason to discount the monolithic scenario and to endorse the hierarchical/inside-out-growth model, which is in agreement with chemodynamical simulations (Kobayashi, 2004).

1.4. Stellar population synthesis

Since most galaxies can not be resolved into single stars one must resort to the use of independent stellar population diagnostics in form of evolutionary population synthesis (EPS) modelling to derive definite or at least well estimated values for the ages and elemental abundances which are correlating to the observed and measurable colors and their gradients. Once cosmological parameters, such as H_0, Ω_Λ and Ω_M are chosen, ages and metallicities derived from local observations can be used to determine the changing properties of galaxies over cosmic time (see Maraston, 2003).

The first works in this field happened already around five decades ago with the perception that colors due to their sensitivity to age can be applied to date extragalactic objects (Crampin & Hoyle, 1961), followed by the comprehensive works of Beatrice Tinsley (e.g. Tinsley, 1972), who established evolutionary population synthesis as a tool to model spectroscopic and photometric properties of galaxies. One respectively two decades later the fuel consumption theorem and the isochrone synthesis technique arose, two methods to compute the 'simplest' form of an EPS, the Simple Stellar Population (SSP) models.

The underlying assumption of these models is that all stars are formed at one epoch and hence display the same chemical composition and age. Since for globular clusters belonging to our Milky Way, ages and metallicities are independently well known, those clusters can be used to calibrate SSP models to examine extragalactic stellar properties. The fuel consumption theorem and the isochrone synthesis technique differ according to the integration variable selected in the post main sequence (PMS) phase (see Maraston, 2005). With the first method the integration variable is represented by the 'fuel', serving as a parameter for the amount of hydrogen and/or helium, which is used during the PMS phase, whereas with the isochrone synthesis the integration is done over the contributions in all wavelengths to the overall emission from all mass bins along one isochrone. Both approaches deliver similar results, although models still sometimes depend on insufficient spectral libraries, especially for non-solar computations. The only distinction in the outcome affects ages ~ 1 Gyr, based on the complicated process of mass loss of stars in advanced stages, like in the Asymptotic Giant Branch (AGB) phase, which shows models based on the fuel theorem calculations displaying higher fluxes in the NIR (Renzini, 2006).

Besides the stellar evolutionary tracks and stellar model atmospheres, with the former describing how stars with different masses and chemical compositions and

therefore their stellar parameters evolve with time and the latter determining the resulting flux, the initial mass function (IMF) is a key component for the modelling of stellar populations. This (empirical) function is an assessment of the distribution of the initial mass for a stellar population and is usually expressed in the form of a power-law with single (e.g. Salpeter, 1955) or multiple slopes (e.g. Chabrier, 2003; Kroupa, 2001). For the calculations of colors however the choice of the IMF plays a negligible role, as the majority of the emission stems from stars in a narrow mass bin, residing near the main sequence turn-off point (Renzini, 2006).

What must be considered by all means on the other hand is the degeneracy of age and metallicity, with a reduction in age and an increase in metallicity leading to a very similar spectral energy distribution in the optical range (Worthey, 1994), which can be quantified as

$$\frac{\Delta\log(t)}{\Delta\log(Z)} \sim \frac{3}{2}. \tag{1.21}$$

One photometric approach to break this degeneracy is to compare one's measurement in two different colors, one being an optical color, whereas the second color is a combination of an optical and an IR band. The first one is almost equally sensitive to age and metallicity, while the second color traces the old stellar population ($\gtrsim$ 1 Gyr), which is much more perceptive to changes in metallicity than age. Using bluer optical colors, including maybe even the NUV range, would result in a setback of breaking the degeneracy, as such colors are more sensitive to the metallicity, because of enclosing the 4000Ångstrom break (Smail et al., 2001).

2. Tools & Software

In this chapter the tools are presented, which have been used to derive results outlined in the course of this thesis. The first section describes software to detect, measure and extract the needed data. The second part outlines the means used to model the evolutionary path of galaxies using SSPs.

2.1. Parametric fitting: Source Extractor, GALFIT and Megamorph

2.1.1. Source Extractor

With the emergence of extensive surveys the need arose to detect, examine, measure and catalogue the final data products in an automatic fashion. One of today's most used software to do this task is called *Source Extractor* (SExtractor) (Bertin & Arnouts, 1996).

Given an input file, where the user can define important parameters, such as detection conditions, background measurements constraints or photometric apertures and zeropoints (see appendix for an example file, used in this work), the programme is capable of automatically detecting, deblending, measuring and classifying objects, including robust sky background measurements. It also provides a very reliable separation of galaxies and stars, as well as, if the user wishes, inspection images, with the detected objects being masked out or depicted with apertures around them.

The order of steps performed start with an estimation of the sky background, followed by thresholding and deblending, proceeding to filtering detections, executing measurements, separating galaxies and stars and finally of course writing all these results into a catalogue with optional check fits-files as well.

Due to its large automation this software is optimally suited for the analysis of comprehensive extragalactic surveys, as the evaluations include amongst other results photometric assessments in user defined apertures and determinations on positions, position angles and axis ratios.

2.1.2. GALFIT

Applying apertures directly on an image to derive photometric measurements is always a challenging method as the probability is very high that either some flux gets missed or the sources' emission gets overestimated due to the contribution of the background as well as maybe neighbouring sources. Both is caused by the fact that the extent of a galaxy is rarely known, which is especially valid for early-type galaxies, due to their intrinsic light profile, which leads to an improper choice of apertures. The whole effort gets even more complicated, if one wants to compare the same object in different wavelengths, as the extent of the source can and will presumably vary, as well as the S/N. A solution of course would be to chose one or more apertures in one band and apply them to all images, showing the source in different passbands. Unfortunately the fluxes will be under- or overestimated, depending on the wavelength in which the aperture has been chosen. The same conclusions can be drawn for size measurements, as they depend on the photometric results.

One way to evade such obstacles would be to classify galaxies with parameters, defined as a ratio of two radii containing a portion of the total emission. A widely used example would be the parameters summarized in the *CAS*-system (Conselice, 2003), describing the compactness (C), asymmetry (A) and clumpiness (S) of a galaxy. For example the compactness C is defined as the ratio of the radii containing 20 and 80 percent of the total flux, $C = 5\log(r_{80}/r_{20})$.

Nevertheless as also for these derivations and similar non-parametric methods the photometric outcomes are vital, these estimations suffer from the same biases found in aperture photometry. A completely alternative approach to avoid such problems is to fit the 2D surface brightness profiles of galaxies with parametric models. Two widely spread tools to do this task are *GIM2D* (Simard et al., 2002) and *GALFIT* (Peng et al., 2002, 2010). The advantages of such a strategy is that all measurements are done in a consistent way and especially that the problem of missing flux is greatly minimized, due to the possibility to extrapolate the best-fitting model to large radii. The disadvantage obviously is that a specific model (or several) has to be assumed a priori for the observed light profile.

As *GIM2D* results show significant higher errors in the modelling of spheroidal galaxies with close neighbouring objects, due to the inability to fit the main galaxy as well as the additional sources simultaneously, and is just rather masking the companions, which leads to overestimated values for n and is also showing a need

for more computational time (Häussler et al., 2007), *GALFIT* has been chosen to model the galaxies analysed in this thesis.

Given a simple input file *GALFIT* has the ability to extract structural parameters like the total magnitude, r_e and n via finding the best fit of a predetermined light profile to the observed one. The selection of possible 2D models include Nuker, Moffat or Sérsic profiles. The latter was used in this thesis, including the special types, Gaussian ($n = 0.5$), exponential ($n = 1$) and de Vaucouleurs ($n = 4$). One of the features *GALFIT* provides is that also a combination of profiles can be easily achieved. Consequently it is possible to specify in the input file that a source should comprise two components, one showing a de Vaucouleurs' profile, the second an exponential one, which would be a typical composition for late-type galaxies. Since only early-type galaxies are considered in this thesis, only a one-component Sérsic profile fit has been applied to the galaxies.

To find the parameters which are describing the best-fitting model *GALFIT* first convolves the model profile with a, from the user defined, point spread function (PSF), multiplying the Fourier transforms of the PSF and the models followed by an inverse transformation of them. Subsequently the convolved profiles are compared with the observed data and χ^2 minimized using the Levenberg-Marquardt algorithm. This process is iterated until convergence is reached.

The output parameters for a Sérsic profile fit are x and y, denoting the position of the source in pixels, the total magnitude, converted from the flux using the exposure time given in the FITS header of the image file and the profile being integrated to $R = \infty$, the effective radius r_e, the Sérsic index n, the axial ratio between major and minor semiaxis Q and the position angle PA. Also uncertainties for those parameters are given but they should only be recognized as lower limits as these errors only reflect the fluctuations in the residual image induced by Poisson noise (Peng et al., 2010). This aspect is mostly valid only for idealized situations, such as modelling image simulations. For real images the errors rather stem from structures within a galaxy, which have not been modelled, like spiral arms or bars.

Additional to the output catalogue multi-frame fits files are provided, including the original image, the model and the residual, which offers a visual verification of the quality of the fit.

2.1.3. Megamorph

Data products from big surveys provide information on a vast number of sources multiplied by the number of observed passbands. Of course applications and algorithms like *SExtractor* and *GALFIT* are simplifying the efforts to extract valuable scientific information out of the data. Nevertheless it would be a tedious, very time consuming and due to the sheer number count almost not manageable work to analyse every single object in every filter. Hence for the specific case regarding *SExtractor* and *GALFIT* Barden et al. (2012) developed a framework for users to - once everything has been set up - execute *SExtractor* and *GALFIT* in an automatic fashion, called *Galapagos* ('Galaxy Analysis over Large Areas: Parameter Assessment by GALFITing Objects from SExtractor').

As a result this wrapper is not only capable of executing first *SExtractor* and subsequently using these preliminary outcomes regarding structural parameters as input variables for *GALFIT*, but it also includes some optimizing modifications in regard to the analysis of large images with sources in a wide magnitude range. So the detection of objects with *SExtractor* is done in a two-way approach according to two by the user defined input files. At first a so-called 'cold' mode is performed to detect bright sources, followed by a 'hot' mode to detect the more numerous faint objects. To do this in one *SExtractor* run would not be possible as either the bright sources would be split up and detected as several individual ones or the fainter objects would simply not be detected. To estimate the extent of a galaxy the Kron radius (Kron, 1980) is used, which as a consequence means that a 'hot', so faint source is only included to the final catalogue of objects, if it is not included in any other Kron ellipse.

Furthermore *Galapagos* has the ability to create postage stamp images of the objects to minimize the time and memory needed for the fitting process and eventually also possesses an own sky estimation routine. This is done by averaging the background flux in elliptical annuli, which are centered on the respective object, while it ignores other sources or image defects contaminating the flux in the respective annuli. Hence the background flux can be expressed as a function of radius and the definitive sky value is measured at the position where the profile's slope turns positive the second time.

Finally *Galapagos* can also judge if an object can be masked in the fitting process or must be fitted simultaneously with the primary source. If the Kron ellipse of an object overlaps with the one of the desired galaxy, this neighbour will be fitted as

well, as it may have a significant influence on the light profile of the primary source. If not it will be masked and will not be considered in the fitting process.

The output is finally summarized in a catalogue listing all detected and fitted sources with their modelled parameters including uncertainties derived with *GALFIT*. Furthermore also the usual multi-frame fits files are delivered, depicting the original image, the model and the residual.

It should be noted that, while the original version of *Galapagos* needs an *IDL* runtime environment, Hiemer et al. (2014) developed a version, which can run in *C* and has been optimized in regard of computational speed and efficiency, as it is capable to parallelize the processes, which is a much needed feature for using supercomputers.

The big disadvantage of *Galapagos* is that, although it can be utilized for multi-band images, each of the passbands have to be considered separately. Therefore a lot of information gets lost, which holds especially true for images in a wavelength with a low S/N, or also clues are missed concerning the wavelength dependence of the flux of a source. To make use of this valuable information *Galapagos* has been further developed into *MegaMorph* (Bamford et al., 2012; Häußler et al., 2013).

To produce such an application a modified version of *GALFIT* has been designed, *GALFIT-M*, which is able to accept multiple input images and for which the model parameters are replaced by wavelength dependent Chebyshev polynomials, with the Chebyshev coefficients being the fitted parameters in the respective passbands. The degree of the polynomials may be defined by the user, ranging from the parameters being constant over all wavelengths to being completely independent. Hence the user can decide to which extent the values for each fitted parameter are connected to each other.

The required input file(s) (see appendix for an example) are very similar to the ones needed to run the original version of *Galapagos*. The only differences are obviously that now images for all bands must be declared and that additionally on one hand one must define one extra band for the *SExtractor* run, which could also be a coadded image to increase the number of detections, and on the other hand one image for deblending and masking.

Also the efficiency has been improved, which results in a factor 4 of less needed CPU time. This has been partially achieved by refining the loop routine. In the original version of *Galapagos* the algorithm postpones the fitting procedure for the next object, if it is contaminated by the object, which is currently fitted. *MegaMorph*

avoids this by skipping this particular source and returning to it as soon as it is safe to fit it.

The most improvement with modelling the galaxy parameters as a function of wavelength is that the user can select a balance between consistency and flexibility. With well chosen input parameters images in bands with low S/N can profit from constraints of images with higher S/N. This leads to more robust measurements, which are conveyed with more useful magnitude assessments for faint galaxies, as well as improved results for sizes and n, especially in comparison to single-band fits. Hence it is possible to conduct a more precise analysis of colors and color gradients within a galaxy, which is particularly of great importance for this thesis.

2.2. Stellar population modeling: EzGal

To be in the position to compare the observed parameters like magnitudes and colors to the modelled ages predicted by SSP calculations, the `Python` wrapper *EzGal* (Mancone & Gonzalez, 2012) has been used in the course of this thesis.

It offers the possibilities to calculate the evolution of a stellar population over redshift, based on different models (e.g. BC03, Bruzual & Charlot (2003) or M05, Maraston (2005)) and varying initial conditions in regard to star formation history, IMF, metallicity or formation redshift. Moreover it is also possible to interpolate between metallicities for a certain set of models. The included filter set contains passbands ranging from the UV, such as *GALEX* filters to optical ones, used by *HST* or *SDSS* to IR bands, utilized for example by *Spitzer* or *WISE*. However the addition of extra filters poses no problem as the user can simply add filters by providing *EzGal* the respective response curves. Magnitudes can be produced in the Vega and AB photometric system, the latter being deployed in this thesis.

A comparison of the synthesis results of an SED evolution between the different models shows that there is a good agreement in the optical wavelength range for old models possessing solar metallicities, with a difference of about 0.1 mag. Turning however to younger ages (< 2 Gyr) and longer wavelengths (> 7500 Ångstrom) the differences increase significantly, presumably due to thermally pulsating AGB stars (Mancone & Gonzalez, 2012), which are differently treated in the various models.

EzGal derives the magnitude evolution over redshift from models, which are describing the SED evolution over age. So based on the default or user defined cosmological parameters, besides the absolute and apparent magnitudes in rest-frame,

EzGal can also derive those magnitudes in the observed frame, which are calculated using the redshift-dependent k-correction (Hogg et al., 2002a). Hence the measured apparent magnitudes in a certain wavelength and colors of the observed galaxies can directly be compared to the modelled values in the same filters at a certain redshift, which would be for this particular analysis the respective cluster redshifts. This in turn makes it possible to infer the corresponding ages and metallicities of the stellar population residing in the galaxies, after careful consideration of the age-metallicity degeneracy.

The concordance cosmology is adopted in this thesis with $H_0 = 70$ km s^{-1} Mpc $^{-1}$, $\Omega_\Lambda = 0.7$ and $\Omega_M = 0.3$ (Spergel et al., 2003).

3. Data

3.1. CLASH

The major part of the data used in this thesis is provided by the 524 orbit *HST* Multi-Cycle Treasury Program *The Cluster Lensing And Supernova survey with Hubble* (CLASH) (Postman et al., 2012). By observing and examining 25 massive galaxy clusters with 16 *HST* filters ranging from near-UV to the near-IR four main goals should be achieved with this program:

- The derivation of accurate measurements of the mass distribution and substructures of dark matter in those clusters. These are obtained by combining the *HST* measurements with weak lensing maps derived from wide-field *Subaru* images produced by *Suprime-Cam* in the bands B, V, Rc, I and z', as well as mm and X-ray images. This wide spectrum of wavelengths, as well as the large field of view allows constraining the mass profiles of the clusters out to large radii, including precise assessments of the central density concentrations together with constraints in regard of the dark matter substructure distribution derived by galaxy-scale lensing.

- The detection of SN Ia out to a redshift $z \sim 2.5$ in order to measure the time dependence of the dark energy equation as well as a possible redshift dependence in the SNe themselves. To accomplish this goal the observations of each cluster are stretched over eight epochs with each cluster being observed at two orientations, which are approximately 30° apart to reduce the overlap between the parallel ACS pointings (Fig. 3.1). At one point ACS observes the respective cluster core, whereas WFC3 views the surrounding parallel fields followed by a reversed observational setup. Thus the observations of the clusters and the search for SNe are done in a parallel mode.

- The utilization of the cluster's lensing capabilities to identify high redshift ($z > 7$) galaxies.

– The gain of additional information about the internal structures of the clusters along with clues regarding the evolution and therefore also possible formation scenarios of the cluster galaxies, as well as galaxies lying behind those clusters in redshift space. This can be achieved by utilizing the 16 different bands, resolving besides possible particular features especially different stellar populations. Hence with this knowledge of the internal structures of galaxies their evolution can be inferred.

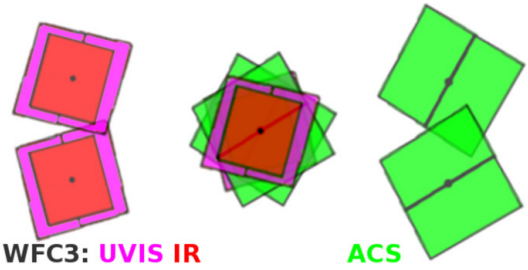

Figure 3.1.: Fields covered by the CLASH observations, which are done twice at two different orientations $\sim$ 30°apart. While the cluster core is observed with ACS, the parallel fields are observed with WFC3 and vice versa. Taken from (Postman et al., 2012).

All 25 clusters in the sample are massive, with masses of $5 \times 10^{14} < M_{vir}/M_{\odot} < 3 \times 10^{15}$, with the cluster-centric redshifts being in the range $0.18 \lesssim z \lesssim 0.9$ with a median redshift $z \sim 0.4$. Out of those 25 clusters 20 were exclusively X-ray selected, with $kT > 5keV$, and five additional clusters were included solely due to their high lensing strength, revealing Einstein radii up to $55''$, to enhance the likelihood of finding high redshift galaxies. Yet at least in 18 of the 20 X-ray selected clusters one or more giant arcs are visible, corresponding to Einstein radii in the range $15''$ to $30''$. The supplementary five clusters are not necessarily relaxed, which is definitely the case for one of the clusters discussed in this thesis, MACS J0416.1-2403.

However most clusters of the X-ray selected sample appear as dynamically relaxed structures as can be confirmed by images done with the *Chandra X-ray Observatory*. They exhibit a well-defined central surface brightness peak and nearly concentric isophotes. Furthermore these observations are supported by X-ray pressure maps, showing almost no deviation from a hydrostatic equilibrium. In fact 14 clusters, including those two, which are analysed in this thesis, were initially detected by the X-ray cluster survey *MAssive Cluster Survey* (MACS) (Ebeling et al., 2001), intended to compile a large, unbiased sample of X-ray luminous, distant clusters with luminosities $L_X \gtrsim 5 \times 10^{44}$ erg s^{-1} (0.1 - 2.4 keV) and redshifts $z \gtrsim 0.3$.

To accomplish the ambitious goals of *CLASH* a total of 16 broadband filters (Fig. 3.2), ranging from near-UV to near-IR ($\sim$ 2000 - 17000 Å) using the *ACS (WFC)*

for its greater throughput efficiency, especially regarding the red wavelength regime, and *WFC3 (UVIS/IR)* detectors are deployed. The region covered by the *ACS* filters spans 4.08 arcmin^2, with the *WFC3/IR* field of view being 88 percent of this area.

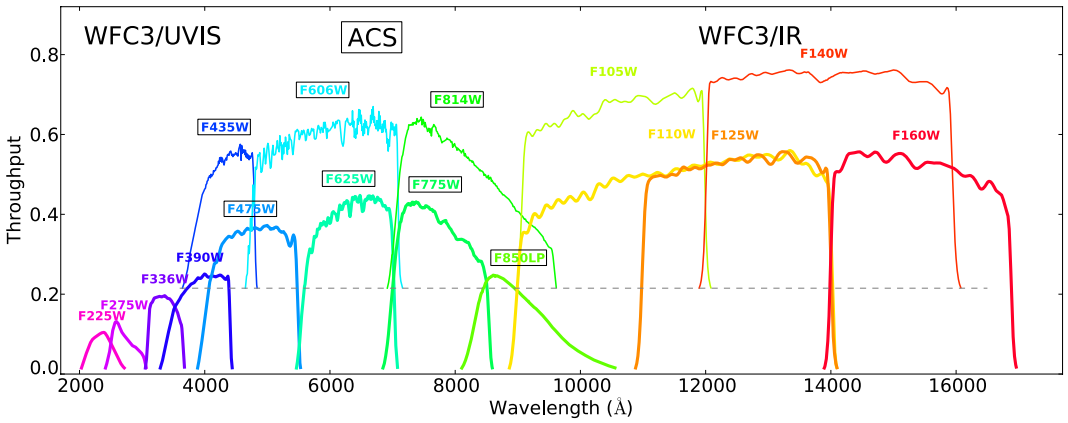

Figure 3.2.: Response curves for the filters used in the CLASH survey ranging from near-UV to near-IR. Just for clarity some filter curves show an offset of 0.2 (dashed line). Plot taken from (Postman et al., 2012).

Table 3.1 lists the central filter wavelengths as well as the limiting magnitudes in the AB photometric system (Oke (1974); Oke & Gunn (1983)) for extended sources at 5σ, which are the mean limits averaged over all extended sources (i.e. galaxies) not considering the sizes of the respective objects (Jouvel et al., 2014).

Table 3.1.: The central wavelengths of the HST filter set used in the CLASH survey and the respective 5σ magnitude limits for extended sources. (Magnitude limits taken from (Jouvel et al., 2014))

Detector	Filter	λ_c [Å]	(5 σ) [AB mag]	Detector	Filter	λ_c [Å]	(5 σ) [AB mag]
WFC3/UVIS	F225W	2359	24.8	ACS/WFC	F775W	7764	26.5
WFC3/UVIS	F275W	2704	24.9	ACS/WFC	F814W	8333	27.5
WFC3/UVIS	F336W	3355	25.2	ACS/WFC	F850LP	9445	26.2
WFC3/UVIS	F390W	3921	26.1	WFC3/IR	F105W	10552	27.0
ACS/WFC	F435W	4297	26.2	WFC3/IR	F110W	11534	27.6
ACS/WFC	F475W	4760	26.7	WFC3/IR	F125W	12486	27.1
ACS/WFC	F606W	5907	27.2	WFC3/IR	F140W	13923	27.3
ACS/WFC	F625W	6318	26.6	WFC3/IR	F160W	15369	27.2

The images were subsequently cleaned, processed, aligned and co-added using the MosaicDrizzle software (Koekemoer et al., 2011) fixing for cosmic ray contamination and working out shifts and rotations. Additionally the exposures were corrected for galactic extinction using IR dust emission maps (Schlegel et al., 1998). The images have a scale of $0.065''$ per pixel with north being upwards and are normalized to counts s^{-1}.

With this abundance of photometric measurements it is possible to derive precise and reliable photometric redshift measurements. This has been done using Le Phare as well as BPZ packages, with the result that both codes show a similar assessment of the photometric redshifts for galaxies in the cluster as well as in the foreground (Jouvel et al., 2014).

Finally it must be noted, that for this thesis the WFC3/UVIS bands were discarded, due to their low S/N, which left 12 bands for the analysis.

3.2. CLASH-VLT

CLASH-VLT is an ESO Large Program, titled *'Dark Matter Mass Distributions of Hubble Treasury Clusters and The Foundations of ΛCDM Structure Formation Models'* (Rosati et al., 2014) and a follow-up of the CLASH survey using the *VIsible MultiObject Spectrograph* (VIMOS) instrument (Le Fèvre et al., 2003) at the ESO-VLT on 13 clusters already observed photometrically with CLASH at $z \sim 0.2 - 0.6$ (median $z \sim 0.4$).

The intention has been to obtain spectroscopic data to be able to identify 500 to 1000 member galaxies for each cluster and over 200 background galaxies with $z \lesssim 7$. This grants the opportunity to determine the cluster's mass density profiles by dynamical analysis of the cluster members and to compare and combine those results with independent mass profile measurements obtained from strong and weak gravitational lensing using Subaru *Suprime-Cam* images or X-ray studies out to a radius of approximately 3 Mpc. Furthermore this dataset also offers the possibility to probe the composition of the inner dark matter structure of the cluster halos.

Twelve masks were utilized, eight with a low resolution ($R = 180$) blue grism between 370 - 670nm and four with medium resolution ($R = 580$) grism in the range of 480 - 1000nm for high-redshifted lensed sources. The observations were done with 8 - 12 separate pointings for each cluster, with one quadrant being fixed focusing on the respective cluster cores to increase the exposure time in order to

detect also the faintest lensed objects. The field of view covers 15 - 20 arcmin^2, which corresponds to $\sim$ 10 Mpc at $z \sim 0.4$. The total exposure time amounts to approximately 200 hours, which leads to the final dataset for all clusters consisting of $\sim$ 30000 spectra with $\sim$ 7000 being cluster members.

The obtained dataset has been reduced using the VIMOS Interactive Pipeline and Graphical Interface (VIPGI).

3.3. MACS 1206

The primary object and first cluster of study in this thesis is MACS J1206.2-0847 (MACS 1206 in the following). Inferring from X-ray observations revealing an X-ray luminosity of $L_X \sim 2.4 \times 10^{45}$ erg s^{-1}, the cluster appears to be in a relaxed state, with the central BCG at $\mathrm{RA}_{2000} = 12^h06^m12^s.15$ and $\mathrm{Dec}_{2000} = -8°48'3.''48$ located at the same position as the peak of the X-ray emission and the, from gravitational lensing determined mass center (Umetsu et al., 2012). Furthermore the mass profiles derived on one hand from dynamical and on the other hand from strong- and weak-lensing methods (Zitrin et al., 2012) are in excellent agreement, with MACS 1206 revealing a virial mass of $M_{200} \sim 1.4 \times 10^{15} M_\odot$ and a virial radius of $r_{200} = 1.98$ Mpc (Biviano et al., 2013), with the '200' subscript referring to the radius where the average density equals 200 times the cosmic mean density at the cluster redshift.

Nevertheless MACS 1206 exhibits a significant, not centrally concentrated, WNW-ESE elongated intracluster light (ICL) component, indicating that interactions between galaxies are still ongoing, resulting in tidal disruptions feeding the ICL, despite the overall relaxed appearance (Eichner et al., 2013). This assessment can be supported by the examination of the stellar mass profile, with the ratio of giant ($M_*/M_\odot > 10^{10.5}$) to subgiant galaxies ($10^{9.5} < M_*/M_\odot < 10^{10.5}$) being at the highest in the innermost regions (> 0.5 Mpc) just to drop to its minimum in the adjoining region (0.5 - 1 Mpc) (Annunziatella et al., 2014). Also the presence of red galaxies showing a strong Hδ absorption, indicating a recent star formation event 1-2 Gyr ago, in the center and along the ICL, implies recent or even ongoing interactions on galaxy scales (Girardi et al., 2015; Mercurio et al., 2015; Presotto et al., 2014).

3.3.1. Selection

The initial selection of the member galaxies (Fig 3.4) of MACS 1206 is based on the analysis and identification by Biviano et al. (2013).

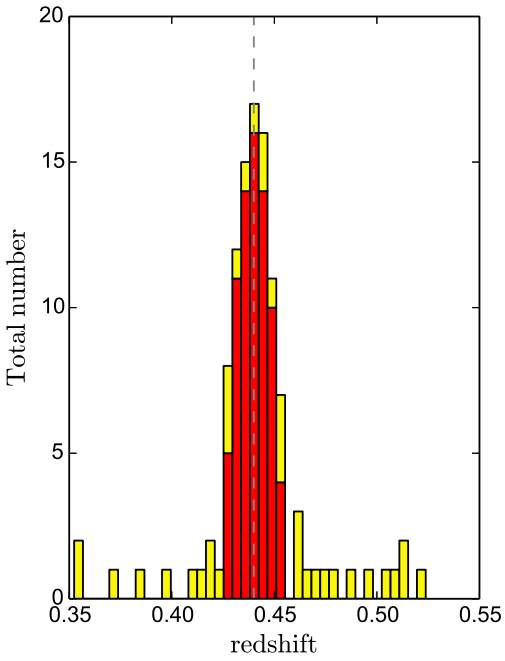

Figure 3.3.: Redshift distribution of the initial selection for MACS 1206. Red shows galaxies with spectroscopic redshift determinations, yellow the ones with photometric redshift estimates. The gray dashed line indicates the cluster redshift at $z \sim 0.44$

Using the spectroscopic results obtained by the *CLASH-VLT VIMOS* program it was possible to determine 600 member galaxies in the *Subaru* field belonging to the cluster via the analysis of their locations in the projected phase space, R and v_{rf} and applying a 'clean' as well as for comparison a 'peak + gap' algorithm.

Aside from that, by utilizing *Subaru's Suprime-Cam's* 5 bands additional photometric redshifts have been derived. Possible cluster membership of galaxies with just photometric but no spectroscopic redshift determinations has been investigated by using a comparison between galaxies possessing z_{spec} and z_{phot} measurements as well as color-color cuts in $R_C - I_C$ vs. $B - V$ (see also Annunziatella et al., 2014), which yields a redshift range of $0.34 < z_{phot} < 0.54$ for galaxies to be in to be defined as cluster members.

Using these membership determinations, combined with the photometric Le Phare redshift determinations by Jouvel et al. (2014) and the *SExtractor* catalogue for the ACS F814W band provided by the *CLASH* collaboration[1], resulted in an initial selection of galaxies visible in the *HST* footprint for the analysis of MACS 1206.

This selection contains 216 sources, but as the field of view of WFC3/IR is significant smaller, all galaxies, which are just being detected in the ACS field of view have been discarded to optimize the accuracy of the output of the modelling process.

[1] https://archive.stsci.edu/prepds/clash/

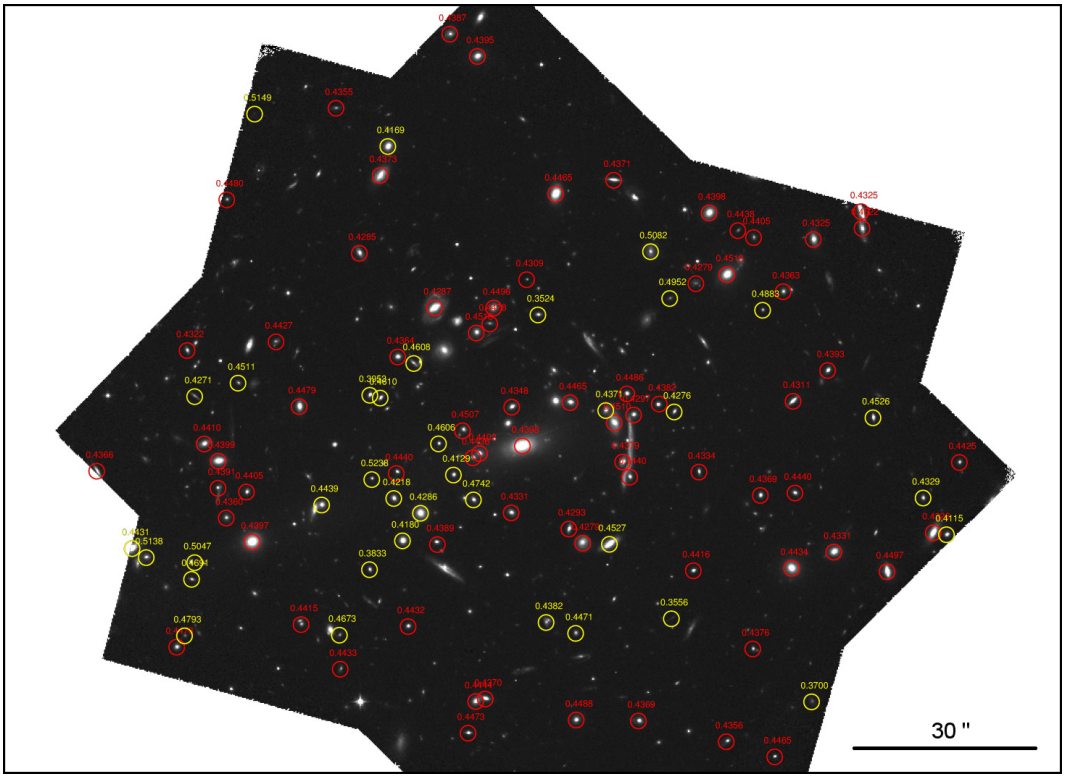

Figure 3.4.: MACS 1206 in the WFC3 F105W band, depicting the initial selection of galaxies to be fitted, distinguished in a sample with spectroscopic redshift determinations (red circles) and photometric redshift estimates (yellow circles).

Doing this cut leaves a total of 110 galaxies (Fig. 3.4) for the fitting process, with 74 possessing a spectroscopic derived redshift, while 36 only have photometric redshift determinations. Fig. 3.3 depicts the redshift distributions of those galaxies, with red showing the spectroscopic and yellow the photometric determined member galaxies. As expected the peak of the distribution is at the cluster redshift of $z \sim 0.44$ indicated by the gray dashed line.

As the field of view of WFC3/IR encompasses less than half of the virial radius r_{200} the galaxies are well located in the innermost regions of the cluster and are evenly distributed as can be seen in Fig. 3.4. This should avoid any biases, i.e. contamination by the ICL, orientation or location in the cluster. At the cluster redshift one arcsecond corresponds to ~ 5.67 kpc.

3.4. MACS 0416

The second cluster examined in this thesis and being one of the five particular clusters in the *CLASH* survey selected due to its high magnification abilities is MACS J0416.1-2403 (MACS 0416).

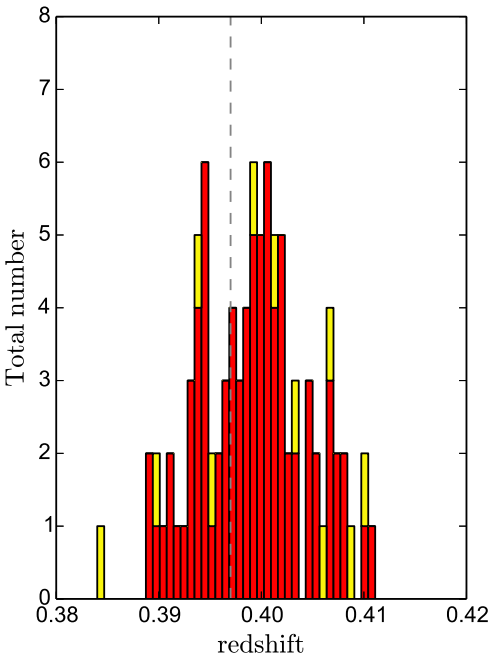

Figure 3.5.: Distribution of sample galaxies in redshift for MACS 0416. The double peak structure is clearly visible. The cluster redshift $z \sim 0.397$ is depicted as the gray dashed line.

Lying at a redshift z $\sim$ 0.397, this system shows a complex structure revealing two subclusters with two BCGs separated by $\sim$ 250 kpc (Ogrean et al., 2015). Despite the clearly, in X-ray visible unrelaxed state of the cluster, the mass profiles derived from galaxy dynamics are in good agreement with the results obtained by strong and weak lensing, as well as X-ray measurements, displaying an X-ray luminosity of $L_X \sim 7.4 \times 10^{44}$ erg s^{-1}. The overall virial mass amounts to $M_{200} \sim 0.9 \times 10^{15} M_\odot$, the virial radius to $r_{200} = 1.82 \pm 0.11$ Mpc (Balestra et al., 2015). With the complex dynamical state of the cluster but its dark matter and gas component being well aligned, it can be assumed that the cluster is in a pre-merging phase. The mass center appears to lie nearly halfway between the two BCGs, nevertheless, following Balestra et al. (2015) the cluster center is adopted to be the NE-BCG at $\mathrm{RA}_{2000} = 04^h16^m09^s.14$ and $\mathrm{Dec}_{2000} = -24°04'03.''1$ coinciding with the peak position of the X-ray emission.

3.4.1. Selection

As is the case for MACS 1206 also for MACS 0416 the basis of the membership determinations for galaxies are the results of the *CLASH-VLT* program.

After comparing the observed spectra with template spectra using the software

EZ and visual inspection of outliers resulting in a final dataset of 4386 redshift determined sources, distributed over the whole *Subaru* field, Balestra et al. (2015), following the approach of Biviano et al. (2013) for MACS 1206, applied the 'peak + gap' method, which yields two overlapping peaks in redshift distribution at $z \sim 0.396$ and $z \sim 0.400$, confirming the complex structure of the cluster.

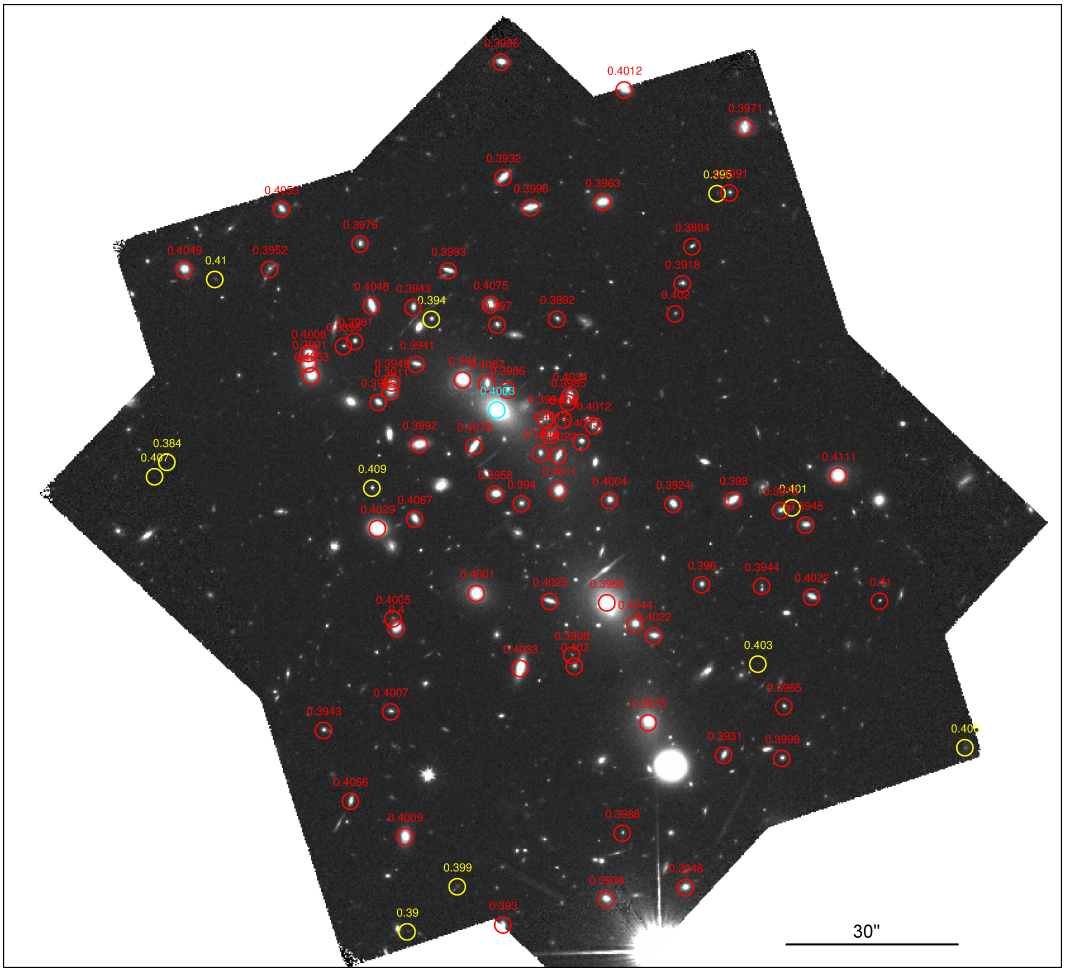

Figure 3.6.: Initial sample selection for MACS 0416. Spectroscopic members are shown with red circles, galaxies with photometric redshifts with yellow circles. The NE BCG, also possessing a spectroscopic redshift determination, is indicated by a cyan circle.

Changing the position of the cluster center from the location of the NE BCG to the position of the barycenter ($\mathrm{RA}_{2000} = 04^h16^m08^s.60$ and $\mathrm{Dec}_{2000} = -24°04'25.''2$) leads to a negligible impact on the selection of galaxies belonging to the cluster, as only galaxies at radii larger than 5' are affected. Hence this factor can be ignored in

this thesis, as only galaxies within the *HST* field of view, which corresponds to less than half of r_{200}, are considered.

Finally employing a 'simple isothermal sphere' model with the center of the cluster being the position of the NE BCG results into a final redshift range of 0.381 $\lesssim z \lesssim$ 0.411. Combining these constraints with *SExtractor* catalogues including photometric redshifts (Jouvel et al., 2014) from the *CLASH* pipeline results into a preliminary selection of 179 galaxies, with 134 possessing spectroscopic data and 45 only photometric redshifts.

Eliminating the galaxies, which are only visible in the ACS field leads to an initial sample containing 92 galaxies, 81 of them having spectroscopic derived redshifts, while 11, mostly very faint sources, got only photometric measurements.

The collection of galaxies chosen to be modelled are shown in Fig. 3.6, with sources surrounded by a red circle including the NE BCG indicated by a cyan circle being spectroscopic measured, whereas the yellow circles denote the photometric assessed galaxies. Evident is the cluster's orientation in NE-SW direction, as well as the diffuse intra cluster-light following this elongation.

The redshift distribution of the dataset is depicted in Fig. 3.5, illustrating the apparent double peak in redshift-space, with the gray dashed line indicating the cluster redshift at $z \sim 0.397$. The color coding is still the same, for galaxies with spectroscopic measurements being represented by the red bars and photometric ones by yellow bars. Due to the slightly lesser distance of MACS 0416 in comparison to MACS 1206 one arcsecond corresponds in this case to ~ 5.39 kpc.

4. Modelling of galaxies

As the focus lies on early-type galaxies and to keep the computational time to a reasonable amount, the choice has been made to fit the sample galaxies with a one-component fit, i.e. a singular Sérsic profile. Although this may seem to be an oversimplification, single component fits have already proven to be sufficient to describe elliptical galaxies (e.g. Häußler et al., 2013), usually by adopting on average $n \sim 4$ for the Sérsic profile.

Due to the big variety even within the spheroidal galaxy population, the modelling of galaxies can be a very delicate task. Using *MegaMorph*, a wrapper for *SExtractor* and *GALFIT* (see Chapter 2), the user has the opportunities to specify and adjust numerous parameters and input variables in regard to a particular scientific scenario in order to optimize the robustness of the output.

The starting point is to detect all the desired sources, which should enter the fitting process. Due to the big dynamical range in magnitude this can pose a challenging exercise, although *MegaMorph* provides a two-way method performing *SExtractor* twice with different setups. The first run intends to detect the bright sources, whereas the second run is used to include the faint ones. Even with this feature this method has to be executed several times in order to identify all the faint objects aimed for, without splitting the brighter ones into numerous sources. An example of a *SExtractor* input file is given in the appendix. The most influential parameter in this regard is `DETECT_MINAREA`, which holds the value of coherent pixels of a source needed, to be identified as such.

Unfortunately for MACS 0416 nine sources could not be included in the subsequent fitting process due to their low surface brightness and also partially due to the very prominent ICL. This leads to a reduced sample for this cluster with 83 objects. However those nine rejected sources were nevertheless much too faint to derive any reasonable results and would be therefore discarded in the subsequent analysis anyway.

Before finally commencing the multi-band fitting routine, PSF models have to be provided for each band. The PSFs used for the modelling processes outlined in this

thesis have been contributed by Alberto Molino, who produced them as part of his PhD thesis[1]. In order to create them he has examined all 25 *CLASH* clusters looking for potential stars and eventually ended up with $\sim$ 200, visually selected possible candidates. After making sure that each individual star is visible in all 16 *HST* filters, not saturated in any of these bands and within an area of 25 pixels free of any contaminating neighbours, he obtained a final sample of $\sim$ 70 stars. Ultimately they have been combined and normalized to compose an average model for each band by combining stars from different positions in the image. This procedure is adequate, as the PSF of *HST* is almost invariant in regard of time, as well as position, so one PSF is sufficient for each band.

The last part of the preparations concerned the setup of the *GALFIT M* algorithm itself. A complete input file is included in the appendix, showing the different parts of the setup, i.e. inputs for the *SExtractor* runs, the creation of postage stamps, the sky determination, the actual modelling using *GALFIT M* and finally the output catalogue. As it would exceed the scope of this chapter to explain every single input variable, only the most important variables, which are influencing more or less the output and are apparently mainly but not only situated in the *GALFIT M* part of the setup, are described.

Although *GALFIT* offers the possibilities to fix or even to fit the sky background by itself, *MegaMorph* makes no use of this option. It rather calculates the background flux using a different method and keeps it fixed during the subsequent fitting process, which appears to be the more reliable approach (Häussler et al., 2007). By averaging the emitted background flux in increasing elliptical isophotes around the current object with masking interfering neighbouring objects, *MegaMorph* is able to derive the background flux in dependence to the radius. The final sky estimate is eventually the value, where the slope of this function turns positive for the second time. Of course these assessments can be manipulated by several parameters, such as the number of the sky measurements included to calculate the slope, in the setup file defined in `D12`, the distance between, as well as the width of the annuli specified in `D06` and `D07`, the initial radius `D08` or also the minimum separation between two sources set in `D19`.

The most important parameters however are placed in the *GALFIT* part, being indicated by an 'E' in front. `E11` constrains the maximum attainable r_e and is very generously defined with 400 pixels in this thesis, a value which is never even nearly

[1] http://www.iaa.es/sites/default/files/MOLINO%20BENITO.pdf

reached. `E14` and `E15` represent the minimum and maximum limits of n, for this work set to 0.2 and 8, as galaxies with higher n are hardly observed, and `E19` holds the value of maximum minutes allowed to model a galaxy.

Nonetheless the big feature distinguishing *MegaMorph* is its ability to utilize the images in all input bands simultaneously in order to derive a wavelength dependent model for each galaxy. This is achieved by replacing the model parameters by wavelength dependent Chebyshev functions. The degrees of freedom of those polynomials can be specified (`E20`), enabling the user to set parameters from constant to completely independent in regard to wavelength. For the fits carried out in this thesis the centre position of a galaxy in the form of x and y coordinates, as well as its axial ratio and position angle are considered constant over wavelength. The reason for fixing the latter two parameters is to avoid artificial color gradients, which may be introduced due to different shapes and/or orientation. The structural parameters r_e and n are assumed to be best described by a second order polynomial, although a linear function is expected to be sufficient for the brightest elliptical galaxies (Häußler et al., 2013). To obtain the most accurate measurements for magnitudes no constraints are given, hence the magnitudes in the different bands can vary completely independent from the wavelength.

It is obvious that due to this multitude in variables the values have to be chosen carefully and in consideration of their impact on the end result. Hence several test runs, with smaller sample sizes were performed in order to obtain the best models. Unfortunately due to the amount of computational time with a cluster requiring several weeks to be completely done (and eventually also licensing issues) a comparison with two-component fits could not be achieved, but would pose a very interesting project.

Eventually the fitting process has been successful for 103 of the 110 galaxies selected in MACS 1206. For the 7 galaxies left, 4 of them possessing spectroscopic measurements, the remaining 3 only photometric assessments, the maximum time allowed to derive a model has been exceeded, which resulted in an omission of those objects.

Unfortunately for MACS 0416 the results are much worse, with only 42 galaxies being successfully fitted in the initial run. The reason for *GALFIT* failing to model such a high number of galaxies lies in the prominent ICL in the center of the cluster. Due to the intense background an extensive part, if not the entire image with all the objects residing in it is fitted by *MegaMorph*, due to their contribution to the

light distribution of the current processed source. This increases the computational time for even just one galaxy to a minimum of several days, which in turn exceeds by far the maximum time allowed to fit a galaxy. In order to raise the number of galaxy models this maximum time parameter had been increased several times in subsequent runs, as well as the number of objects selected for each run had been constraint to a handful. This method has allowed to obtain additional 16 model fits, resulting in a final number of 58 galaxies. Regrettably it has not been possible to finish the analysis over the total sample due to a missing *IDL* license.

An example output by *GALFIT* is shown in Fig. 4.1. The left column displays the example galaxy in the respective postage stamps of the different filters, in the middle column the corresponding models are shown, while eventually the right column depicts the various residuals. Clearly visible is the increase in flux with increasing wavelength, indicating that an old stellar population is observed. As the data images further possess the same flux scaling, also the growth in S/N towards redder filters is obvious.

The results of the fits are shown in the form of a color-magnitude diagram in Fig. 4.2. The coloured points represent the fitted galaxies, depicting their apparent integrated magnitude in the AB photometric system in Y_{105} on the x axis and their $r_{625} - Y_{105}$ color, corresponding to $B - I$ in rest-frame, on the ordinate. The points themselves are color coded according to the derived Sérsic index n of the galaxies, with blue indicating the lower end, while red denotes the high-n objects.

The underlying gray dots are the corresponding measurements taken from the *CLASH SExtractor* catalogue, depicting all sources, independent of redshift, which are visible in the WFC3/IR field of view. The good agreement in regard of the location of the clearly recognizable red sequence proves the good quality of the *MegaMorph* results. Furthermore it is fairly obvious that the majority of the fitted objects lies in the red sequence and possesses n values corresponding to early-type galaxies. This observation meets the expectations, as the focus lies on the innermost part of the cluster, which is supposed to be populated mainly by bright, massive elliptical galaxies.

The subsequent analysis required a separation in early and late type galaxies, which has been achieved by combining two different methods. Following several publications (e.g. Shen et al., 2003; Barden et al., 2005; Vulcani et al., 2014) the galaxies have been separated at first by their n measurements in F814W, which has been the reference band for the fit, with the distinction being drawn at $n = 2.5$.

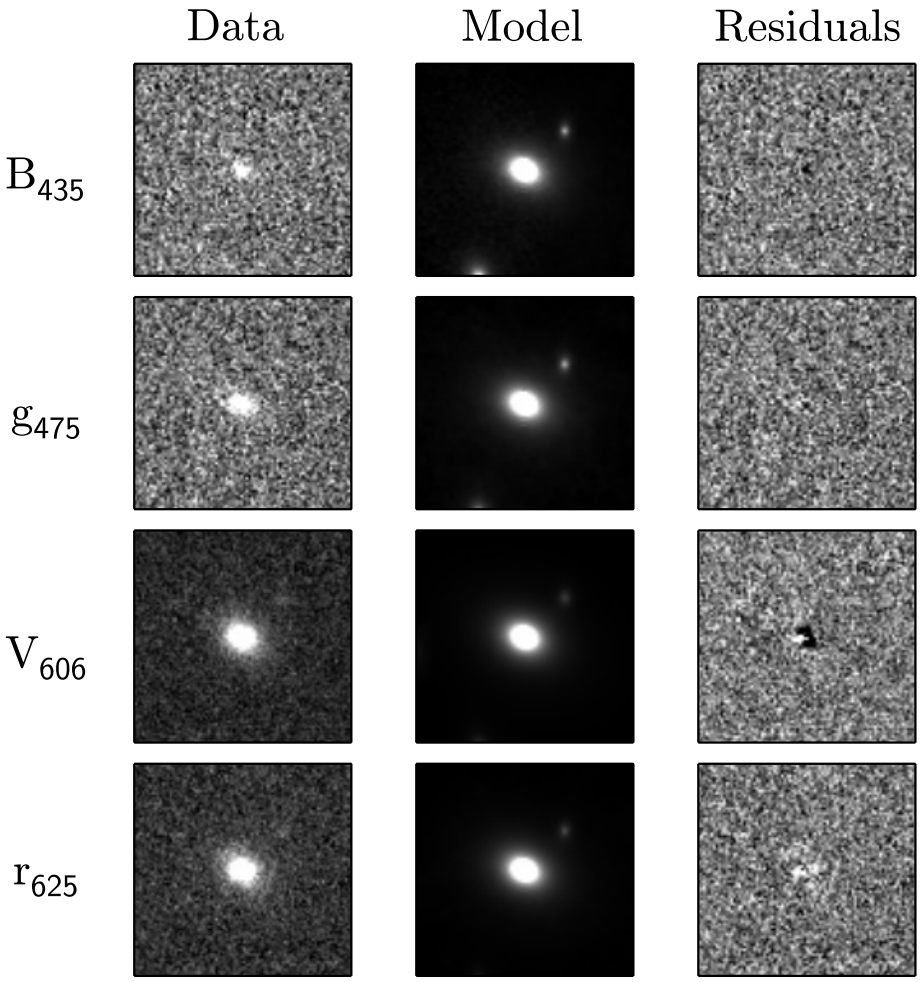

Figure 4.1.: Example of a multi-band *GALFIT* fitting output for a galaxy of the MACS 1206 sample. From left to right: Original input images, models and residuals for the respective fits. The scaling of the images is matched, which in turn also illustrates the different detection levels in the different filters.

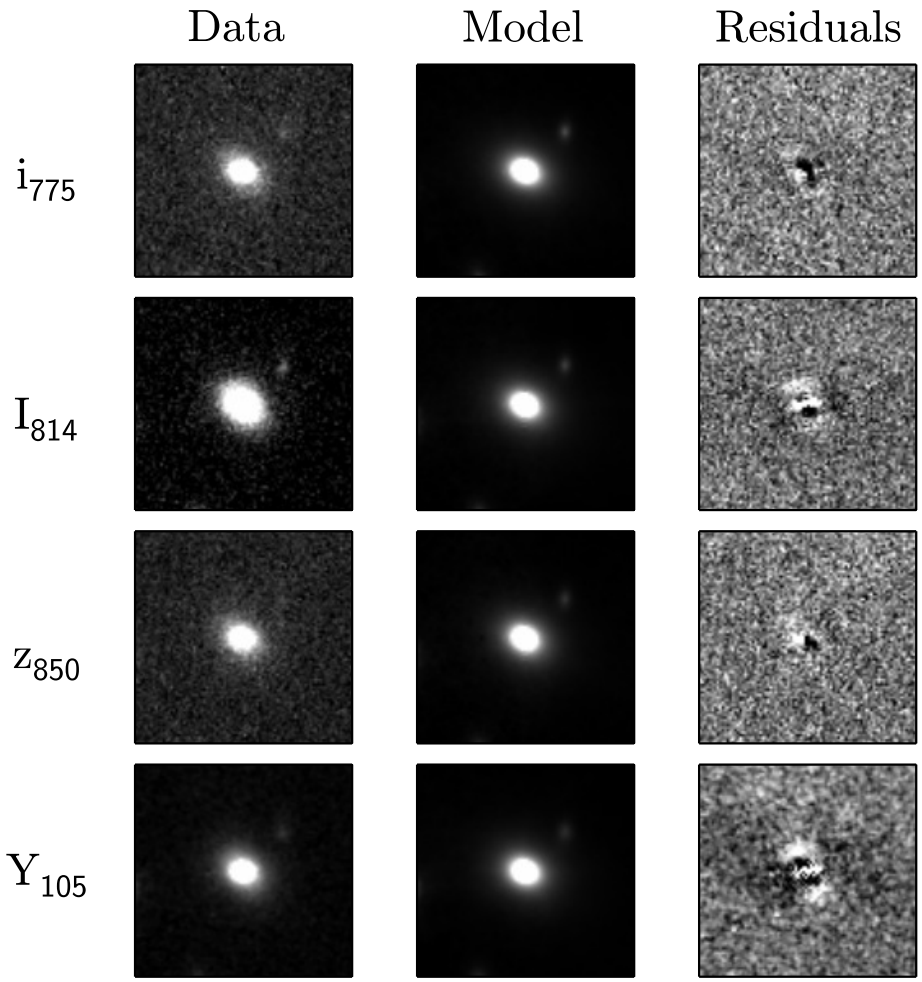

Figure 4.1. (cont.)

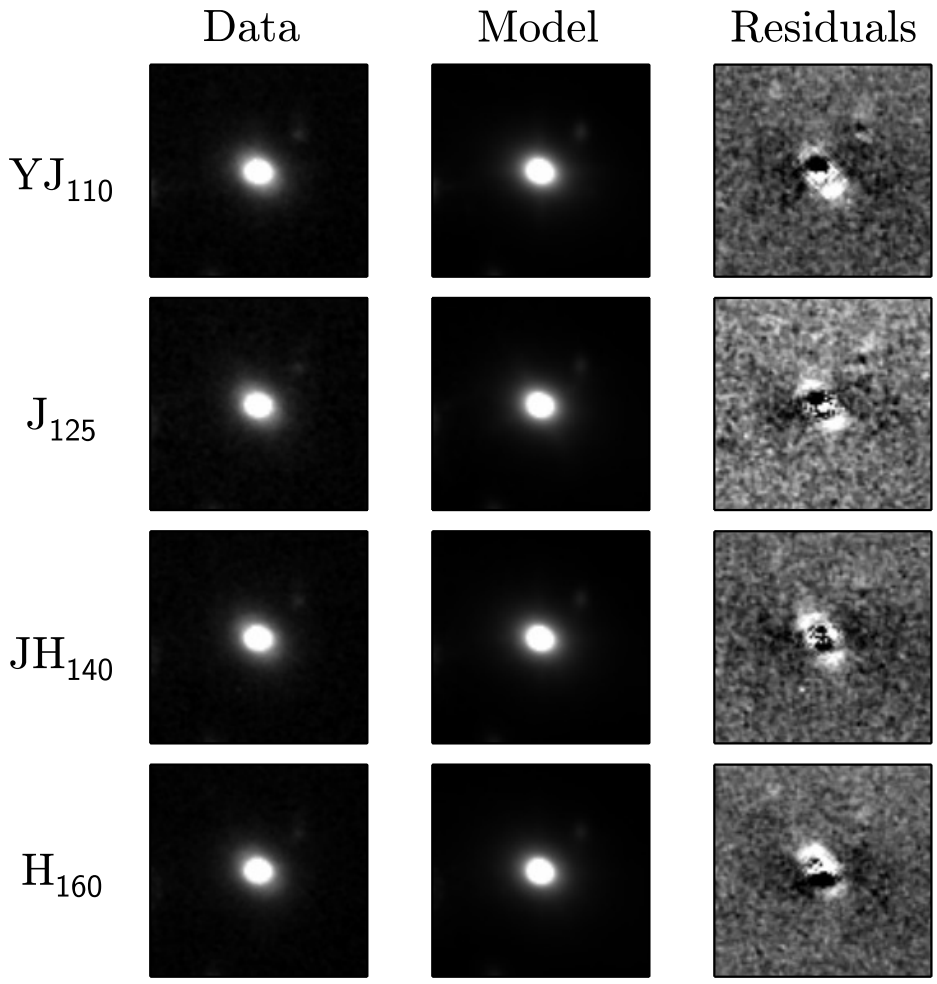

Figure 4.1. (cont.)

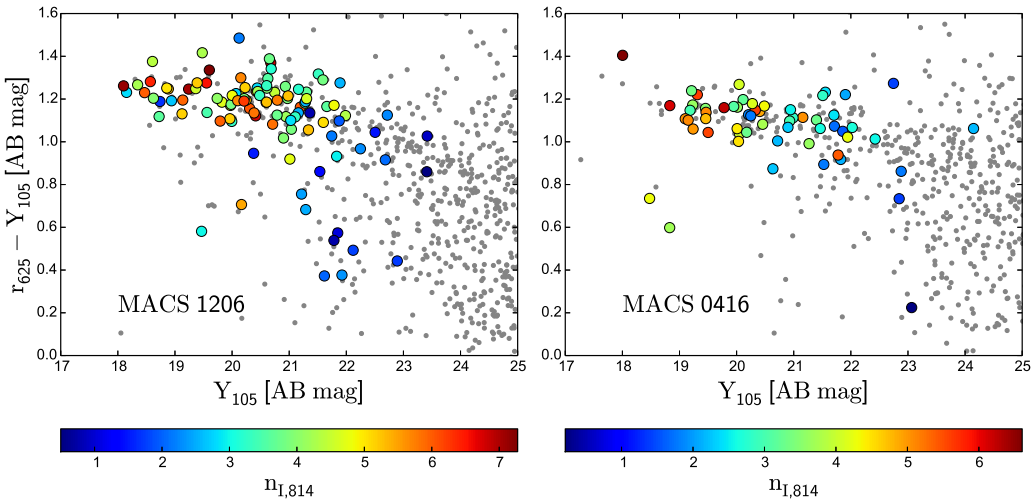

Figure 4.2.: Color-magnitude diagrams for MACS 1206 (left) and MACS 0416 (right). The gray dots represent all detected sources in the WFC3/IR field of view, overlayed by the fitted galaxies, color coded according to their Sérsic index n.

Hence galaxies with $n < 2.5$ have been discarded from further considerations. Additionally a visual inspection of the sources in the F814W band has been performed three times for each cluster, with the objects being examined each time in a different order. As a result all galaxies displaying $n \gtrsim 2.5$, but showing spiral or peculiar features are being rejected as well. Applying these constraints leads to two final samples, one for each cluster, consisting of 79 galaxies (57 of them spectroscopically analyzed) for MACS 1206 and 38 galaxies (37 of them possessing spectroscopic measurements) for MACS 0416. The tables containing the determinations in total magnitude, r_e and n for both clusters can be found in the appendix.

With the deduction of the magnitude and the structural parameters r_e and n for each galaxy in each band it is now possible to analyze the variation of those values over wavelength. Additionally it is feasible to produce the respective surface brightness profiles based on the model arguments for each selected galaxy in each observed filter. This eventually has been achieved by utilizing the formula (1.9) and all the pre-calculations necessary presented in section 3 of chapter 1 (Fig. 4.3). The 5σ magnitude assessments for extended sources by Annunziatella et al. (2014) (Tab. 3.1) serve as limiting magnitudes to calculate the surface brightness profiles for the respective filters. However as these profiles are purely modelled being based on the galaxy properties, there is no real need to truncate the profiles at exactly these limits and any restraints can be chosen, as long as the desired radius intervals

are within those constraints. Hence due to the completely modelled nature of the profile, the precision in radius can be chosen as accurately as desired as well as the differences of the two profiles, e.g. the colors (see formula (1.18)), can be calculated at any predetermined radii (Fig. 4.3). The slopes of the color profiles, i.e. the color gradient in a chosen interval, are then derived by applying a least squares approximation to the calculated color profiles on a logarithmic radius scale.

The combinations chosen to proceed are the optical color $r_{625} - Y_{105}$ and the optical-infrared color $Y_{105} - H_{160}$, which correspond to rest-frame $B - I$ and $I - Y$. Since the 4000Å break at $z \sim 0.4$ lies approximately at 5500Å, both colors are well situated on the redder wavelength side of the break and are tracing therefore a stellar population of intermediate and older ages, representing the majority of stars in a typical elliptical galaxy. Such a combination of rest-frame optical and optical-IR colors appears to be best suitable to break the age-metallicity degeneracy, with the first color tracing age as well as metallicity, whereas the latter color traces primarily metallicity (Smail et al., 2001; Worthey, 1994).

To be consistent with other studies examining the color gradients of early-type galaxies (e.g. Guo et al., 2011; La Barbera et al., 2002, 2003; Saglia et al., 2000; Tamura & Ohta, 2000), but also to benefit from the high quality and deep imaging of the *HST*, which is capable of observing galaxies out to large radii, the gradients are derived in an interval between $0.1r_e$ and $2r_e$ of the respective bluer band. The subsequent discrete color measurements in respect to the SSP comparisons are performed at five different, predetermined radii, 0.1, 0.5, 1 and $2r_e$, again in regard to the bluer band in order to probe the potentially, different stellar subpopulations. Furthermore just for the color gradient analysis the colors $g_{475} - I_{814}$ and $I_{814} - H_{160}$, resembling in rest-frame $U - V$ and $V - Y$, are included.

In Fig. 4.3 an example output for one of the galaxies of the MACS 1206 sample is shown. The upper plot depicts in blue the surface brightness profile for r_{625} as well as the position of the respective 0.1, 1 and $2r_e$, represented by the dashed lines. The same, just with red colors applies for Y_{105}. As expected the magnitude in the redder band is higher, since the old stellar population dominates the longer wavelength regime. In the lower part of the figure with the x-axis being logarithmically scaled the according color profile in black as well as the respective least squares fit in magenta are displayed. The coloured dashed lines ranging from red to blue illustrate the location of 0.1, 0.2, 0.5, 1 and $2r_e$ of the bluer band, in this case the r_{625} filter.

The second method to derive the color gradients is a more 'analytical' one following La Barbera et al. (2002) (see formula (1.20)). This approach quantifies the ratios of the effective radii of the processed bands in respect to the interval boundaries r_m and r_M, in which the color profiles and gradients should be calculated in. To be consistent with La Barbera et al. (2002), $r_m = 0.1\ r_{e,625}$ and $r_M = r_{e,625}$ are adopted.

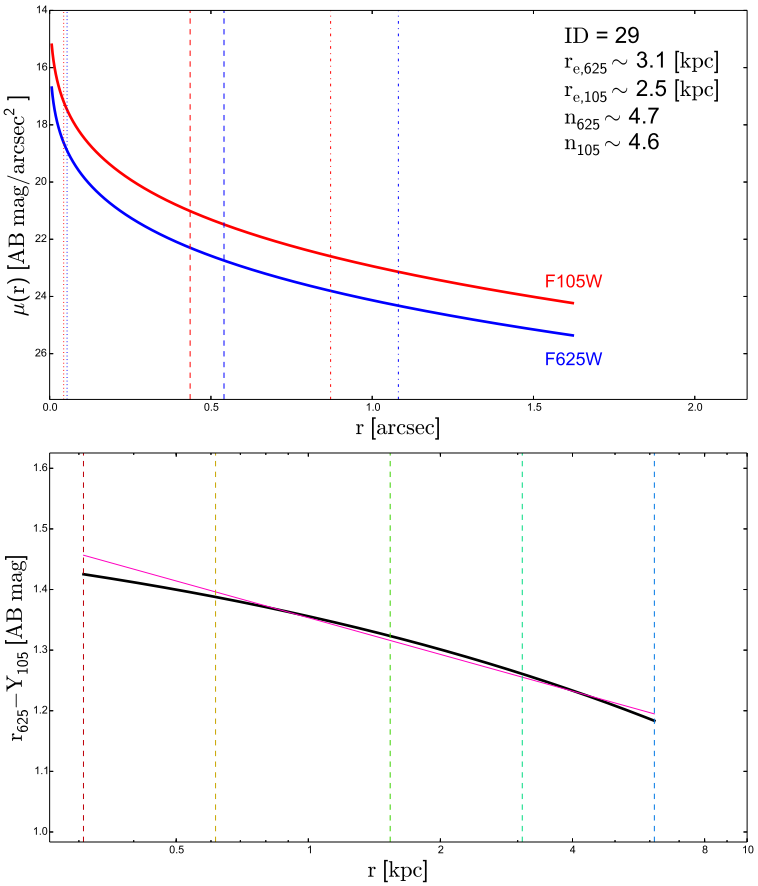

Figure 4.3.: Surface brightness profiles (upper plot) and color profile with overlayed fit (lower plot) for a MACS 1206 early-type galaxy. The blue and red dotted and dashed lines in the upper diagram correspond to 0.1, 1 and $2r_e$ of the respective bands. The, from red to blue coloured, dashed lines in the lower figure correspond to 0.1, 0.2, 0.5, 1 and $2r_e$ of the bluer band, in this particular case the r_{625} filter.

5. Comparison with SSP models

In order to infer information about the ages and metallicities of the underlying stellar population from the derived colors, it is necessary to compare them to predictions produced by stellar population synthesis models. To achieve that goal in this thesis SSP models have been adopted in several ways making use of the tool *EzGal* (Mancone & Gonzalez, 2012).

This `Python` wrapper allows to produce synthetic magnitudes and colors depending on formation redshift z_f, metallicity Z, starformation history and IMF based on different input models, such as the ones published by Bruzual & Charlot (2003) (BC03) or Maraston (2005). Additionally it is capable of calculating these values in an observed frame for the desired filters at a predetermined redshift by redshifting the model spectra and convolving it with the filter curves and applying the corresponding k-corrections. Thus it is possible to compare directly the measured colors to several modelled ones, differing due to varying input ages and metallicities, with these parameters in turn being linked to the formation and evolution conditions of a galaxy.

The models chosen were the ones by BC03, as only those are supplied with different metallicities, which makes it also possible to interpolate additional SED evolutions with other metallicities than the predetermined ones. Furthermore a Chabrier IMF (Chabrier, 2003) has been adopted. As only early-type galaxies are analyzed, simple stellar population (SSP) models are utilized, characterized by a singular important star formation epoch - a so-called star formation burst - at the formation redshift and a subsequent passive evolution. The following cosmological parameters $H_0 = 70$ km s^{-1} Mpc^{-1}, $\Omega_\Lambda = 0.7$ and $\Omega_M = 0.3$ (Spergel et al., 2003) are used, being in agreement with other studies examining the *CLASH* clusters (e.g. Annunziatella et al., 2014; Balestra et al., 2015; Biviano et al., 2013; Girardi et al., 2015; Jouvel et al., 2014; Ogrean et al., 2015; Presotto et al., 2014; Zitrin et al., 2012).

The first approach to derive indications about the development and properties of the stellar population of the selected elliptical galaxies consisted of using models with their metallicities at cluster redshift being fixed to the solar value, so $Z_\odot = 0.02$.

The formation redshifts employed range from $z = 0.5$ to $z = 10$ with eleven steps in between, corresponding to ages between ~ 5 Gyr and ~ 13 Gyr at $z = 0$. The modelled colors are consequently matched with the measured ones and the corresponding age of the best fit allows drawing conclusions about the formation epoch of the respective galaxy, assuming solar metallicity.

The second method applied is very much alike to the first one, only this time metallicity is allowed to vary and the age of the models is fixed to an age of 12 Gyr at $z = 0$, which corresponds to a formation redshift $z_f \sim 4$. The supplied BC03 models provide predictions for $Z = [0.008,\ 0.02,\ 0.05]$, which corresponds to $Z \sim [-0.4,\ 0.0,\ 0.4]$ [Log($Z/Z_\odot$)]. Additionally the interpolation capabilities of *EzGal* are exploited by adding three models with $Z = 0.015$, $Z = 0.03$ and $Z = 0.04$ equaling to $Z = -0.1$ [Log($Z/Z_\odot$)], $Z = 0.2$ [Log($Z/Z_\odot$)] and $Z = 0.3$ [Log($Z/Z_\odot$)]. By matching again the predicted and the observed colors, constraints on the metallicities of the underlying stellar populations can be applied with the limitation of an assumed age.

The issue with both of these approaches is that either the current metallicities or the ages must be fixed for the galaxies. Even with deploying these methods on several colors to minimize the effects of the age-metallicity degeneracy, a significant impact of this phenomenon cannot be ruled out.

To break this degeneracy one can create a grid of two colors at a certain redshift, whose predicted values depend on different SSPs based on varying ages and metallicities. Such a grid is not unlike the one spanned by the right choice of Lick abundance indices and is therefore also capable to trace age in one direction and metallicity in the other, provided the right color combination is chosen. Following Smail et al. (2001) and also La Barbera et al. (2002) a combination of optical and optical-infrared colors appears best suited to resolve this issue. Hence the two colors chosen are $r_{625} - Y_{105}$ for the optical part and $Y_{105} - H_{160}$ for the optical-IR one. Those colors translate at the redshift $z \sim 0.4$, which is applicable for both clusters, to $B - I$ and $I - Y$ in the rest-frame.

Once the grid is finally generated, one can match the individual measured colors with the nearest point of the grid and hence can infer the best fitting age and metallicity for this particular color at this distinct redshift.

6. Results

This chapter outlines the main results of this thesis, split into three sections. The first part considers potential wavelength dependencies of the structural parameters r_e and n. The second part presents the derived color gradients, whereas in the last section the comparison of the color measurements at different radii with the colors predicted by the SSP models and the effect on age and metallicity determinations of the stellar populations of the galaxies are described.

6.1. Wavelength-dependence of parameters

The eventually obtained samples of galaxy models for both clusters consists of 117 early-type galaxies in total, fitted in each of the 12 bands, providing - among other things - measurements for n and r_e for each filter. Hence it is possible to examine potential trends of these parameters with wavelength, which are already observed by numerous studies (Chan et al., 2016; La Barbera et al., 2002, 2003, 2010; Kelvin et al., 2012; Kennedy et al., 2015; Vulcani et al., 2014).

The trends presented in this thesis consider the average across both cluster samples for each passband with the uncertainties being estimated as $1.253\sigma/\sqrt{N}$, with σ denoting the standard deviation, whereas N is the number of galaxies in the respective sample, following the evaluation by Kennedy et al. (2015) and Vulcani et al. (2014).

The distributions in form of histograms for both clusters and both parameters are shown in the Figures 6.1 - 6.4. It is evident that a relatively high number of MACS 1206 galaxies in B_{435} adopt the maximum attainable $n = 8$ (Fig. 6.1). This is presumably due to the low S/N in this particular band, causing *MegaMorph* to encounter difficulties determining the right profile. Nevertheless the lack of galaxies obtaining such a high value for n in the other bands, proves that those fits can be treated with a reasonable confidence. The distribution of r_e of the MACS 1206 sample (Fig. 6.2) shows no conspicuous features in all bands and, as mentioned earlier, the maximum allowed value for a fit of 400 pixels, which corresponds to $\sim$ 150 kpc

at z $\sim$ 0.4, is not even nearly reached. Instead the median values for r_e adopt expectable values of $\sim$ 2 kpc.

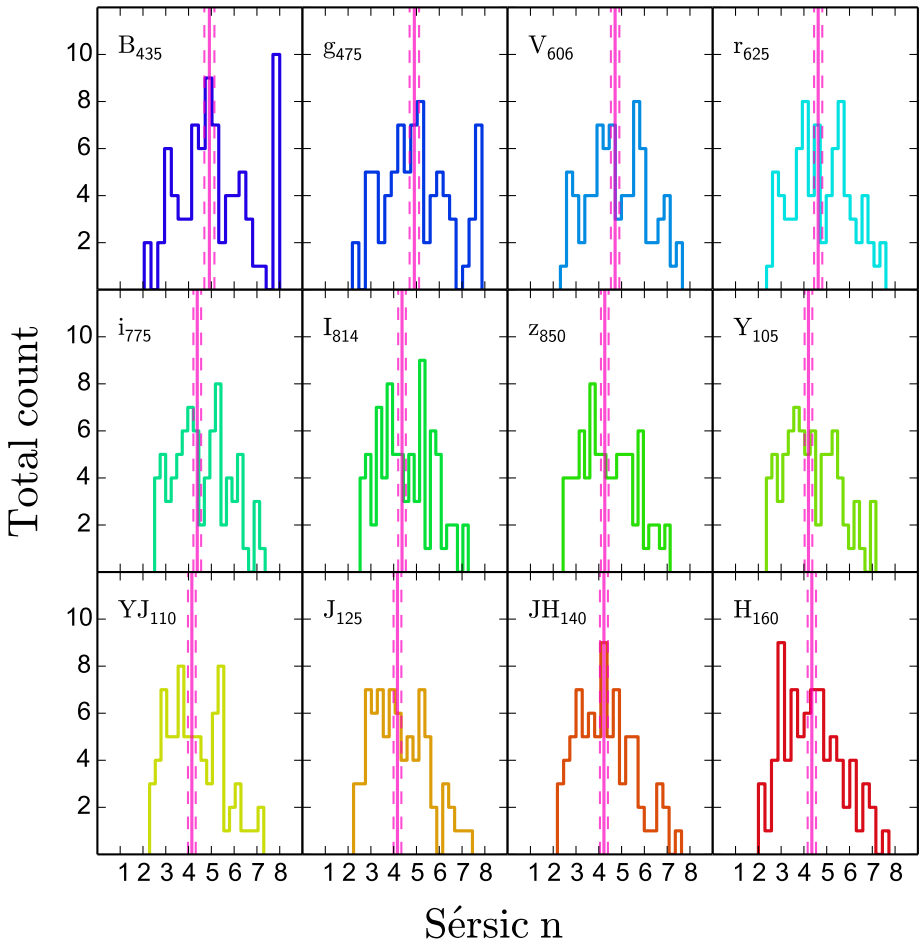

Figure 6.1.: Distribution of the Sérsic index n for the MACS 1206 sample in the individual bands. The solid magenta line indicates the median, while the dashed magenta lines denotes the uncertainty interval. The respective filters are given in the upper left corners.

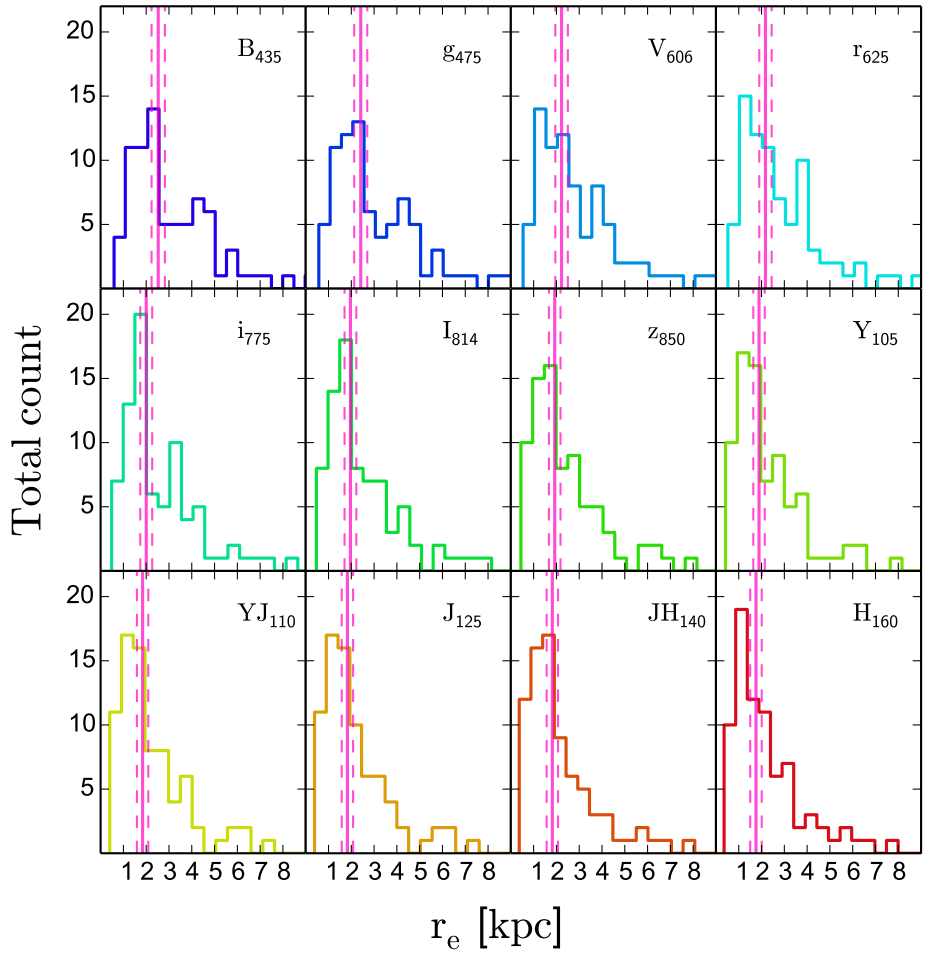

Figure 6.2.: Distribution of the effective radius r_e for the MACS 1206 sample in the individual bands. The solid magenta line indicates the median, while the dashed magenta lines denotes the uncertainty interval. The respective filters are given in the upper left corners.

Unfortunately the results for MACS 0416 do not look to be as trustworthy as the assessments for MACS 1206, with approximately 15 percent of the galaxies in the sample attaining an $n = 8$ in the B_{435} and g_{475} bands (Fig. 6.3). However the r_e measurements (Fig. 6.4) present themselves very similar to the r_e distributions of MACS 1206, showing also average effective radii of $r_e \sim 2$ kpc over all bands.

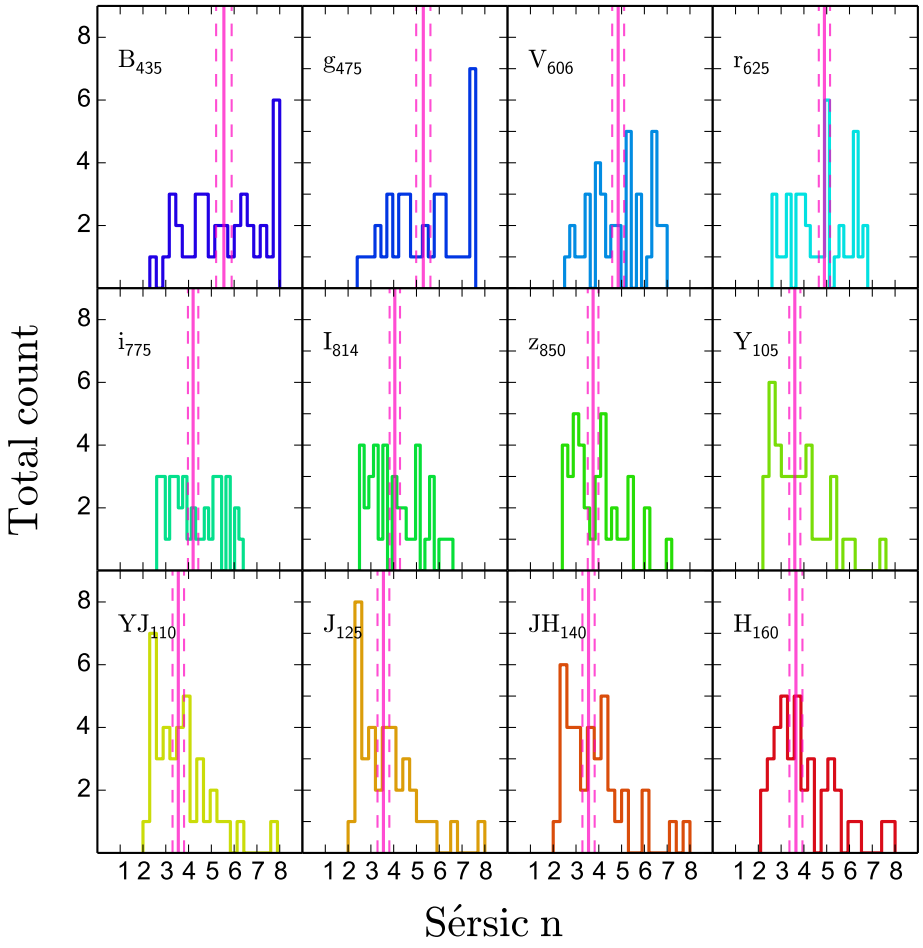

Figure 6.3.: Same as figure 6.1 only for the MACS 0416 sample.

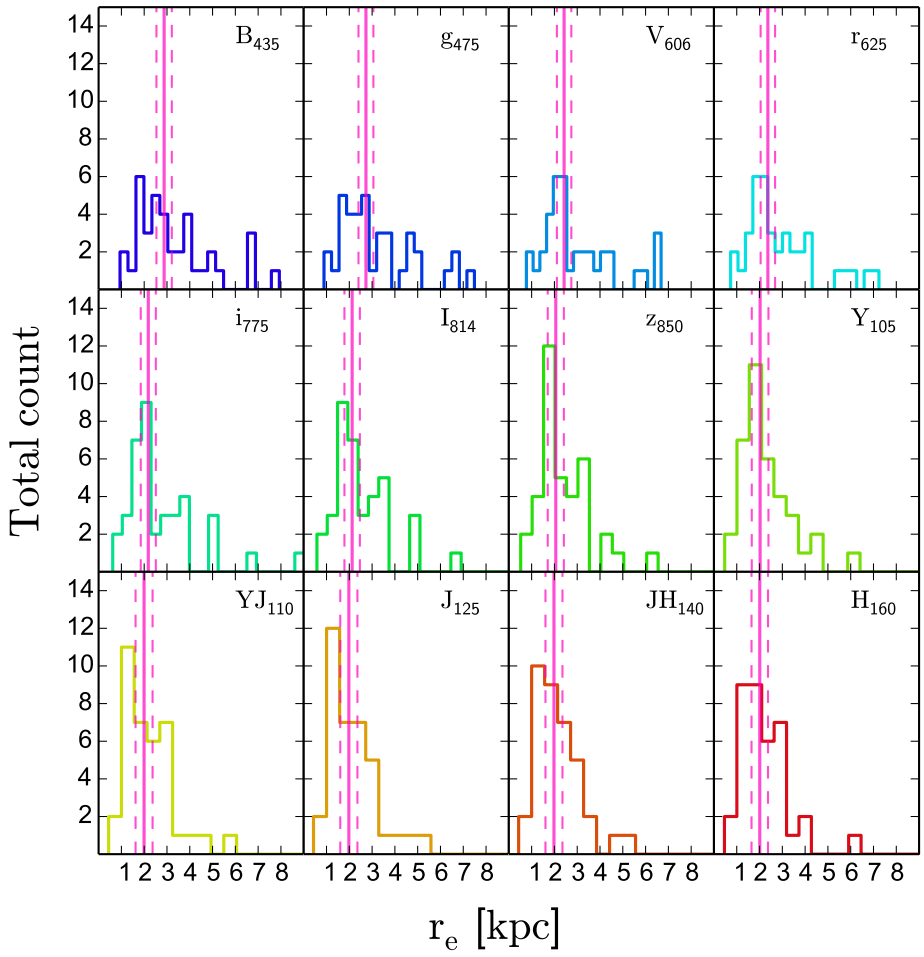

Figure 6.4.: Same as figure 6.2 only for the MACS 0416 sample.

Still the distributions of n and r_e vary significantly with wavelength, proving thereby that the parameters were not too constrained in regard to the degrees of freedom for the Chebyshev polynomials during the fit. This is especially satisfying with respect to the results for MACS 1206, as the same setup as for MACS 0416 has been used[1], but with the distributions for n and r_e differing hardly over the different passbands.

Nevertheless it seems that due to the much more prominent ICL of MACS 0416, the modelling of the galaxies requires a much more comprehensive treatment. Also it can not be ruled out that a significant amount of galaxies in the MACS 0416 sample possess a much more complex stellar population, due to the merging process of the subclusters and the resulting galaxy interactions. For such galaxies a one-component fit would not be sufficient and a fit with at least two Sérsic profiles would perhaps clarify this issue. Another approach to gain insights on this matter is to obtain information on the ages of those galaxies at different radii, which coincides with the main goal of this thesis.

To evaluate the measurements, the tables 6.1 and 6.2 list the medians of n and r_e for both clusters and for each band including the mentioned error estimates. Already with a first glimpse it is noticeable that for the early-type galaxies in MACS 1206 as well as to a lesser extent in MACS 0416, n appears to be relatively independent of wavelength, while r_e definitely seems to decrease with increasing wavelength.

Table 6.1.: Median values for n and r_e for the MACS 1206 sample in each filter. The uncertainties are derived by using $1.253\sigma/\sqrt{N}$.

	B_{435}	g_{475}	V_{606}	r_{625}	I_{775}	I_{814}
n	4.91 ± 0.22	4.91 ± 0.21	4.72 ± 0.19	4.63 ± 0.18	4.38 ± 0.17	4.37 ± 0.17
r_e	2.53 ± 0.29	2.41 ± 0.29	2.23 ± 0.28	2.17 ± 0.27	2 ± 0.26	1.96 ± 0.26

	z_{850}	Y_{105}	YJ_{110}	J_{125}	JH_{140}	H_{160}
n	4.26 ± 0.17	4.2 ± 0.17	4.14 ± 0.17	4.17 ± 0.17	4.23 ± 0.18	4.35 ± 0.18
r_e	1.93 ± 0.26	1.89 ± 0.25	1.84 ± 0.25	1.83 ± 0.25	1.82 ± 0.25	1.76 ± 0.25

[1] Except in regard of computational time, as described in chapter 4.

Table 6.2.: The same as table 6.1, only for the MACS 0416 sample.

	B_{435}	g_{475}	V_{606}	r_{625}	I_{775}	I_{814}
n	5.54 ± 0.35	5.27 ± 0.32	4.85 ± 0.26	4.9 ± 0.25	4.2 ± 0.23	4.07 ± 0.23
r_e	2.88 ± 0.34	2.73 ± 0.33	2.43 ± 0.32	2.37 ± 0.32	2.18 ± 0.34	2.12 ± 0.34

	z_{850}	Y_{105}	YJ_{110}	J_{125}	JH_{140}	H_{160}
n	3.77 ± 0.24	3.58 ± 0.25	3.54 ± 0.26	3.51 ± 0.26	3.54 ± 0.27	3.65 ± 0.29
r_e	2.06 ± 0.36	2.02 ± 0.37	2 ± 0.38	1.98 ± 0.38	1.98 ± 0.38	2.01 ± 0.37

To quantify the dependence on wavelength, $\mathcal{N}$ and $\mathcal{R}$ are introduced. These variables describe the medians of the ratios between the n and r_e measurements in the H_{160} and the r_{625} band and can therefore provide information on how those parameters vary with wavelength. These two filters have been selected on one hand because they are also used throughout the color gradient and subsequent SSP analysis and on the other hand due to their provision of the widest range in wavelength. This interval could only be increased by relying on the B_{435} or g_{475} band, but both of these filters possess a significant lower S/N and, as already mentioned above, especially some of the assessments of n in B_{435} should be treated with caution.

Now as n describes the shape of the light profile, an $\mathcal{N} < 1$ in this context corresponds to a higher central light concentration in the bluer r_{625} band than in the redder H_{160} filter. Hence $\mathcal{N} > 1$ obviously results in an opposite behavior, while an $\mathcal{N} \sim 1$ implies a similar shape of the light profile in those two passbands.

The parameter $\mathcal{R}$ describes the variation in size in these two filters, with $\mathcal{R} < 1$ indicating a smaller size in the redder H_{160} band. As a result the centers appear redder, while the outskirts present themselves bluer in comparison. For $\mathcal{R} > 1$ the opposite is true, with the centers being bluer than the outskirts, whereas $\mathcal{R} \sim 1$ implies a similar size in both passbands. Hence, much like color gradients, $\mathcal{R}$ serves as an indicator of the color variation with radius within an object.

Calculating the medians for $\mathcal{N}$ and $\mathcal{R}$ for both cluster samples yield the results presented in table 6.3. The uncertainties are again calculated using the $1.253\sigma/\sqrt{N}$ estimation.

Although the n measurements for the MACS 0416 sample are not as robust as the assessments for galaxies in MACS 1206, it is feasible to consider $\mathcal{N} \sim 1$ for both populations, which means that the observed objects can be described indeed

by a one-component profile. These conclusions hold true especially for the MACS 1206 sample with $\langle n_{H,160} \rangle \sim 0.9 \langle n_{r,625} \rangle$. For galaxies in MACS 0416 the value is with $\langle n_{H,160} \rangle \sim 0.8 \langle n_{r,625} \rangle$ a little bit lower. This result can be explained by considering the decreased accuracy for n measurements and a possible contamination by non-truly elliptical galaxies possessing two or more significant stellar components. Nevertheless the majority of the MACS 0416 galaxies can be also characterized by a singular light profile.

Table 6.3.: Medians of the $n_{H,160}/n_{r,625}$ ($\mathcal{N}$) and $r_{e_{H,160}}/r_{e_{r,625}}$ ($\mathcal{R}$) measurements for both cluster samples.

	$\mathcal{N}$	$\mathcal{R}$
MACS 1206	0.92 ± 0.02	0.75 ± 0.02
MACS 0416	0.84 ± 0.04	0.77 ± 0.04

Examining $\mathcal{R}$, the results for MACS 1206 and MACS 0416 hold the same outcome with the effective radii being ~ 25 percent smaller in H_{160} than in r_{625}. This already indicates that the majority of the scrutinized galaxies possess redder centers and bluer outskirts, hence negative color gradients.

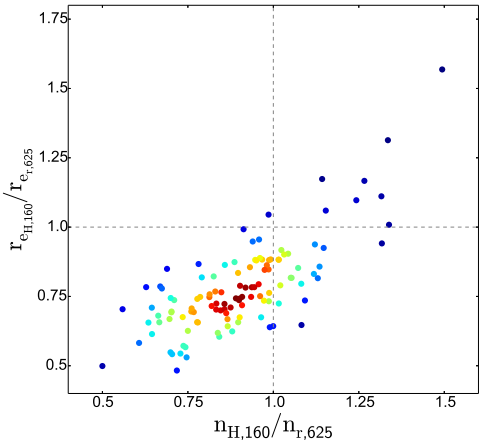

Figure 6.5.: $\mathcal{N}$ against $\mathcal{R}$ for every galaxy. The peak of $\mathcal{N}$ tends to ~ 0.9, while $\langle \mathcal{R} \rangle \sim 0.75$.

To visualize the ratios for every individual galaxy, Fig. 6.5 displays the $\mathcal{N} = n_{H,160}/n_{r,625}$ versus the $\mathcal{R} = r_{e_{H,160}}/r_{e_{r,625}}$ for the entire elliptical galaxies sample, without making a distinction between MACS 1206 and MACS 0416 objects. The uncertainties returned by *GALFIT* for the n and r_e assessments are smaller than the size of the markers. The gray dashed lines are indicating unity in $\mathcal{N}$ and $\mathcal{R}$. The trend for $\mathcal{N}$ and especially $\mathcal{R}$ is fairly obvious with them being smaller in the redder band. This suggests the tracing of different superimposed stellar populations, with the bluer one extending to larger radii, but showing a similar light distribution.

Also a possible correlation between n and r_e has been examined. However independent of the inspected passbands or cluster samples no trends are observed.

6.2. Color gradients

To derive the color gradients two approaches have been used. The first one has been to fit linear least squares (lsq) fits to the derived color profiles with the radii being logarithmically scaled (Fig. 4.3). The slopes of these fits equal the change in color in a predetermined radius interval, e.g. the color gradient.

The second method applied has been the utilization of the formula by La Barbera et al. (2002) (see formula (1.20)) with $r_m = 0.1\ r_{e,625}$ and $r_M = r_{e,625}$.

The interval for which the color gradient has been derived ranges from 0.1 - $2r_e$ in regard to the bluer band of the color for each galaxy. The colors examined are $g_{475} - I_{814}$, $r_{625} - Y_{105}$, $I_{814} - H_{160}$ and $Y_{105} - H_{160}$, which are corresponding at $z \sim 0.4$ to $U - V$, $B - R$, $V - Y$ and $R - Y$ in rest-frame. As the g_{475} band lies on the bluer end of the 4000 Ångstrom break at the cluster redshifts, it is also possible to detect a potential younger stellar population and their subsequent probable impact on the color variation with increasing radius. The order of magnitude of the errors returned by *GALFIT* lies in the range of $10^{-3} - 10^{-4}$ for all parameters and is therefore not considered in the subsequent analysis, as an inclusion of those uncertainties would result in a non discernable effect. To derive more accurate uncertainty estimates it would have been necessary to rely on simulations of the respective clusters containing similar galaxy populations as the observed ones. An ensuing *MegaMorph* analysis of those clusters would then deliver more information on the introduced errors, as the results of both modelling processes, one for the observed and one for the simulated galaxies, whose properties are known beforehand, can be compared. Unfortunately such a procedure has not been able to be completed in the given timeframe, but is currently conducted by Ulrike Kuchner as a part of her PhD thesis.

The individual results for each galaxy are presented in the tables, which can be found in the appendix, while the medians of the color gradients for each color and cluster are presented in the Tables 6.4 and 6.5. The first columns display the respective colors, whereas the second and third columns contain the medians of the fitted respectively calculated color gradients. The uncertainties in regard to the medians are again calculated using $1.253\sigma/\sqrt{N}$. The fourth columns indicate the results of Kolmogorov-Smirnov (KS) tests between the respective fitted and calcu-

lated color gradients assessments. Quantifying the distance between two distributions, the smaller the respective value derived by the KS test, the more equal are the two examined distributions.

Table 6.4.: Medians of the color gradients for the MACS 1206 sample in four different colors.

Color	$\nabla_{median,fit}$ [mag dex^{-1}]	$\nabla_{median,calc}$ [mag dex^{-1}]	KS
$g_{475} - I_{814}$	-0.17 ± 0.01	-0.13 ± 0.01	0.33
$r_{625} - Y_{105}$	-0.18 ± 0.01	-0.15 ± 0.01	0.24
$I_{814} - H_{160}$	-0.13 ± 0.02	-0.13 ± 0.02	0.08
$Y_{105} - H_{160}$	-0.06 ± 0.01	-0.07 ± 0.01	0.08

Table 6.5.: Medians of the color gradients for the MACS 0416 sample in four different colors.

Color	$\nabla_{median,fit}$ [mag dex^{-1}]	$\nabla_{median,calc}$ [mag dex^{-1}]	KS
$g_{475} - I_{814}$	-0.11 ± 0.02	0.02 ± 0.02	0.45
$r_{625} - Y_{105}$	-0.13 ± 0.02	-0.05 ± 0.02	0.32
$I_{814} - H_{160}$	-0.12 ± 0.02	-0.11 ± 0.02	0.11
$Y_{105} - H_{160}$	-0.07 ± 0.02	-0.08 ± 0.02	0.08

All averaged fitted color gradients show a negative result, i.e. a decrease in magnitude with radius, indicating that the centers of the majority of the galaxies are redder than their exterior regions. For MACS 1206 this holds also true for the calculated color gradient measurements, being in good agreement with the assessments by the lsq fitting method. However for MACS 0416 these observations are only completely valid for the two 'redder' colors $I_{814} - H_{160}$ and $Y_{105} - H_{160}$. While the calculated median color gradient for $r_{625} - Y_{105}$ is still negative, the discrepancy with a factor ~ 2 between the fitted and the calculated result is quite significant. Even more prominent is this effect for the $g_{475} - I_{814}$ color, with the calculated median color gradient being neutral or slightly positive. These implications are also reflected in the outcome of the KS tests, with the 'redder' colors for both clusters obtaining values implying both distributions to originate from the same sample.

The reason for the deviating results in regard to the calculated color gradients for the MACS 0416 sample lies presumably in the approach itself. While the fitting

method directly compares the two respective bands and returns expected results, the recipe by La Barbera et al. (2002) introduces additional parameters r_m and r_M, with these being chosen to be 0.1 and $1r_e$ from the r_{625} band to be consistent with previous publications (La Barbera et al., 2002, and references therein). A subsequent utilization of this procedure on a color containing the g_{475} band, amplifies potential misinterpretations, which can not be ruled out in these both bands due to the low S/N because of the prominent ICL, and leads eventually to inaccurate results.

To visualize the assessments for the galaxies more individually Fig. 6.6 and 6.8 show the distributions of the gradients in form of histograms for the four respective colors, distinguished into the color gradients derived by the fitting method in red and by the calculative approach in blue. The corresponding colored, dashed lines denote the medians, the dotted, gray line the position of a neutral color gradient, e.g. $\nabla(\lambda_1 - \lambda_2) = 0$.

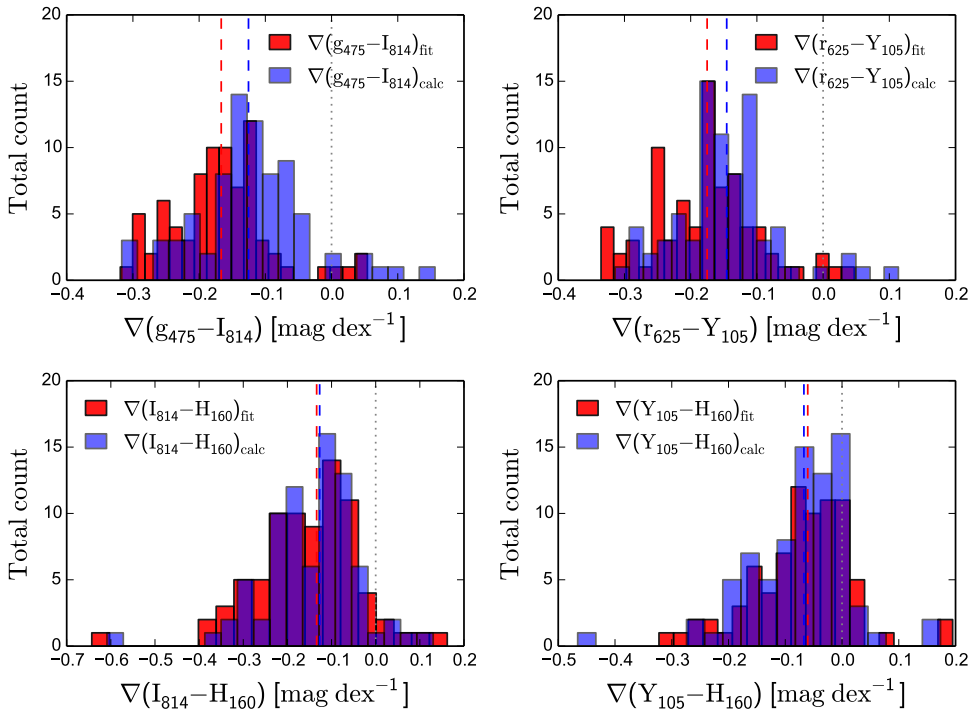

Figure 6.6.: Distributions of the color gradients for the four colors depending on the deriving method. Red indicates the color gradients assessed by lsq fitting, blue displays the calculated gradients. The corresponding dashed lines denotes the respective medians, whereas the gray dotted line indicates a color gradient = 0.

For the MACS 1206 sample an overwhelming majority shows negative or in the case of $Y_{105} - H_{160}$ at least neutral color gradients ranging from $\sim$ 0.1 to $\sim$ -0.3 difference in magnitude per dex in radius. The distinction between the fitted and calculated color gradients decrease with wavelength of the bands constituting the respective colors. In this sense the differences are most striking for the $g_{475} - I_{814}$ color, which is not surprising considering the low S/N in g_{475} and the resulting potential miscalculation of the structural parameters for some of the galaxies.

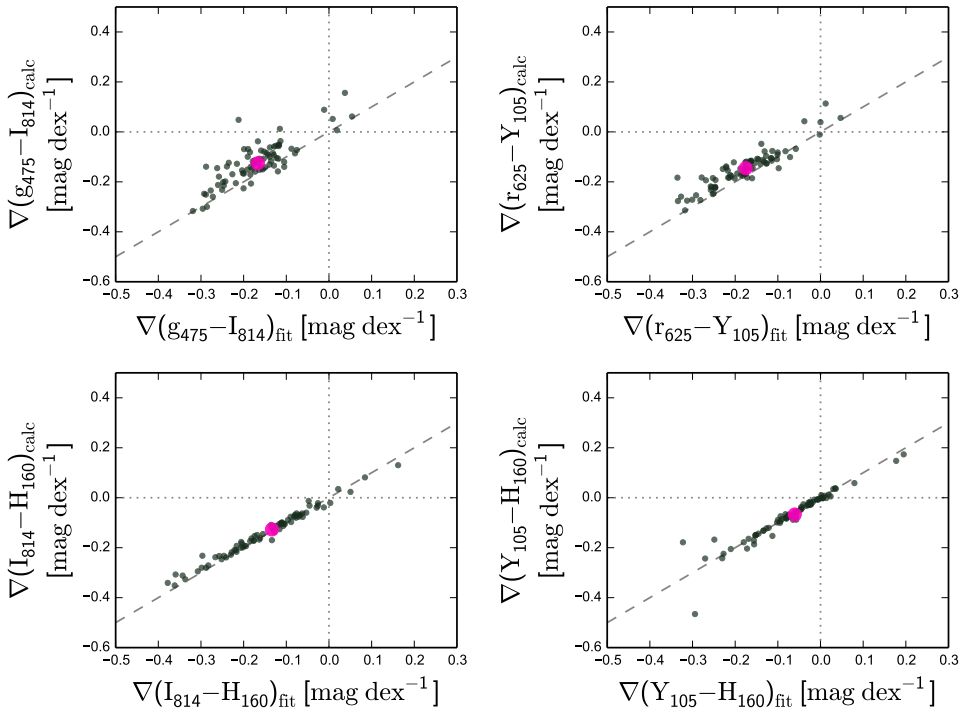

Figure 6.7.: Differences in the color gradient results for the MACS 1206 galaxies in the four colors between the lsq approach and the calculations following La Barbera et al. (2002). The magenta dot represents the median value for both measurements, the gray dashed line unity and the gray dotted lines a color gradient = 0.

Nevertheless the obvious general trend for the 79 galaxies is to have negative color gradients, with no more than two galaxies exhibiting at any point color gradients > 0.1 mag dex^{-1}, independent of color or method:

- For $g_{475} - I_{814}$ and $r_{625} - Y_{105}$ none of the galaxies possess a fitted color gradient > 0.1 mag dex^{-1} and only one galaxy does that in regard to the calculated gradients, which corresponds to $\sim$ 1.3 percent out of the whole sample.

– In $I_{814} - H_{160}$ again only one galaxy ($\sim 1.3\%$) shows an analogous behavior having a color gradient > 0.1 mag dex^{-1} with both approaches.

– Finally for $Y_{105} - H_{160}$, two galaxies ($\sim 2.6\%$) display such a color gradient in the fitted category as well as the calculated section, with one being the implied galaxy in $I_{814} - H_{160}$.

Fig. 6.7 gives a summary of the color gradient calculations for the elliptical galaxies in MACS 1206. The abscissa denotes the fitted color gradients, while the ordinate represents the calculated ones. The gray dots represent the individual galaxy measurements, the magenta dot the median of the color gradients of the respective assessment method, with its size indicating the uncertainty. The gray, dashed line indicates unity between the color gradients, while the dotted, gray lines distinguish the results into positive and negative measurements. Again the negligible amounts of galaxies possessing positive color gradients are evident, as well as the increasing scatter between the derivation methods with 'bluer' colors.

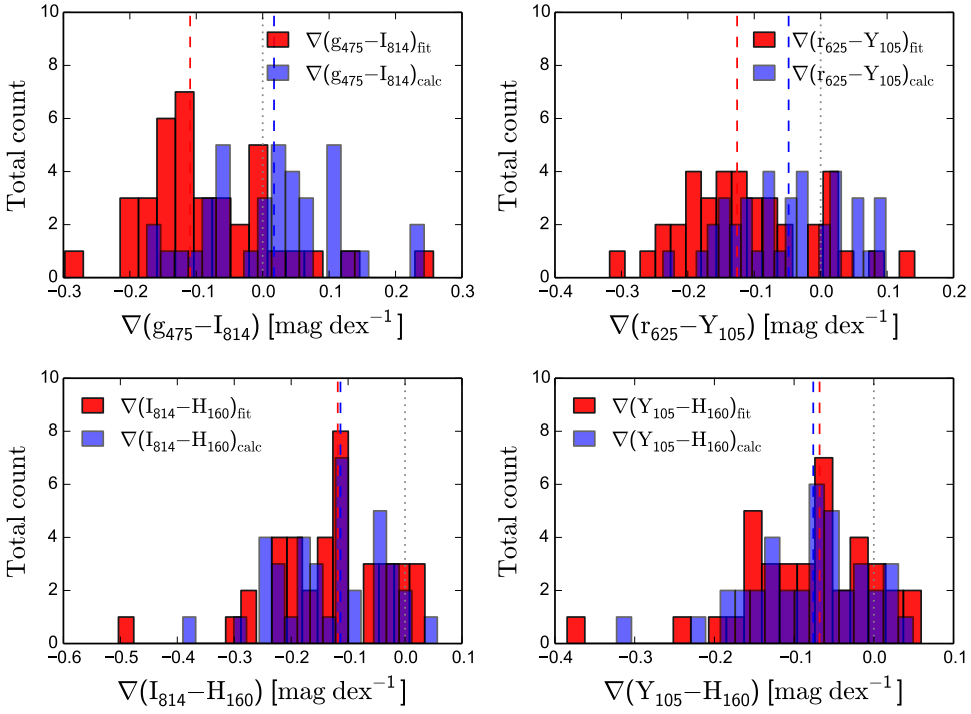

Figure 6.8.: Same as Fig. 6.6, only for the MACS 0416 sample.

Unfortunately as expected, the assessments are less coherent for the MACS 0416 sample, as can be seen in Fig. 6.8. Especially in $g_{475} - I_{814}$ the color gradients show a significant separation in the methods how they are derived, with the median of the calculated gradients being even slightly positive.

For $r_{625} - Y_{105}$ the separation is still distinct, however the majority of the galaxies already display a negative color gradient. For the two 'redder' bands $I_{814} - H_{160}$ and $Y_{105} - H_{160}$ the results are very similar to those for MACS 1206 with the medians being as good as identical and only a negligible amount of objects shows a positive color gradient. This overall behaviour reflects again the impact of r_m and r_M on the global result, especially with the measurements in the bluer bands g_{475} and r_{625} being significantly influenced by the ICL.

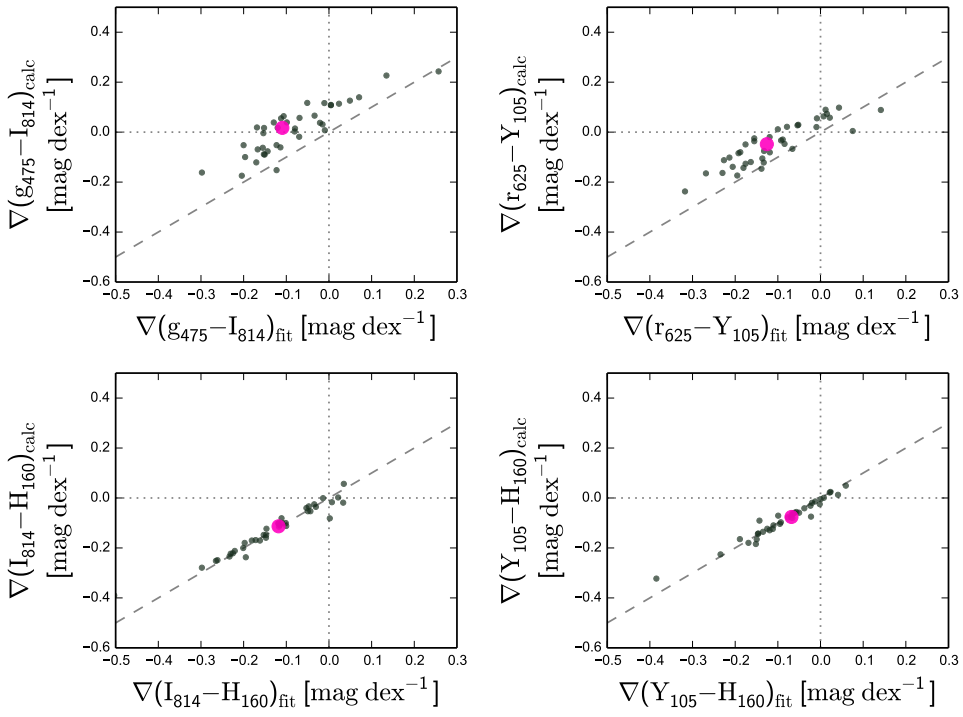

Figure 6.9.: Same as Fig. 6.7, only for the MACS 0416 sample.

Still also for these less precise measurements in comparison to MACS 1206 the number of galaxies showing a color gradient > 0.1 mag dex^{-1} is minor:

– The number of galaxies in $g_{475} - I_{814}$ with a fitted color gradient > 0.1 mag dex^{-1} amounts only to 2, which corresponds to ~ 2.5 percent of the sample,

while for the calculated sample 6 galaxies ($\sim 7.6\%$) show such a behavior.

– In $r_{625} - Y_{105}$ only one galaxy ($\sim 1.3\%$) surpasses this condition with its fitted color gradient, while none of the galaxies achieve that with the respective calculated color gradients.

– Finally for $I_{814} - H_{160}$ and $Y_{105} - H_{160}$ no galaxy shows a color gradient > 0.1 mag dex^{-1}, independent of the method.

Analogically to Fig. 6.7, Fig. 6.9 also summarizes the color gradient results for MACS 0416. The larger scatter in $g_{475} - I_{814}$ and $r_{625} - Y_{105}$ is clearly visible, but so is also the relative low number of positive color gradients, except for the calculated color gradients in $g_{475} - I_{814}$.

To determine any potential correlations of the color gradients Fig. 6.10 and Fig. 6.11 depict the gradients in all four colors versus different galactic properties.

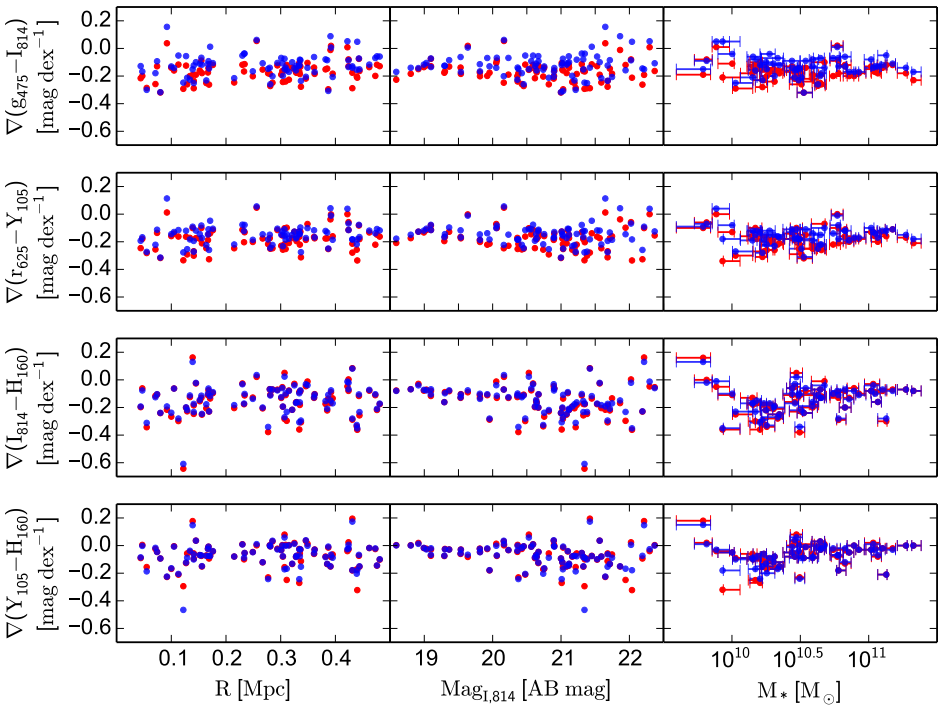

Figure 6.10.: Fitted and calculated color gradients in the four colors for the MACS 1206 galaxies versus projected cluster-centric distance R [Mpc] (left), total magnitude in I_{814} $\mathrm{Mag}_{I,814}$ [AB mag] (middle) and stellar mass M_* [$\mathrm{M}_\odot$] (right).

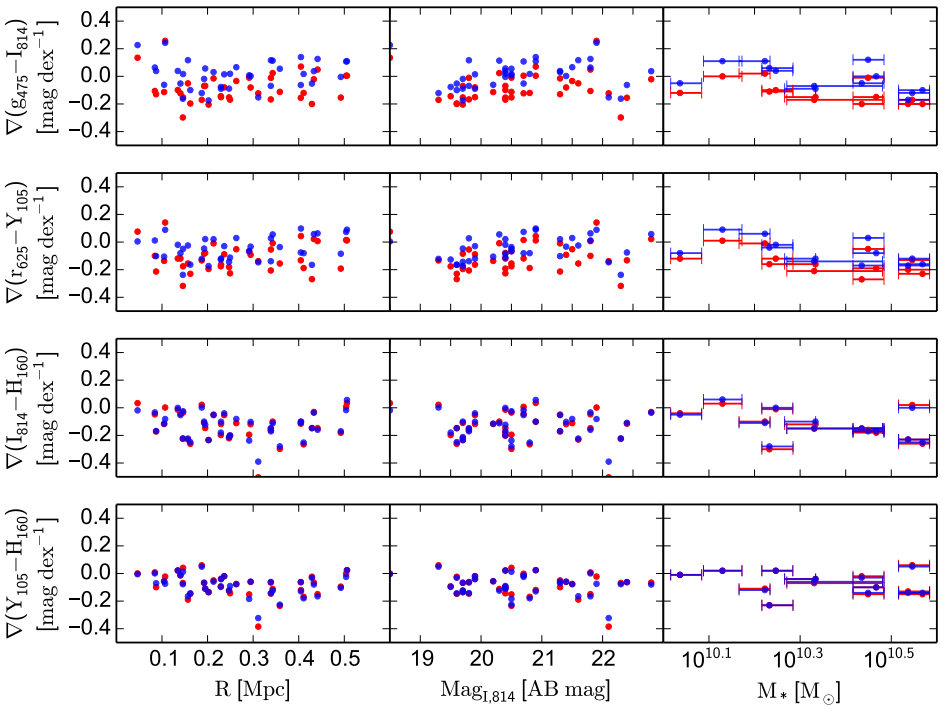

Figure 6.11.: Same as Fig. 6.10, only for MACS 0416.

The fitted gradients are again indicated by the red dots, the calculated ones by the blue markers. Neither for the galaxies in MACS 1206 nor for the objects in MACS 0416 any dependency on the projected cluster centric distance (left columns) can be found. The distances are calculated by moving all galaxies into a plane situated at the respective mean cluster redshift.

Also plotting the gradients of both clusters versus the respective total integrated magnitudes in I_{814}, which has been the reference band for the fitting process, reveals no visible scaling relations.

Finally the stellar masses have been derived for 56 out of the 79 galaxies in MACS 1206 and 13 out of the 38 objects in MACS 0416 using the photometric measurements by Subaru. The mass range of the galaxies covers mainly an interval of $10^{10} \lesssim M_* \lesssim 10^{11}$, which are typical values for bright elliptical galaxies situated in the centers of clusters. Likewise no dependencies for the color gradients on the stellar mass of the respective galaxies can be found.

As the gradients are calculated out to $2r_e$ it can be excluded that a lack of cor-

relations is caused by a truncation of the measurements of the color variations and a subsequent comparison with global galactic properties. Hence the position of an early-type galaxy in a cluster, as well as its luminosity and stellar mass does not influence the color gradients and therefore also the mechanisms responsible for the creation of different stellar populations.

6.3. Determination of age and metallicity

To infer information about the ages and metallicities of the individual galaxies and their stellar populations, SSP models have been employed in three different ways. Models from BC 03 have been utilized, as *EzGal* already provides them with three different metallicities ($Z \sim [-0.4,\ 0.0,\ 0.4]$ $[\mathrm{Log}(\mathrm{Z}/\mathrm{Z}_{\odot})]$), which hence offers the possibility to interpolate additional models with metallicities in between those supplied values.

For the first two approaches each time one of the two parameters age and metallicity got fixed to a certain value, while the other has been allowed to vary in order to model the colors $r_{625} - Y_{105}$ and $Y_{105} - H_{160}$ in the observed frame at the respective cluster redshifts. After applying the extinction correction on those calculated colors, they were compared to the, at different radii measured colors to derive potential constraints on the ages and metallicities of the stellar populations at these particular locations within a galaxy. The radii applied are meant to encompass a large portion of a galaxy and are therefore chosen to be $0.1r_e$, $0.5r_e$, $1r_e$ and $2r_e$.

The first method used a fixed overall metallicity to the solar value $Z = 0$ $[\mathrm{Log}(\mathrm{Z}/\mathrm{Z}_{\odot})]$, while the age has been allowed to vary, which has been achieved by utilizing different formation redshifts, ranging from $z = 0.5$ to $z = 10$[2], resulting in ages between 5 and 13 Gyr at $z = 0$. This leads to a number of discrete values for each respective color at the cluster redshifts, making it possible to compare them with the measured colors. The best matches between models and observations would then give clues about the ages of the stellar populations at the different positions within a galaxy.

The second approach is done analogously to the first one, just with the roles of age and metallicity swapped. Including the interpolated ones, the implemented metallicities are $Z \sim [-0.4,\ -0.1,\ 0.0,\ 0.2,\ 0.3,\ 0.4]$ $[\mathrm{Log}(\mathrm{Z}/\mathrm{Z}_{\odot})]$, while a formation redshift of $z_f = 4$ has been assumed, corresponding to an overall age for the galaxy

[2] The formation redshifts were z_f=[0.5, 0.55, 0.6, 0.7, 0.75, 0.85, 0.95, 1.3, 1.75, 2, 4, 10]

of 12 Gyr at $z = 0$.

The individual assessments for each galaxy and color are attached in the appendix, while the tables 6.6 and 6.7 contain the results for the median ages and metallicities for both colors and clusters at the predetermined radii. As usual the errors are calculated using $1.253\sigma/\sqrt{N}$.

These results should be treated with some caution due to several reasons. The most obvious one is of course, that either an age or a metallicity has to be assumed, therefore already introducing a bias. Also the extinction correction, which ranges from ~ 0.2 mag for r_{625} to ~ 0.03 mag for H_{160}, as well as a possible dust presence can have a significant impact on the colors. Finally as shown in the previous sections the results in r_{625} for the MACS 0416 sample appear to be error-prone.

Table 6.6.: Median results of the SSP analysis for ages and metallicities of the MACS 1206 galaxies at different radii and for both colors.

Color	$0.1r_e$	$0.5r_e$	$1r_e$	$2r_e$
		Age [Gyr]		
$r_{625} - Y_{105}$	13 ± 0.3	12 ± 0.3	9.8 ± 0.3	7.5 ± 0.3
$Y_{105} - H_{160}$	13 ± 0.3	10.2 ± 0.3	10.2 ± 0.3	8.7 ± 0.3
		Z [Log(Z/Z$_\odot$)]		
$r_{625} - Y_{105}$	0.2 ± 0.03	0.0 ± 0.03	-0.1 ± 0.03	-0.4 ± 0.02
$Y_{105} - H_{160}$	0.2 ± 0.02	0.2 ± 0.02	0.0 ± 0.02	0.0 ± 0.02

Table 6.7.: Median results of the SSP analysis for ages and metallicities of the MACS 0416 galaxies at different radii and for both colors.

Color	$0.1r_e$	$0.5r_e$	$1r_e$	$2r_e$
		Age [Gyr]		
$r_{625} - Y_{105}$	8.7 ± 0.4	12 ± 0.4	10 ± 0.4	7.3 ± 0.3
$Y_{105} - H_{160}$	12.5 ± 0.5	8.7 ± 0.5	7.5 ± 0.4	7.5 ± 0.4
		Z [Log(Z/Z$_\odot$)]		
$r_{625} - Y_{105}$	-0.4 ± 0.04	0.0 ± 0.04	-0.1 ± 0.04	-0.4 ± 0.03
$Y_{105} - H_{160}$	0.2 ± 0.03	0.0 ± 0.03	0.0 ± 0.04	0.0 ± 0.03

One technique to avoid such issues for example would be to enhance the already applied constraints. For instance in the course of the first method one can assign a solar metallicity to the measured colors at $0.1r_e$ for each individual galaxy as opposed to the entire objects. A corresponding approach for the second procedure would be to assume an average age of 12 Gyr at $z = 0$ for the, at $0.1r_e$ measured colors instead for the galaxy itself. Both of these premises would perhaps lead to improved results, but only at the cost of completely assuming the properties of (one of) the underlying stellar populations. So would possess an exterior population of a galaxy with a significant positive color gradient due to an age variance ages much older than 12 Gyrs, which would not agree with any of today's formation scenarios.

However despite all these setbacks, especially in regard to total values, it is still feasible to extract relative results for age and metallicity between the distinct regions. Consequently all assessments show a decrease of age and metallicity with radius with the exception of $r_{625} - Y_{105}$ in MACS 0416. For this particular color the median age difference in MACS 1206 between 0.1 and $2r_e$ amounts to $\sim 4.3 \pm 0.3$ Gyr, while the metallicity difference is $\sim 0.4 \pm 0.03$ [Log($Z/Z_\odot$)]. For the same range and sample the median age and metallicity variations in $Y_{105} - H_{160}$ add up to $\sim 1.9 \pm 0.4$ Gyr and 0.1 ± 0.03 [Log($Z/Z_\odot$)]. Regarding the MACS 0416 galaxies in the same range and the same color one finds an age discrepancy of $\sim 2.8 \pm 0.6$ Gyr and a metallicity difference of 0.2 ± 0.04 [Log($Z/Z_\odot$)].

To avoid the need of any assumptions at all and to break the age-metallicity degeneracy a third approach has been employed in the form of a grid spanned by two colors. While the optical-infrared color $r_{625} - Y_{105}$ is mainly tracing the age of the stars, the infrared color $Y_{105} - H_{160}$ is primarily influenced by the metallicity of the stellar populations. Other combinations of colors are not that well suited, as both or at least one can be affected equally by age and metallicity.

Fig. 6.12 depicts such a grid in addition to the colors of the individual galaxies of the MACS 1206 sample shown in green. The colors are calculated utilizing the outputs by *MegaMorph* for the total integrated magnitudes in the respective bands. The magenta dot denotes the median of the age and metallicity assessments with the error being indicated by its size.

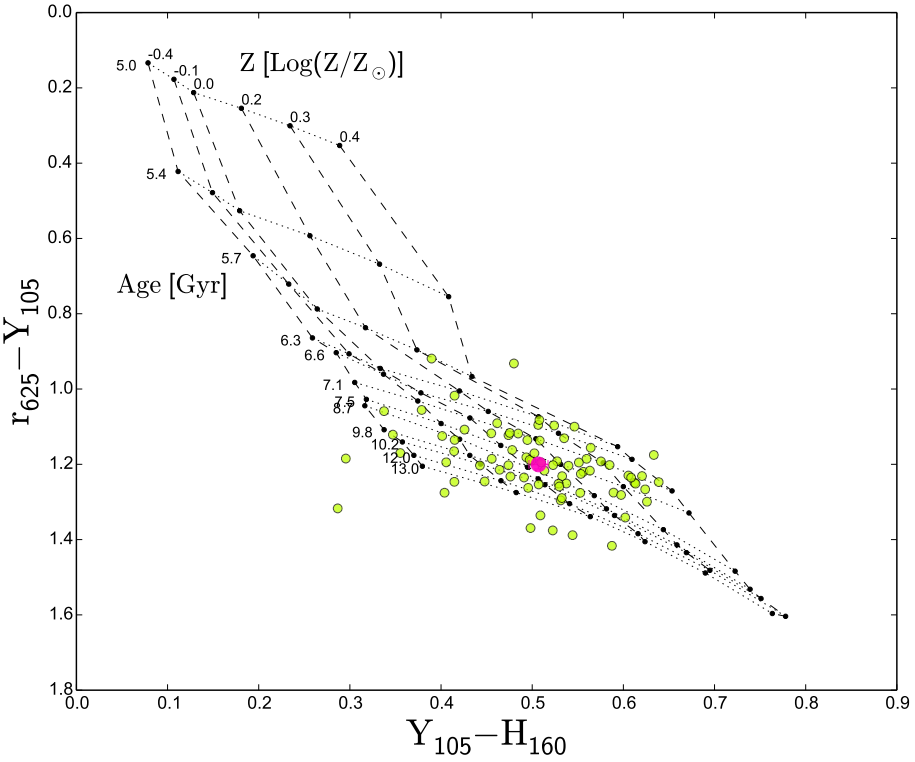

Figure 6.12.: $r_{625} - Y_{105}$ vs. $Y_{105} - H_{160}$ diagram with the overall colors of the MACS 1206 galaxies overlayed in green. The magenta dot represents the median of the ages and metallicites of the sample, with the errors being of the order of the size of the marker.

The affiliated histograms (Fig. 6.13) show the distributions of the ages and metallicities of the galaxies, with the median and its errors being again illustrated as the solid respectively dashed magenta lines. The median age lies at 8.7 ± 0.3 Gyr, while the median metallicity appears to attains a solar value of $Z = 0.0 \pm 0.03$ [Log(Z/Z$_\odot$)].

However it must be noted that in addition to the significant impact of extinction and dust, the different age tracks between 7 and 9 Gyr are almost identical at solar metallicities, hence introducing an additional error source.

Nevertheless serving as a consistency check it is satisfying to see that, even though there is a high number of potential error contributors, the majority of galaxies lie within the grid and display feasible values.

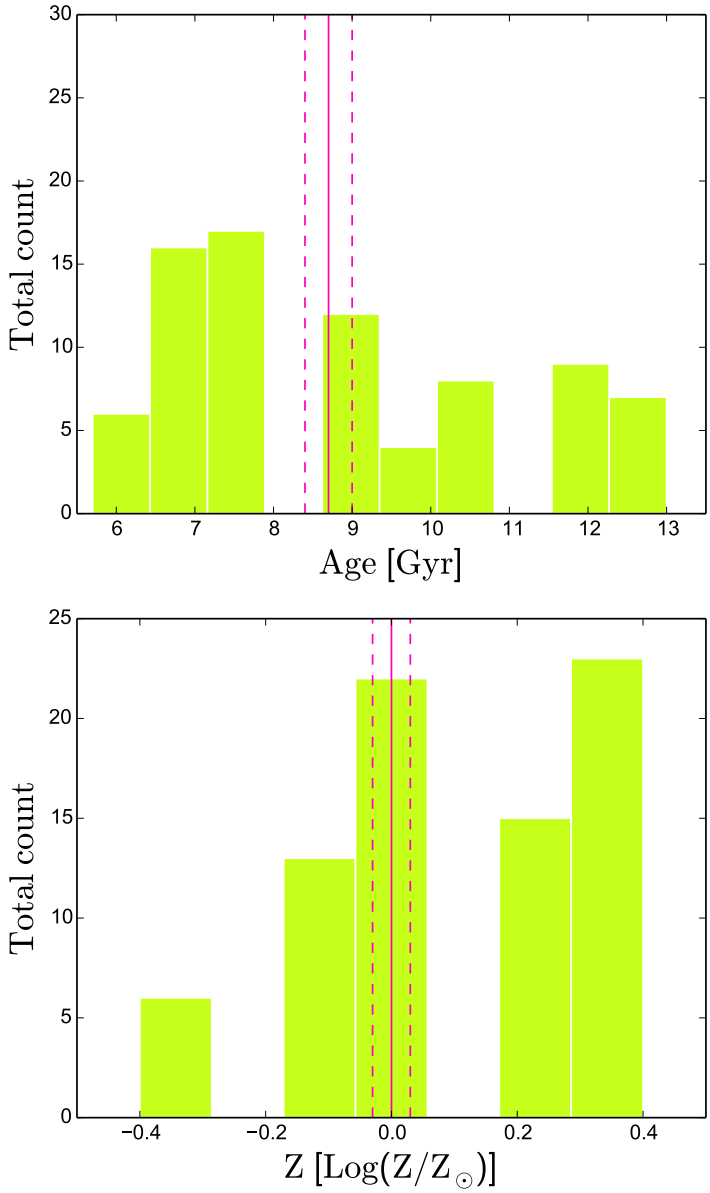

Figure 6.13.: Distributions for the derived ages and metallicities for the MACS 1206 sample. The medians are indicated by the solid magenta line, the according uncertainties by the dashed lines.

The same analysis has been done for the MACS 0416 galaxies with Fig. 6.14 showing the color-color diagram and Fig. 6.15 the distributions of the ages and metallicities of the individual objects. In addition to the above mentioned uncertainty sources, the error-prone determinations in r_{625} may also be an explanation for the handful of outliers in Fig. 6.14. Nevertheless as can also be seen in Fig. 6.15 the properties seem to be very similar to the MACS 1206 sample with the median age being 7.1 $\pm$ 0.4 Gyr and the median metallicity $Z = 0.1 \pm 0.04$.

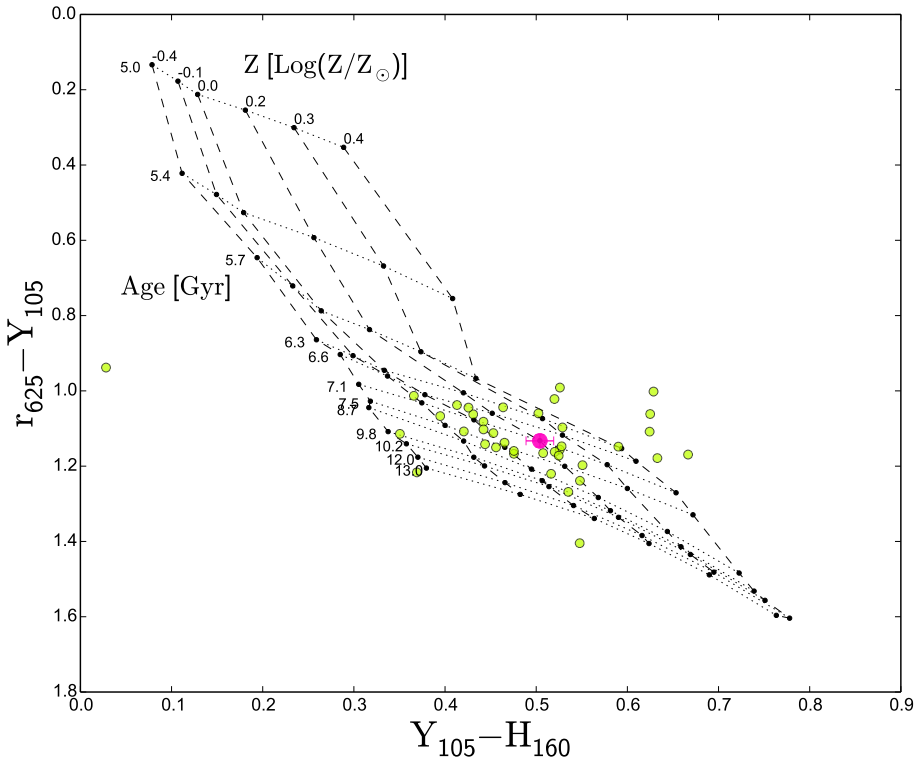

Figure 6.14.: $r_{625} - Y_{105}$ vs. $Y_{105} - H_{160}$ diagram with the overall colors of the MACS 0416 galaxies overlayed in green. The magenta dot represents the median of the ages and metallicites of the sample, with the errors being of the order of the size of the marker.

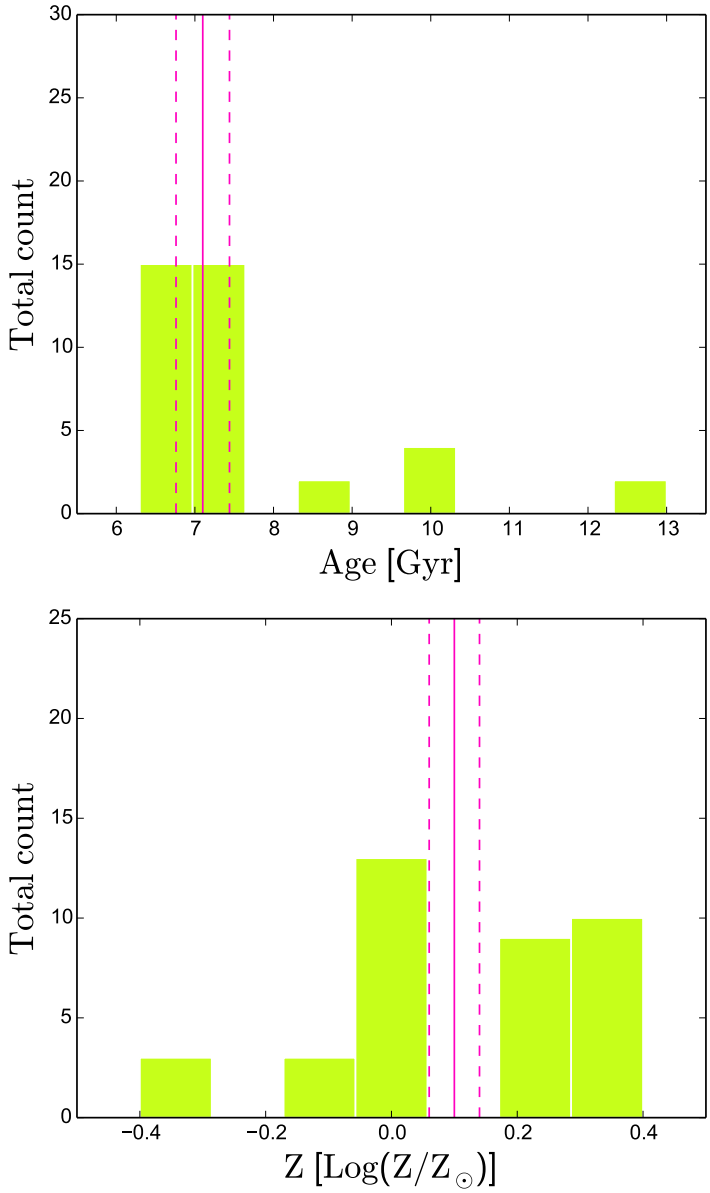

Figure 6.15.: Distributions for the derived ages and metallicities for the MACS 0416 sample. The medians are indicated by the solid magenta line, the according uncertainties by the dashed lines.

One of the main goals of this thesis has been to apply this method not only to the overall colors, but also to the colors at certain radii, namely 0.1, 0.5, 1 and $2r_e$ in order to at least reveal the age and metallicity variances within a galaxy.

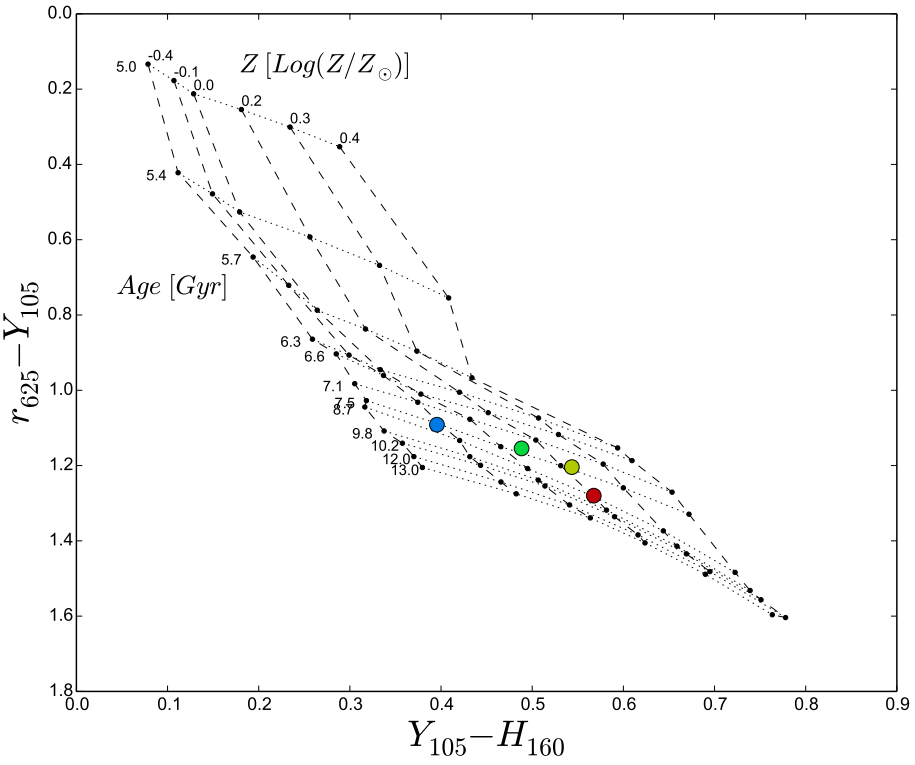

Figure 6.16.: Color-color diagram for one of the galaxies in the MACS 1206 sample. The red dot represents the color values at $0.1r_e$, the yellow one at $0.5r_e$, the green one at $1r_e$ and finally the blue one at $2r_e$.

To illustrate this approach Fig. 6.16 shows the color values for one example galaxy belonging to the MACS 1206 sample. The measurements at the four different radii are denoted by the coloured markers with the red dot illustrating the assessment at $0.1r_e$, the yellow one at $0.5r_e$, the green one at $1r_e$ and eventually the blue one at $2r_e$. Such an approach reveals that for this particular galaxy the age as well as the metallicity decrease with radius and that therefore both parameters are responsible for the observed color gradient.

Subsequently this analysis has been applied to the entire MACS 1206 sample. Fig. 6.17 illustrates the results with the same color coding as in Fig. 6.16 and

the additional median values depicted by the magenta dots. A significant part of the measurements at $0.1r_e$ show higher ages than the maximum age of 13 Gyr, which holds also true to a lesser extent for the determinations at 0.5 and 1 r_e. The extinction correction can play a critical role as the difference in $r_{625} - Y_{105}$ accounts for ~ 0.1 mag, yet it is not enough to explain this behavior in its entirety.

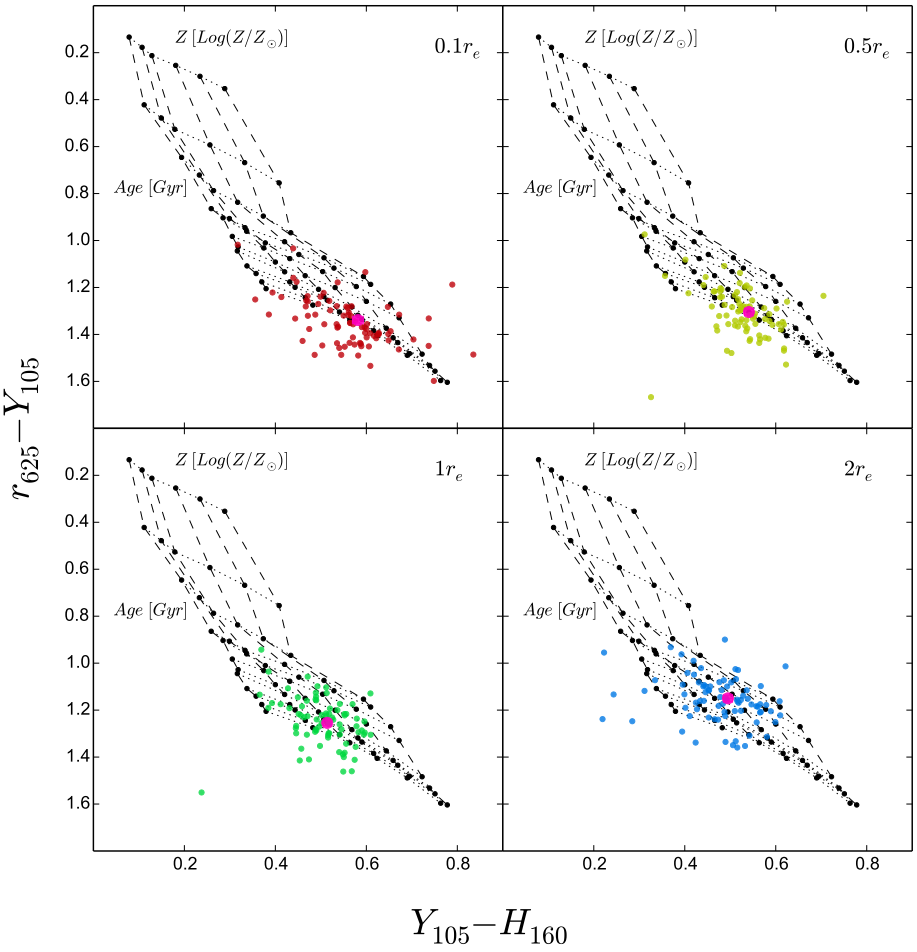

Figure 6.17.: Color-color diagrams for the color measurements in the MACS 1206 at the four different discrete radii. The color coding is the same as in Fig. 6.16, the magenta dots represent the respective median values with its size indicating the error. The grid points are determined by the same ages and metallicities as in Fig. 6.14.

Dust, errors in the measurements and also uncertainties in the models themselves cannot be ruled out. The need to constrain the possible reasons and their contributions to the errors leads back to the essential requirements of applicable uncertainties concerning the *MegaMorph* measurements, which are unfortunately not available. As expected the measurements at $2r_e$ are very similar to the ones utilizing the total integrated magnitudes (Fig. 6.12), as the flux contribution at radii $> 2\ r_e$ gets insignificant.

Nevertheless even with the absolute values being problematic, one can still infer some constraints by considering the relative age and metallicity variations with radius. The histograms in Fig. 6.18 and Fig. 6.19 show the distributions in age respectively metallicity for the measurements at the four distinct radii.

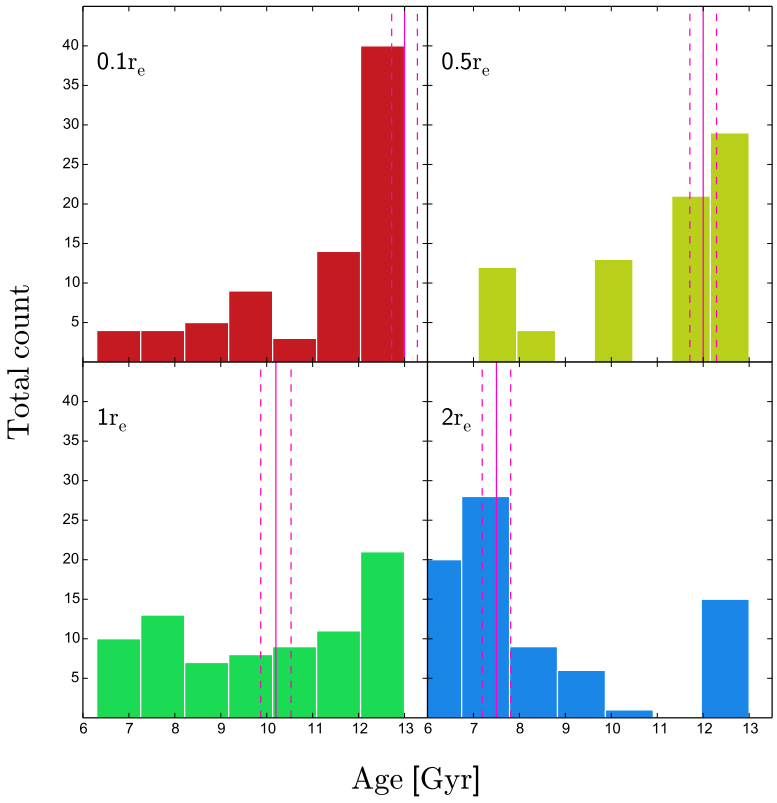

Figure 6.18.: Distributions of the assessed ages for the measurements in the MACS 1206 sample at the four different radii, which are indicated in the upper left corner and accordingly color coded. The median and its errors are again depicted as solid respectively dashed magenta lines.

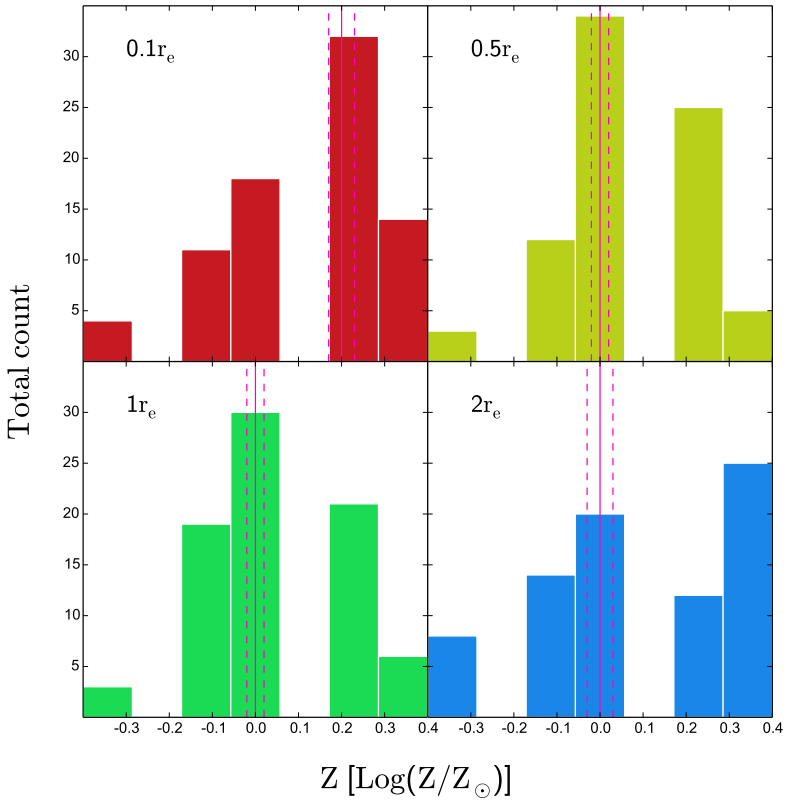

Figure 6.19.: Distributions of the assessed metallicities for the measurements in the MACS 1206 sample at the four different radii, which are indicated in the upper left corner and accordingly color coded. The median and its errors are again depicted as solid respectively dashed magenta lines.

While for $0.1r_e$ approximately half of the galaxies are in the 13 Gyr bin, as this age constitutes as the maximum attainable age, only $\sim$ 20 percent of the sample also display such an age at $2r_e$. To quantify this assessment: By averaging the age differences of the individual galaxies the centers appear to be 1.2 $\pm$ 0.4 Gyr older than the exterior regions.

The variety in metallicities does not display such a behavior, nevertheless the metallicity decreases from supersolar values at 0.1 r_e to a solar regime already at 0.5 r_e and remains constant. The median metallicity difference therefore measures up to 0.1 $\pm$ 0.03 [Log(Z/Z$_\odot$)].

As expected the results for MACS 0416 are less encouraging (Fig. 6.20). Especially the age distribution at $0.1r_e$ (Fig. 6.21) with a median of 7.3 ± 0.4 Gyr seems to be significantly out of line with the other age determinations.

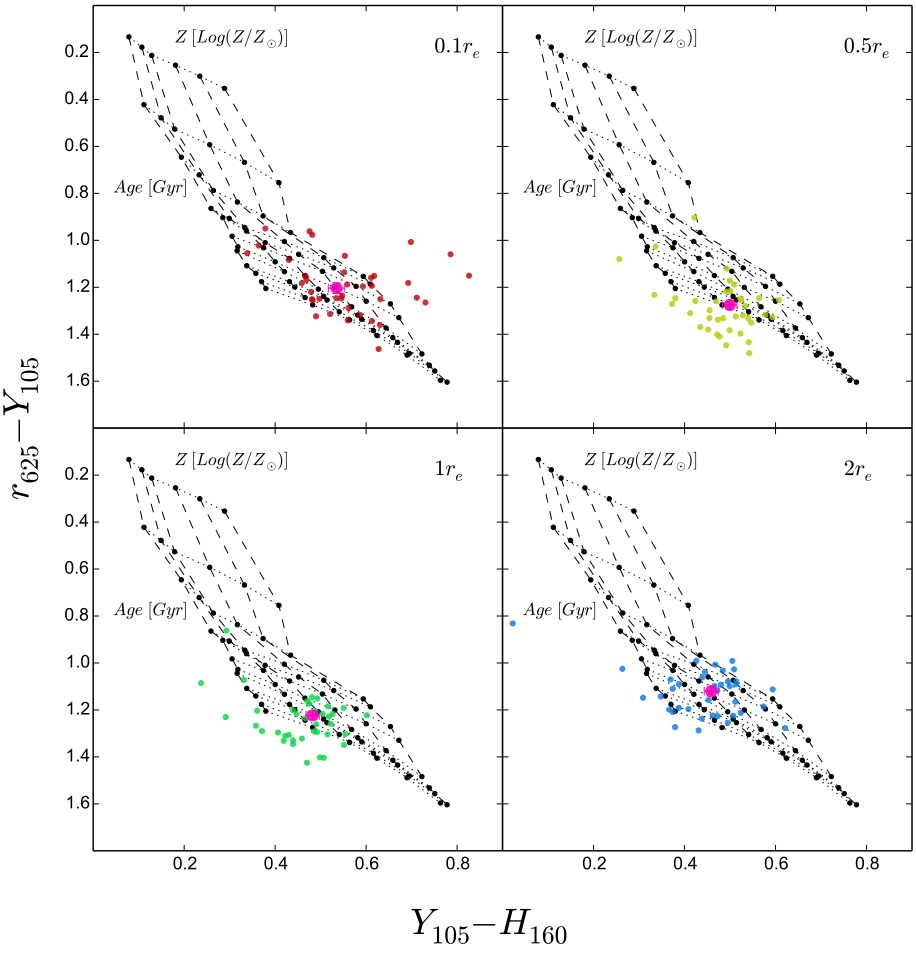

Figure 6.20.: Color-color diagrams for the color measurements in the MACS 0416 at the four different discrete radii. The color coding is the same as in Fig. 6.16, the magenta dots represent the respective median values with its size indicating the error. The grid points are determined by the same ages and metallicities as in Fig. 6.14

This demeanor is presumably again explained by the errors in the r_{625} band. As n determines the shape of the surface brightness profile, its influence is particularly considerable at small radii. Hence imprecise measurements of n can lead to substan-

tially wrong colors, which appears to apply in this case. To verify this hypothesis the individual ages have been derived for a radius $r = 0.2r_e$. As predicted the impact of an inaccurate n does not vanish but decreases, which results into a median age of 10.2 ± 0.5 Gyr. However neglecting the measurements at the most inner parts and considering a range of 0.5 - 2 r_e the sources show the expected trend with the galaxies being on average 3.0 ± 0.6 Gyr older in the centers than in the outskirts. Furthermore like it is the case for MACS 1206 also the MACS 0416 sample at $2r_e$ shows a very similar distribution to the one, for which the colors are derived from the total integrated magnitudes (Fig. 6.14).

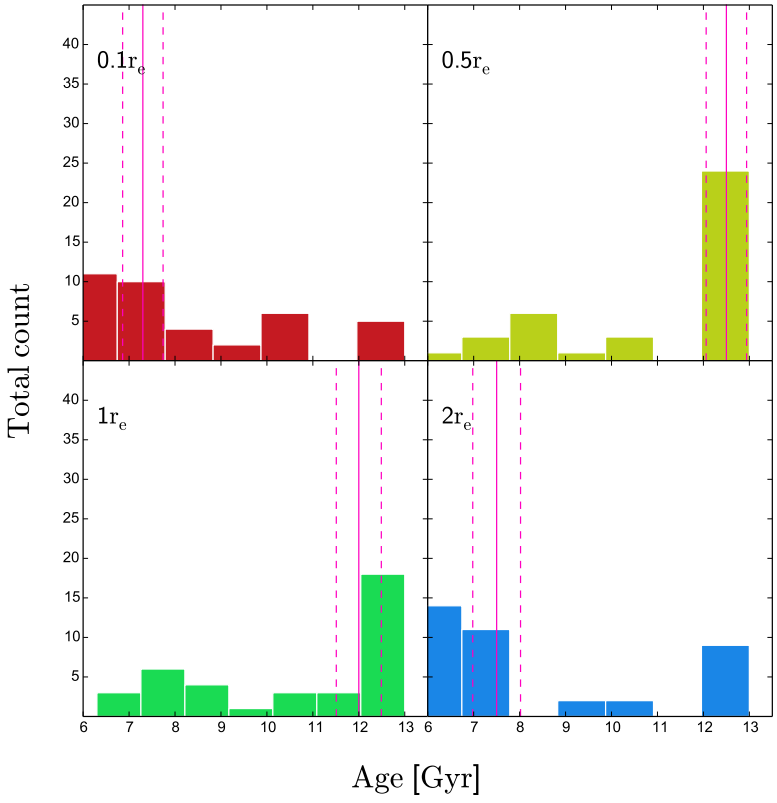

Figure 6.21.: Distributions of the assessed ages for the measurements in the MACS 0416 sample at the four different radii, which are indicated in the upper left corner and accordingly color coded. The median and its errors are again depicted as solid respectively dashed magenta lines.

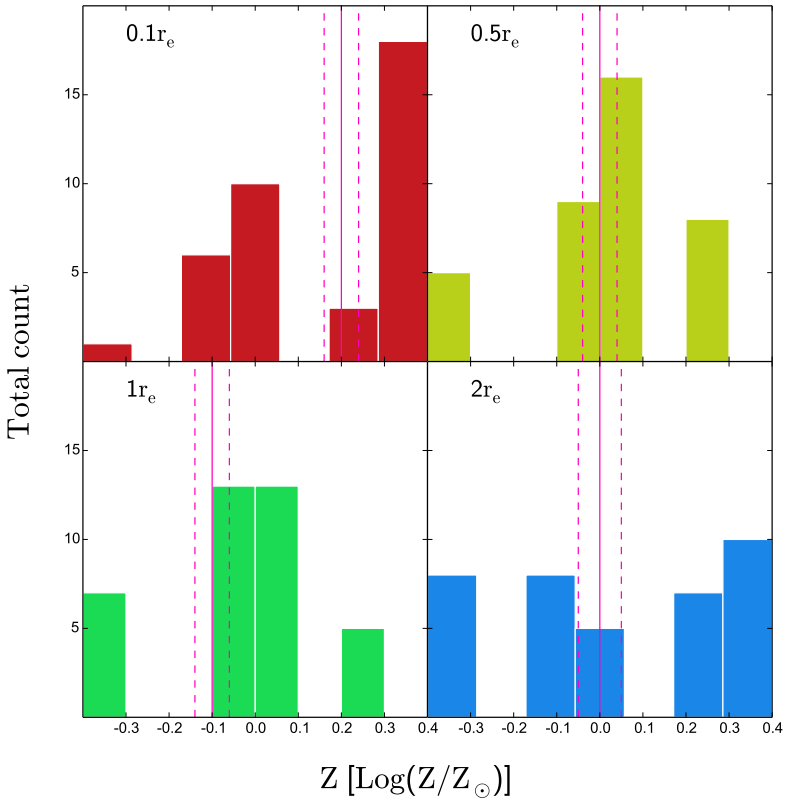

Figure 6.22.: Distributions of the assessed metallicities for the measurements in the MACS 0416 sample at the four different radii, which are indicated in the upper left corner and accordingly color coded. The median and its errors are again depicted as solid respectively dashed magenta lines.

As the metallicity is mainly described by the infrared color $Y_{105} - H_{160}$, with both bands possessing much more accurate measurements, the distributions of the galaxies' metallicities at the different radii are in good agreement with the expectations and also the MACS 1206 sample. At $0.1r_e$ more than 50 percent of the galaxies' stellar populations display supersolar metallicities, with additional $\sim$ 25 percent revealing metallicities in the solar range.

Increasing the radius confirms the trend of decreasing metallicities, with the median of the individual metallicity variations within a galaxy being 0.1 $\pm$ 0.06 [Log(Z/Z$_\odot$)].

Table 6.8 summarizes the median assessments of the individual changes in age and

metallicity in both samples. The simultaneous decrease of age and metallicity with radius in both clusters is evident, with the already presented exception of the ages in MACS 0416 at $0.1r_e$. This suggests that both galactic properties are responsible for the color gradients.

Table 6.8.: Medians of the individual measurements for ages and metallicities for both clusters at the four predetermined radii.

Cluster	$0.1r_e$	$0.5r_e$	$1r_e$	$2r_e$
		Age [Gyr]		
MACS 1206	13 ± 0.3	12 ± 0.3	10.2 ± 0.3	10.2 ± 0.3
MACS 0416	7.3 ± 0.4	12.5 ± 0.5	12 ± 0.5	7.5 ± 0.5
		Z [Log($Z/Z_\odot$)]		
MACS 1206	0.2 ± 0.03	0.0 ± 0.02	0.0 ± 0.02	0.0 ± 0.02
MACS 0416	0.2 ± 0.04	0.0 ± 0.04	-0.1 ± 0.04	0.0 ± 0.05

In comparison to the first two approaches with assuming a fixed overall metallicity respectively age the SSP grid results show a significant lower variation in both parameters, especially in the respective colors tracing the corresponding properties. This supports the assumption that differences in metallicity as well as age are origins for the color gradients.

7. Conclusions

The analyses of the early-type galaxies of the clusters MACS 1206 and MACS 0416 done in the course of this thesis revealed several characteristics of the examined galaxies, which appear to be mostly in good agreement with the current scientific consensus and also previous studies. However in order to derive more confident results it is vital to include in the future a robust error budget. As a consequence the impacts of galactic extinction as well as a potential dust presence in the observed galaxies could be better estimated.

Nevertheless a clear trend has been found for the effective radii to be ~ 25 percent smaller in the infrared H_{160} band than in the optical r_{625} filter, while the Sérsic index n can be assumed constant over this range. The medians of n over the whole examined wavelength range amounts to $n \sim 4.44 \pm 0.19$ for the MACS 1206 sample and 4.05 ± 0.29 for the MACS 0416 selection. These values turn out to be smaller than the median of $\langle n \rangle \sim 6$ La Barbera et al. (2010) found for local galaxies. However their analysis commenced from the g-band and extended down to the K-band, which could also explain their r_e assessments in these two bands decreasing by 35 percent. On the other hand Vulcani et al. (2014) likewise found an $\langle n \rangle \sim 4$, which can be considered constant over all filters, by also using the multi-band capabilities of *MegaMorph* for their local galaxy sample ranging from u to K and being provided through the *GAMA* survey. Additionally they also detected a decrease of ~ 40 percent for r_e going from u to H. Similar trends have been found by Kelvin et al. (2012), who established a 38 percent reduction in r_e for the same sample as well but by utilizing only single component fits. Finally Kennedy et al. (2015) confirms these results with examining the data supplied by *GAMA II*.

The same trends are discovered for early-type galaxies at intermediate redshifts, similar to the ones treated in this thesis. La Barbera et al. (2002, 2003) obtain comparable ratios of r_e and n for approximately 270 galaxies in three different clusters lying between $z = 0.21$ and $z = 0.64$. Utilizing filters corresponding to U, V and H in rest-frame their analyses reveal $r_{e,UV}/r_{e,opt} = 1.2 \pm 0.05$, $r_{e,opt}/r_{e,IR} = 1.26 \pm 0.06$ and $n_{UV}/n_{opt} = 1.0 \pm 0.1$, $n_{opt}/n_{IR} = 0.88 \pm 0.03$. Those determinations are in

excellent agreement with the assessments of this thesis and also consistent with the local values. Finally also for passive cluster galaxies at $z = 1.39$ those trends are still valid, as Chan et al. (2016) derived in a range between i_{775} and H_{160} a ~ 20 percent decrease in size for those objects.

The decrease in r_e with n remaining constant over wavelength can be explained by intrinsic negative color gradients being inherent in the early-type galaxies. Hence the bulk of the treated galaxies possess redder centers and a bluer stellar population in the exterior regions. According to the derived decrease of r_e the majority of the in this thesis examined galaxies show indeed negative color gradients with the medians of the gradients in four different colors being negative except for one, ranging between -0.05 $\pm$ 0.02 and -0.18 $\pm$ 0.01 mag dex^{-1} for the entire data sample containing all galaxies.

These outcomes are perfectly consistent with the findings of Saglia et al. (2000), who also derived the color gradients for $z \sim 0.4$ cluster galaxies in the rest-frame $U-B$, $U-V$ and $B-V$ colors, as all their objects have at least in one color a negative gradient in the same range presented in this thesis. Other studies treating galaxies at similar redshifts, like Tamura & Ohta (2000) with finding a median gradient of $\nabla(\lambda_{B,450} - \lambda_{I,814}) = -0.23 \pm 0.05$ mag dex^{-1}, La Barbera et al. (2002, 2003) derive likewise similar values for color gradients in elliptical galaxies and confirm the determinations. The values found in this thesis are especially consistent with the mean color gradients obtained by La Barbera et al. (2003) with $\nabla(\lambda_{UV} - \lambda_{opt}) = -0.18 \pm 0.04$ mag dex^{-1} and $\nabla(\lambda_{opt} - \lambda_{IR}) = -0.4 \pm 0.1$ mag dex^{-1}.

Similar results have already been described by Peletier et al. (1990a,b), who found mean color gradients of -0.20 $\pm$ 0.02 mag dex^{-1} in $U - R$, respectively -0.09 $\pm$ 0.02 in $B - R$ for local early-type galaxies and also by La Barbera & de Carvalho (2009), who expanded the analysis to seven different colors ranging from $g - r$ to $g - K$.

Many of the newest studies focus on higher redshift elliptical galaxies detecting on average steeper negative gradients than for local and intermediate-z galaxies. Gargiulo et al. (2012) found gradients between -0.1 $\pm$ 0.1 and -1.0 $\pm$ 0.1 mag dex^{-1} for their sample of early-type galaxies at $1.0 < z < 1.9$. Also Guo et al. (2011) reported for their $z \sim 2$ galaxies steeper color gradients, as well as De Propris et al. (2015), who derived a median color gradient of -0.25 mag dex^{-1} for their high-redshift ($\langle z \rangle \sim 1.25$) selection. Finally very recently Chan et al. (2016) found a median value of ~ 0.45 mag dex^{-1} for passive cluster galaxies at $z \sim 1.39$, which corresponds to being a factor 2 steeper than the local values.

Furthermore no correlation of the color gradients with cluster-centric distance, magnitude nor stellar mass can be found confirming that the variations in stellar populations are independent of those galactic properties. Saglia et al. (2000) came to the same conclusions in regard to the magnitudes, as well as Guo et al. (2011) and Gargiulo et al. (2012) concerning the stellar mass of the galaxies.

Interpreting the yield of the SSP models performed in the course of this thesis the origins of the color gradients, can be explained by a combination of age and metallicity gradients. The age differences from the innermost region to the outskirts of the galaxies appear rather shallow and add up on median to 1.2 ± 0.4 for MACS 1206 respectively 3.0 ± 0.6 Gyr for the less accurate modelled MACS 0416 sample, if the determinations at $0.1r_e$ are not considered. The metallicity gradients are characterized for both clusters to be $\sim$ -0.2 dex per decade in radius. Similar results are found by Saglia et al. (2000), La Barbera et al. (2003) and Tamura et al. (2000). Although the age variations found in this thesis appear to be stronger than the ones found in these publications, they are still well within the error estimates of these studies, especially considering that the age determinations done in this work required the results of the less precise r_{625} band, in particular regarding the assessments in MACS 0416. Hence this confirms that variations in metallicity are the dominant reason for the observed color gradients in elliptical galaxies.

Consequently all this coherent findings including the ones presented in this thesis can be used to constrain possible evolutionary scenarios. Early-type galaxies showing a decrease in r_e with wavelength and therefore also negative color gradients display differences in stellar populations. The order of these variations can support and disprove the different theories of galactic developments. In this context a monolithic collapse scenario would require much steeper negative gradients than observed, with logarithmic metallicity gradients between -0.5 and -1 dex per radial decade, due to the continuing inflow of metal rich gas towards the center during the formation process. As a result of this gas enrichment the younger stellar population must be situated in the interior, innermost regions of a galaxy, with ages of the stars increasing with radius. Hence a positive age gradient should be detectable, but rather the exact opposite is the case with the elliptical galaxies showing rather negative age gradients.

Also the assumption of gas rich mergers playing an important role in the recent evolution ($z \lesssim 0.5 - 1$) can be omitted, as this would result into an old, red and extended component superimposed by a younger and bluer stellar population with

an in comparison smaller r_e. Also this would contradict the similar determinations of n and r_e for local galaxies and those at intermediate redshifts. The observations in color variations as well as the findings of decreasing age and metallicity with radius support rather the hierarchical scenario with dry mergers contributing to an inside-out growth of the primary early-type galaxy. During this process the stars of lower mass galaxies with a younger and metal poorer population get accreted and settle into a more extended component compared to the original stellar distribution. This does not only lead to a significant increase in radius, whereas the mass is to a lesser extent enlarged, but also to a dilution of the age and metallicity variations, which subsequently match the observed gradients at different redshifts. This assumption is supported by the observations of very compact but massive quiescent galaxies at $z \sim 2$, with their size estimates being not an effect of errors in the modelling process and a resulting absence of flux detections at larger radii (Davari et al., 2014, and references therein).

8. Summary

In this thesis a total of 117 early-type galaxies at $z \sim 0.4$ are treated, with 79 belonging to the MACS 1206 cluster, while the remaining sources are part of the MACS 0416 structure. The photometric data is provided by the *CLASH* survey in 12 bands ranging from B_{435} to H_{160}, while the spectroscopic measurements and hence also the membership determinations are supplied from the follow-up program *CLASH-VLT*.

After determining an initial membership selection for the respective clusters, 2D models are produced for the observations in the 12 different filters utilizing the tool *MegaMorph*. A subsequent visual selection combined with the choice to only consider galaxies with $n > 2.5$ yields the final sample of elliptical galaxies. Using the structural parameters being delivered by the models, surface brightness profiles are created in order to produce in turn the radial profiles for the colors $g_{475} - I_{814}$, $r_{625} - Y_{105}$, $I_{814} - H_{160}$ and $Y_{105} - H_{160}$. Consequently the color gradients are derived as the logarithmic slopes of these color profiles by either approximating an lsq fit or calculating the ratios of the effective radii in both respective bands. Finally the contributions of age and metallicity to the color gradients are analyzed by employing BC03 SSP models each time adopting a Chabrier IMF, with the models being based on different formation redshifts, ranging from $z_f = 0.5$ to $z_f = 10$ and metallicities with a super-solar value $Z = 0.05$ at the one end and sub-solar $Z = 0.008$ on the other one. An ensuing comparison between the simulated colors at the cluster redshift with the observed ones, delivers the aimed for constraints.

Although better error estimates are needed to obtain improved insights on the impacts of dust and extinction, as well as better constraints on absolute values, the relative results acquired for elliptical galaxies in the course of this thesis are consistent with those of previous studies:

- For the whole sample the effective radius decreases on median with wavelength, with $r_{e,160} \sim 0.75 r_{e,625}$, describing already indirectly a negative color gradient, due to the presence of distinct stellar populations at different radii.

- The Sérsic index n can be assumed on median constant over the same wavelength range, restricting already the potential development scenarios to those, which leave n unchanged.

- The majority of the galaxies and the overall median show negative color gradients lying between -0.05 $\pm$ 0.02 and -0.18 $\pm$ 0.01 mag dex^{-1}, indicating a redder, older stellar population in the centers and bluer, younger stars in the outskirts. The results are independent of the derivation method, lsq fit or calculation, and also differ insignificantly between the employed colors.

- No correlation or dependence of the color gradients on stellar mass, magnitude or cluster-centric distance can be found, implying that all those properties are not directly responsible for the radial color variations.

- Age as well as more dominantly metallicity are driving the color gradients. While the centers appear to be $\sim$ 1 (MACS 1206) to $\sim$ 3 (MACS 0416) Gyr older than the exterior regions, the metallicity drops from super-solar $Z \sim 0.03$ in the innermost parts to values similar to the solar metallicity in the outer domains.

- Considering all those observations the most probable evolutionary scenario for elliptical galaxies is that they already assemble a majority of their stellar mass at very high redshifts ($z \gtrsim 2$), followed by a passive evolution of the initial stellar population. With time the galaxies undergo several dry and minor mergers, resulting in a much more notable increase in size than in mass, as the metal poorer and younger populations of the accreted galaxies settle into more extended structures.

The options to improve and/or broaden the determinations done in this thesis are manifold. One choice may be to distinguish the galaxies into late- and early-type galaxies not only by morphological criteria, but also to consider spectroscopic measurements. Consequently a much better differentiation even within those two main branches would be possible, offering the chance to examine potential trends with morphological type. In general it would also be intriguing to determine the results for field galaxies and to analyze the differences between galaxies in diverging environments. Finally an expansion of these investigations to different redshifts, in particular going to greater distances, could deliver compelling new insights on the formation and evolution of galaxies.

Acknowledgements

Mein erster Dank geht an Bodo Ziegler für die Idee dieses äußerst interessante und aktuelle Thema in einer Masterarbeit zu behandeln, die außerordentlich geduldige Betreuung und dafür, dass es mir ermöglicht wurde, Teil seiner Arbeitsgruppe zu sein, wodurch ich in das aktuelle Forschungsgeschehen eintauchen durfte. Insbesondere möchte ich mich auch bei allen anderen Mitgliedern bedanken, allen voran Ulli Kuchner, deren wertvolle Ratschläge speziell am Anfang unentbehrlich waren, Helmut Dannerbauer für seine kollegialen Ratschläge, Miguel Verdugo für die allzeitbereite Hilfe und auch für die Bereitstellung der Massen, Christian Maier für die Kataloge der Mitglieder der Galaxienhaufen und nicht zuletzt Lucas Ellmeier für immer wieder anregende Gesprächsthemen abseits der Astronomie. Mein Dank gilt auch Alberto Molino für das Erstellen der PSFs, sowie dem CLASH als auch dem CLASH-VLT Team für die umfangreichen Beobachtungen, Messungen und Daten.

Mein tiefster Dank gebührt selbstredend natürlich auch meinen Eltern, die mich im Zuge dieses langen Studiums stets unterstützt und ermutigt haben, ebenso Christian und Elisabeth, die mich nicht nur mit Korrekturen sondern auch mit immer wieder notwendigen Abwechslungen versorgt haben.

Zu guter Letzt gebührt mein innigster Dank Tanja, meiner Frau. Ihr jederzeitiger Rückhalt und immerwährender Zuspruch werden mir immer in Erinnerung bleiben, ebenso ihr offenes Ohr für die sich mir immer wieder neu darbietenden Herausforderungen, sowie Ihre aufmunternden Worte. Ohne Sie wäre all dies nicht möglich gewesen.

Bibliography

Annunziatella M., et al., 2014, A&A, 571, A80

Balestra I., et al., 2015, preprint, (arXiv:1511.02522)

Bamford S. P., Häußler B., Rojas A., Vika M., Cresswell J., 2012, in Tuffs R. J., Popescu C. C., eds, IAU Symposium Vol. 284, The Spectral Energy Distribution of Galaxies - SED 2011. pp 301–305, doi:10.1017/S1743921312009301

Barden M., et al., 2005, ApJ, 635, 959

Barden M., Häußler B., Peng C. Y., McIntosh D. H., Guo Y., 2012, MNRAS, 422, 449

Bender R., Burstein D., Faber S. M., 1992, ApJ, 399, 462

Bertin E., Arnouts S., 1996, A&AS, 117, 393

Bezanson R., van Dokkum P. G., Tal T., Marchesini D., Kriek M., Franx M., Coppi P., 2009, ApJ, 697, 1290

Biviano A., et al., 2013, A&A, 558, A1

Bruzual G., Charlot S., 2003, MNRAS, 344, 1000

Buitrago F., Trujillo I., Conselice C. J., Bouwens R. J., Dickinson M., Yan H., 2008, ApJL, 687, L61

Buitrago F., Trujillo I., Conselice C. J., Häußler B., 2013, MNRAS, 428, 1460

Buta R. J., 2011, preprint, (arXiv:1102.0550)

Chabrier G., 2003, PASP, 115, 763

Chan J. C. C., et al., 2016, MNRAS, 458, 3181

Ciotti L., 1991, A&A, 249, 99

Ciotti L., Bertin G., 1999, A&A, 352, 447

Conselice C. J., 2003, ApJS, 147, 1

Conselice C. J., 2006, MNRAS, 373, 1389

Conselice C. J., 2014, ARA&A, 52, 291

Crampin J., Hoyle F., 1961, MNRAS, 122, 27

Daddi E., et al., 2005, ApJ, 626, 680

Davari R., Ho L. C., Peng C. Y., Huang S., 2014, ApJ, 787, 69

De Propris R., Bremer M. N., Phillipps S., 2015, MNRAS, 450, 1268

Dressler A., 1980, ApJ, 236, 351

Dressler A., 1984, ARA&A, 22, 185

Driver S. P., et al., 2006, MNRAS, 368, 414

Driver S. P., Robotham A. S. G., Bland-Hawthorn J., Brown M., Hopkins A., Liske J., Phillipps S., Wilkins S., 2013, MNRAS, 430, 2622

Ebeling H., Edge A. C., Henry J. P., 2001, ApJ, 553, 668

Eichner T., et al., 2013, ApJ, 774, 124

Freeman K. C., 1970, ApJ, 160, 811

Gargiulo A., Saracco P., Longhetti M., 2011, MNRAS, 412, 1804

Gargiulo A., Saracco P., Longhetti M., La Barbera F., Tamburri S., 2012, MNRAS, 425, 2698

Girardi M., et al., 2015, A&A, 579, A4

Graham A. W., Driver S. P., 2005, PASA, 22, 118

Guo Y., et al., 2011, ApJ, 735, 18

Häussler B., et al., 2007, ApJS, 172, 615

Häußler B., et al., 2013, MNRAS, 430, 330

Hiemer A., Barden M., Kelvin L. S., Häußler B., Schindler S., 2014, MNRAS, 444, 3089

Hogg D. W., Baldry I. K., Blanton M. R., Eisenstein D. J., 2002a, ArXiv Astrophysics e-prints,

Hogg D. W., et al., 2002b, AJ, 124, 646

Holmberg E., 1958, Meddelanden fran Lunds Astronomiska Observatorium Serie II, 136, 1

Hubble E. P., 1926, ApJ, 64

Jouvel S., et al., 2014, A&A, 562, A86

Kelvin L. S., et al., 2012, MNRAS, 421, 1007

Kennedy R., et al., 2015, MNRAS, 454, 806

Kobayashi C., 2004, MNRAS, 347, 740

Kodama T., Arimoto N., 1997, A&A, 320, 41

Koekemoer A. M., et al., 2011, ApJS, 197, 36

Kormendy J., Bender R., 2012, ApJS, 198, 2

Kron R. G., 1980, ApJS, 43, 305

Kroupa P., 2001, MNRAS, 322, 231

La Barbera F., de Carvalho R. R., 2009, ApJL, 699, L76

La Barbera F., Busarello G., Merluzzi P., Massarotti M., Capaccioli M., 2002, ApJ, 571, 790

La Barbera F., Busarello G., Massarotti M., Merluzzi P., Mercurio A., 2003, A&A, 409, 21

La Barbera F., de Carvalho R. R., de La Rosa I. G., Lopes P. A. A., Kohl-Moreira J. L., Capelato H. V., 2010, MNRAS, 408, 1313

Le Fèvre O., et al., 2003, in Iye M., Moorwood A. F. M., eds, Proc. SPIE Vol. 4841, Instrument Design and Performance for Optical/Infrared Ground-based Telescopes. pp 1670–1681, doi:10.1117/12.460959

Longhetti M., et al., 2007, MNRAS, 374, 614

Mancone C. L., Gonzalez A. H., 2012, PASP, 124, 606

Maraston C., 2003, in Kissler-Patig M., ed., Extragalactic Globular Cluster Systems. p. 237 (arXiv:astro-ph/0301419), doi:10.1007/10857603_37

Maraston C., 2005, MNRAS, 362, 799

Mercurio A., et al., 2015, preprint, (arXiv:1510.08097)

Montes M., Trujillo I., Prieto M. A., Acosta-Pulido J. A., 2014, MNRAS, 439, 990

Mortlock A., et al., 2013, MNRAS, 433, 1185

Naab T., Johansson P. H., Ostriker J. P., 2009, ApJL, 699, L178

Ogrean G. A., et al., 2015, ApJ, 812, 153

Oke J. B., 1974, ApJS, 27, 21

Oke J. B., Gunn J. E., 1983, ApJ, 266, 713

Peletier R. F., Davies R. L., Illingworth G. D., Davis L. E., Cawson M., 1990a, AJ, 100, 1091

Peletier R. F., Valentijn E. A., Jameson R. F., 1990b, A&A, 233, 62

Peng C. Y., Ho L. C., Impey C. D., Rix H.-W., 2002, AJ, 124, 266

Peng C. Y., Ho L. C., Impey C. D., Rix H.-W., 2010, AJ, 139, 2097

Postman M., et al., 2012, ApJS, 199, 25

Presotto V., et al., 2014, A&A, 565, A126

Renzini A., 2006, ARA&A, 44, 141

Rosati P., et al., 2014, The Messenger, 158, 48

Saglia R. P., Maraston C., Greggio L., Bender R., Ziegler B., 2000, A&A, 360, 911

Salpeter E. E., 1955, ApJ, 121, 161

Sandage A., 1961, The Hubble atlas of galaxies

Schlegel D. J., Finkbeiner D. P., Davis M., 1998, ApJ, 500, 525

Sérsic J. L., 1963, Boletin de la Asociacion Argentina de Astronomia La Plata Argentina, 6, 41

Sérsic J. L., 1968, Atlas de galaxias australes

Shen S., Mo H. J., White S. D. M., Blanton M. R., Kauffmann G., Voges W., Brinkmann J., Csabai I., 2003, MNRAS, 343, 978

Silk J., Mamon G. A., 2012, Research in Astronomy and Astrophysics, 12, 917

Simard L., et al., 2002, ApJS, 142, 1

Smail I., Kuntschner H., Kodama T., Smith G. P., Packham C., Fruchter A. S., Hook R. N., 2001, MNRAS, 323, 839

Spergel D. N., et al., 2003, ApJS, 148, 175

Tamura N., Ohta K., 2000, AJ, 120, 533

Tamura N., Kobayashi C., Arimoto N., Kodama T., Ohta K., 2000, AJ, 119, 2134

Thomas D., Maraston C., Bender R., Mendes de Oliveira C., 2005, ApJ, 621, 673

Thomas J., Saglia R. P., Bender R., Thomas D., Gebhardt K., Magorrian J., Corsini E. M., Wegner G., 2009, ApJ, 691, 770

Tinsley B. M., 1972, A&A, 20, 383

Trujillo I., Conselice C. J., Bundy K., Cooper M. C., Eisenhardt P., Ellis R. S., 2007, MNRAS, 382, 109

Trujillo I., Ferreras I., de La Rosa I. G., 2011, MNRAS, 415, 3903

Umetsu K., et al., 2012, ApJ, 755, 56

Vader J. P., Vigroux L., Lachieze-Rey M., Souviron J., 1988, A&A, 203, 217

Vulcani B., et al., 2014, MNRAS, 441, 1340

Worthey G., 1994, ApJS, 95, 107

Wu H., Shao Z., Mo H. J., Xia X., Deng Z., 2005, ApJ, 622, 244

Ziegler B. L., Bender R., 1997, MNRAS, 291, 527

Zitrin A., et al., 2012, ApJ, 749, 97

de Vaucouleurs G., 1948, Annales d'Astrophysique, 11, 247

van Dokkum P. G., et al., 2008, ApJL, 677, L5

van Dokkum P. G., et al., 2010, ApJ, 709, 1018

van Dokkum P. G., et al., 2013, ApJL, 771, L35

van den Bergh S., Abraham R. G., Ellis R. S., Tanvir N. R., Santiago B. X., Glazebrook K. G., 1996, AJ, 112, 359

van der Wel A., et al., 2014, ApJ, 788, 28

List of Figures

1.1. A modern version of the conventional Hubble tuning fork to classify galaxies. Taken from Kormendy & Bender (2012). 6
1.2. Left side: Color-magnitude diagram depicting the red sequence of early-type galaxies, shown as red squares. Later-types are displayed as blue crosses and intermediates as green triangles. Right side: Fractions of different morphological types at different stellar masses. The solid, red line represents early-types, the dashed green line spirals and the blue dotted line irregular galaxies. Diagrams taken from (Conselice, 2006). 7
1.3. Different Sérsic profiles with same I_e and r_e. The distinctions in the center and large radii depending on n can easily be seen. Diagram from (Peng et al., 2010). 12

3.1. Fields covered by the CLASH observations, which are done twice at two different orientations $\sim 30°$apart. While the cluster core is observed with ACS, the parallel fields are observed with WFC3 and vice versa. Taken from (Postman et al., 2012). 30
3.2. Response curves for the filters used in the CLASH survey ranging from near-UV to near-IR. Just for clarity some filter curves show an offset of 0.2 (dashed line). Plot taken from (Postman et al., 2012). . 31
3.3. Redshift distribution of the initial selection for MACS 1206. Red shows galaxies with spectroscopic redshift determinations, yellow the ones with photometric redshift estimates. The gray dashed line indicates the cluster redshift at $z \sim 0.44$ 34
3.4. MACS 1206 in the WFC3 F105W band, depicting the initial selection of galaxies to be fitted, distinguished in a sample with spectroscopic redshift determinations (red circles) and photometric redshift estimates (yellow circles). 35

3.5. Distribution of sample galaxies in redshift for MACS 0416. The double peak structure is clearly visible. The cluster redshift $z \sim 0.397$ is depicted as the gray dashed line. 36
3.6. Initial sample selection for MACS 0416. Spectroscopic members are shown with red circles, galaxies with photometric redshifts with yellow circles. The NE BCG, also possessing a spectroscopic redshift determination, is indicated by a cyan circle. 37

4.1. Example of a multi-band *GALFIT* fitting output for a galaxy of the MACS 1206 sample. From left to right: Original input images, models and residuals for the respective fits. The scaling of the images is matched, which in turn also illustrates the different detection levels in the different filters. 43
4.2. Color-magnitude diagrams for MACS 1206 (left) and MACS 0416 (right). The gray dots represent all detected sources in the WFC3/IR field of view, overlayed by the fitted galaxies, color coded according to their Sérsic index n. 46
4.3. Surface brightness profiles (upper plot) and color profile with overlayed fit (lower plot) for a MACS 1206 early-type galaxy. The blue and red dotted and dashed lines in the upper diagram correspond to 0.1, 1 and $2r_e$ of the respective bands. The, from red to blue coloured, dashed lines in the lower figure correspond to 0.1, 0.2, 0.5, 1 and $2r_e$ of the bluer band, in this particular case the r_{625} filter. 48

6.1. Distribution of the Sérsic index n for the MACS 1206 sample in the individual bands. The solid magenta line indicates the median, while the dashed magenta lines denotes the uncertainty interval. The respective filters are given in the upper left corners. 52
6.2. Distribution of the effective radius r_e for the MACS 1206 sample in the individual bands. The solid magenta line indicates the median, while the dashed magenta lines denotes the uncertainty interval. The respective filters are given in the upper left corners. 53
6.3. Same as figure 6.1 only for the MACS 0416 sample. 54
6.4. Same as figure 6.2 only for the MACS 0416 sample. 55
6.5. $\mathcal{N}$ against $\mathcal{R}$ for every galaxy. The peak of $\mathcal{N}$ tends to ~ 0.9, while $\langle \mathcal{R} \rangle \sim 0.75$. 58

6.6. Distributions of the color gradients for the four colors depending on the deriving method. Red indicates the color gradients assessed by lsq fitting, blue displays the calculated gradients. The corresponding dashed lines denotes the respective medians, whereas the gray dotted line indicates a color gradient = 0. 61

6.7. Differences in the color gradient results for the MACS 1206 galaxies in the four colors between the lsq approach and the calculations following La Barbera et al. (2002). The magenta dot represents the median value for both measurements, the gray dashed line unity and the gray dotted lines a color gradient = 0. 62

6.8. Same as Fig. 6.6, only for the MACS 0416 sample. 63

6.9. Same as Fig. 6.7, only for the MACS 0416 sample. 64

6.10. Fitted and calculated color gradients in the four colors for the MACS 1206 galaxies versus projected cluster-centric distance R [Mpc] (left), total magnitude in I_{814} $\mathrm{Mag}_{I,814}$ [AB mag] (middle) and stellar mass M_* [$\mathrm{M}_\odot$] (right). 65

6.11. Same as Fig. 6.10, only for MACS 0416. 66

6.12. $r_{625} - Y_{105}$ vs. $Y_{105} - H_{160}$ diagram with the overall colors of the MACS 1206 galaxies overlayed in green. The magenta dot represents the median of the ages and metallicites of the sample, with the errors being of the order of the size of the marker. 70

6.13. Distributions for the derived ages and metallicities for the MACS 1206 sample. The medians are indicated by the solid magenta line, the according uncertainties by the dashed lines. 71

6.14. $r_{625} - Y_{105}$ vs. $Y_{105} - H_{160}$ diagram with the overall colors of the MACS 0416 galaxies overlayed in green. The magenta dot represents the median of the ages and metallicites of the sample, with the errors being of the order of the size of the marker. 72

6.15. Distributions for the derived ages and metallicities for the MACS 0416 sample. The medians are indicated by the solid magenta line, the according uncertainties by the dashed lines. 73

6.16. Color-color diagram for one of the galaxies in the MACS 1206 sample. The red dot represents the color values at $0.1r_e$, the yellow one at $0.5r_e$, the green one at $1r_e$ and finally the blue one at $2r_e$. 74

6.17. Color-color diagrams for the color measurements in the MACS 1206 at the four different discrete radii. The color coding is the same as in Fig. 6.16, the magenta dots represent the respective median values with its size indicating the error. The grid points are determined by the same ages and metallicities as in Fig. 6.14. 75
6.18. Distributions of the assessed ages for the measurements in the MACS 1206 sample at the four different radii, which are indicated in the upper left corner and accordingly color coded. The median and its errors are again depicted as solid respectively dashed magenta lines. 76
6.19. Distributions of the assessed metallicities for the measurements in the MACS 1206 sample at the four different radii, which are indicated in the upper left corner and accordingly color coded. The median and its errors are again depicted as solid respectively dashed magenta lines. 77
6.20. Color-color diagrams for the color measurements in the MACS 0416 at the four different discrete radii. The color coding is the same as in Fig. 6.16, the magenta dots represent the respective median values with its size indicating the error. The grid points are determined by the same ages and metallicities as in Fig. 6.14 78
6.21. Distributions of the assessed ages for the measurements in the MACS 0416 sample at the four different radii, which are indicated in the upper left corner and accordingly color coded. The median and its errors are again depicted as solid respectively dashed magenta lines. 79
6.22. Distributions of the assessed metallicities for the measurements in the MACS 0416 sample at the four different radii, which are indicated in the upper left corner and accordingly color coded. The median and its errors are again depicted as solid respectively dashed magenta lines. 80

List of Tables

3.1. The central wavelengths of the HST filter set used in the CLASH survey and the respective 5σ magnitude limits for extended sources. (Magnitude limits taken from (Jouvel et al., 2014)) 31

6.1. Median values for n and r_e for the MACS 1206 sample in each filter. The uncertainties are derived by using $1.253\sigma/\sqrt{N}$. 56
6.2. The same as table 6.1, only for the MACS 0416 sample. 57
6.3. Medians of the $n_{H,160}/n_{r,625}$ ($\mathcal{N}$) and $r_{e_{H,160}}/r_{e_{r,625}}$ ($\mathcal{R}$) measurements for both cluster samples. 58
6.4. Medians of the color gradients for the MACS 1206 sample in four different colors. 60
6.5. Medians of the color gradients for the MACS 0416 sample in four different colors. 60
6.6. Median results of the SSP analysis for ages and metallicities of the MACS 1206 galaxies at different radii and for both colors. 68
6.7. Median results of the SSP analysis for ages and metallicities of the MACS 0416 galaxies at different radii and for both colors. 68
6.8. Medians of the individual measurements for ages and metallicities for both clusters at the four predetermined radii. 81

C.1. Magnitude assessments in the ACS bands for the fitted early-type galaxies in MACS 1206. 114
C.2. Magnitude assessments in the WFC3/IR bands for the fitted early-type galaxies in MACS 1206. 118
C.3. r_e assessments in the ACS bands for the fitted early-type galaxies in MACS 1206. To calculate the values in kpc the cosmological parameters $H_0 = 70$ km s^{-1} Mpc $^{-1}$, $\Omega_\Lambda = 0.7$ and $\Omega_M = 0.3$ have been adopted with a pixelscale of 0.065”/px and a cluster redshift $z \sim 0.44$. 121

C.4. r_e assessments in the WFC3/IR bands for the fitted early-type galaxies in MACS 1206. To calculate the values in kpc the cosmological parameters $H_0 = 70$ km s^{-1} Mpc $^{-1}$, $\Omega_\Lambda = 0.7$ and $\Omega_M = 0.3$ have been adopted with a pixelscale of 0.065"/px and a cluster redshift $z \sim 0.44$. 125

C.5. Measurements of n in the ACS bands for the selected early-type galaxies in MACS 1206. 128

C.6. Measurements of n in the WFC3/IR bands for the selected early-type galaxies in MACS 1206. 132

C.7. Magnitude assessments in the ACS bands for the fitted early-type galaxies in MACS 0416 135

C.8. Magnitude assessments in the WFC3/IR bands for the fitted early-type galaxies in MACS 0416 137

C.9. r_e assessments in the ACS bands for the fitted early-type galaxies in MACS 0416. To calculate the values in kpc the cosmological parameters $H_0 = 70$ km s^{-1} Mpc $^{-1}$, $\Omega_\Lambda = 0.7$ and $\Omega_M = 0.3$ have been adopted with a pixelscale of 0.065"/px and a cluster redshift $z \sim 0.397$. 138

C.10. r_e assessments in the WFC3/IR bands for the fitted early-type galaxies in MACS 0416. To calculate the values in kpc the cosmological parameters $H_0 = 70$ km s^{-1} Mpc $^{-1}$, $\Omega_\Lambda = 0.7$ and $\Omega_M = 0.3$ have been adopted with a pixelscale of 0.065"/px and a cluster redshift $z \sim 0.397$. 140

C.11. Measurements of n in the ACS bands for the selected early-type galaxies in MACS 0416. 142

C.12. Measurements of n in the WFC3/IR bands for the selected early-type galaxies in MACS 0416. 144

C.13. Color gradients of the early-type galaxy sample of MACS 1206. . . 145

C.14. Color gradients of the early-type galaxy sample of MACS 0416. . . 148

C.15. SSP results for the MACS 1206 sample in the $r_{625} - Y_{105}$ color. The first column contains the IDs of the galaxies. The ages for the populations located at the respective radii are derived by assuming a fixed solar metallicity. The metallicities are determined by fixing the age to 12 Gyr at $z = 0$. 149

C.16. SSP results for the MACS 1206 sample in the $Y_{105} - H_{160}$ color. The first column contains the IDs of the galaxies. The ages for the populations located at the respective radii are derived by assuming a fixed solar metallicity. The metallicities are determined by fixing the age to 12 Gyr at $z = 0$. 152

C.17. SSP results for the MACS 0416 sample in the $r_{625} - Y_{105}$ color. The first column contains the IDs of the galaxies. The ages for the populations located at the respective radii are derived by assuming a fixed solar metallicity. The metallicities are determined by fixing the age to 12 Gyr at $z = 0$. 155

C.18. SSP results for the MACS 0416 sample in the $Y_{105} - H_{160}$ color. The first column contains the IDs of the galaxies. The ages for the populations located at the respective radii are derived by assuming a fixed solar metallicity. The metallicities are determined by fixing the age to 12 Gyr at $z = 0$. 157

C.19. SSP results for the MACS 1206 sample using a color-color grid with $r_{625} - Y_{105}$ and $Y_{105} - H_{160}$. The first column contains the IDs of the galaxies. The ages and metallicities for the stellar populations at the respective radii are derived by finding the nearest grid points with their colors corresponding to modelled ages and metallicities. 159

C.20. SSP results for the MACS 0416 sample using a color-color grid with $r_{625} - Y_{105}$ and $Y_{105} - H_{160}$. The first column contains the IDs of the galaxies. The ages and metallicities for the stellar populations at the respective radii are derived by finding the nearest grid points with their colors corresponding to modelled ages and metallicities. 162

Appendix

A. Source Extractor input file

```
# Default configuration file for SExtractor 2.8.6

#-------------------------------- Catalog ------------------------------------
CATALOG_NAME     /no_need_for_a_name.cat
# Will be overwritten anyway! name of the output catalog
CATALOG_TYPE     ASCII_HEAD
# NONE,ASCII,ASCII_HEAD, ASCII_SKYCAT, ASCII_VOTABLE, FITS_1.0
#or FITS_LDAC
PARAMETERS_NAME  /no_need.params
# Will be overwritten anyway! name of the file
#containing catalog contents

#------------------------------- Extraction ----------------------------------
DETECT_TYPE      CCD
# CCD (linear) or PHOTO (with gamma correction)
DETECT_MINAREA   80
# minimum number of pixels above threshold default: 100
THRESH_TYPE      RELATIVE
# threshold type: RELATIVE (in sigmas) or ABSOLUTE (in ADUs)
DETECT_THRESH    2.5
# <sigmas> or <threshold>,<ZP> in mag.arcsec-2  #default: 2.8
ANALYSIS_THRESH  2.5
# <sigmas> or <threshold>,<ZP> in mag.arcsec-2 #default: 2.8
FILTER           Y
# apply filter for detection (Y or N)?
FILTER_NAME      tophat_3.0_3x3.conv
# name of the file containing the filter
FILTER_THRESH
# Threshold[s] for retina filtering
DEBLEND_NTHRESH  32
# Number of deblending sub-thresholds #default: 64
DEBLEND_MINCONT  0.002
# Minimum contrast parameter for deblending
```

```
34 CLEAN               Y
35 # Clean spurious detections? (Y or N)?
36 CLEAN_PARAM         0.5
37 # Cleaning efficiency
38 MASK_TYPE           CORRECT
39 # type of detection MASKing: can be one of NONE, BLANK or CORRECT
40
41 #-------------------------- Weighting ----------------------------------
42 WEIGHT_TYPE         NONE
43 # type of WEIGHTing: NONE, BACKGROUND, MAP_RMS,
44 #MAP_VAR or MAP_WEIGHT
45 WEIGHT_IMAGE        /no_need.fits
46 # Will be overwritten anyway! weight-map filename
47 WEIGHT_GAIN         Y
48 # modulate gain (E/ADU) with weights? (Y/N)
49 WEIGHT_THRESH
50 # weight threshold[s] for bad pixels
51
52 #-------------------------- Flaging ------------------------------------
53 FLAG_IMAGE          flag.fits
54 # filename for an input FLAG-image
55 FLAG_TYPE           OR
56 # flag pixel combination: OR, AND, MIN, MAX or MOST
57
58 #------------------------ Photometry -----------------------------------
59 PHOT_APERTURES      60
60 # MAG_APER aperture diameter(s) in pixels
61 PHOT_AUTOPARAMS     2.5, 3.5
62 # MAG_AUTO parameters: <Kron_fact>,<min_radius>
63 PHOT_PETROPARAMS    2.0, 3.5
64 # MAG_PETRO parameters: <Petrosian_fact>, <min_radius>
65 PHOT_AUTOAPERS      0.0,0.0
66 # <estimation>,<measurement> minimum apertures for MAG_AUTO
67 #and MAG_PETRO
68 PHOT_FLUXFRAC       0.5
69 # flux fraction[s] used for FLUX_RADIUS
70 SATUR_LEVEL         60000.0
71 # level (in ADUs) at which arises saturation
72 #SATUR_KEY           NOEXIT
73 # keyword for saturation level (in ADUs) - don't trust SATURATE
74 MAG_ZEROPOINT       25.9433
75 # magnitude zero-point
76 MAG_GAMMA           4.0
```

```
77 # gamma of emulsion (for photographic scans)
78 GAIN                    2.0
79 # detector gain in e-/ADU
80 #GAIN_KEY               GAIN
81 # keyword for detector gain in e-/ADU
82 PIXEL_SCALE             0.065
83 # size of pixel in arcsec (0=use FITS WCS info)
84
85 #-------------------- Star/Galaxy Separation ------------------------
86 SEEING_FWHM             0.1
87 # stellar FWHM in arcsec
88 STARNNW_NAME            default.nnw
89 # Neural-Network_Weight table filename
90
91 #------------------------- Background ---------------------------------
92 BACK_TYPE               AUTO
93 # AUTO or MANUAL
94 #BACK_TYPE               MANUAL
95 # AUTO or MANUAL
96 BACK_VALUE              3951.
97 # Default background value in MANUAL mode
98 BACK_SIZE               214
99 # Background mesh: <size> or <width>,<height>
100 BACK_FILTERSIZE         5
101 # Background filter: <size> or <width>,<height>
102 BACKPHOTO_TYPE          LOCAL
103 # can be GLOBAL or LOCAL
104 BACKPHOTO_THICK         60
105 # thickness of the background LOCAL annulus
106 BACK_FILTTHRESH         0.0
107 # Threshold above which the background-map filter operates
108
109 #------------------------- Check Image ---------------------------------
110 CHECKIMAGE_TYPE         NONE
111 # can be NONE, BACKGROUND, BACKGROUND_RMS, MINIBACKGROUND,
112 # MINIBACK_RMS, -BACKGROUND,nFILTERED, OBJECTS, -OBJECTS,
113 # SEGMENTATION or APERTURES
114 CHECKIMAGE_NAME         /check.fits
115 # Filename for the check-image
116
117 #--------------- Memory (change with caution!) -----------------------
118 MEMORY_OBJSTACK         30000
119 # 3000 number of objects in stack
```

```
MEMORY_PIXSTACK   10000000
# 1200000 number of pixels in stack - x4 from default
MEMORY_BUFSIZE    4096
# 1024 number of lines in buffer

#-------------------- Association -----------------------------
ASSOC_NAME        sky.list
# name of the ASCII file to Associate
ASSOC_DATA        2,3,4
# columns of the data to replicate (0=all)
ASSOC_PARAMS      2,3,4
# columns of xpos,ypos[,mag]
ASSOC_RADIUS      2.0
# cross-matching radius (pixels)
ASSOC_TYPE        NEAREST
# Association method: FIRST, NEAREST, MEAN, MAG_MEAN, SUM,
# MAG_SUM, MIN or MAX
ASSOCSELEC_TYPE   MATCHED
# ASSOC selection type: ALL, MATCHED or -MATCHED

#-------------------- Miscellaneous ---------------------------
VERBOSE_TYPE      QUIET
# can be QUIET, NORMAL or FULL
WRITE_XML         N
# Write XML file (Y/N)?
XML_NAME          sex.xml
# Filename for XML output
XSL_URL       file:///usr/share/sextractor/sextractor.xsl
# Filename for XSL style-sheet
NTHREADS           1
# Number of simultaneous threads for the SMP version of SExtractor
# 0 = automatic
FITS_UNSIGNED     N
# Treat FITS integer values as unsigned (Y/N)?
INTERP_MAXXLAG    16
# Max. lag along X for 0-weight interpolation
INTERP_MAXYLAG    16
# Max. lag along Y for 0-weight interpolation
INTERP_TYPE       ALL
# Interpolation type: NONE, VAR_ONLY or ALL
```

B. MegaMorph setup file

```
#==========FILE LOCATIONS==========
A00) /home/marian/data/member_run_1/images.gala
#file containing ALL input files, including SExtractor
#(1st line) and all bands, weight,...)
A01) /home/marian/data/member_run_1/output_tier_1
#output directory for catalogues
#
#==========SEXTRACTOR SETUP==========
B00) execute
#execute the SExtractor block
B01) /home/marian/programs/sextractor/usr/bin/sex
#SExtractor executable including path
B02) /home/marian/data/member_run_1/gala.param
 #output parameters in .param-format
B03) /home/marian/data/member_run_1/M1206_cold.sex
#SExtractor setup file (cold),
#it has to properly deblend all brighter objects
B04) coldcat
#output catalogue (cold)
B05) coldseg.fits
#output segmentation map (cold)
B06) /home/marian/data/member_run_1/M1206_hot.sex
#SExtractor setup file (hot), tuned to pick up faint objects
B07) hotcat
#output catalogue (hot)
B08) hotseg.fits
 #output segmentation map (hot)
B09) 1.05
#enlarge the cold isophotes for catalogue combination by a factor.
#1.1 = by 10%. If the source in hot mode lies "sufficiently"
#outside of all cold Kron ellipses, it enters the output catalogue
B10) outcat
#output combined catalogue
B11) outseg.fits
#output combined segmentation map
B12) outparam
#output parameter file
B13) check.fits
#check image filename
B14) apertures
#check image type
```

```
B15) none
# ('rms' = true) is the SEXtractor 'weight' map a RMS map
#that should be used for SExtractor?
B16) none
#list of positions to be excluded from the individual SExtractor
#catalogues (to remove bad detections; format: x y)
B17) 1.5
#radius in pix used to exclude objects: gala rejects any
#detection within a certain radius B16 automatically from the
#SEx catalogue on a subsequent run of the code.
#Thus, if one wants to refine the cat, the sex section of the
#code has to run twice, i.e. gala needs to be started first
#with only the sex section activated and then run a 2nd time with
#the SEx section and optionally others enables as well.
#the first exec is for identifying bad detections,
#the 2nd run then treats them.
B18)
#if set "outonly": hot/cold catalogues/segmaps are deleted,
#else: all catalogues/segmaps are kept
B19) none
#list of positions to be excluded from the final
B20) combined_se_cat
#only gets created with C)
#combined sextractor catalogue put in A01)
#
#==========STAMP SETUP==========
C00) execute
#execute the Stamps creation block
C01) stamps
#descriptor file for postage stamps
C02)
#postposition for postage stamps (only used for single image run,
#NOT for mutli-wavelength) #preposition for postage stamps
#only works if left blank! (can't find rms image otherwise)
C03) 1.5
#scale factor by which the sextractor isophotes are enlarged
#
#==========SKY PREPARATION SETUP==========
D00) execute
#execute the sky preparation block
#always perform D, E and F together
D01) skymap
#output object/sky-mapfile
```

```
D02) outsky
#output filename for sky values
D03) 1.1
#scale factor by which SEx isophote is enlarged (for skymap)
D04) 1.1
#scale factor by which SEx isophote is enlarged (for neighbours)
D05) 15
#additional offset to scale factor
D06) 15
#distance between individual sky isophotes
D07) 30
#width of individual sky isophotes
D08) 15
#gap between sextractor isophote and inner sky isophote
D09) 2.5
#cut below which objects are considered as contributing
D10) 3
#nobj_max; max number of allowed contributing sources
D11) 1.4
#power by which the flux_radius is raised to convert to Re
D12) 15
#calculate the slope of the sky from the x last determinations
D13) -0.25
#slope in fwhm_image vs. mag_best below which object is star
D14) 2.75
# here: Flux-radius vs. Ic_aper
#zeropoint in fwhm_image vs. mag_best below which object is star
D15) 5
#magnitude faint end limit for secondaries when fitting galaxies
D16) 2
#magnitude faint end limit for secondaries when fitting stars
D17) 3
#number of neighbouring frames (see text for details)
D18) 16    #!!
#maximum number of parallel processes (see text for details)
D19) 200
#minimum distance (in arcseconds) between sources processed
D20) 60
#minimum distance (in arcseconds) to already blocked objects
#(to make sure that no faint object next to a very bright one is
# fit. standard value: 0.3*D20 )
D21) /home/marian/data/member_run_1/all_members.coords
#optional list containing primary targets
```

```
D22) 1.0
#search/correlation radius for the above list [arcsec]

#==========GALFIT SETUP==========#
E00) /home/marian/programs/megamorph/galfitm/galfitm-1.2.0-linux-x86_64
#Galfit executable including path
E01)
#filename for list of tiles in current batch (format: image)
#feature switched off when file does not exist, all images are done
E02) obj
#object file preposition
E03) galfit
#preposition for GALFIT output files
E04) /home/marian/data/original_data/psf/55psf_f814w_norm.fits,
/home/marian/data/original_data/psf/45psf_f435w_norm.fits,
/home/marian/data/original_data/psf/15psf_f475w_norm.fits,
/home/marian/data/original_data/psf/f606w.psfmos.fits,
/home/marian/data/original_data/psf/55psf_f625w_norm.fits,
/home/marian/data/original_data/psf/55psf_f775w_norm.fits,
/home/marian/data/original_data/psf/55psf_f850LPw_norm.fits,
/home/marian/data/original_data/psf/15psf_f105w_norm.fits,
/home/marian/data/original_data/psf/15psf_f110w_norm.fits,
/home/marian/data/original_data/psf/15psf_f125w_norm.fits,
/home/marian/data/original_data/psf/15psf_f140w_norm.fits,
/home/marian/data/original_data/psf/15psf_f160w_norm.fits
#PSF file names including paths
E05) mask
#mask file preposition
E06) constr
#constraint file preposition
E07) 150
#convolution box size
E08) 0
#zeropoint, #here without extinction correction
E09) 0.065
#plate scale of the images [arcsec/pixel]
E10) 1
#exposure time
E11) 400
#constraint max Re
E12) -5
#constraint min magnitude deviation (minus)
E13) 5
```

```
#constraint max magnitude deviation (plus)
E14) 0.2
#constraint min sersic index
E15) 8
#constraint max sersic index
E16)
#nice?
E17) 4.0
#GALFIT version string. E.g. 2.0.3c; 4.0 = GalfitM
E18) input,model,residual,psf
E19) 450
#time (in minutes) after which galfit processes are killed
#feature switched off when time == 0
E20) 0,0,11,2,2,0,0
# x,y,mag,re,n,AR,PA
#order of Chebyshev polynomials in the individual parameters
#to be used in GALFIT
# 0 = constant over all wavelength,
#1 = linear over wavelength,...
#band-1 = free
E21) galfit
# outputnfolder name for all galfit output files
E22) restrict
# restrict the maxiumum number of degrees of freedom to the
#number of band for an object? ("restrict" = true)
E23) 30
# fraction of data pixels ==0 which restricts the polynomial (in %),
# larger value allows more pixels to be 0 before taking action
E24) 3
# minimum number of good images that are needed for the fit
#(is set to be >1 by the code),
#e.g. objects without any good data are NEVER fit)

#==========B/D DECOMPOSITION SETUP==========
F00)
# execute the B/D fitting block. Mostly assumes that single
#sersic fitting (block E) is also or had previsouly been run
F01) 0,0,11,0,-1,0,0
#similar to E18 for BULGE
F02) 0,0,11,0,-1,0,0
#similar to E18 for DISK
F03) bdfix
# output label
```

```
214 F04)
215 #optional list containing primary targets
216 F05) 1.0
217 #search/correlation radius for the above list
218 F06) 40.0
219 F07) input,model,residual,component,psf
220
221 #============OUTPUT CATALOGUE SETUP============
222 G00) execute
223 #execute catalogue combination block (read single_sersic)
224 G01) execute
225 #execute catalogue combination block (read single-sersic & B/D)
226 G02) final_catalog.fits
227 #filename for output catalogue in A01)
```

C. MegaMorph results

This section contains the results provided by the *MegaMorph* fitting process. The assessments are split into twelve tables separated by the parameters magnitude, r_e and n, the seven ACS and five WFC3/IR bands and finally the two clusters MACS 1206 and MACS 0416. The uncertainties are the ones returned by *GALFIT*.

Table C.1.: Magnitude assessments in the ACS bands for the fitted early-type galaxies in MACS 1206.

ID	MACS 1206 ACS AB Magnitudes						
	B_{435}	g_{475}	V_{606}	r_{625}	i_{775}	I_{814}	z_{850}
1	22.6 ± 0.0027	22.2 ± 0.0041	21.0 ± 0.0015	20.7 ± 0.0015	20.1 ± 0.0008	19.9 ± 0.0007	19.6 ± 0.0004
3	22.6 ± 0.0033	22.4 ± 0.0021	21.1 ± 0.0019	20.9 ± 0.0019	20.2 ± 0.0016	20.0 ± 0.0013	19.6 ± 0.0009
4	24.3 ± 0.0067	24.0 ± 0.0057	23.0 ± 0.0036	22.8 ± 0.0032	22.3 ± 0.0017	22.0 ± 0.0014	21.7 ± 0.0021
5	22.2 ± 0.0343	21.6 ± 0.0193	20.4 ± 0.0096	20.1 ± 0.0089	19.7 ± 0.0054	19.4 ± 0.0045	19.1 ± 0.0035
6	21.7 ± 0.0009	21.2 ± 0.0006	20.0 ± 0.0005	19.6 ± 0.0004	19.1 ± 0.0003	18.8 ± 0.0003	18.5 ± 0.0003
8	24.8 ± 0.0884	24.4 ± 0.062	23.3 ± 0.0333	23.2 ± 0.0318	22.5 ± 0.0199	22.3 ± 0.0157	22.0 ± 0.0155
10	22.2 ± 0.0006	21.7 ± 0.0004	20.5 ± 0.0003	20.1 ± 0.0003	19.6 ± 0.0002	19.3 ± 0.0003	19.0 ± 0.0002
11	23.0 ± 0.0048	22.5 ± 0.0032	21.5 ± 0.0019	21.1 ± 0.002	20.7 ± 0.0015	20.4 ± 0.0014	20.1 ± 0.0017
12	22.5 ± 0.0	22.1 ± 0.0	20.8 ± 0.0	20.5 ± 0.0	19.9 ± 0.0	19.6 ± 0.0	19.3 ± 0.0
15	22.9 ± 0.0025	22.4 ± 0.0018	21.5 ± 0.0017	21.1 ± 0.0017	20.7 ± 0.0014	20.4 ± 0.0011	20.1 ± 0.0008
17	22.0 ± 0.0015	21.4 ± 0.0013	20.2 ± 0.001	19.8 ± 0.0011	19.4 ± 0.0005	19.0 ± 0.0004	18.7 ± 0.0002
19	23.6 ± 0.0563	23.2 ± 0.0419	22.4 ± 0.0293	21.9 ± 0.0269	21.5 ± 0.0197	21.2 ± 0.0165	20.9 ± 0.0118
20	24.1 ± 0.0096	23.8 ± 0.0097	23.0 ± 0.0059	22.8 ± 0.0056	22.5 ± 0.0024	22.2 ± 0.0023	21.9 ± 0.0018
21	22.9 ± 0.0074	22.4 ± 0.0064	21.4 ± 0.0045	21.1 ± 0.004	20.6 ± 0.0028	20.4 ± 0.002	20.1 ± 0.0013
22	23.0 ± 0.0043	22.7 ± 0.0042	21.8 ± 0.0035	21.3 ± 0.0033	20.8 ± 0.0021	20.6 ± 0.0016	20.3 ± 0.0011
23	24.0 ± 0.0022	23.4 ± 0.0021	22.4 ± 0.0018	22.1 ± 0.0016	21.6 ± 0.0011	21.3 ± 0.001	21.0 ± 0.0005
24	24.2 ± 0.0059	23.6 ± 0.0046	22.5 ± 0.0032	22.1 ± 0.0029	21.6 ± 0.0024	21.3 ± 0.0026	21.1 ± 0.0028
25	23.6 ± 0.0024	23.1 ± 0.0018	21.9 ± 0.0013	21.5 ± 0.0012	21.0 ± 0.0008	20.7 ± 0.0007	20.4 ± 0.0004
26	23.6 ± 0.0017	22.9 ± 0.0013	21.7 ± 0.0009	21.3 ± 0.001	20.8 ± 0.0005	20.5 ± 0.0005	20.2 ± 0.0004
28	23.2 ± 0.0034	22.6 ± 0.0012	21.4 ± 0.0007	21.0 ± 0.0006	20.5 ± 0.0004	20.2 ± 0.0003	20.0 ± 0.0003
29	23.0 ± 0.0012	22.2 ± 0.0011	21.0 ± 0.001	20.6 ± 0.0006	20.2 ± 0.0005	19.8 ± 0.0004	19.6 ± 0.0003
30	22.6 ± 0.005	22.4 ± 0.0044	21.4 ± 0.0038	21.2 ± 0.0036	20.7 ± 0.0031	20.4 ± 0.0023	20.1 ± 0.0019
31	22.8 ± 0.0043	22.3 ± 0.0038	21.3 ± 0.0022	20.8 ± 0.0019	20.3 ± 0.0012	20.1 ± 0.0011	19.7 ± 0.0008

ID	MACS 1206 ACS AB Magnitudes cont.						
	B_{435}	g_{475}	V_{606}	r_{625}	i_{775}	I_{814}	z_{850}
32	22.4 ± 0.0032	21.7 ± 0.0028	20.5 ± 0.0023	20.1 ± 0.0021	19.6 ± 0.0012	19.3 ± 0.0011	19.0 ± 0.0005
33	24.2 ± 0.0505	23.8 ± 0.0404	22.6 ± 0.0297	22.4 ± 0.0273	21.7 ± 0.0196	21.5 ± 0.0165	21.2 ± 0.0127
35	24.0 ± 0.0026	23.5 ± 0.0022	22.3 ± 0.0017	21.9 ± 0.0015	21.4 ± 0.0005	21.1 ± 0.0005	20.8 ± 0.0011
37	23.4 ± 0.0702	23.0 ± 0.0575	22.2 ± 0.0398	21.8 ± 0.0356	21.3 ± 0.0232	21.0 ± 0.0197	20.7 ± 0.0144
38	23.8 ± 0.003	23.5 ± 0.0026	22.8 ± 0.002	22.4 ± 0.0019	21.9 ± 0.0019	21.7 ± 0.0012	21.4 ± 0.0009
39	24.0 ± 0.0061	23.3 ± 0.0046	22.3 ± 0.0034	21.8 ± 0.0034	21.3 ± 0.0021	21.0 ± 0.002	20.8 ± 0.001
40	23.8 ± 0.0451	23.4 ± 0.0319	22.3 ± 0.0185	22.0 ± 0.0173	21.4 ± 0.0119	21.2 ± 0.0101	20.9 ± 0.0076
41	23.9 ± 0.0014	23.4 ± 0.0012	22.3 ± 0.0007	21.9 ± 0.0012	21.3 ± 0.0004	21.0 ± 0.0002	20.7 ± 0.0004
42	23.1 ± 0.0002	22.6 ± 0.0002	21.3 ± 0.0001	20.9 ± 0.0001	20.4 ± 0.0001	20.1 ± 0.0001	19.8 ± 0.0001
43	21.4 ± 0.0012	20.9 ± 0.0009	19.7 ± 0.0005	19.4 ± 0.0005	18.9 ± 0.0004	18.6 ± 0.0002	18.3 ± 0.0002
45	23.4 ± 0.0026	22.9 ± 0.0021	21.8 ± 0.0016	21.4 ± 0.0014	21.0 ± 0.0011	20.7 ± 0.001	20.4 ± 0.001
46	23.4 ± 0.0019	22.9 ± 0.0017	21.8 ± 0.0014	21.4 ± 0.0014	20.9 ± 0.0012	20.6 ± 0.001	20.4 ± 0.0008
47	21.9 ± 0.0016	21.5 ± 0.0012	20.1 ± 0.0008	19.9 ± 0.0008	19.2 ± 0.0005	19.0 ± 0.0005	18.7 ± 0.0004
48	23.3 ± 0.0017	23.0 ± 0.0014	22.1 ± 0.0011	21.7 ± 0.001	21.1 ± 0.0007	20.8 ± 0.0006	20.5 ± 0.0005
50	23.7 ± 0.0012	23.3 ± 0.0005	22.0 ± 0.0003	21.7 ± 0.0002	21.2 ± 0.0	20.9 ± 0.0	20.6 ± 0.0001
51	22.4 ± 0.0004	21.8 ± 0.0001	20.7 ± 0.0001	20.3 ± 0.0001	19.8 ± 0.0	19.5 ± 0.0	19.2 ± 0.0
52	21.9 ± 0.0004	21.3 ± 0.0002	20.1 ± 0.0002	19.7 ± 0.0001	19.2 ± 0.0	18.9 ± 0.0001	18.6 ± 0.0001
55	23.5 ± 0.0027	23.1 ± 0.0025	22.0 ± 0.0021	21.7 ± 0.002	21.2 ± 0.0014	20.9 ± 0.0012	20.6 ± 0.0007
56	24.1 ± 0.0022	23.7 ± 0.0016	22.9 ± 0.0009	22.5 ± 0.0009	21.9 ± 0.0006	21.7 ± 0.0005	21.4 ± 0.0004
57	21.8 ± 0.001	21.3 ± 0.0008	20.2 ± 0.0006	19.8 ± 0.0004	19.3 ± 0.0003	19.1 ± 0.0002	18.8 ± 0.0001
58	24.1 ± 0.0134	23.5 ± 0.0106	22.4 ± 0.0082	22.0 ± 0.0075	21.5 ± 0.0057	21.2 ± 0.005	20.9 ± 0.0044
59	24.2 ± 0.0094	23.6 ± 0.0053	22.6 ± 0.0027	22.2 ± 0.0027	21.6 ± 0.0018	21.3 ± 0.0019	21.1 ± 0.0011
61	23.8 ± 0.0307	23.3 ± 0.0201	22.1 ± 0.0105	21.7 ± 0.0092	21.2 ± 0.006	20.9 ± 0.0049	20.6 ± 0.0042
62	23.9 ± 0.0056	23.5 ± 0.0052	22.6 ± 0.004	22.2 ± 0.0038	21.7 ± 0.0031	21.4 ± 0.0021	21.1 ± 0.0015

ID	MACS 1206 ACS AB Magnitudes cont.						
	B_{435}	g_{475}	V_{606}	r_{625}	i_{775}	I_{814}	z_{850}
63	25.0 ± 0.0718	24.4 ± 0.0485	23.2 ± 0.0242	22.8 ± 0.0217	22.3 ± 0.012	21.9 ± 0.0107	21.6 ± 0.0089
64	23.7 ± 0.0119	23.2 ± 0.0108	22.4 ± 0.0089	21.9 ± 0.0082	21.6 ± 0.0063	21.3 ± 0.0042	21.1 ± 0.0025
65	23.3 ± 0.0066	23.1 ± 0.005	21.8 ± 0.0034	21.5 ± 0.0029	21.0 ± 0.0026	20.7 ± 0.002	20.5 ± 0.0015
68	23.3 ± 0.0139	22.7 ± 0.0102	21.6 ± 0.0074	21.2 ± 0.0067	20.7 ± 0.0038	20.5 ± 0.0036	20.2 ± 0.0022
69	22.7 ± 0.003	22.3 ± 0.0025	21.2 ± 0.0022	20.9 ± 0.002	20.5 ± 0.0015	20.2 ± 0.0014	19.9 ± 0.0013
70	23.1 ± 0.0052	22.7 ± 0.0041	21.7 ± 0.003	21.3 ± 0.0027	20.8 ± 0.0015	20.5 ± 0.0012	20.3 ± 0.0008
71	23.3 ± 0.0009	22.8 ± 0.0008	21.8 ± 0.0006	21.4 ± 0.0006	20.9 ± 0.0004	20.6 ± 0.0004	20.4 ± 0.0004
72	23.7 ± 0.0061	23.3 ± 0.0051	22.3 ± 0.0035	22.0 ± 0.0041	21.4 ± 0.0021	21.1 ± 0.0018	20.9 ± 0.0013
73	24.4 ± 0.0099	23.9 ± 0.0059	22.8 ± 0.0033	22.5 ± 0.0029	22.0 ± 0.0028	21.7 ± 0.0013	21.4 ± 0.001
74	24.4 ± 0.0574	24.1 ± 0.0395	23.0 ± 0.0254	22.9 ± 0.0233	22.2 ± 0.0166	22.0 ± 0.0131	21.8 ± 0.0112
76	22.6 ± 0.0014	22.0 ± 0.0011	20.7 ± 0.001	20.3 ± 0.0009	19.8 ± 0.0008	19.5 ± 0.0008	19.3 ± 0.0007
77	22.3 ± 0.0307	22.0 ± 0.0262	21.3 ± 0.018	20.9 ± 0.016	20.5 ± 0.009	20.2 ± 0.009	19.8 ± 0.0061
80	24.9 ± 0.0044	24.4 ± 0.0033	23.4 ± 0.0021	23.1 ± 0.0019	22.7 ± 0.0013	22.4 ± 0.0011	22.1 ± 0.0011
81	23.9 ± 0.0075	23.5 ± 0.0065	22.6 ± 0.0045	22.3 ± 0.0043	21.9 ± 0.0027	21.6 ± 0.0022	21.3 ± 0.0019
82	24.6 ± 0.0064	24.2 ± 0.0051	23.4 ± 0.0038	23.0 ± 0.0034	22.4 ± 0.0025	22.2 ± 0.0022	21.9 ± 0.0016
83	23.6 ± 0.034	22.9 ± 0.0242	21.8 ± 0.0164	21.5 ± 0.0151	20.9 ± 0.0102	20.6 ± 0.0088	20.3 ± 0.0064
84	24.2 ± 0.001	23.6 ± 0.0026	22.4 ± 0.0005	22.0 ± 0.0004	21.4 ± 0.0003	21.1 ± 0.0003	20.8 ± 0.0002
85	23.8 ± 0.0079	23.3 ± 0.0062	22.4 ± 0.0035	21.9 ± 0.0031	21.4 ± 0.0023	21.2 ± 0.0018	20.9 ± 0.0018
87	23.8 ± 0.0042	23.1 ± 0.0034	22.0 ± 0.0024	21.5 ± 0.0021	21.0 ± 0.0016	20.8 ± 0.0016	20.5 ± 0.0016
88	23.9 ± 0.0309	23.4 ± 0.0204	22.3 ± 0.0095	21.9 ± 0.0087	21.3 ± 0.0052	21.0 ± 0.0047	20.7 ± 0.0038
89	24.1 ± 0.0039	23.6 ± 0.0026	22.6 ± 0.0018	22.2 ± 0.0016	21.7 ± 0.0014	21.4 ± 0.0009	21.2 ± 0.0006
90	24.5 ± 0.0453	24.0 ± 0.0313	22.9 ± 0.0174	22.5 ± 0.0157	22.0 ± 0.0104	21.7 ± 0.0086	21.4 ± 0.0066
91	24.4 ± 0.003	24.1 ± 0.0016	22.9 ± 0.0011	22.7 ± 0.001	22.1 ± 0.0007	21.9 ± 0.0006	21.6 ± 0.0004
93	23.9 ± 0.0102	23.8 ± 0.0076	22.5 ± 0.0047	22.2 ± 0.0047	21.6 ± 0.0035	21.3 ± 0.0037	21.0 ± 0.0033

ID	MACS 1206 ACS AB Magnitudes cont.						
	B_{435}	g_{475}	V_{606}	r_{625}	i_{775}	I_{814}	z_{850}
94	24.5 ± 0.0038	24.0 ± 0.0029	22.9 ± 0.0021	22.5 ± 0.0012	21.9 ± 0.0011	21.6 ± 0.0007	21.4 ± 0.0004
96	24.1 ± 0.0038	23.7 ± 0.0034	22.3 ± 0.0028	22.0 ± 0.0024	21.4 ± 0.0021	21.1 ± 0.0016	20.8 ± 0.0012
97	22.9 ± 0.0076	22.2 ± 0.0045	21.0 ± 0.0028	20.7 ± 0.0024	20.1 ± 0.0016	19.8 ± 0.0013	19.5 ± 0.001
98	22.1 ± 0.013	21.6 ± 0.0091	20.3 ± 0.0057	20.0 ± 0.0049	19.3 ± 0.0026	19.1 ± 0.0023	18.7 ± 0.0029
99	23.8 ± 0.0236	23.4 ± 0.0083	22.4 ± 0.0068	22.1 ± 0.0066	21.6 ± 0.0031	21.4 ± 0.0027	21.1 ± 0.0019
100	23.4 ± 0.0019	23.0 ± 0.0014	21.9 ± 0.0009	21.5 ± 0.0009	20.9 ± 0.0006	20.6 ± 0.0006	20.4 ± 0.0004
101	23.3 ± 0.0018	23.0 ± 0.0015	22.1 ± 0.0015	21.8 ± 0.0016	21.3 ± 0.0011	21.0 ± 0.0012	20.8 ± 0.0011
104	24.3 ± 0.0146	23.9 ± 0.0098	22.7 ± 0.0052	22.4 ± 0.0046	21.9 ± 0.003	21.6 ± 0.0024	21.3 ± 0.0022

Table C.2.: Magnitude assessments in the WFC3/IR bands for the fitted early-type galaxies in MACS 1206.

ID	MACS 1206 WFC3/IR AB Magnitudes				
	Y_{105}	YJ_{110}	J_{125}	JH_{140}	H_{160}
1	19.6 ± 0.0004	19.5 ± 0.0003	19.1 ± 0.0059	19.2 ± 0.0003	19.1 ± 0.0004
3	19.5 ± 0.0006	19.3 ± 0.0004	19.1 ± 0.0026	19.1 ± 0.0002	18.9 ± 0.0002
4	21.7 ± 0.0016	21.6 ± 0.008	21.5 ± 0.002	21.4 ± 0.0025	21.2 ± 0.0024
5	18.9 ± 0.0027	18.8 ± 0.0022	18.7 ± 0.0024	18.6 ± 0.0026	18.4 ± 0.0044
6	18.3 ± 0.0003	18.2 ± 0.0003	18.1 ± 0.0002	17.9 ± 0.0002	17.7 ± 0.0004
8	21.9 ± 0.0134	21.8 ± 0.0787	21.7 ± 0.0119	21.6 ± 0.0113	21.5 ± 0.0162
10	18.9 ± 0.0002	18.8 ± 0.0003	18.6 ± 0.0002	18.4 ± 0.0001	18.2 ± 0.0004
11	20.0 ± 0.0015	19.9 ± 0.0016	19.8 ± 0.0021	19.7 ± 0.0031	19.5 ± 0.0038
12	19.2 ± 0.0	19.3 ± 0.0	19.0 ± 0.0	18.9 ± 0.0	18.8 ± 0.0
15	20.0 ± 0.0006	19.9 ± 0.0006	19.8 ± 0.0007	19.7 ± 0.0013	19.6 ± 0.0025
17	18.6 ± 0.0001	18.5 ± 0.0001	18.4 ± 0.0002	18.2 ± 0.0002	18.1 ± 0.0002
19	20.9 ± 0.0081	20.8 ± 0.0068	20.7 ± 0.0069	20.6 ± 0.0076	20.5 ± 0.0137
20	21.8 ± 0.0015	21.8 ± 0.0022	21.6 ± 0.0027	21.5 ± 0.0035	21.4 ± 0.0057
21	20.0 ± 0.0012	19.9 ± 0.0014	19.8 ± 0.0021	19.7 ± 0.0042	19.5 ± 0.0089
22	20.1 ± 0.0006	20.0 ± 0.0005	19.9 ± 0.0005	19.8 ± 0.0011	19.6 ± 0.0024
23	20.9 ± 0.0002	20.9 ± 0.0004	20.7 ± 0.0008	20.6 ± 0.0014	20.5 ± 0.0018
24	21.0 ± 0.0043	20.9 ± 0.0028	20.9 ± 0.0029	20.8 ± 0.0023	20.7 ± 0.0033
25	20.3 ± 0.0004	20.2 ± 0.0005	20.1 ± 0.0005	19.9 ± 0.0007	19.7 ± 0.0009
26	20.1 ± 0.0005	19.9 ± 0.0004	19.8 ± 0.0005	19.7 ± 0.0005	19.5 ± 0.0007
28	19.8 ± 0.0002	19.7 ± 0.0001	19.6 ± 0.0002	19.5 ± 0.0002	19.3 ± 0.0004
29	19.4 ± 0.0002	19.2 ± 0.0001	19.1 ± 0.0001	18.9 ± 0.0002	18.8 ± 0.0003
30	20.0 ± 0.0012	19.9 ± 0.0011	19.7 ± 0.0008	19.6 ± 0.0009	19.3 ± 0.0014
31	19.6 ± 0.0007	19.4 ± 0.0012	19.3 ± 0.0021	19.1 ± 0.0042	19.0 ± 0.0069
32	18.9 ± 0.0003	18.7 ± 0.0006	18.6 ± 0.0009	18.4 ± 0.0011	18.2 ± 0.0012
33	21.2 ± 0.0104	21.1 ± 0.01	20.7 ± 0.1308	20.9 ± 0.0098	20.7 ± 0.0146
35	20.6 ± 0.0012	20.5 ± 0.0012	20.4 ± 0.0012	20.3 ± 0.0017	20.1 ± 0.0014
37	20.6 ± 0.0122	20.5 ± 0.011	20.5 ± 0.0106	20.4 ± 0.0099	20.3 ± 0.0132
38	21.3 ± 0.0007	21.3 ± 0.0005	21.2 ± 0.0005	21.1 ± 0.0006	21.0 ± 0.0009
39	20.7 ± 0.0008	20.6 ± 0.0012	20.5 ± 0.0014	20.4 ± 0.0011	20.2 ± 0.0011
40	20.7 ± 0.0057	20.6 ± 0.0048	20.5 ± 0.0048	20.4 ± 0.0052	20.2 ± 0.0079
41	20.6 ± 0.0004	20.5 ± 0.0002	20.4 ± 0.0002	20.2 ± 0.0004	20.1 ± 0.0004
42	19.6 ± 0.0001	19.5 ± 0.0	19.4 ± 0.0001	19.2 ± 0.0004	19.1 ± 0.0009
43	18.2 ± 0.0001	18.0 ± 0.0001	17.9 ± 0.0001	17.7 ± 0.0001	17.5 ± 0.0001
45	20.2 ± 0.0005	20.2 ± 0.0004	20.0 ± 0.0005	19.9 ± 0.0006	19.7 ± 0.0009
46	20.2 ± 0.0007	20.1 ± 0.0005	20.0 ± 0.0004	19.9 ± 0.0004	19.7 ± 0.0006
47	18.6 ± 0.0004	18.4 ± 0.0004	18.1 ± 0.0045	18.2 ± 0.0004	18.0 ± 0.0006

ID	MACS 1206 WFC3/IR AB Magnitudes cont.				
	Y_{105}	YJ_{110}	J_{125}	JH_{140}	H_{160}
48	20.4 ± 0.0004	20.4 ± 0.0003	20.2 ± 0.0003	20.1 ± 0.0003	19.9 ± 0.0005
50	20.4 ± 0.0001	20.3 ± 0.0001	20.2 ± 0.0001	20.1 ± 0.0005	19.9 ± 0.0012
51	19.1 ± 0.0	19.0 ± 0.0	18.9 ± 0.0001	18.8 ± 0.0002	18.6 ± 0.0005
52	18.5 ± 0.0001	18.3 ± 0.0	18.2 ± 0.0001	18.1 ± 0.0003	17.9 ± 0.0005
55	20.4 ± 0.0005	20.3 ± 0.0005	20.2 ± 0.0008	20.0 ± 0.0013	19.8 ± 0.0022
56	21.3 ± 0.0003	21.2 ± 0.0002	21.1 ± 0.0003	21.0 ± 0.0002	20.8 ± 0.0003
57	18.7 ± 0.0001	18.6 ± 0.0002	18.2 ± 0.0023	18.4 ± 0.0002	18.2 ± 0.0002
58	20.8 ± 0.0045	20.7 ± 0.0048	20.6 ± 0.0051	20.5 ± 0.0059	20.4 ± 0.008
59	20.9 ± 0.0009	20.9 ± 0.0006	20.7 ± 0.0007	20.6 ± 0.0007	20.4 ± 0.001
61	20.5 ± 0.0036	20.4 ± 0.0033	20.3 ± 0.0033	20.1 ± 0.0033	20.0 ± 0.005
62	21.0 ± 0.001	20.9 ± 0.0008	20.8 ± 0.0011	20.7 ± 0.0015	20.5 ± 0.0027
63	21.5 ± 0.0081	21.4 ± 0.0074	21.3 ± 0.0072	21.3 ± 0.0066	21.2 ± 0.0095
64	21.0 ± 0.0011	20.9 ± 0.0008	20.9 ± 0.0009	20.8 ± 0.0013	20.6 ± 0.0024
65	20.4 ± 0.001	20.4 ± 0.0037	20.3 ± 0.0009	20.2 ± 0.001	20.1 ± 0.002
68	20.0 ± 0.0021	19.9 ± 0.0027	19.8 ± 0.0028	19.6 ± 0.0032	19.4 ± 0.0048
69	19.8 ± 0.0005	19.7 ± 0.0004	19.6 ± 0.0005	19.5 ± 0.0006	19.3 ± 0.0007
70	20.1 ± 0.0007	20.0 ± 0.0009	19.9 ± 0.0009	19.7 ± 0.0008	19.5 ± 0.0011
71	20.2 ± 0.0005	20.1 ± 0.0008	20.0 ± 0.0013	19.9 ± 0.0024	19.7 ± 0.0046
72	20.7 ± 0.001	20.6 ± 0.0011	20.5 ± 0.0012	20.4 ± 0.0015	20.2 ± 0.0023
73	21.3 ± 0.0005	21.2 ± 0.0004	21.1 ± 0.0005	21.0 ± 0.0005	20.8 ± 0.0007
74	21.6 ± 0.0083	21.4 ± 0.0605	21.4 ± 0.0082	21.3 ± 0.0084	21.1 ± 0.0135
76	19.1 ± 0.0006	19.1 ± 0.0008	18.9 ± 0.001	18.8 ± 0.0014	18.6 ± 0.0018
77	19.7 ± 0.0051	19.7 ± 0.0047	19.5 ± 0.0047	19.4 ± 0.0047	19.3 ± 0.0063
80	22.0 ± 0.0008	21.9 ± 0.0009	21.8 ± 0.0009	21.7 ± 0.0009	21.5 ± 0.001
81	21.2 ± 0.0017	21.1 ± 0.0018	21.0 ± 0.0021	20.8 ± 0.0026	20.7 ± 0.003
82	21.8 ± 0.0019	21.7 ± 0.0015	21.6 ± 0.0013	21.5 ± 0.001	21.3 ± 0.0017
83	20.2 ± 0.0053	20.0 ± 0.0048	19.9 ± 0.0047	19.7 ± 0.0048	19.5 ± 0.0075
84	20.7 ± 0.0002	20.5 ± 0.0002	20.4 ± 0.0001	20.3 ± 0.0001	20.1 ± 0.0002
85	20.8 ± 0.0014	20.7 ± 0.0012	20.6 ± 0.0012	20.5 ± 0.0017	20.4 ± 0.0035
87	20.4 ± 0.0016	20.3 ± 0.0015	20.2 ± 0.0016	20.1 ± 0.003	20.0 ± 0.0063
88	20.6 ± 0.0032	20.5 ± 0.0028	20.4 ± 0.0029	20.3 ± 0.0027	20.1 ± 0.0039
89	21.1 ± 0.0004	21.0 ± 0.0003	20.9 ± 0.0003	20.8 ± 0.0003	20.6 ± 0.0004
90	21.3 ± 0.0053	21.2 ± 0.0047	21.1 ± 0.0045	21.0 ± 0.0042	20.8 ± 0.0061
91	21.6 ± 0.0004	21.6 ± 0.0016	21.3 ± 0.0003	21.3 ± 0.0003	21.1 ± 0.0004
93	21.0 ± 0.0036	20.8 ± 0.0037	20.5 ± 0.0189	20.7 ± 0.0034	20.5 ± 0.0036
94	21.3 ± 0.0003	21.1 ± 0.0002	21.1 ± 0.0002	20.9 ± 0.0002	20.7 ± 0.0004
96	20.7 ± 0.0008	20.5 ± 0.001	20.3 ± 0.0089	20.3 ± 0.0006	20.1 ± 0.0009
97	19.4 ± 0.0008	19.3 ± 0.0006	19.2 ± 0.0006	19.0 ± 0.0008	18.8 ± 0.0014
98	18.6 ± 0.0036	18.6 ± 0.0041	18.4 ± 0.004	18.3 ± 0.0043	18.1 ± 0.0054
99	21.0 ± 0.0023	21.0 ± 0.0035	20.8 ± 0.0023	20.7 ± 0.0018	20.5 ± 0.0034

ID	MACS 1206 WFC3/IR AB Magnitudes cont.				
	Y_{105}	YJ_{110}	J_{125}	JH_{140}	H_{160}
100	20.2 ± 0.0003	20.1 ± 0.0003	20.0 ± 0.0003	19.9 ± 0.0003	19.7 ± 0.0004
101	20.6 ± 0.0009	20.5 ± 0.0007	20.4 ± 0.0006	20.3 ± 0.0004	20.1 ± 0.0003
104	21.2 ± 0.0013	21.1 ± 0.0011	21.0 ± 0.0012	20.9 ± 0.0011	20.7 ± 0.0017

Table C.3.: r_e assessments in the ACS bands for the fitted early-type galaxies in MACS 1206. To calculate the values in kpc the cosmological parameters $H_0 = 70$ km s^{-1} Mpc $^{-1}$, $\Omega_\Lambda = 0.7$ and $\Omega_M = 0.3$ have been adopted with a pixelscale of 0.065"/px and a cluster redshift $z \sim 0.44$.

ID	MACS 1206 ACS r_e [kpc]						
	B_{435}	g_{475}	V_{606}	r_{625}	i_{775}	I_{814}	z_{850}
1	5.9 ± 0.04	5.6 ± 0.036	5.0 ± 0.026	4.9 ± 0.023	4.3 ± 0.014	4.1 ± 0.011	3.8 ± 0.007
3	4.9 ± 0.021	4.7 ± 0.019	4.4 ± 0.014	4.3 ± 0.013	3.9 ± 0.009	3.8 ± 0.007	3.5 ± 0.005
4	4.0 ± 0.087	4.0 ± 0.072	3.9 ± 0.042	3.9 ± 0.034	3.9 ± 0.024	3.8 ± 0.026	3.8 ± 0.033
5	9.5 ± 0.139	9.3 ± 0.123	8.9 ± 0.089	8.7 ± 0.078	8.3 ± 0.047	8.1 ± 0.038	7.9 ± 0.024
6	6.4 ± 0.034	6.2 ± 0.03	5.7 ± 0.023	5.6 ± 0.021	5.1 ± 0.013	5.0 ± 0.011	4.7 ± 0.008
8	1.5 ± 0.067	1.5 ± 0.059	1.5 ± 0.042	1.4 ± 0.037	1.4 ± 0.023	1.4 ± 0.019	1.4 ± 0.014
10	4.8 ± 0.011	4.6 ± 0.01	4.2 ± 0.008	4.0 ± 0.007	3.6 ± 0.005	3.5 ± 0.004	3.3 ± 0.003
11	5.8 ± 0.055	5.6 ± 0.049	5.1 ± 0.036	4.9 ± 0.031	4.4 ± 0.019	4.2 ± 0.015	3.9 ± 0.01
12	5.3 ± 0.0	5.5 ± 0.0	5.7 ± 0.0	5.8 ± 0.0	5.9 ± 0.0	6.0 ± 0.0	6.0 ± 0.0
15	6.0 ± 0.049	5.8 ± 0.044	5.4 ± 0.032	5.3 ± 0.028	4.8 ± 0.017	4.6 ± 0.014	4.3 ± 0.009
17	4.9 ± 0.011	4.8 ± 0.01	4.6 ± 0.007	4.5 ± 0.007	4.3 ± 0.004	4.2 ± 0.004	4.1 ± 0.003
19	4.2 ± 0.034	4.1 ± 0.029	3.7 ± 0.019	3.5 ± 0.016	3.1 ± 0.007	3.0 ± 0.006	2.8 ± 0.006
20	3.8 ± 0.159	3.7 ± 0.136	3.5 ± 0.088	3.4 ± 0.074	3.2 ± 0.041	3.2 ± 0.036	3.1 ± 0.034
21	4.1 ± 0.11	4.0 ± 0.098	3.9 ± 0.071	3.8 ± 0.063	3.6 ± 0.039	3.5 ± 0.032	3.4 ± 0.024
22	2.4 ± 0.028	2.4 ± 0.025	2.2 ± 0.018	2.1 ± 0.016	1.9 ± 0.01	1.9 ± 0.008	1.8 ± 0.005
23	2.8 ± 0.035	2.7 ± 0.032	2.5 ± 0.024	2.4 ± 0.021	2.2 ± 0.014	2.1 ± 0.012	2.0 ± 0.008
24	1.5 ± 0.052	1.5 ± 0.046	1.4 ± 0.034	1.3 ± 0.03	1.2 ± 0.02	1.1 ± 0.018	1.0 ± 0.015
25	1.9 ± 0.017	1.8 ± 0.015	1.6 ± 0.01	1.6 ± 0.009	1.4 ± 0.005	1.3 ± 0.004	1.2 ± 0.004
26	1.6 ± 0.006	1.6 ± 0.005	1.5 ± 0.003	1.5 ± 0.003	1.4 ± 0.002	1.3 ± 0.002	1.3 ± 0.002
28	4.5 ± 0.017	4.2 ± 0.015	3.8 ± 0.01	3.6 ± 0.009	3.1 ± 0.004	2.9 ± 0.003	2.7 ± 0.002
29	3.6 ± 0.007	3.4 ± 0.006	3.2 ± 0.004	3.1 ± 0.004	2.8 ± 0.002	2.7 ± 0.002	2.6 ± 0.001

ID	MACS 1206 ACS r_e [kpc] cont.						
	B_{435}	g_{475}	V_{606}	r_{625}	i_{775}	I_{814}	z_{850}
30	3.5 ± 0.05	3.3 ± 0.045	3.0 ± 0.033	2.9 ± 0.029	2.5 ± 0.018	2.4 ± 0.015	2.3 ± 0.01
31	4.1 ± 0.075	4.1 ± 0.064	4.0 ± 0.041	4.0 ± 0.035	4.1 ± 0.021	4.1 ± 0.02	4.1 ± 0.02
32	4.2 ± 0.03	4.1 ± 0.027	3.7 ± 0.021	3.6 ± 0.02	3.3 ± 0.014	3.2 ± 0.012	3.0 ± 0.009
33	2.4 ± 0.147	2.3 ± 0.131	2.1 ± 0.095	2.0 ± 0.083	1.8 ± 0.05	1.7 ± 0.04	1.5 ± 0.026
35	1.1 ± 0.008	1.1 ± 0.007	1.0 ± 0.006	1.0 ± 0.005	0.9 ± 0.003	0.9 ± 0.003	0.8 ± 0.002
37	4.4 ± 0.238	4.4 ± 0.215	4.4 ± 0.163	4.4 ± 0.146	4.2 ± 0.097	4.2 ± 0.082	4.0 ± 0.058
38	2.5 ± 0.02	2.4 ± 0.018	2.2 ± 0.013	2.1 ± 0.012	1.8 ± 0.007	1.7 ± 0.006	1.5 ± 0.004
39	2.3 ± 0.034	2.2 ± 0.03	2.0 ± 0.023	1.9 ± 0.021	1.6 ± 0.014	1.5 ± 0.012	1.4 ± 0.008
40	2.1 ± 0.06	2.0 ± 0.054	1.8 ± 0.04	1.8 ± 0.035	1.6 ± 0.022	1.5 ± 0.018	1.4 ± 0.012
41	1.5 ± 0.003	1.5 ± 0.003	1.4 ± 0.002	1.4 ± 0.002	1.3 ± 0.001	1.2 ± 0.001	1.2 ± 0.001
42	3.7 ± 0.009	3.6 ± 0.008	3.4 ± 0.005	3.3 ± 0.005	3.1 ± 0.002	3.0 ± 0.002	2.9 ± 0.002
43	7.4 ± 0.005	7.2 ± 0.005	6.7 ± 0.004	6.5 ± 0.003	6.0 ± 0.002	5.9 ± 0.002	5.7 ± 0.001
45	2.9 ± 0.031	2.8 ± 0.027	2.6 ± 0.019	2.5 ± 0.016	2.3 ± 0.01	2.3 ± 0.008	2.2 ± 0.006
46	2.5 ± 0.009	2.4 ± 0.008	2.2 ± 0.006	2.1 ± 0.006	1.9 ± 0.004	1.8 ± 0.003	1.7 ± 0.002
47	9.2 ± 0.092	8.9 ± 0.083	8.2 ± 0.063	8.0 ± 0.057	7.4 ± 0.04	7.2 ± 0.035	6.8 ± 0.028
48	1.6 ± 0.009	1.5 ± 0.008	1.3 ± 0.006	1.3 ± 0.006	1.1 ± 0.004	1.0 ± 0.003	0.9 ± 0.002
50	2.2 ± 0.004	2.2 ± 0.004	2.1 ± 0.002	2.1 ± 0.002	2.0 ± 0.001	1.9 ± 0.001	1.9 ± 0.001
51	4.3 ± 0.003	4.2 ± 0.002	3.9 ± 0.002	3.8 ± 0.002	3.5 ± 0.001	3.4 ± 0.001	3.2 ± 0.0
52	8.4 ± 0.008	8.1 ± 0.007	7.5 ± 0.004	7.4 ± 0.003	6.8 ± 0.002	6.7 ± 0.002	6.5 ± 0.003
55	2.9 ± 0.027	2.8 ± 0.023	2.6 ± 0.016	2.5 ± 0.013	2.3 ± 0.008	2.2 ± 0.006	2.1 ± 0.006
56	1.4 ± 0.006	1.3 ± 0.005	1.2 ± 0.003	1.2 ± 0.003	1.0 ± 0.001	1.0 ± 0.001	0.9 ± 0.001
57	2.1 ± 0.016	2.1 ± 0.014	2.1 ± 0.009	2.0 ± 0.008	2.0 ± 0.005	2.0 ± 0.004	1.9 ± 0.004
58	1.7 ± 0.072	1.7 ± 0.065	1.5 ± 0.05	1.5 ± 0.046	1.3 ± 0.032	1.3 ± 0.028	1.2 ± 0.022
59	1.4 ± 0.02	1.4 ± 0.018	1.2 ± 0.013	1.2 ± 0.012	1.1 ± 0.008	1.0 ± 0.006	0.9 ± 0.004

ID	MACS 1206 ACS r_e [kpc] cont.						
	B_{435}	g_{475}	V_{606}	r_{625}	i_{775}	I_{814}	z_{850}
61	2.0 ± 0.029	1.9 ± 0.026	1.8 ± 0.018	1.8 ± 0.016	1.7 ± 0.01	1.7 ± 0.008	1.6 ± 0.006
62	2.1 ± 0.025	2.0 ± 0.023	1.8 ± 0.017	1.8 ± 0.015	1.6 ± 0.01	1.5 ± 0.008	1.4 ± 0.005
63	1.3 ± 0.079	1.4 ± 0.07	1.5 ± 0.05	1.5 ± 0.044	1.6 ± 0.028	1.6 ± 0.024	1.6 ± 0.019
64	2.0 ± 0.043	1.9 ± 0.038	1.7 ± 0.028	1.7 ± 0.025	1.5 ± 0.016	1.5 ± 0.013	1.4 ± 0.008
65	4.9 ± 0.18	4.7 ± 0.162	4.1 ± 0.124	3.9 ± 0.112	3.4 ± 0.075	3.2 ± 0.063	2.8 ± 0.044
68	3.4 ± 0.058	3.2 ± 0.051	2.9 ± 0.036	2.8 ± 0.032	2.6 ± 0.02	2.5 ± 0.017	2.3 ± 0.014
69	4.9 ± 0.05	4.7 ± 0.042	4.1 ± 0.025	3.9 ± 0.02	3.4 ± 0.011	3.2 ± 0.01	2.9 ± 0.013
70	3.2 ± 0.064	3.1 ± 0.055	2.8 ± 0.035	2.8 ± 0.03	2.6 ± 0.016	2.6 ± 0.014	2.5 ± 0.014
71	3.0 ± 0.03	2.9 ± 0.026	2.6 ± 0.019	2.6 ± 0.017	2.3 ± 0.01	2.3 ± 0.008	2.1 ± 0.005
72	2.0 ± 0.05	2.0 ± 0.042	1.8 ± 0.026	1.7 ± 0.021	1.5 ± 0.01	1.5 ± 0.009	1.4 ± 0.011
73	1.8 ± 0.017	1.8 ± 0.015	1.7 ± 0.011	1.7 ± 0.01	1.7 ± 0.006	1.7 ± 0.005	1.7 ± 0.003
74	0.9 ± 0.024	0.9 ± 0.021	0.7 ± 0.015	0.7 ± 0.013	0.6 ± 0.007	0.5 ± 0.006	0.5 ± 0.004
76	4.7 ± 0.04	4.5 ± 0.036	4.0 ± 0.027	3.9 ± 0.024	3.4 ± 0.016	3.2 ± 0.013	3.0 ± 0.009
77	10.5 ± 0.695	10.5 ± 0.606	10.6 ± 0.415	10.6 ± 0.357	10.7 ± 0.201	10.7 ± 0.163	10.7 ± 0.133
80	1.2 ± 0.012	1.2 ± 0.011	1.1 ± 0.008	1.0 ± 0.007	1.0 ± 0.004	0.9 ± 0.003	0.9 ± 0.002
81	2.6 ± 0.042	2.5 ± 0.037	2.3 ± 0.027	2.3 ± 0.024	2.1 ± 0.016	2.0 ± 0.013	2.0 ± 0.009
82	0.9 ± 0.012	0.8 ± 0.011	0.7 ± 0.008	0.7 ± 0.007	0.6 ± 0.005	0.5 ± 0.004	0.5 ± 0.002
83	2.4 ± 0.057	2.3 ± 0.05	2.1 ± 0.036	2.0 ± 0.032	1.8 ± 0.019	1.7 ± 0.015	1.6 ± 0.01
84	1.1 ± 0.003	1.1 ± 0.003	1.0 ± 0.001	1.0 ± 0.001	1.0 ± 0.001	0.9 ± 0.001	0.9 ± 0.001
85	2.5 ± 0.109	2.4 ± 0.1	2.2 ± 0.078	2.2 ± 0.071	2.0 ± 0.05	1.9 ± 0.043	1.8 ± 0.032
87	3.1 ± 0.029	3.0 ± 0.026	2.9 ± 0.019	2.8 ± 0.016	2.6 ± 0.011	2.5 ± 0.009	2.4 ± 0.008
88	1.9 ± 0.019	1.9 ± 0.017	1.8 ± 0.012	1.8 ± 0.011	1.7 ± 0.006	1.6 ± 0.005	1.6 ± 0.003
89	2.4 ± 0.01	2.3 ± 0.009	2.1 ± 0.007	2.1 ± 0.006	1.9 ± 0.004	1.8 ± 0.003	1.7 ± 0.002
90	1.2 ± 0.031	1.2 ± 0.027	1.1 ± 0.02	1.1 ± 0.018	1.0 ± 0.011	0.9 ± 0.009	0.9 ± 0.006

ID	MACS 1206 ACS r_e [kpc] cont.						
	B_{435}	g_{475}	V_{606}	r_{625}	i_{775}	I_{814}	z_{850}
91	2.1 ± 0.003	2.1 ± 0.003	1.9 ± 0.002	1.9 ± 0.002	1.7 ± 0.001	1.7 ± 0.001	1.6 ± 0.001
93	1.6 ± 0.064	1.6 ± 0.056	1.5 ± 0.041	1.5 ± 0.036	1.4 ± 0.022	1.3 ± 0.018	1.3 ± 0.013
94	0.6 ± 0.003	0.6 ± 0.002	0.5 ± 0.002	0.5 ± 0.001	0.5 ± 0.001	0.5 ± 0.001	0.4 ± 0.0
96	1.3 ± 0.018	1.3 ± 0.016	1.2 ± 0.01	1.2 ± 0.009	1.1 ± 0.005	1.1 ± 0.004	1.0 ± 0.004
97	2.5 ± 0.03	2.4 ± 0.027	2.2 ± 0.02	2.1 ± 0.017	1.9 ± 0.01	1.8 ± 0.008	1.7 ± 0.005
98	6.8 ± 0.126	6.7 ± 0.108	6.5 ± 0.068	6.5 ± 0.057	6.3 ± 0.031	6.2 ± 0.028	6.1 ± 0.033
99	3.1 ± 0.051	3.0 ± 0.045	2.6 ± 0.032	2.5 ± 0.028	2.2 ± 0.018	2.1 ± 0.016	2.0 ± 0.014
100	3.9 ± 0.015	3.8 ± 0.013	3.5 ± 0.009	3.4 ± 0.008	3.0 ± 0.004	2.9 ± 0.003	2.7 ± 0.002
101	1.8 ± 0.006	1.7 ± 0.005	1.5 ± 0.004	1.5 ± 0.004	1.3 ± 0.002	1.2 ± 0.002	1.1 ± 0.002
104	1.7 ± 0.02	1.7 ± 0.018	1.6 ± 0.013	1.5 ± 0.011	1.4 ± 0.007	1.4 ± 0.005	1.3 ± 0.003

Table C.4.: r_e assessments in the WFC3/IR bands for the fitted early-type galaxies in MACS 1206. To calculate the values in kpc the cosmological parameters $H_0 = 70$ km s^{-1} Mpc $^{-1}$, $\Omega_\Lambda = 0.7$ and $\Omega_M = 0.3$ have been adopted with a pixelscale of 0.065"/px and a cluster redshift $z \sim 0.44$.

ID	MACS 1206 WFC3/IR r_e [kpc]				
	Y_{105}	YJ_{110}	J_{125}	JH_{140}	H_{160}
1	3.6 ± 0.005	3.5 ± 0.005	3.5 ± 0.005	3.5 ± 0.005	3.6 ± 0.007
3	3.4 ± 0.004	3.2 ± 0.003	3.1 ± 0.003	3.0 ± 0.003	2.9 ± 0.003
4	3.8 ± 0.036	3.9 ± 0.035	3.9 ± 0.03	4.0 ± 0.021	4.1 ± 0.032
5	7.7 ± 0.018	7.6 ± 0.017	7.6 ± 0.018	7.6 ± 0.021	7.7 ± 0.033
6	4.6 ± 0.006	4.5 ± 0.006	4.5 ± 0.007	4.5 ± 0.009	4.7 ± 0.013
8	1.3 ± 0.013	1.3 ± 0.013	1.3 ± 0.012	1.3 ± 0.011	1.2 ± 0.015
10	3.1 ± 0.002	3.0 ± 0.002	2.9 ± 0.001	2.9 ± 0.002	3.0 ± 0.002
11	3.7 ± 0.007	3.6 ± 0.007	3.5 ± 0.007	3.5 ± 0.007	3.6 ± 0.01
12	6.0 ± 0.0	5.9 ± 0.0	5.8 ± 0.0	5.5 ± 0.0	5.1 ± 0.0
15	4.0 ± 0.006	3.8 ± 0.006	3.5 ± 0.006	3.2 ± 0.005	3.0 ± 0.005
17	4.0 ± 0.002	4.0 ± 0.002	4.0 ± 0.002	4.0 ± 0.002	4.1 ± 0.003
19	2.6 ± 0.006	2.5 ± 0.006	2.4 ± 0.004	2.3 ± 0.003	2.3 ± 0.011
20	3.1 ± 0.034	3.2 ± 0.032	3.3 ± 0.032	3.6 ± 0.05	4.0 ± 0.096
21	3.3 ± 0.021	3.2 ± 0.022	3.2 ± 0.023	3.1 ± 0.028	3.0 ± 0.039
22	1.7 ± 0.004	1.6 ± 0.004	1.6 ± 0.004	1.6 ± 0.004	1.6 ± 0.007
23	1.9 ± 0.006	1.8 ± 0.005	1.8 ± 0.004	1.7 ± 0.004	1.7 ± 0.006
24	0.9 ± 0.014	0.9 ± 0.013	0.8 ± 0.012	0.7 ± 0.011	0.7 ± 0.012
25	1.1 ± 0.004	1.1 ± 0.003	1.0 ± 0.003	1.0 ± 0.003	1.0 ± 0.006
26	1.2 ± 0.002	1.2 ± 0.002	1.2 ± 0.002	1.1 ± 0.002	1.1 ± 0.003
28	2.5 ± 0.002	2.4 ± 0.002	2.3 ± 0.002	2.3 ± 0.001	2.4 ± 0.004
29	2.5 ± 0.001	2.4 ± 0.001	2.4 ± 0.001	2.4 ± 0.001	2.6 ± 0.002
30	2.2 ± 0.008	2.2 ± 0.007	2.2 ± 0.008	2.3 ± 0.011	2.4 ± 0.017
31	4.1 ± 0.019	4.2 ± 0.017	4.3 ± 0.016	4.4 ± 0.024	4.5 ± 0.048
32	2.9 ± 0.007	2.9 ± 0.006	2.9 ± 0.006	2.9 ± 0.008	3.1 ± 0.01
33	1.4 ± 0.02	1.4 ± 0.019	1.3 ± 0.02	1.3 ± 0.02	1.3 ± 0.028
35	0.8 ± 0.001	0.7 ± 0.001	0.7 ± 0.001	0.7 ± 0.001	0.7 ± 0.001
37	3.8 ± 0.043	3.6 ± 0.035	3.4 ± 0.031	3.1 ± 0.027	2.6 ± 0.029
38	1.4 ± 0.002	1.3 ± 0.002	1.2 ± 0.002	1.1 ± 0.002	1.1 ± 0.002
39	1.3 ± 0.005	1.2 ± 0.004	1.1 ± 0.003	1.1 ± 0.003	1.0 ± 0.004
40	1.3 ± 0.008	1.3 ± 0.007	1.3 ± 0.007	1.2 ± 0.008	1.3 ± 0.012
41	1.1 ± 0.001	1.1 ± 0.001	1.0 ± 0.001	1.0 ± 0.0	1.0 ± 0.001
42	2.7 ± 0.002	2.6 ± 0.002	2.5 ± 0.002	2.4 ± 0.002	2.3 ± 0.002
43	5.5 ± 0.001	5.4 ± 0.001	5.4 ± 0.001	5.5 ± 0.001	5.8 ± 0.001
45	2.1 ± 0.005	2.0 ± 0.005	2.0 ± 0.004	2.0 ± 0.004	2.0 ± 0.009
46	1.6 ± 0.002	1.5 ± 0.001	1.5 ± 0.001	1.5 ± 0.001	1.5 ± 0.002
47	6.5 ± 0.024	6.3 ± 0.022	6.2 ± 0.021	6.2 ± 0.023	6.3 ± 0.032

ID	MACS 1206 WFC3/IR r_e [kpc] cont.				
	Y_{105}	YJ_{110}	J_{125}	JH_{140}	H_{160}
48	0.8 ± 0.002	0.8 ± 0.001	0.8 ± 0.001	0.7 ± 0.001	0.7 ± 0.001
50	1.9 ± 0.001	1.9 ± 0.001	1.8 ± 0.001	1.9 ± 0.001	1.9 ± 0.003
51	3.1 ± 0.0	3.0 ± 0.001	3.0 ± 0.001	3.0 ± 0.001	3.1 ± 0.001
52	6.3 ± 0.003	6.3 ± 0.002	6.3 ± 0.002	6.5 ± 0.003	6.9 ± 0.007
55	2.1 ± 0.006	2.1 ± 0.007	2.1 ± 0.007	2.2 ± 0.009	2.3 ± 0.013
56	0.9 ± 0.001	0.8 ± 0.001	0.8 ± 0.001	0.8 ± 0.001	0.8 ± 0.001
57	1.9 ± 0.004	1.9 ± 0.004	1.8 ± 0.004	1.8 ± 0.004	1.8 ± 0.006
58	1.1 ± 0.019	1.0 ± 0.017	0.9 ± 0.015	0.8 ± 0.015	0.8 ± 0.018
59	0.9 ± 0.002	0.9 ± 0.002	0.8 ± 0.002	0.8 ± 0.002	0.9 ± 0.003
61	1.6 ± 0.005	1.5 ± 0.005	1.5 ± 0.005	1.5 ± 0.005	1.5 ± 0.007
62	1.3 ± 0.004	1.3 ± 0.003	1.2 ± 0.003	1.2 ± 0.004	1.2 ± 0.005
63	1.6 ± 0.018	1.6 ± 0.018	1.5 ± 0.017	1.4 ± 0.015	1.2 ± 0.016
64	1.3 ± 0.005	1.3 ± 0.004	1.3 ± 0.004	1.2 ± 0.006	1.3 ± 0.01
65	2.5 ± 0.031	2.3 ± 0.024	2.2 ± 0.02	2.0 ± 0.018	1.9 ± 0.026
68	2.2 ± 0.013	2.2 ± 0.012	2.2 ± 0.012	2.2 ± 0.017	2.3 ± 0.029
69	2.8 ± 0.014	2.7 ± 0.012	2.7 ± 0.009	2.7 ± 0.007	3.0 ± 0.021
70	2.5 ± 0.014	2.6 ± 0.013	2.7 ± 0.011	2.9 ± 0.012	3.2 ± 0.025
71	2.0 ± 0.005	1.9 ± 0.005	1.9 ± 0.005	1.9 ± 0.006	1.9 ± 0.008
72	1.3 ± 0.011	1.2 ± 0.01	1.2 ± 0.006	1.1 ± 0.007	1.1 ± 0.023
73	1.7 ± 0.003	1.7 ± 0.002	1.7 ± 0.002	1.7 ± 0.002	1.8 ± 0.003
74	0.4 ± 0.003	0.4 ± 0.003	0.4 ± 0.002	0.4 ± 0.003	0.4 ± 0.006
76	2.8 ± 0.006	2.7 ± 0.005	2.6 ± 0.005	2.6 ± 0.005	2.7 ± 0.007
77	10.7 ± 0.134	10.7 ± 0.135	10.7 ± 0.125	10.6 ± 0.107	10.5 ± 0.17
80	0.9 ± 0.002	0.8 ± 0.001	0.8 ± 0.001	0.9 ± 0.002	0.9 ± 0.003
81	1.9 ± 0.007	1.9 ± 0.006	1.9 ± 0.006	1.9 ± 0.009	2.0 ± 0.013
82	0.4 ± 0.002	0.4 ± 0.001	0.4 ± 0.001	0.4 ± 0.001	0.4 ± 0.002
83	1.6 ± 0.008	1.6 ± 0.007	1.6 ± 0.007	1.6 ± 0.008	1.8 ± 0.013
84	0.9 ± 0.001	0.9 ± 0.001	0.9 ± 0.001	0.9 ± 0.001	0.9 ± 0.002
85	1.7 ± 0.024	1.7 ± 0.02	1.6 ± 0.017	1.6 ± 0.017	1.5 ± 0.022
87	2.3 ± 0.008	2.2 ± 0.008	2.0 ± 0.008	1.9 ± 0.01	1.7 ± 0.014
88	1.5 ± 0.003	1.5 ± 0.003	1.4 ± 0.003	1.4 ± 0.003	1.4 ± 0.004
89	1.6 ± 0.001	1.5 ± 0.001	1.5 ± 0.001	1.5 ± 0.001	1.5 ± 0.001
90	0.9 ± 0.004	0.8 ± 0.004	0.8 ± 0.003	0.8 ± 0.003	0.8 ± 0.004
91	1.5 ± 0.0	1.4 ± 0.0	1.4 ± 0.0	1.3 ± 0.0	1.3 ± 0.001
93	1.2 ± 0.011	1.1 ± 0.01	1.1 ± 0.01	1.0 ± 0.008	0.9 ± 0.009
94	0.4 ± 0.0	0.4 ± 0.0	0.4 ± 0.0	0.4 ± 0.0	0.4 ± 0.0
96	1.0 ± 0.005	1.0 ± 0.005	0.9 ± 0.005	0.9 ± 0.005	0.9 ± 0.008
97	1.6 ± 0.004	1.5 ± 0.003	1.5 ± 0.003	1.5 ± 0.004	1.5 ± 0.007
98	6.0 ± 0.04	5.9 ± 0.042	5.8 ± 0.042	5.6 ± 0.043	5.5 ± 0.056
99	1.9 ± 0.013	1.8 ± 0.013	1.8 ± 0.012	1.9 ± 0.014	2.0 ± 0.023

ID	MACS 1206 WFC3/IR r_e [kpc] cont.				
	Y_{105}	YJ_{110}	J_{125}	JH_{140}	H_{160}
100	2.6 ± 0.003	2.5 ± 0.003	2.4 ± 0.003	2.4 ± 0.002	2.4 ± 0.003
101	1.1 ± 0.001	1.0 ± 0.001	1.0 ± 0.001	0.9 ± 0.001	1.0 ± 0.002
104	1.3 ± 0.003	1.2 ± 0.002	1.2 ± 0.002	1.1 ± 0.002	1.1 ± 0.003

Table C.5.: Measurements of n in the ACS bands for the selected early-type galaxies in MACS 1206.

ID	MACS 1206 ACS Sérsic n						
	B_{435}	g_{475}	V_{606}	r_{625}	i_{775}	I_{814}	z_{850}
1	4.9 ± 0.019	4.7 ± 0.017	4.2 ± 0.012	4.1 ± 0.011	3.6 ± 0.007	3.5 ± 0.005	3.2 ± 0.004
3	4.8 ± 0.013	4.8 ± 0.012	4.6 ± 0.009	4.5 ± 0.008	4.3 ± 0.005	4.3 ± 0.004	4.2 ± 0.003
4	3.4 ± 0.057	3.4 ± 0.047	3.5 ± 0.027	3.5 ± 0.022	3.6 ± 0.015	3.6 ± 0.017	3.7 ± 0.022
5	3.0 ± 0.031	2.9 ± 0.028	2.8 ± 0.02	2.8 ± 0.018	2.7 ± 0.011	2.7 ± 0.009	2.6 ± 0.006
6	4.7 ± 0.012	4.6 ± 0.011	4.5 ± 0.008	4.4 ± 0.008	4.3 ± 0.005	4.2 ± 0.004	4.2 ± 0.003
8	3.0 ± 0.144	3.0 ± 0.127	2.8 ± 0.089	2.8 ± 0.078	2.6 ± 0.047	2.5 ± 0.039	2.4 ± 0.032
10	6.1 ± 0.009	6.0 ± 0.008	5.7 ± 0.006	5.6 ± 0.005	5.3 ± 0.003	5.2 ± 0.003	5.1 ± 0.002
11	4.2 ± 0.03	4.0 ± 0.027	3.8 ± 0.018	3.7 ± 0.016	3.4 ± 0.009	3.3 ± 0.008	3.1 ± 0.006
12	6.3 ± 0.0	6.4 ± 0.0	6.7 ± 0.0	6.8 ± 0.0	7.0 ± 0.0	7.1 ± 0.0	7.1 ± 0.0
15	5.2 ± 0.024	5.1 ± 0.021	5.0 ± 0.016	5.0 ± 0.014	4.9 ± 0.009	4.8 ± 0.007	4.7 ± 0.005
17	4.1 ± 0.005	4.1 ± 0.004	4.1 ± 0.003	4.0 ± 0.003	4.0 ± 0.002	4.0 ± 0.002	4.0 ± 0.001
19	5.3 ± 0.033	5.1 ± 0.028	4.7 ± 0.018	4.6 ± 0.015	4.1 ± 0.008	4.0 ± 0.008	3.7 ± 0.008
20	3.2 ± 0.096	3.1 ± 0.082	3.0 ± 0.054	3.0 ± 0.046	3.0 ± 0.028	2.9 ± 0.025	2.9 ± 0.024
21	4.3 ± 0.071	4.4 ± 0.062	4.7 ± 0.044	4.8 ± 0.039	5.1 ± 0.025	5.2 ± 0.021	5.3 ± 0.018
22	5.8 ± 0.04	5.7 ± 0.035	5.4 ± 0.025	5.3 ± 0.022	5.1 ± 0.013	5.0 ± 0.011	4.8 ± 0.009
23	5.2 ± 0.034	5.1 ± 0.031	4.7 ± 0.024	4.6 ± 0.022	4.3 ± 0.015	4.2 ± 0.013	4.0 ± 0.01
24	4.0 ± 0.114	4.0 ± 0.102	4.0 ± 0.076	4.0 ± 0.067	3.9 ± 0.044	3.8 ± 0.039	3.7 ± 0.035
25	8.0 ± 0.06	7.7 ± 0.051	7.0 ± 0.034	6.8 ± 0.029	6.2 ± 0.019	6.0 ± 0.018	5.8 ± 0.018
26	3.4 ± 0.018	3.3 ± 0.015	3.1 ± 0.01	3.0 ± 0.008	2.9 ± 0.006	2.8 ± 0.006	2.7 ± 0.006
28	6.8 ± 0.019	6.5 ± 0.016	5.8 ± 0.01	5.6 ± 0.009	4.9 ± 0.005	4.7 ± 0.004	4.3 ± 0.004
29	4.9 ± 0.005	4.9 ± 0.004	4.7 ± 0.003	4.7 ± 0.003	4.6 ± 0.002	4.6 ± 0.002	4.5 ± 0.001
30	4.6 ± 0.045	4.5 ± 0.039	4.2 ± 0.028	4.1 ± 0.024	3.9 ± 0.015	3.8 ± 0.013	3.8 ± 0.011
31	5.1 ± 0.05	5.3 ± 0.042	5.7 ± 0.027	5.9 ± 0.023	6.4 ± 0.015	6.5 ± 0.015	6.8 ± 0.015

ID	MACS 1206 ACS Sérsic n cont.						
	B_{435}	g_{475}	V_{606}	r_{625}	i_{775}	I_{814}	z_{850}
32	5.6 ± 0.021	5.5 ± 0.02	5.3 ± 0.016	5.2 ± 0.015	5.0 ± 0.011	5.0 ± 0.01	5.0 ± 0.008
33	8 ± 0.351	7.7 ± 0.312	7.1 ± 0.226	6.8 ± 0.2	6.2 ± 0.124	6.0 ± 0.102	5.8 ± 0.075
35	4.2 ± 0.024	4.1 ± 0.022	3.9 ± 0.017	3.8 ± 0.016	3.6 ± 0.011	3.6 ± 0.01	3.5 ± 0.007
37	4.8 ± 0.14	5.0 ± 0.126	5.2 ± 0.097	5.3 ± 0.087	5.4 ± 0.06	5.5 ± 0.052	5.5 ± 0.039
38	5.7 ± 0.029	5.6 ± 0.026	5.5 ± 0.019	5.5 ± 0.017	5.3 ± 0.012	5.3 ± 0.01	5.1 ± 0.008
39	8.0 ± 0.07	7.7 ± 0.063	7.0 ± 0.047	6.8 ± 0.042	6.1 ± 0.028	5.8 ± 0.024	5.5 ± 0.019
40	4.9 ± 0.151	4.8 ± 0.135	4.6 ± 0.099	4.6 ± 0.088	4.5 ± 0.058	4.4 ± 0.049	4.4 ± 0.037
41	4.5 ± 0.008	4.4 ± 0.007	4.2 ± 0.004	4.2 ± 0.003	4.0 ± 0.002	4.0 ± 0.002	3.9 ± 0.003
42	8.0 ± 0.013	7.9 ± 0.011	7.7 ± 0.007	7.6 ± 0.006	7.4 ± 0.003	7.3 ± 0.003	7.1 ± 0.003
43	3.1 ± 0.001	3.1 ± 0.001	3.0 ± 0.001	2.9 ± 0.001	2.9 ± 0.001	2.8 ± 0.0	2.8 ± 0.0
45	6.0 ± 0.038	5.9 ± 0.033	5.6 ± 0.023	5.6 ± 0.02	5.3 ± 0.013	5.3 ± 0.011	5.2 ± 0.01
46	4.9 ± 0.012	4.8 ± 0.011	4.4 ± 0.008	4.3 ± 0.007	4.0 ± 0.005	3.9 ± 0.004	3.8 ± 0.003
47	6.8 ± 0.035	6.7 ± 0.031	6.6 ± 0.023	6.6 ± 0.021	6.5 ± 0.014	6.4 ± 0.013	6.3 ± 0.01
48	6.3 ± 0.029	6.2 ± 0.026	6.1 ± 0.02	6.0 ± 0.019	5.8 ± 0.014	5.7 ± 0.012	5.5 ± 0.01
50	2.8 ± 0.008	2.8 ± 0.007	2.8 ± 0.004	2.8 ± 0.003	2.8 ± 0.002	2.8 ± 0.002	2.8 ± 0.003
51	5.2 ± 0.003	5.2 ± 0.003	5.2 ± 0.002	5.2 ± 0.002	5.2 ± 0.001	5.2 ± 0.001	5.2 ± 0.001
52	6.0 ± 0.003	6.0 ± 0.003	5.9 ± 0.001	5.9 ± 0.001	6.0 ± 0.001	6.0 ± 0.001	6.0 ± 0.001
55	4.5 ± 0.034	4.5 ± 0.029	4.4 ± 0.019	4.3 ± 0.017	4.3 ± 0.01	4.3 ± 0.009	4.3 ± 0.009
56	4.5 ± 0.026	4.4 ± 0.023	4.0 ± 0.015	3.9 ± 0.013	3.6 ± 0.007	3.5 ± 0.005	3.3 ± 0.005
57	3.4 ± 0.031	3.4 ± 0.027	3.5 ± 0.017	3.5 ± 0.015	3.6 ± 0.009	3.6 ± 0.009	3.6 ± 0.009
58	5.0 ± 0.17	5.1 ± 0.15	5.5 ± 0.112	5.5 ± 0.101	5.7 ± 0.075	5.8 ± 0.07	5.8 ± 0.066
59	5.6 ± 0.075	5.3 ± 0.066	4.7 ± 0.048	4.5 ± 0.042	4.0 ± 0.025	3.8 ± 0.021	3.5 ± 0.014
61	3.2 ± 0.06	3.2 ± 0.053	3.3 ± 0.037	3.3 ± 0.033	3.3 ± 0.02	3.3 ± 0.017	3.3 ± 0.014
62	4.0 ± 0.049	4.0 ± 0.044	4.0 ± 0.033	4.0 ± 0.03	3.9 ± 0.02	3.9 ± 0.018	3.9 ± 0.014

ID	MACS 1206 ACS Sérsic n cont.						
	B_{435}	g_{475}	V_{606}	r_{625}	i_{775}	I_{814}	z_{850}
63	2.1 ± 0.156	2.3 ± 0.137	2.7 ± 0.097	2.8 ± 0.085	3.2 ± 0.054	3.3 ± 0.046	3.5 ± 0.04
64	6.3 ± 0.097	6.1 ± 0.085	5.6 ± 0.059	5.4 ± 0.051	4.9 ± 0.03	4.8 ± 0.024	4.5 ± 0.018
65	8.0 ± 0.156	7.8 ± 0.143	7.5 ± 0.114	7.4 ± 0.104	6.9 ± 0.076	6.8 ± 0.067	6.5 ± 0.052
68	4.7 ± 0.072	4.7 ± 0.061	4.8 ± 0.038	4.8 ± 0.032	4.8 ± 0.023	4.9 ± 0.023	4.9 ± 0.026
69	6.7 ± 0.058	6.6 ± 0.046	6.3 ± 0.023	6.2 ± 0.018	6.0 ± 0.017	6.0 ± 0.02	5.9 ± 0.025
70	5.6 ± 0.07	5.6 ± 0.06	5.5 ± 0.038	5.6 ± 0.032	5.6 ± 0.019	5.7 ± 0.018	5.8 ± 0.018
71	6.4 ± 0.046	6.3 ± 0.041	6.3 ± 0.028	6.2 ± 0.024	6.2 ± 0.015	6.2 ± 0.013	6.3 ± 0.012
72	7.9 ± 0.258	7.7 ± 0.215	7.3 ± 0.128	7.2 ± 0.105	6.9 ± 0.069	6.8 ± 0.071	6.6 ± 0.08
73	2.1 ± 0.025	2.2 ± 0.022	2.3 ± 0.016	2.4 ± 0.015	2.5 ± 0.009	2.6 ± 0.008	2.7 ± 0.006
74	8.0 ± 0.484	7.3 ± 0.421	5.9 ± 0.285	5.4 ± 0.243	4.2 ± 0.132	3.8 ± 0.105	3.3 ± 0.083
76	8.0 ± 0.034	7.7 ± 0.031	7.0 ± 0.023	6.8 ± 0.021	6.2 ± 0.014	5.9 ± 0.012	5.6 ± 0.008
77	4.3 ± 0.113	4.3 ± 0.098	4.2 ± 0.067	4.2 ± 0.057	4.1 ± 0.032	4.1 ± 0.026	4.0 ± 0.022
80	5.1 ± 0.055	5.0 ± 0.048	4.7 ± 0.033	4.6 ± 0.028	4.4 ± 0.016	4.3 ± 0.014	4.2 ± 0.012
81	3.1 ± 0.036	3.0 ± 0.032	2.8 ± 0.023	2.8 ± 0.021	2.6 ± 0.013	2.5 ± 0.011	2.4 ± 0.009
82	6.7 ± 0.081	6.4 ± 0.073	5.8 ± 0.055	5.6 ± 0.049	5.0 ± 0.034	4.8 ± 0.03	4.6 ± 0.024
83	7.4 ± 0.126	7.1 ± 0.112	6.5 ± 0.08	6.4 ± 0.071	5.9 ± 0.043	5.7 ± 0.036	5.5 ± 0.026
84	3.8 ± 0.018	3.8 ± 0.015	3.8 ± 0.008	3.8 ± 0.006	3.8 ± 0.006	3.8 ± 0.007	3.8 ± 0.008
85	3.7 ± 0.132	3.7 ± 0.117	3.7 ± 0.086	3.7 ± 0.076	3.7 ± 0.052	3.7 ± 0.046	3.7 ± 0.039
87	5.8 ± 0.032	5.9 ± 0.027	5.9 ± 0.018	5.9 ± 0.016	5.9 ± 0.011	5.8 ± 0.01	5.8 ± 0.011
88	2.8 ± 0.043	2.9 ± 0.038	3.1 ± 0.025	3.1 ± 0.022	3.3 ± 0.013	3.3 ± 0.011	3.3 ± 0.011
89	4.8 ± 0.015	4.6 ± 0.013	4.1 ± 0.009	3.9 ± 0.008	3.4 ± 0.004	3.3 ± 0.003	3.0 ± 0.003
90	4.4 ± 0.178	4.3 ± 0.158	4.0 ± 0.114	3.9 ± 0.101	3.7 ± 0.062	3.7 ± 0.052	3.5 ± 0.039
91	8.0 ± 0.011	7.6 ± 0.009	6.6 ± 0.006	6.3 ± 0.006	5.4 ± 0.003	5.1 ± 0.003	4.6 ± 0.002
93	5.3 ± 0.196	5.3 ± 0.174	5.3 ± 0.126	5.3 ± 0.111	5.3 ± 0.071	5.3 ± 0.061	5.2 ± 0.049

ID	MACS 1206 ACS Sérsic n cont.						
	B_{435}	g_{475}	V_{606}	r_{625}	i_{775}	I_{814}	z_{850}
94	8.0 ± 0.046	7.5 ± 0.04	6.4 ± 0.028	6.0 ± 0.024	5.0 ± 0.014	4.6 ± 0.012	4.1 ± 0.009
96	3.8 ± 0.067	3.7 ± 0.057	3.5 ± 0.035	3.4 ± 0.029	3.2 ± 0.016	3.2 ± 0.015	3.1 ± 0.017
97	6.3 ± 0.064	6.1 ± 0.057	5.8 ± 0.041	5.7 ± 0.036	5.3 ± 0.022	5.2 ± 0.018	5.0 ± 0.013
98	4.3 ± 0.046	4.3 ± 0.039	4.3 ± 0.025	4.4 ± 0.02	4.4 ± 0.011	4.4 ± 0.011	4.4 ± 0.013
99	3.9 ± 0.047	3.7 ± 0.042	3.4 ± 0.03	3.3 ± 0.026	3.0 ± 0.018	2.8 ± 0.016	2.6 ± 0.014
100	6.0 ± 0.016	5.9 ± 0.014	5.6 ± 0.009	5.5 ± 0.008	5.3 ± 0.004	5.2 ± 0.003	5.0 ± 0.004
101	4.8 ± 0.016	4.9 ± 0.014	5.0 ± 0.01	5.1 ± 0.009	5.2 ± 0.007	5.3 ± 0.006	5.4 ± 0.006
104	3.3 ± 0.046	3.3 ± 0.04	3.3 ± 0.029	3.2 ± 0.026	3.2 ± 0.016	3.2 ± 0.014	3.2 ± 0.011

Table C.6.: Measurements of n in the WFC3/IR bands for the selected early-type galaxies in MACS 1206.

ID	MACS 1206 WFC3/IR Sérsic n				
	Y_{105}	YJ_{110}	J_{125}	JH_{140}	H_{160}
1	3.1 ± 0.003	3.0 ± 0.003	3.0 ± 0.003	3.0 ± 0.004	3.2 ± 0.005
3	4.2 ± 0.002	4.1 ± 0.002	4.2 ± 0.002	4.2 ± 0.003	4.3 ± 0.004
4	3.7 ± 0.024	3.8 ± 0.024	3.8 ± 0.021	3.9 ± 0.015	4.0 ± 0.023
5	2.6 ± 0.005	2.6 ± 0.005	2.6 ± 0.005	2.6 ± 0.006	2.6 ± 0.009
6	4.1 ± 0.002	4.1 ± 0.003	4.2 ± 0.003	4.2 ± 0.004	4.4 ± 0.006
8	2.4 ± 0.031	2.3 ± 0.032	2.2 ± 0.032	2.2 ± 0.032	2.2 ± 0.044
10	5.1 ± 0.002	5.1 ± 0.002	5.1 ± 0.002	5.3 ± 0.002	5.5 ± 0.003
11	3.0 ± 0.006	2.9 ± 0.006	2.9 ± 0.006	2.8 ± 0.006	2.9 ± 0.008
12	7.2 ± 0.0	7.1 ± 0.0	7.1 ± 0.0	6.9 ± 0.0	6.7 ± 0.0
15	4.5 ± 0.004	4.4 ± 0.004	4.2 ± 0.004	4.0 ± 0.004	3.7 ± 0.005
17	4.0 ± 0.001	4.0 ± 0.001	4.0 ± 0.001	4.1 ± 0.001	4.2 ± 0.002
19	3.5 ± 0.008	3.3 ± 0.007	3.2 ± 0.005	3.1 ± 0.005	3.0 ± 0.014
20	3.0 ± 0.025	3.0 ± 0.024	3.1 ± 0.024	3.2 ± 0.032	3.4 ± 0.058
21	5.3 ± 0.018	5.3 ± 0.019	5.3 ± 0.021	5.2 ± 0.026	4.9 ± 0.037
22	4.7 ± 0.008	4.6 ± 0.008	4.5 ± 0.008	4.4 ± 0.009	4.4 ± 0.014
23	3.8 ± 0.008	3.7 ± 0.007	3.6 ± 0.006	3.5 ± 0.008	3.5 ± 0.01
24	3.5 ± 0.039	3.2 ± 0.048	3.0 ± 0.058	2.5 ± 0.077	2.0 ± 0.1
25	5.6 ± 0.017	5.5 ± 0.016	5.6 ± 0.015	5.8 ± 0.021	6.1 ± 0.039
26	2.7 ± 0.007	2.6 ± 0.007	2.6 ± 0.008	2.7 ± 0.01	2.8 ± 0.016
28	4.1 ± 0.004	3.9 ± 0.004	3.9 ± 0.003	3.9 ± 0.004	4.1 ± 0.009
29	4.6 ± 0.001	4.7 ± 0.001	4.7 ± 0.001	5.0 ± 0.001	5.2 ± 0.002
30	3.8 ± 0.01	3.9 ± 0.01	4.0 ± 0.01	4.3 ± 0.013	4.7 ± 0.021
31	7.1 ± 0.015	7.3 ± 0.014	7.5 ± 0.013	7.6 ± 0.018	7.7 ± 0.035
32	5.0 ± 0.007	5.0 ± 0.006	5.1 ± 0.007	5.3 ± 0.008	5.6 ± 0.011
33	5.6 ± 0.065	5.5 ± 0.066	5.5 ± 0.07	5.6 ± 0.084	5.9 ± 0.119
35	3.4 ± 0.006	3.4 ± 0.005	3.5 ± 0.005	3.6 ± 0.006	3.7 ± 0.007
37	5.5 ± 0.031	5.4 ± 0.028	5.2 ± 0.026	4.9 ± 0.027	4.4 ± 0.034
38	4.9 ± 0.007	4.8 ± 0.006	4.6 ± 0.005	4.3 ± 0.005	4.0 ± 0.008
39	5.1 ± 0.016	4.9 ± 0.014	4.8 ± 0.012	4.7 ± 0.012	4.7 ± 0.02
40	4.4 ± 0.031	4.4 ± 0.03	4.4 ± 0.03	4.5 ± 0.037	4.7 ± 0.054
41	3.9 ± 0.003	3.8 ± 0.003	3.9 ± 0.002	3.9 ± 0.002	4.0 ± 0.004
42	7.0 ± 0.003	6.8 ± 0.003	6.7 ± 0.003	6.6 ± 0.003	6.4 ± 0.004
43	2.8 ± 0.0	2.8 ± 0.0	2.8 ± 0.0	2.9 ± 0.0	3 ± 0.0
45	5.1 ± 0.009	5.1 ± 0.008	5.1 ± 0.007	5.2 ± 0.009	5.3 ± 0.017
46	3.7 ± 0.003	3.6 ± 0.002	3.6 ± 0.002	3.7 ± 0.003	3.9 ± 0.005
47	6.3 ± 0.01	6.2 ± 0.009	6.2 ± 0.009	6.2 ± 0.011	6.2 ± 0.015
48	5.3 ± 0.009	5.1 ± 0.008	4.9 ± 0.008	4.7 ± 0.008	4.4 ± 0.01
50	2.8 ± 0.003	2.8 ± 0.002	2.8 ± 0.002	2.9 ± 0.003	2.9 ± 0.006

ID	MACS 1206 WFC3/IR Sérsic n cont.				
	Y_{105}	YJ_{110}	J_{125}	JH_{140}	H_{160}
51	5.2 ± 0.001	5.3 ± 0.001	5.3 ± 0.001	5.4 ± 0.001	5.4 ± 0.001
52	6.1 ± 0.001	6.2 ± 0.001	6.3 ± 0.001	6.5 ± 0.001	6.7 ± 0.003
55	4.3 ± 0.01	4.4 ± 0.01	4.5 ± 0.011	4.7 ± 0.014	5.0 ± 0.021
56	3.1 ± 0.006	3.0 ± 0.007	3 ± 0.007	3.0 ± 0.006	3.0 ± 0.008
57	3.7 ± 0.01	3.7 ± 0.01	3.6 ± 0.01	3.6 ± 0.011	3.5 ± 0.017
58	5.7 ± 0.066	5.5 ± 0.067	5.3 ± 0.071	4.8 ± 0.088	4.1 ± 0.123
59	3.4 ± 0.012	3.3 ± 0.011	3.3 ± 0.011	3.5 ± 0.013	3.8 ± 0.021
61	3.3 ± 0.014	3.3 ± 0.014	3.2 ± 0.014	3.2 ± 0.015	3.1 ± 0.022
62	3.8 ± 0.011	3.8 ± 0.011	3.7 ± 0.01	3.7 ± 0.012	3.6 ± 0.016
63	3.6 ± 0.039	3.6 ± 0.04	3.5 ± 0.04	3.3 ± 0.041	3.0 ± 0.053
64	4.3 ± 0.017	4.2 ± 0.015	4.2 ± 0.015	4.2 ± 0.02	4.4 ± 0.037
65	6.2 ± 0.042	6.0 ± 0.036	5.8 ± 0.034	5.5 ± 0.038	5.3 ± 0.05
68	5.0 ± 0.026	5.1 ± 0.024	5.1 ± 0.022	5.2 ± 0.03	5.4 ± 0.055
69	5.8 ± 0.026	5.8 ± 0.022	5.8 ± 0.015	6.0 ± 0.011	6.2 ± 0.038
70	5.9 ± 0.019	6.1 ± 0.018	6.3 ± 0.015	6.6 ± 0.015	7.0 ± 0.03
71	6.3 ± 0.012	6.4 ± 0.012	6.5 ± 0.012	6.6 ± 0.014	6.8 ± 0.021
72	6.6 ± 0.078	6.6 ± 0.065	6.6 ± 0.051	6.8 ± 0.084	7.2 ± 0.189
73	2.8 ± 0.005	2.9 ± 0.004	2.9 ± 0.004	3.1 ± 0.005	3.2 ± 0.007
74	3.1 ± 0.085	3.2 ± 0.09	3.4 ± 0.095	4.2 ± 0.125	5.4 ± 0.212
76	5.4 ± 0.007	5.3 ± 0.006	5.3 ± 0.006	5.5 ± 0.007	5.8 ± 0.01
77	3.9 ± 0.023	3.9 ± 0.023	3.9 ± 0.022	3.8 ± 0.018	3.8 ± 0.03
80	4.2 ± 0.011	4.2 ± 0.01	4.3 ± 0.009	4.4 ± 0.011	4.7 ± 0.022
81	2.4 ± 0.007	2.3 ± 0.007	2.3 ± 0.007	2.4 ± 0.009	2.5 ± 0.014
82	4.4 ± 0.02	4.4 ± 0.018	4.4 ± 0.017	4.6 ± 0.021	4.9 ± 0.031
83	5.4 ± 0.023	5.4 ± 0.022	5.4 ± 0.022	5.7 ± 0.025	6.2 ± 0.039
84	3.7 ± 0.008	3.7 ± 0.006	3.7 ± 0.005	3.7 ± 0.007	3.7 ± 0.017
85	3.6 ± 0.036	3.6 ± 0.034	3.5 ± 0.032	3.3 ± 0.035	3.1 ± 0.052
87	5.7 ± 0.011	5.6 ± 0.012	5.4 ± 0.013	5.2 ± 0.017	4.9 ± 0.026
88	3.3 ± 0.011	3.3 ± 0.011	3.2 ± 0.01	3.1 ± 0.01	2.9 ± 0.015
89	2.8 ± 0.003	2.7 ± 0.003	2.7 ± 0.002	2.7 ± 0.002	2.8 ± 0.004
90	3.5 ± 0.034	3.4 ± 0.033	3.4 ± 0.033	3.5 ± 0.037	3.6 ± 0.053
91	4.3 ± 0.002	4.1 ± 0.002	4.0 ± 0.002	4.1 ± 0.002	4.4 ± 0.003
93	5.2 ± 0.047	5.1 ± 0.047	5.0 ± 0.048	4.8 ± 0.052	4.6 ± 0.068
94	3.7 ± 0.008	3.5 ± 0.007	3.4 ± 0.006	3.6 ± 0.007	4.0 ± 0.013
96	3.0 ± 0.02	3.0 ± 0.022	3.0 ± 0.023	3.1 ± 0.029	3.2 ± 0.046
97	4.8 ± 0.011	4.7 ± 0.01	4.7 ± 0.011	4.6 ± 0.013	4.6 ± 0.021
98	4.4 ± 0.016	4.3 ± 0.017	4.3 ± 0.017	4.3 ± 0.019	4.2 ± 0.027
99	2.5 ± 0.015	2.4 ± 0.015	2.3 ± 0.016	2.2 ± 0.02	2.2 ± 0.028

ID	MACS 1206 WFC3/IR Sérsic n cont.				
	Y_{105}	YJ_{110}	J_{125}	JH_{140}	H_{160}
100	4.9 ± 0.004	4.8 ± 0.004	4.8 ± 0.004	4.8 ± 0.004	4.8 ± 0.005
101	5.4 ± 0.006	5.5 ± 0.005	5.5 ± 0.005	5.5 ± 0.005	5.5 ± 0.009
104	3.1 ± 0.01	3.1 ± 0.009	3.0 ± 0.008	3.0 ± 0.008	2.9 ± 0.014

Table C.7.: Magnitude assessments in the ACS bands for the fitted early-type galaxies in MACS 0416

ID	MACS 0416 ACS AB Magnitudes						
	B_{435}	g_{475}	V_{606}	r_{625}	i_{775}	I_{814}	z_{850}
21	23.5 ± 0.0295	22.8 ± 0.0173	21.8 ± 0.011	21.5 ± 0.0104	21.0 ± 0.0067	20.9 ± 0.0055	20.6 ± 0.0042
25	23.0 ± 0.7552	22.5 ± 0.4667	21.2 ± 0.2749	21.1 ± 0.2653	20.6 ± 0.1841	20.4 ± 0.1563	20.1 ± 0.1731
26	22.2 ± 0.0022	21.8 ± 0.0018	20.5 ± 0.0014	20.3 ± 0.0014	19.8 ± 0.0011	19.6 ± 0.001	19.3 ± 0.0009
30	24.4 ± 0.0097	24.5 ± 0.008	23.6 ± 0.0057	23.4 ± 0.0045	22.9 ± 0.003	22.8 ± 0.0022	22.5 ± 0.0019
31	23.7 ± 0.0109	23.1 ± 0.0068	21.8 ± 0.0046	21.5 ± 0.0038	21.0 ± 0.0026	20.8 ± 0.0022	20.5 ± 0.0012
33	23.6 ± 0.0008	23.1 ± 0.001	21.8 ± 0.0008	21.7 ± 0.0005	21.1 ± 0.0004	20.9 ± 0.0003	20.6 ± 0.0002
38	24.3 ± 0.0029	23.9 ± 0.0025	22.6 ± 0.0021	22.5 ± 0.002	22.0 ± 0.0015	21.8 ± 0.0011	21.4 ± 0.0008
43	24.0 ± 0.0205	23.9 ± 0.0161	23.2 ± 0.0101	23.1 ± 0.0098	22.6 ± 0.0065	22.4 ± 0.0052	22.1 ± 0.0045
45	22.5 ± 0.0004	22.1 ± 0.0002	20.8 ± 0.0001	20.6 ± 0.0001	20.1 ± 0.0001	19.9 ± 0.0001	19.5 ± 0.0001
50	22.6 ± 0.0022	22.2 ± 0.0023	21.2 ± 0.0021	21.1 ± 0.0021	20.6 ± 0.0018	20.4 ± 0.0013	20.1 ± 0.0008
53	23.3 ± 0.0015	22.8 ± 0.001	21.4 ± 0.001	21.3 ± 0.0007	20.8 ± 0.0005	20.5 ± 0.0004	20.2 ± 0.0004
54	24.1 ± 0.0017	23.6 ± 0.0015	22.4 ± 0.0014	22.3 ± 0.0013	21.7 ± 0.0011	21.5 ± 0.0009	21.2 ± 0.0008
55	24.7 ± 0.0291	23.9 ± 0.0227	22.9 ± 0.02	22.7 ± 0.0185	22.3 ± 0.0184	22.1 ± 0.017	21.8 ± 0.0179
57	23.1 ± 0.0017	22.8 ± 0.002	21.6 ± 0.0016	21.5 ± 0.0014	20.9 ± 0.0009	20.7 ± 0.0008	20.4 ± 0.0002
63	22.8 ± 0.0027	22.5 ± 0.0025	21.3 ± 0.0018	21.2 ± 0.0022	20.6 ± 0.0011	20.4 ± 0.0007	20.1 ± 0.0001
65	22.2 ± 0.0004	21.8 ± 0.0005	20.6 ± 0.0004	20.4 ± 0.0002	19.9 ± 0.0004	19.7 ± 0.0004	19.3 ± 0.0003
66	21.3 ± 0.0018	21.0 ± 0.0008	19.6 ± 0.0006	19.4 ± 0.0007	18.8 ± 0.0002	18.5 ± 0.0002	18.1 ± 0.0005
68	24.0 ± 0.0034	23.5 ± 0.0018	22.3 ± 0.0015	22.1 ± 0.0012	21.6 ± 0.0008	21.4 ± 0.0005	21.0 ± 0.0004
70	22.9 ± 0.0004	22.5 ± 0.0003	21.2 ± 0.0002	21.1 ± 0.0002	20.6 ± 0.0001	20.4 ± 0.0001	20.0 ± 0.0001
71	23.6 ± 0.008	23.3 ± 0.0054	22.1 ± 0.0031	22.0 ± 0.0029	21.5 ± 0.002	21.3 ± 0.0017	21.0 ± 0.0013
85	21.9 ± 0.0178	21.5 ± 0.0127	20.2 ± 0.0088	20.0 ± 0.0082	19.5 ± 0.0056	19.3 ± 0.0048	18.9 ± 0.0036
87	22.0 ± 0.0005	21.7 ± 0.0003	20.5 ± 0.0002	20.3 ± 0.0002	19.8 ± 0.0003	19.6 ± 0.0002	19.2 ± 0.0003
88	22.6 ± 0.0023	22.1 ± 0.0018	20.6 ± 0.0015	20.5 ± 0.0014	20.0 ± 0.0013	19.7 ± 0.001	19.4 ± 0.0009

ID	MACS 0416 ACS AB Magnitudes cont.						
	B_{435}	g_{475}	V_{606}	r_{625}	i_{775}	I_{814}	z_{850}
93	23.6 ± 0.0003	23.5 ± 0.0002	22.4 ± 0.0001	22.3 ± 0.0003	21.8 ± 0.0001	21.6 ± 0.0001	21.3 ± 0.0001
94	22.6 ± 0.0018	22.3 ± 0.0013	21.1 ± 0.0009	20.9 ± 0.0008	20.4 ± 0.0006	20.2 ± 0.0005	19.8 ± 0.0004
95	23.8 ± 0.0024	23.7 ± 0.0021	22.6 ± 0.0019	22.5 ± 0.0018	22.0 ± 0.0011	21.8 ± 0.0009	21.5 ± 0.0002
96	22.4 ± 0.0252	21.9 ± 0.0156	20.7 ± 0.0105	20.5 ± 0.0103	20.1 ± 0.0081	19.8 ± 0.0063	19.6 ± 0.005
98	24.9 ± 0.0043	24.1 ± 0.0025	22.8 ± 0.0013	22.7 ± 0.0009	22.1 ± 0.0012	21.9 ± 0.0008	21.6 ± 0.0008
102	23.7 ± 0.0764	23.4 ± 0.0434	22.2 ± 0.0208	22.1 ± 0.0198	21.6 ± 0.0125	21.3 ± 0.0099	21.0 ± 0.0086
103	22.5 ± 0.0014	22.4 ± 0.0009	21.4 ± 0.0005	21.2 ± 0.0005	20.7 ± 0.0003	20.5 ± 0.0003	20.2 ± 0.0002
104	22.1 ± 0.0005	21.7 ± 0.0005	20.4 ± 0.0004	20.2 ± 0.0004	19.7 ± 0.0002	19.5 ± 0.0001	19.1 ± 0.0
105	23.3 ± 0.0276	22.8 ± 0.0152	21.5 ± 0.0086	21.3 ± 0.0084	20.8 ± 0.0069	20.5 ± 0.0062	20.2 ± 0.0061
107	22.4 ± 0.0006	22.0 ± 0.0004	20.6 ± 0.0003	20.5 ± 0.0003	19.9 ± 0.0001	19.7 ± 0.0001	19.3 ± 0.0001
109	22.6 ± 0.0012	22.1 ± 0.0007	20.7 ± 0.0005	20.6 ± 0.0005	20.1 ± 0.0009	19.9 ± 0.001	19.5 ± 0.0009
113	23.3 ± 0.0198	22.0 ± 0.0105	20.7 ± 0.0073	20.6 ± 0.0066	20.0 ± 0.0046	19.8 ± 0.0038	19.5 ± 0.0028
115	23.5 ± 0.0814	22.6 ± 0.0342	21.3 ± 0.0188	21.0 ± 0.0181	20.7 ± 0.0128	20.3 ± 0.0097	20.1 ± 0.0102
133	23.4 ± 0.0803	23.0 ± 0.054	21.6 ± 0.0313	21.5 ± 0.0279	20.9 ± 0.0171	20.7 ± 0.0142	20.4 ± 0.0166
154	24.0 ± 0.0012	23.9 ± 0.0009	23.1 ± 0.0015	23.0 ± 0.0009	22.5 ± 0.0007	22.3 ± 0.0007	22.0 ± 0.0005

Table C.8.: Magnitude assessments in the WFC3/IR bands for the fitted early-type galaxies in MACS 0416

ID	MACS 0416 WFC3/IR AB Magnitudes				
	Y_{105}	YJ_{110}	J_{125}	JH_{140}	H_{160}
21	20.5 ± 0.0039	20.3 ± 0.0039	20.3 ± 0.0035	20.1 ± 0.0028	20.0 ± 0.0044
25	20.0 ± 0.1749	19.9 ± 0.7321	19.9 ± 0.1774	19.8 ± 0.1822	19.6 ± 0.2743
26	19.2 ± 0.0007	19.2 ± 0.0006	19.2 ± 0.0005	18.9 ± 0.0006	18.7 ± 8.0
30	22.4 ± 0.0018	22.4 ± 0.0012	22.3 ± 0.0011	22.2 ± 0.0011	22.1 ± 0.0
31	20.4 ± 0.0008	20.3 ± 0.0008	20.1 ± 0.0128	19.9 ± 0.0892	20.0 ± 0.0011
33	20.5 ± 0.0001	20.4 ± 0.0001	20.3 ± 0.0001	20.2 ± 0.0001	20.0 ± 1.848
38	21.4 ± 0.0005	21.3 ± 0.0003	21.2 ± 0.0002	21.1 ± 0.0002	21.0 ± 3.35
43	22.0 ± 0.0028	21.9 ± 0.0022	21.9 ± 0.0022	21.7 ± 0.0019	21.6 ± 0.0026
45	19.5 ± 0.0	19.3 ± 0.0	19.2 ± 0.0	19.1 ± 0.0	18.9 ± 3.354
50	20.0 ± 0.0005	19.9 ± 0.0003	19.8 ± 0.0003	19.6 ± 0.0006	19.4 ± 0.0015
53	20.1 ± 0.0001	20.0 ± 0.0001	19.9 ± 0.0001	19.7 ± 0.0001	19.6 ± 1.3645
54	21.2 ± 0.0006	21.1 ± 0.0005	21.0 ± 0.0004	20.9 ± 0.0005	20.8 ± 8.3619
55	21.8 ± 0.0179	21.7 ± 0.0181	21.7 ± 0.0185	21.7 ± 0.0168	21.7 ± 0.0137
57	20.3 ± 0.0002	20.2 ± 0.0004	20.1 ± 0.0004	19.9 ± 0.0003	19.7 ± 3.06
63	20.0 ± 0.0005	19.9 ± 0.0006	19.8 ± 0.0006	19.6 ± 0.0004	19.5 ± 3.81
65	19.2 ± 0.0002	19.1 ± 0.0	19.0 ± 0.0	18.8 ± 0.0002	18.7 ± 3.8695
66	18.0 ± 0.0001	17.9 ± 0.0008	17.7 ± 0.0011	17.6 ± 0.0002	17.5 ± 8.0
68	21.0 ± 0.0002	20.9 ± 0.0002	20.8 ± 0.0002	20.7 ± 0.0002	20.5 ± 4.0
70	19.9 ± 0.0001	19.8 ± 0.0001	19.7 ± 0.0	19.6 ± 0.0	19.4 ± 5.0
71	20.9 ± 0.0012	20.8 ± 0.001	20.8 ± 0.001	20.6 ± 0.0011	20.4 ± 0.0
85	18.8 ± 0.003	18.7 ± 0.0026	18.6 ± 0.0024	18.4 ± 0.0026	18.2 ± 0.0
87	19.2 ± 0.0002	19.1 ± 0.0003	19.0 ± 0.0003	18.8 ± 0.0004	18.7 ± 4.05
88	19.3 ± 0.0008	19.2 ± 0.001	19.1 ± 0.0013	18.9 ± 0.0021	18.8 ± 0.0
93	21.3 ± 0.0	21.1 ± 0.0	21 ± 0.0	20.9 ± 0.0	20.7 ± 6.2
94	19.8 ± 0.0003	19.7 ± 0.0003	19.6 ± 0.0003	19.4 ± 0.0003	19.3 ± 3.7
95	21.5 ± 0.0002	21.4 ± 0.0004	21.3 ± 0.0007	21.2 ± 0.0008	21.0 ± 2.0
96	19.5 ± 0.0035	19.4 ± 0.0044	19.3 ± 0.1181	19.3 ± 1.128	19.0 ± 0.0072
98	21.5 ± 0.0008	21.4 ± 0.0004	21.3 ± 0.0002	21.2 ± 0.0007	21.1 ± 7.6235
102	20.9 ± 0.0053	20.9 ± 0.0039	20.7 ± 0.0042	20.6 ± 0.0036	20.5 ± 0.0052
103	20.2 ± 0.0002	20.1 ± 0.0001	20.0 ± 0.0001	19.9 ± 0.0001	19.8 ± 1.0
104	19.1 ± 0.0001	19.0 ± 0.0001	18.9 ± 0.0	18.8 ± 0.0002	18.7 ± 5.37
105	20.0 ± 0.0057	19.9 ± 0.0043	20.0 ± 0.0299	20.2 ± 0.2371	19.5 ± 0.0102
107	19.2 ± 0.0001	19.1 ± 0.0001	19.0 ± 0.0001	18.8 ± 0.0001	18.7 ± 4.0
109	19.5 ± 0.0006	19.4 ± 0.0004	19.3 ± 0.0004	19.1 ± 0.0009	19.0 ± 0.0018
113	19.5 ± 0.0023	19.4 ± 0.0021	19.2 ± 0.0071	18.1 ± 0.0291	18.8 ± 0.0
115	20.0 ± 0.007	19.0 ± 0.049	19.7 ± 0.0055	19.5 ± 0.0046	19.4 ± 0.0079
133	20.3 ± 0.0175	20.1 ± 0.0674	20.0 ± 0.018	19.8 ± 0.0217	19.6 ± 0.0323
154	21.9 ± 0.0003	21.8 ± 0.0002	21.7 ± 0.0001	21.6 ± 0.0002	21.4 ± 0.0007

Table C.9.: r_e assessments in the ACS bands for the fitted early-type galaxies in MACS 0416. To calculate the values in kpc the cosmological parameters $H_0 = 70$ km s^{-1} Mpc $^{-1}$, $\Omega_\Lambda = 0.7$ and $\Omega_M = 0.3$ have been adopted with a pixelscale of 0.065"/px and a cluster redshift $z \sim 0.397$.

ID	MACS 0416 ACS r_e [kpc]						
	B_{435}	g_{475}	V_{606}	r_{625}	i_{775}	I_{814}	z_{850}
21	2.6 ± 0.0898	2.6 ± 0.0801	2.4 ± 0.0585	2.4 ± 0.0517	2.2 ± 0.0318	2.2 ± 0.0258	2.1 ± 0.0173
25	2.8 ± 0.8873	2.7 ± 0.7813	2.4 ± 0.5513	2.3 ± 0.4807	2.0 ± 0.2862	1.9 ± 0.2352	1.8 ± 0.1801
26	7.9 ± 0.0348	7.5 ± 0.0313	6.5 ± 0.0234	6.2 ± 0.0208	5.2 ± 0.0131	4.9 ± 0.0106	4.3 ± 0.0065
30	1.8 ± 0.0205	1.8 ± 0.0181	1.7 ± 0.013	1.7 ± 0.0114	1.7 ± 0.0068	1.6 ± 0.0055	1.6 ± 0.0037
31	3.0 ± 0.024	2.8 ± 0.0214	2.5 ± 0.0155	2.4 ± 0.0136	2.1 ± 0.0079	2.0 ± 0.0061	1.8 ± 0.0032
33	1.9 ± 0.0038	1.9 ± 0.0033	1.8 ± 0.0024	1.8 ± 0.0021	1.7 ± 0.0012	1.7 ± 0.001	1.6 ± 0.0006
38	1.4 ± 0.0062	1.4 ± 0.0056	1.3 ± 0.0042	1.3 ± 0.0038	1.2 ± 0.0025	1.2 ± 0.0021	1.2 ± 0.0014
43	1.8 ± 0.0272	1.7 ± 0.0243	1.6 ± 0.0179	1.6 ± 0.0158	1.5 ± 0.0097	1.4 ± 0.0079	1.4 ± 0.005
45	3.1 ± 0.0056	3.0 ± 0.005	2.8 ± 0.0036	2.8 ± 0.0031	2.6 ± 0.0019	2.5 ± 0.0015	2.4 ± 0.0009
50	2.9 ± 0.037	2.8 ± 0.0326	2.4 ± 0.023	2.3 ± 0.02	1.9 ± 0.0117	1.8 ± 0.0093	1.6 ± 0.0064
53	2.5 ± 0.0036	2.4 ± 0.0032	2.2 ± 0.0025	2.1 ± 0.0022	1.9 ± 0.0014	1.8 ± 0.0012	1.7 ± 0.0007
54	2.2 ± 0.0151	2.1 ± 0.0139	2.0 ± 0.0112	1.9 ± 0.0103	1.8 ± 0.0074	1.7 ± 0.0064	1.6 ± 0.0047
55	6.6 ± 0.9888	6.6 ± 0.8939	6.7 ± 0.6812	6.7 ± 0.6127	6.6 ± 0.405	6.5 ± 0.3378	6.2 ± 0.2312
57	2.4 ± 0.0112	2.3 ± 0.0099	2.0 ± 0.007	2.0 ± 0.0061	1.8 ± 0.0034	1.7 ± 0.0027	1.6 ± 0.0017
63	3.4 ± 0.0184	3.2 ± 0.0164	2.9 ± 0.012	2.8 ± 0.0106	2.6 ± 0.0065	2.5 ± 0.0051	2.3 ± 0.0032
65	3.4 ± 0.0054	3.3 ± 0.0049	3.1 ± 0.0036	3.0 ± 0.0032	2.8 ± 0.002	2.7 ± 0.0016	2.6 ± 0.0011
66	4.0 ± 0.0174	4.8 ± 0.0152	6.7 ± 0.012	7.2 ± 0.0115	9.0 ± 0.0116	9.6 ± 0.012	10.6 ± 0.0125
68	2.4 ± 0.0121	2.3 ± 0.0109	2.2 ± 0.0082	2.1 ± 0.0073	2.0 ± 0.0048	2.0 ± 0.0039	1.9 ± 0.0027
70	2.2 ± 0.0027	2.1 ± 0.0024	2.0 ± 0.0018	1.9 ± 0.0016	1.7 ± 0.001	1.7 ± 0.0008	1.6 ± 0.0005
71	1.9 ± 0.0533	1.8 ± 0.0473	1.6 ± 0.0341	1.6 ± 0.0299	1.4 ± 0.0179	1.4 ± 0.0143	1.3 ± 0.0092
85	6.7 ± 0.0458	6.4 ± 0.0406	5.7 ± 0.0291	5.4 ± 0.0256	4.9 ± 0.0154	4.7 ± 0.0125	4.5 ± 0.0087

ID	MACS 0416 ACS r_e [kpc] cont.						
	B_{435}	g_{475}	V_{606}	r_{625}	i_{775}	I_{814}	z_{850}
87	3.9 ± 0.0229	3.7 ± 0.0205	3.4 ± 0.0151	3.3 ± 0.0134	3.0 ± 0.0082	2.9 ± 0.0066	2.8 ± 0.0041
88	4.4 ± 0.044	4.3 ± 0.0396	4.0 ± 0.0298	3.9 ± 0.0267	3.6 ± 0.0172	3.5 ± 0.0142	3.3 ± 0.0095
93	1.0 ± 0.0003	1.0 ± 0.0003	0.9 ± 0.0002	0.9 ± 0.0002	0.8 ± 0.0001	0.7 ± 0.0001	0.7 ± 0.0001
94	4.8 ± 0.0173	4.6 ± 0.0154	4.3 ± 0.0114	4.1 ± 0.0101	3.7 ± 0.0061	3.6 ± 0.0048	3.4 ± 0.0028
95	2.8 ± 0.0117	2.7 ± 0.0104	2.4 ± 0.0074	2.4 ± 0.0064	2.2 ± 0.0036	2.1 ± 0.0027	2.0 ± 0.0014
96	5.2 ± 0.1297	5.0 ± 0.1157	4.4 ± 0.0844	4.2 ± 0.0744	3.6 ± 0.0445	3.4 ± 0.0351	3.1 ± 0.0211
98	1.6 ± 0.0263	1.7 ± 0.0218	1.9 ± 0.0127	2.0 ± 0.0104	2.2 ± 0.0073	2.3 ± 0.0079	2.4 ± 0.0093
102	3.5 ± 0.0899	3.5 ± 0.0804	3.4 ± 0.0592	3.3 ± 0.0525	3.2 ± 0.0325	3.2 ± 0.0263	3.2 ± 0.017
103	4.8 ± 0.0435	4.6 ± 0.039	4.1 ± 0.0289	3.9 ± 0.0256	3.5 ± 0.0158	3.3 ± 0.0126	3.1 ± 0.0076
104	6.7 ± 0.0095	6.5 ± 0.0082	5.9 ± 0.0053	5.7 ± 0.0045	5.2 ± 0.0022	5.0 ± 0.0017	4.6 ± 0.0014
105	2.2 ± 0.0453	2.1 ± 0.0401	2.1 ± 0.0287	2.1 ± 0.0251	2.1 ± 0.0148	2.1 ± 0.0118	2.0 ± 0.0081
107	3.8 ± 0.0048	3.7 ± 0.0043	3.5 ± 0.0033	3.4 ± 0.0029	3.2 ± 0.002	3.1 ± 0.0016	3.0 ± 0.0011
109	5.0 ± 0.0343	4.9 ± 0.0306	4.4 ± 0.0225	4.3 ± 0.0198	3.9 ± 0.0119	3.7 ± 0.0094	3.5 ± 0.0055
113	3.8 ± 0.0862	3.7 ± 0.0764	3.3 ± 0.0548	3.2 ± 0.048	2.9 ± 0.0278	2.8 ± 0.0217	2.7 ± 0.0132
115	2.6 ± 0.1185	2.5 ± 0.1052	2.3 ± 0.076	2.3 ± 0.0668	2.1 ± 0.0408	2.1 ± 0.0333	2.0 ± 0.0232
133	1.9 ± 0.1281	1.9 ± 0.1088	1.7 ± 0.0683	1.7 ± 0.0565	1.6 ± 0.0291	1.6 ± 0.026	1.5 ± 0.0284
154	0.9 ± 0.0028	0.9 ± 0.0025	0.8 ± 0.0018	0.7 ± 0.0016	0.6 ± 0.001	0.6 ± 0.0007	0.5 ± 0.0004

Table C.10.: r_e assessments in the WFC3/IR bands for the fitted early-type galaxies in MACS 0416. To calculate the values in kpc the cosmological parameters $H_0 = 70$ km s^{-1} Mpc $^{-1}$, $\Omega_\Lambda = 0.7$ and $\Omega_M = 0.3$ have been adopted with a pixelscale of 0.065"/px and a cluster redshift $z \sim 0.397$.

ID	MACS 0416 WFC3/IR r_e [kpc]				
	Y_{105}	YJ_{110}	J_{125}	JH_{140}	H_{160}
21	2.0 ± 0.013	2.0 ± 0.0116	2.0 ± 0.0108	2.0 ± 0.0098	2.0 ± 0.014
25	1.6 ± 0.1687	1.5 ± 0.1691	1.5 ± 0.1675	1.5 ± 0.1784	1.5 ± 0.2641
26	3.9 ± 0.0037	3.7 ± 0.0024	3.6 ± 0.0022	3.6 ± 0.0023	3.8 ± 0.003
30	1.6 ± 0.0029	1.6 ± 0.0027	1.6 ± 0.0025	1.6 ± 0.0026	1.6 ± 0.0045
31	1.6 ± 0.0017	1.5 ± 0.0018	1.5 ± 0.002	1.4 ± 0.0018	1.4 ± 0.0016
33	1.6 ± 0.0005	1.6 ± 0.0004	1.5 ± 0.0004	1.5 ± 0.0004	1.5 ± 0.0003
38	1.2 ± 0.0009	1.1 ± 0.0007	1.1 ± 0.0006	1.1 ± 0.0007	1.1 ± 0.001
43	1.3 ± 0.0035	1.3 ± 0.0029	1.3 ± 0.0027	1.3 ± 0.0026	1.3 ± 0.0038
45	2.3 ± 0.0006	2.2 ± 0.0006	2.2 ± 0.0005	2.2 ± 0.0004	2.3 ± 0.0007
50	1.5 ± 0.0053	1.5 ± 0.0051	1.4 ± 0.0051	1.5 ± 0.0067	1.6 ± 0.012
53	1.6 ± 0.0004	1.5 ± 0.0003	1.4 ± 0.0002	1.4 ± 0.0003	1.4 ± 0.0003
54	1.5 ± 0.0032	1.5 ± 0.0022	1.4 ± 0.0015	1.4 ± 0.0011	1.4 ± 0.0014
55	5.9 ± 0.1586	5.6 ± 0.1206	5.2 ± 0.0997	4.5 ± 0.0741	3.6 ± 0.0577
57	1.6 ± 0.0014	1.5 ± 0.0015	1.6 ± 0.0015	1.6 ± 0.0018	1.8 ± 0.0029
63	2.2 ± 0.002	2.1 ± 0.0016	2.1 ± 0.0015	2.1 ± 0.0013	2.2 ± 0.0022
65	2.5 ± 0.0007	2.4 ± 0.0006	2.3 ± 0.0005	2.3 ± 0.0005	2.3 ± 0.0003
66	11.3 ± 0.0125	11.7 ± 0.012	11.9 ± 0.0114	11.8 ± 0.012	11.4 ± 0.0164
68	1.8 ± 0.0018	1.8 ± 0.0014	1.8 ± 0.0012	1.7 ± 0.0011	1.7 ± 0.0017
70	1.5 ± 0.0003	1.5 ± 0.0002	1.4 ± 0.0002	1.4 ± 0.0002	1.4 ± 2.489
71	1.2 ± 0.0069	1.2 ± 0.0064	1.1 ± 0.0063	1.1 ± 0.0073	1.2 ± 0.0122
85	4.4 ± 0.007	4.5 ± 0.0066	4.7 ± 0.0066	5.2 ± 0.0085	6.0 ± 0.0144
87	2.6 ± 0.0027	2.5 ± 0.0022	2.5 ± 0.0021	2.4 ± 0.0019	2.4 ± 0.0026
88	3.2 ± 0.0065	3.1 ± 0.0051	3.0 ± 0.0046	3.0 ± 0.0048	3.0 ± 0.0068
93	0.6 ± 0.0	0.6 ± 0.0	0.6 ± 0.0	0.6 ± 0.0	0.6 ± 0.4806
94	3.2 ± 0.0019	3.1 ± 0.0021	3.0 ± 0.0026	3.0 ± 0.0032	3.1 ± 0.0037
95	1.9 ± 0.0011	1.8 ± 0.0014	1.8 ± 0.0016	1.8 ± 0.0016	1.9 ± 0.0014
96	2.9 ± 0.0141	2.7 ± 0.0134	2.7 ± 0.014	2.6 ± 0.0135	2.8 ± 0.0146
98	2.5 ± 0.0095	2.6 ± 0.0082	2.6 ± 0.0059	2.6 ± 0.0052	2.6 ± 0.0148
102	3.1 ± 0.0117	3.1 ± 0.0099	3.1 ± 0.0093	3.1 ± 0.009	3.2 ± 0.013
103	2.9 ± 0.0044	2.8 ± 0.0032	2.7 ± 0.003	2.7 ± 0.0027	2.8 ± 0.0037
104	4.3 ± 0.0014	4.1 ± 0.0013	4.0 ± 0.0009	3.8 ± 0.0013	3.8 ± 0.0036
105	2.0 ± 0.0072	2.0 ± 0.0075	2.0 ± 0.0077	2.0 ± 0.008	2.0 ± 0.0103
107	2.9 ± 0.0007	2.8 ± 0.0006	2.8 ± 0.0005	2.7 ± 0.0004	2.7 ± 0.0006
109	3.3 ± 0.0035	3.2 ± 0.0033	3.1 ± 0.0036	3.0 ± 0.0037	3.0 ± 0.0036

ID	MACS 0416 WFC3/IR r_e [kpc] cont.				
	Y_{105}	YJ_{110}	J_{125}	JH_{140}	H_{160}
113	2.6 ± 0.0103	2.5 ± 0.0108	2.5 ± 0.0115	2.5 ± 0.0112	2.6 ± 0.0132
115	2.0 ± 0.0186	1.9 ± 0.0166	1.9 ± 0.0148	1.9 ± 0.0134	2.0 ± 0.0229
133	1.5 ± 0.0319	1.5 ± 0.0325	1.6 ± 0.0323	1.6 ± 0.0415	1.8 ± 0.0726
154	0.5 ± 0.0003	0.4 ± 0.0002	0.4 ± 0.0002	0.4 ± 0.0002	0.5 ± 3.3667

Table C.11.: Measurements of n in the ACS bands for the selected early-type galaxies in MACS 0416.

ID	MACS 0416 ACS Sérsic n						
	B_{435}	g_{475}	V_{606}	r_{625}	i_{775}	I_{814}	z_{850}
21	5.5 ± 0.1398	5.3 ± 0.1244	4.7 ± 0.0905	4.5 ± 0.08	3.9 ± 0.0496	3.7 ± 0.0408	3.4 ± 0.029
25	6.4 ± 1.7148	6.0 ± 1.4384	5.3 ± 0.87	5.0 ± 0.7131	4.3 ± 0.4355	4.0 ± 0.4454	3.6 ± 0.5226
26	8.0 ± 0.0153	7.6 ± 0.0139	6.6 ± 0.0106	6.3 ± 0.0095	5.3 ± 0.0063	5.0 ± 0.0053	4.5 ± 0.0036
30	3.2 ± 0.0335	3.1 ± 0.0291	2.9 ± 0.0198	2.8 ± 0.017	2.6 ± 0.0096	2.6 ± 0.008	2.5 ± 0.0067
31	8.0 ± 0.0447	7.6 ± 0.0397	6.5 ± 0.0287	6.2 ± 0.0252	5.2 ± 0.0149	4.9 ± 0.0117	4.3 ± 0.0072
33	6.2 ± 0.0074	5.9 ± 0.0065	5.3 ± 0.0047	5.1 ± 0.0041	4.5 ± 0.0025	4.3 ± 0.002	4.1 ± 0.0015
38	4.6 ± 0.0141	4.4 ± 0.0127	3.9 ± 0.0097	3.8 ± 0.0087	3.4 ± 0.0058	3.3 ± 0.0048	3.1 ± 0.0034
43	3.4 ± 0.06	3.3 ± 0.0523	3.1 ± 0.0359	3.0 ± 0.031	2.7 ± 0.018	2.7 ± 0.015	2.6 ± 0.0125
45	4.7 ± 0.006	4.6 ± 0.0054	4.2 ± 0.0039	4.0 ± 0.0034	3.6 ± 0.002	3.5 ± 0.0016	3.3 ± 0.0011
50	8.0 ± 0.064	7.4 ± 0.056	6.2 ± 0.0391	5.9 ± 0.034	4.8 ± 0.0203	4.4 ± 0.0168	3.9 ± 0.0131
53	5.2 ± 0.0044	4.9 ± 0.0041	4.2 ± 0.0032	4.0 ± 0.0029	3.4 ± 0.002	3.2 ± 0.0017	2.9 ± 0.0012
54	7.8 ± 0.0576	7.4 ± 0.0494	6.5 ± 0.0318	6.2 ± 0.0265	5.3 ± 0.0128	5.1 ± 0.0103	4.6 ± 0.0105
55	4.3 ± 0.362	4.5 ± 0.3289	4.9 ± 0.255	5.0 ± 0.2313	5.3 ± 0.1603	5.4 ± 0.1375	5.4 ± 0.1017
57	7.4 ± 0.0228	7.1 ± 0.02	6.5 ± 0.0139	6.3 ± 0.0121	5.7 ± 0.0068	5.6 ± 0.0054	5.4 ± 0.004
63	5.6 ± 0.0182	5.3 ± 0.0162	4.6 ± 0.0118	4.4 ± 0.0105	3.8 ± 0.0065	3.6 ± 0.0053	3.3 ± 0.0036
65	4.3 ± 0.0053	4.2 ± 0.0048	4.0 ± 0.0036	3.9 ± 0.0032	3.7 ± 0.0021	3.6 ± 0.0018	3.5 ± 0.0013
66	3.2 ± 0.0062	3.7 ± 0.0055	4.8 ± 0.0043	5.1 ± 0.004	6.2 ± 0.0036	6.6 ± 0.0035	7.2 ± 0.0035
68	3.6 ± 0.0141	3.5 ± 0.0125	3.2 ± 0.009	3.2 ± 0.0079	2.9 ± 0.0048	2.8 ± 0.004	2.7 ± 0.003
70	4.7 ± 0.0038	4.4 ± 0.0034	3.9 ± 0.0026	3.8 ± 0.0023	3.3 ± 0.0016	3.1 ± 0.0013	2.8 ± 0.0009
71	4.9 ± 0.1268	4.6 ± 0.112	4.0 ± 0.0799	3.8 ± 0.07	3.2 ± 0.0423	3.0 ± 0.0345	2.7 ± 0.0248
85	7.2 ± 0.0265	7.0 ± 0.0231	6.6 ± 0.016	6.4 ± 0.0139	6.2 ± 0.0084	6.1 ± 0.0071	6.1 ± 0.0059
87	3.8 ± 0.0202	3.7 ± 0.0181	3.4 ± 0.0134	3.4 ± 0.012	3.1 ± 0.0077	3.0 ± 0.0064	2.9 ± 0.0045
88	7.0 ± 0.0368	6.8 ± 0.0332	6.4 ± 0.0251	6.2 ± 0.0225	5.8 ± 0.0149	5.6 ± 0.0125	5.4 ± 0.0088

ID	MACS 0416 ACS Sérsic n cont.						
	B_{435}	g_{475}	V_{606}	r_{625}	i_{775}	I_{814}	z_{850}
93	6.6 ± 0.0012	6.1 ± 0.0011	5.2 ± 0.0009	4.8 ± 0.0008	3.9 ± 0.0006	3.6 ± 0.0005	3.2 ± 0.0004
94	7.7 ± 0.0142	7.5 ± 0.0126	7.0 ± 0.009	6.8 ± 0.0078	6.4 ± 0.0045	6.2 ± 0.0035	6.0 ± 0.0024
95	4.1 ± 0.0133	3.9 ± 0.0117	3.4 ± 0.0083	3.3 ± 0.0072	2.8 ± 0.004	2.6 ± 0.003	2.4 ± 0.0018
96	8.0 ± 0.1075	7.6 ± 0.0961	6.8 ± 0.0707	6.6 ± 0.0627	5.8 ± 0.0392	5.6 ± 0.0321	5.2 ± 0.0223
98	2.3 ± 0.0379	2.4 ± 0.0315	2.5 ± 0.0188	2.6 ± 0.0155	2.8 ± 0.0108	2.8 ± 0.0113	2.9 ± 0.0127
102	3.0 ± 0.0606	2.9 ± 0.0542	2.8 ± 0.0399	2.7 ± 0.0354	2.6 ± 0.0222	2.5 ± 0.0181	2.5 ± 0.0123
103	5.2 ± 0.0341	5.0 ± 0.0306	4.3 ± 0.0229	4.1 ± 0.0204	3.5 ± 0.013	3.3 ± 0.0106	2.9 ± 0.007
104	6.3 ± 0.0062	6.1 ± 0.0053	5.7 ± 0.0033	5.6 ± 0.0028	5.2 ± 0.0016	5.0 ± 0.0015	4.8 ± 0.0016
105	4.5 ± 0.0808	4.4 ± 0.0712	4.2 ± 0.0504	4.2 ± 0.044	4.1 ± 0.0261	4.1 ± 0.0213	4.1 ± 0.0163
107	3.5 ± 0.0038	3.4 ± 0.0034	3.4 ± 0.0025	3.4 ± 0.0022	3.3 ± 0.0014	3.3 ± 0.0012	3.3 ± 0.0009
109	6.3 ± 0.0272	6.1 ± 0.0243	5.8 ± 0.0178	5.6 ± 0.0157	5.2 ± 0.0096	5.1 ± 0.0077	4.9 ± 0.005
113	8.0 ± 0.0978	7.5 ± 0.0866	6.4 ± 0.062	6.0 ± 0.0542	5.0 ± 0.0318	4.7 ± 0.0252	4.3 ± 0.0169
115	6.8 ± 0.2237	6.5 ± 0.1975	5.7 ± 0.1407	5.4 ± 0.1232	4.7 ± 0.0747	4.5 ± 0.0616	4.2 ± 0.0461
133	6.2 ± 0.3148	5.9 ± 0.2663	5.2 ± 0.1644	5.0 ± 0.1347	4.3 ± 0.0691	4.1 ± 0.064	3.9 ± 0.0744
154	6.0 ± 0.0261	5.7 ± 0.0224	5.2 ± 0.0148	5.0 ± 0.0126	4.4 ± 0.0077	4.3 ± 0.007	4.0 ± 0.0068

Table C.12.: Measurements of n in the WFC3/IR bands for the selected early-type galaxies in MACS 0416.

ID	MACS 0416 WFC3/IR Sérsic n				
	Y_{105}	YJ_{110}	J_{125}	JH_{140}	H_{160}
21	3.2 ± 0.0237	3.1 ± 0.0221	3.0 ± 0.021	3.0 ± 0.0202	3.1 ± 0.028
25	3.3 ± 0.5588	3.2 ± 0.5262	3.1 ± 0.4549	3.0 ± 0.479	3.2 ± 0.9391
26	4.1 ± 0.0025	3.9 ± 0.002	3.8 ± 0.0018	3.8 ± 0.0019	4.0 ± 0.0024
30	2.4 ± 0.0067	2.4 ± 0.0065	2.5 ± 0.0057	2.5 ± 0.0053	2.7 ± 0.01
31	3.9 ± 0.0054	3.7 ± 0.0054	3.6 ± 0.0057	3.6 ± 0.0056	3.8 ± 0.0067
33	3.9 ± 0.0012	3.8 ± 0.0011	3.9 ± 0.001	4.0 ± 0.0011	4.4 ± 0.0
38	3.0 ± 0.0025	3.0 ± 0.0021	3.1 ± 0.0021	3.3 ± 0.0025	3.7 ± 0.0036
43	2.5 ± 0.0122	2.5 ± 0.0116	2.5 ± 0.0101	2.5 ± 0.0086	2.7 ± 0.0164
45	3.2 ± 0.0009	3.1 ± 0.0008	3.0 ± 0.0008	3.1 ± 0.0007	3.2 ± 0.001
50	3.7 ± 0.0122	3.6 ± 0.0124	3.7 ± 0.0136	4.2 ± 0.0197	5.0 ± 0.0327
53	2.6 ± 0.0007	2.5 ± 0.0005	2.5 ± 0.0005	2.6 ± 0.0008	2.8 ± 0.001
54	4.2 ± 0.0123	4.0 ± 0.0126	3.9 ± 0.0111	3.8 ± 0.0068	4.0 ± 0.0124
55	5.4 ± 0.077	5.2 ± 0.0628	4.9 ± 0.054	4.3 ± 0.0464	3.5 ± 0.0507
57	5.3 ± 0.0038	5.3 ± 0.004	5.5 ± 0.0042	5.9 ± 0.0051	6.5 ± 0.0078
63	3.0 ± 0.0027	2.9 ± 0.0023	2.8 ± 0.0021	2.8 ± 0.0019	3.0 ± 0.0
65	3.5 ± 0.001	3.5 ± 0.0009	3.5 ± 0.0008	3.5 ± 0.0009	3.6 ± 0.0013
66	7.6 ± 0.0035	7.9 ± 0.0033	8.0 ± 0.0032	8.0 ± 0.0034	7.7 ± 0.004
68	2.6 ± 0.0025	2.6 ± 0.0023	2.5 ± 0.002	2.5 ± 0.0019	2.6 ± 0.0033
70	2.6 ± 0.0006	2.5 ± 0.0005	2.5 ± 0.0004	2.5 ± 0.0005	2.6 ± 6.5
71	2.6 ± 0.0213	2.5 ± 0.0209	2.5 ± 0.0217	2.7 ± 0.0277	3.1 ± 0.0446
85	6.2 ± 0.0056	6.4 ± 0.0054	6.7 ± 0.0051	7.2 ± 0.0058	8.0 ± 0.01
87	2.8 ± 0.0035	2.7 ± 0.0031	2.7 ± 0.0029	2.8 ± 0.0032	2.9 ± 0.004
88	5.2 ± 0.0066	5.1 ± 0.0056	5.1 ± 0.0054	5.1 ± 0.0061	5.3 ± 0.0086
93	2.9 ± 0.0003	2.7 ± 0.0002	2.7 ± 0.0002	2.9 ± 0.0002	3.4 ± 2.0
94	5.9 ± 0.0023	5.8 ± 0.0027	5.8 ± 0.003	5.9 ± 0.0034	6.2 ± 0.0041
95	2.2 ± 0.0017	2.0 ± 0.002	2.0 ± 0.0023	2.0 ± 0.0023	2.1 ± 0.0024
96	4.9 ± 0.0179	4.8 ± 0.0172	4.7 ± 0.0176	4.8 ± 0.0188	5.1 ± 0.0236
98	3.1 ± 0.0126	3.2 ± 0.0108	3.2 ± 0.0084	3.4 ± 0.0118	3.5 ± 0.0266
102	2.4 ± 0.0091	2.4 ± 0.0079	2.4 ± 0.0075	2.5 ± 0.0076	2.6 ± 0.0112
103	2.6 ± 0.0048	2.5 ± 0.0039	2.3 ± 0.0035	2.3 ± 0.0035	2.3 ± 0.0048
104	4.6 ± 0.0016	4.5 ± 0.0013	4.4 ± 0.001	4.3 ± 0.0014	4.3 ± 0.0
105	4.3 ± 0.0159	4.4 ± 0.0172	4.6 ± 0.0187	5.0 ± 0.0225	5.5 ± 0.0311
107	3.3 ± 0.0007	3.4 ± 0.0007	3.4 ± 0.0006	3.5 ± 0.0006	3.6 ± 9.3
109	4.7 ± 0.0039	4.5 ± 0.004	4.4 ± 0.0043	4.3 ± 0.0047	4.3 ± 0.0054
113	4.1 ± 0.0147	4.1 ± 0.0155	4.2 ± 0.0166	4.6 ± 0.0184	5.4 ± 0.0245
115	4.0 ± 0.0407	4.0 ± 0.0387	4.1 ± 0.0364	4.5 ± 0.0372	5.1 ± 0.0598
133	3.8 ± 0.0849	3.8 ± 0.0871	3.9 ± 0.0876	4.3 ± 0.1122	4.9 ± 0.1917
154	3.8 ± 0.0067	3.6 ± 0.006	3.6 ± 0.0046	3.6 ± 0.0045	3.7 ± 0.0108

D. Gradient results

Table C.13.: Color gradients of the early-type galaxy sample of MACS 1206.

	$\nabla(g_{475} - I_{814})$ [mag dex^{-1}]		$\nabla(r_{625} - Y_{105})$ [mag dex^{-1}]		$\nabla(I_{814} - H_{160})$ [mag dex^{-1}]		$\nabla(Y_{105} - H_{160})$ [mag dex^{-1}]	
ID	fitted	calculated	fitted	calculated	fitted	calculated	fitted	calculated
1	-0.20	-0.07	-0.22	-0.14	-0.11	-0.10	-0.03	-0.02
3	-0.18	-0.13	-0.21	-0.18	-0.29	-0.28	-0.18	-0.18
4	-0.08	-0.09	-0.06	-0.07	0.00	-0.02	0.02	0.01
5	-0.13	-0.08	-0.13	-0.10	-0.08	-0.08	-0.03	-0.03
6	-0.18	-0.14	-0.17	-0.15	-0.07	-0.07	0.00	0.00
8	0.01	0.05	0.00	0.04	-0.05	-0.01	-0.04	-0.03
10	-0.18	-0.13	-0.20	-0.17	-0.16	-0.16	-0.08	-0.07
11	-0.24	-0.14	-0.25	-0.18	-0.11	-0.10	0.01	0.00
12	0.02	0.01	0.00	-0.01	-0.09	-0.08	-0.08	-0.07
15	-0.18	-0.15	-0.22	-0.18	-0.38	-0.34	-0.23	-0.24
17	-0.12	-0.11	-0.11	-0.11	-0.07	-0.08	-0.02	-0.03
19	-0.19	-0.08	-0.22	-0.14	-0.18	-0.16	-0.06	-0.08
20	-0.19	-0.15	-0.10	-0.09	0.16	0.13	0.18	0.15
21	-0.20	-0.23	-0.17	-0.18	-0.12	-0.11	-0.05	-0.04
22	-0.14	-0.09	-0.15	-0.11	-0.08	-0.06	-0.01	-0.01
23	-0.15	-0.08	-0.18	-0.12	-0.17	-0.15	-0.08	-0.08
24	-0.29	-0.25	-0.33	-0.28	-0.64	-0.61	-0.29	-0.47
25	-0.12	-0.06	-0.16	-0.12	-0.20	-0.20	-0.13	-0.12
26	-0.12	-0.05	-0.16	-0.12	-0.30	-0.28	-0.21	-0.21
28	-0.19	-0.07	-0.23	-0.15	-0.13	-0.13	-0.03	-0.03
29	-0.20	-0.17	-0.20	-0.19	-0.13	-0.14	-0.05	-0.05
30	-0.26	-0.18	-0.26	-0.22	-0.12	-0.13	-0.02	-0.02
31	-0.10	-0.14	-0.07	-0.10	-0.01	-0.04	0.01	0.00
32	-0.17	-0.13	-0.16	-0.14	-0.09	-0.10	-0.02	-0.03
33	-0.13	-0.06	-0.16	-0.12	-0.18	-0.17	-0.10	-0.10
35	-0.18	-0.12	-0.21	-0.17	-0.25	-0.25	-0.15	-0.15
37	-0.10	-0.12	-0.13	-0.13	-0.36	-0.31	-0.27	-0.24
38	-0.28	-0.23	-0.31	-0.28	-0.31	-0.29	-0.11	-0.15
39	-0.16	-0.07	-0.22	-0.16	-0.28	-0.27	-0.16	-0.17
40	-0.24	-0.20	-0.26	-0.23	-0.19	-0.19	-0.08	-0.08
41	-0.15	-0.11	-0.18	-0.15	-0.21	-0.20	-0.12	-0.12
42	-0.09	-0.07	-0.10	-0.08	-0.13	-0.11	-0.07	-0.07
43	-0.23	-0.17	-0.21	-0.18	-0.08	-0.08	0.00	0.00
45	-0.13	-0.09	-0.14	-0.11	-0.11	-0.10	-0.05	-0.05
46	-0.22	-0.13	-0.25	-0.19	-0.20	-0.19	-0.09	-0.09

	$\nabla(g_{475} - I_{814})$ [mag dex^{-1}]		$\nabla(r_{625} - Y_{105})$ [mag dex^{-1}]		$\nabla(I_{814} - H_{160})$ [mag dex^{-1}]		$\nabla(Y_{105} - H_{160})$ [mag dex^{-1}]	
ID	fitted	calculated	fitted	calculated	fitted	calculated	fitted	calculated
47	-0.14	-0.12	-0.13	-0.12	-0.08	-0.07	-0.02	-0.02
48	-0.26	-0.21	-0.29	-0.25	-0.23	-0.22	-0.06	-0.09
50	-0.16	-0.14	-0.14	-0.13	-0.06	-0.06	0.00	-0.01
51	-0.18	-0.17	-0.18	-0.17	-0.10	-0.11	-0.03	-0.03
52	-0.15	-0.14	-0.13	-0.13	-0.03	-0.04	0.02	0.01
55	-0.20	-0.17	-0.18	-0.17	-0.06	-0.08	0.00	0.00
56	-0.23	-0.12	-0.27	-0.19	-0.18	-0.17	-0.06	-0.06
57	-0.13	-0.13	-0.11	-0.12	-0.08	-0.07	-0.03	-0.02
58	-0.29	-0.30	-0.28	-0.27	-0.34	-0.31	-0.16	-0.19
59	-0.17	-0.04	-0.20	-0.12	-0.18	-0.17	-0.10	-0.09
61	-0.22	-0.21	-0.19	-0.17	-0.05	-0.03	0.03	0.04
62	-0.29	-0.25	-0.30	-0.27	-0.25	-0.23	-0.09	-0.10
63	-0.12	-0.16	-0.10	-0.15	-0.30	-0.23	-0.25	-0.17
64	-0.11	-0.04	-0.13	-0.08	-0.11	-0.10	-0.05	-0.05
65	-0.20	-0.15	-0.26	-0.22	-0.34	-0.33	-0.17	-0.20
68	-0.27	-0.26	-0.25	-0.25	-0.11	-0.11	-0.01	-0.01
69	-0.25	-0.20	-0.25	-0.22	-0.07	-0.07	0.03	0.03
70	-0.16	-0.15	-0.10	-0.11	0.05	0.02	0.08	0.06
71	-0.17	-0.16	-0.18	-0.18	-0.16	-0.17	-0.08	-0.08
72	-0.14	-0.10	-0.17	-0.15	-0.22	-0.22	-0.13	-0.13
73	-0.18	-0.21	-0.16	-0.19	-0.13	-0.17	-0.06	-0.09
74	-0.21	0.05	-0.34	-0.18	-0.36	-0.35	-0.32	-0.18
76	-0.14	-0.06	-0.17	-0.12	-0.13	-0.13	-0.06	-0.06
77	0.05	0.06	0.05	0.06	0.02	0.03	0.00	0.01
80	-0.16	-0.11	-0.15	-0.13	-0.05	-0.06	0.00	0.00
81	-0.19	-0.10	-0.17	-0.12	-0.03	-0.02	0.04	0.04
82	-0.26	-0.15	-0.33	-0.26	-0.23	-0.23	-0.09	-0.07
83	-0.12	-0.05	-0.11	-0.08	-0.03	-0.03	0.01	0.01
84	-0.12	-0.11	-0.12	-0.11	-0.10	-0.09	-0.04	-0.04
85	-0.25	-0.23	-0.25	-0.22	-0.21	-0.18	-0.07	-0.07
87	-0.14	-0.13	-0.16	-0.14	-0.27	-0.24	-0.17	-0.16
88	-0.30	-0.31	-0.25	-0.25	-0.14	-0.11	-0.01	-0.01
89	-0.12	0.01	-0.14	-0.05	-0.14	-0.12	-0.07	-0.08
90	-0.15	-0.08	-0.18	-0.13	-0.22	-0.21	-0.13	-0.13
91	-0.01	0.09	-0.04	0.04	-0.17	-0.15	-0.15	-0.15
93	-0.16	-0.15	-0.18	-0.17	-0.26	-0.23	-0.15	-0.15
94	0.04	0.16	0.01	0.11	-0.22	-0.19	-0.23	-0.22
96	-0.12	-0.06	-0.15	-0.11	-0.22	-0.21	-0.15	-0.14

	$\nabla(g_{475} - I_{814})$ [mag dex^{-1}]		$\nabla(r_{625} - Y_{105})$ [mag dex^{-1}]		$\nabla(I_{814} - H_{160})$ [mag dex^{-1}]		$\nabla(Y_{105} - H_{160})$ [mag dex^{-1}]	
ID	fitted	calculated	fitted	calculated	fitted	calculated	fitted	calculated
97	-0.17	-0.11	-0.19	-0.15	-0.11	-0.10	-0.02	-0.02
98	-0.08	-0.07	-0.08	-0.08	-0.12	-0.11	-0.07	-0.07
99	-0.29	-0.14	-0.28	-0.18	0.08	0.08	0.19	0.17
100	-0.16	-0.11	-0.18	-0.14	-0.15	-0.15	-0.07	-0.07
101	-0.32	-0.32	-0.32	-0.31	-0.24	-0.24	-0.09	-0.09
104	-0.25	-0.22	-0.25	-0.22	-0.20	-0.18	-0.08	-0.08

Table C.14.: Color gradients of the early-type galaxy sample of MACS 0416.

	$\nabla(g_{475} - I_{814})$ [mag dex^{-1}]		$\nabla(r_{625} - Y_{105})$ [mag dex^{-1}]		$\nabla(I_{814} - H_{160})$ [mag dex^{-1}]		$\nabla(Y_{105} - H_{160})$ [mag dex^{-1}]	
ID	fitted	calculated	fitted	calculated	fitted	calculated	fitted	calculated
21	0.00	0.11	0.01	0.09	0.03	0.06	0.02	0.02
25	-0.15	0.00	-0.19	-0.08	-0.18	-0.17	-0.10	-0.10
26	-0.20	-0.05	-0.27	-0.17	-0.15	-0.15	-0.02	-0.03
30	-0.02	0.04	0.02	0.06	-0.03	-0.04	-0.07	-0.08
31	-0.12	0.02	-0.19	-0.08	-0.26	-0.25	-0.17	-0.18
33	0.07	0.14	0.04	0.10	-0.10	-0.10	-0.12	-0.13
38	0.05	0.13	0.01	0.06	-0.15	-0.16	-0.15	-0.17
43	-0.16	-0.06	-0.13	-0.08	-0.12	-0.11	-0.06	-0.06
45	-0.08	0.01	-0.09	-0.03	-0.05	-0.04	-0.02	-0.02
50	-0.17	0.02	-0.23	-0.11	-0.20	-0.20	-0.14	-0.09
53	-0.11	0.06	-0.16	-0.04	-0.30	-0.28	-0.23	-0.23
54	-0.03	0.07	-0.05	0.03	-0.11	-0.08	-0.08	-0.08
55	-0.12	-0.15	-0.14	-0.15	-0.50	-0.39	-0.38	-0.32
57	-0.12	-0.05	-0.12	-0.08	-0.04	-0.05	-0.01	-0.01
63	-0.10	0.04	-0.12	-0.02	-0.01	0.00	0.02	0.02
65	-0.15	-0.09	-0.18	-0.14	-0.22	-0.21	-0.12	-0.12
66	0.13	0.23	0.08	0.00	0.03	-0.02	0.00	0.00
68	-0.08	0.00	-0.09	-0.03	-0.12	-0.10	-0.06	-0.06
70	-0.07	0.06	-0.08	0.02	-0.15	-0.12	-0.11	-0.11
71	-0.13	0.04	-0.21	-0.10	-0.17	-0.17	-0.10	-0.07
85	-0.17	-0.12	-0.13	-0.12	0.02	0.00	0.06	0.05
87	-0.20	-0.10	-0.23	-0.16	-0.26	-0.25	-0.15	-0.14
88	-0.07	-0.02	-0.08	-0.05	-0.11	-0.10	-0.07	-0.07
93	-0.05	0.12	-0.16	-0.02	-0.23	-0.22	-0.19	-0.16
94	-0.11	-0.06	-0.14	-0.11	-0.12	-0.11	-0.06	-0.06
95	-0.11	0.06	-0.10	0.01	-0.05	-0.03	0.01	0.00
96	-0.17	-0.07	-0.21	-0.14	-0.15	-0.15	-0.07	-0.06
98	0.26	0.24	0.14	0.09	0.00	-0.08	-0.02	-0.07
102	-0.02	0.03	-0.01	0.02	-0.05	-0.05	-0.05	-0.06
103	-0.15	0.02	-0.18	-0.05	-0.03	-0.03	0.04	0.01
104	-0.14	-0.08	-0.18	-0.13	-0.20	-0.18	-0.09	-0.10
105	-0.01	0.01	-0.07	-0.07	-0.19	-0.24	-0.15	-0.18
107	-0.20	-0.17	-0.20	-0.17	-0.23	-0.23	-0.13	-0.14
109	-0.15	-0.09	-0.16	-0.12	-0.12	-0.10	-0.04	-0.04
113	-0.01	0.12	-0.05	0.03	-0.16	-0.17	-0.15	-0.14
115	0.02	0.11	-0.01	0.06	-0.10	-0.11	-0.11	-0.12
133	0.00	0.11	0.01	0.07	0.01	-0.02	0.00	-0.02
154	-0.30	-0.16	-0.32	-0.24	-0.23	-0.22	-0.07	-0.08

E. SSP results

Table C.15.: SSP results for the MACS 1206 sample in the $r_{625} - Y_{105}$ color. The first column contains the IDs of the galaxies. The ages for the populations located at the respective radii are derived by assuming a fixed solar metallicity. The metallicities are determined by fixing the age to 12 Gyr at $z = 0$.

ID	Age [Gyr]				Z [Log(Z/Z$_\odot$)]			
	$0.1r_e$	$0.5r_e$	$1r_e$	$2r_e$	$0.1r_e$	$0.5r_e$	$1r_e$	$2r_e$
1	10.2	13.0	12.0	7.1	0.0	0.2	0.0	-0.4
3	13.0	13.0	13.0	13.0	0.3	0.3	0.3	0.2
4	8.7	7.5	7.5	7.5	-0.1	-0.4	-0.4	-0.4
5	12.0	12.0	9.8	7.5	0.0	0.0	-0.1	-0.4
6	13.0	13.0	12.0	8.7	0.2	0.2	0.0	-0.1
8	9.8	13.0	13.0	12.0	-0.1	0.2	0.2	0
10	13.0	13.0	12.0	8.7	0.2	0.2	0.0	-0.4
11	10.2	12.0	8.7	6.6	-0.1	0.0	-0.4	-0.4
12	9.8	8.7	8.7	9.8	-0.1	-0.1	-0.1	-0.1
15	13.0	12.0	8.7	7.5	0.2	0.0	-0.1	-0.4
17	12.0	10.2	8.7	7.5	0.0	-0.1	-0.1	-0.4
19	7.5	9.8	7.5	6.6	-0.4	-0.1	-0.4	-0.4
20	6.6	6.3	6.3	6.3	-0.4	-0.4	-0.4	-0.4
21	10.2	7.1	7.1	6.6	-0.1	-0.4	-0.4	-0.4
22	13.0	13.0	12.0	8.7	0.2	0.0	0.0	-0.4
23	10.2	12.0	8.7	7.1	-0.1	0.0	-0.1	-0.4
24	12.0	9.8	7.5	6.3	0.0	-0.1	-0.4	-0.4
25	12.0	12.0	10.2	7.5	0.0	0.0	-0.1	-0.4
26	13.0	13.0	12.0	8.7	0.0	0.2	0.0	-0.4
28	13.0	13.0	13.0	7.5	0.2	0.2	0.0	-0.4
29	13.0	13.0	10.2	8.7	0.2	0.0	-0.1	-0.4
30	13.0	12.0	8.7	7.1	0.2	0.0	-0.1	-0.4
31	12.0	8.7	7.5	8.7	0	-0.4	-0.4	-0.4
32	13.0	13.0	12.0	8.7	0.2	0.0	0.0	-0.1
33	12.0	12.0	10.2	7.5	0.0	0.0	-0.1	-0.4
35	13.0	13.0	13.0	9.8	0.3	0.2	0.2	-0.1
37	12.0	8.7	7.5	7.5	0.0	-0.4	-0.4	-0.4
38	12.0	8.7	7.1	6.3	0.0	-0.4	-0.4	-0.4
39	12.0	12.0	8.7	7.1	0.0	0.0	-0.1	-0.4
40	13.0	13.0	10.2	7.5	0.3	0.0	-0.1	-0.4
41	13.0	13.0	12.0	8.7	0.2	0.2	0.0	-0.4
42	13.0	13.0	13.0	13.0	0.3	0.2	0.2	0.0
43	13.0	13.0	10.2	7.5	0.2	0.0	-0.1	-0.4
45	12.0	12.0	9.8	7.5	0.0	0.0	-0.1	-0.4

ID	Age [Gyr]				Z [Log(Z/Z$_\odot$)]			
	$0.1r_e$	$0.5r_e$	$1r_e$	$2r_e$	$0.1r_e$	$0.5r_e$	$1r_e$	$2r_e$
46	13.0	13.0	12.0	7.5	0.2	0.2	0.0	-0.4
47	13.0	13.0	12.0	10.2	0.2	0.2	0.0	-0.1
48	13.0	13.0	12.0	7.5	0.3	0.2	0.0	-0.4
50	13.0	12.0	10.2	8.7	0.2	0.0	-0.1	-0.4
51	12.0	8.7	7.5	7.1	0.0	-0.4	-0.4	-0.4
52	13.0	10.2	8.7	7.5	0.0	-0.1	-0.1	-0.4
55	13.0	12.0	9.8	7.5	0.2	0.0	-0.1	-0.4
56	13.0	13.0	12.0	7.5	0.2	0.2	0.0	-0.4
57	8.7	7.5	7.1	7.1	-0.1	-0.4	-0.4	-0.4
58	13.0	10.2	7.5	7.1	0.3	-0.1	-0.4	-0.4
59	13.0	13.0	13.0	9.8	0.2	0.3	0.2	-0.1
61	13.0	12.0	8.7	7.5	0.2	0.0	-0.1	-0.4
62	13.0	12.0	9.8	7.1	0.3	0.0	-0.1	-0.4
63	13.0	8.7	8.7	9.8	0.2	-0.1	-0.4	-0.1
64	6.6	7.1	6.6	6.3	-0.4	-0.4	-0.4	-0.4
65	13.0	10.2	8.7	7.1	0.2	0.0	-0.4	-0.4
68	13.0	10.2	8.7	7.5	0.3	-0.1	-0.4	-0.4
69	12.0	8.7	7.5	6.6	0.0	-0.4	-0.4	-0.4
70	12.0	8.7	7.5	7.5	0.0	-0.4	-0.4	-0.4
71	13.0	9.8	8.7	7.5	0.2	-0.1	-0.4	-0.4
72	13.0	13.0	13.0	13.0	0.3	0.3	0.2	0.0
73	13.0	7.5	7.1	7.5	0.2	-0.4	-0.4	-0.4
74	13.0	13.0	13.0	10.2	0.3	0.3	0.3	-0.1
76	13.0	13.0	12.0	8.7	0.2	0.2	0.0	-0.4
77	7.5	8.7	9.8	9.8	-0.4	-0.1	-0.1	-0.1
80	10.2	9.8	7.5	7.1	-0.1	-0.1	-0.4	-0.4
81	9.8	12.0	9.8	7.1	-0.1	0.0	-0.1	-0.4
82	13.0	13.0	10.2	7.1	0.3	0.2	0.0	-0.4
83	13.0	13.0	13.0	12.0	0.2	0.2	0.2	0.0
84	13.0	13.0	13.0	13.0	0.3	0.3	0.2	0.2
85	13.0	8.7	7.5	6.6	0.0	-0.1	-0.4	-0.4
87	12.0	8.7	7.5	7.1	0.0	-0.4	-0.4	-0.4
88	13.0	12.0	9.8	7.5	0.3	0.0	-0.1	-0.4
89	7.5	13.0	12.0	7.5	-0.4	0.0	0.0	-0.4
90	13.0	13.0	12.0	8.7	0.2	0.2	0.0	-0.4
91	7.5	12.0	12.0	8.7	-0.4	0.0	0.0	-0.4
93	13.0	12.0	9.8	7.5	0.2	0.0	-0.1	-0.4
94	8.7	13.0	13.0	13.0	-0.4	0.3	0.3	0.0
96	13.0	13.0	13.0	12.0	0.3	0.3	0.2	0.0

ID	Age [Gyr]				Z [Log(Z/Z$_\odot$)]			
	$0.1r_e$	$0.5r_e$	$1r_e$	$2r_e$	$0.1r_e$	$0.5r_e$	$1r_e$	$2r_e$
97	13.0	13.0	13.0	10.2	0.3	0.2	0.2	-0.1
98	13.0	13.0	13.0	13.0	0.3	0.2	0.2	0.2
99	10.2	13.0	10.2	6.6	-0.1	0.0	-0.1	-0.4
100	13.0	13.0	12.0	9.8	0.2	0.2	0.0	-0.1
101	13.0	9.8	7.5	7.1	0.3	-0.1	-0.4	-0.4
104	13.0	13.0	10.2	7.5	0.3	0.2	-0.1	-0.4

Table C.16.: SSP results for the MACS 1206 sample in the $Y_{105} - H_{160}$ color. The first column contains the IDs of the galaxies. The ages for the populations located at the respective radii are derived by assuming a fixed solar metallicity. The metallicities are determined by fixing the age to 12 Gyr at $z = 0$.

ID	Age [Gyr]				Z [Log(Z/Z$_\odot$)]			
	$0.1r_e$	$0.5r_e$	$1r_e$	$2r_e$	$0.1r_e$	$0.5r_e$	$1r_e$	$2r_e$
1	12.0	8.7	8.7	8.7	0.2	0.0	0.0	0.0
3	13.0	13.0	13.0	10.2	0.3	0.3	0.2	0.0
4	6.6	6.6	6.6	6.6	-0.1	-0.4	-0.1	-0.1
5	13.0	10.2	10.2	10.2	0.2	0.2	0.0	0.0
6	13.0	13.0	13.0	13.0	0.3	0.2	0.2	0.3
8	7.1	7.5	7.5	6.6	-0.1	0.0	0.0	-0.1
10	13.0	13.0	13.0	13.0	0.3	0.3	0.3	0.2
11	8.7	12.0	12.0	10.2	0.0	0.2	0.2	0.0
12	8.7	7.5	7.5	7.1	0.0	0.0	0.0	-0.1
15	12.0	12.0	7.5	6.3	0.2	0.2	0.0	-0.4
17	13.0	10.2	10.2	10.2	0.2	0.0	0.0	0.0
19	7.1	9.8	8.7	7.1	0.0	0.0	0.0	-0.1
20	6.3	6.3	6.6	8.7	-0.4	-0.4	-0.1	0.0
21	7.5	8.7	7.5	7.1	0.0	0.0	0.0	-0.1
22	13.0	13.0	13.0	13.0	0.2	0.2	0.2	0.2
23	10.2	12.0	9.8	7.1	0.0	0.2	0.0	0.0
24	6.6	13.0	13.0	5.7	-0.1	0.3	0.3	-0.4
25	13.0	13.0	10.2	8.7	0.3	0.2	0.0	0.0
26	13.0	13.0	12.0	7.5	0.3	0.3	0.2	0.0
28	13.0	13.0	13.0	12.0	0.2	0.2	0.2	0.2
29	13.0	13.0	12.0	13.0	0.3	0.2	0.2	0.2
30	13.0	10.2	10.2	13.0	0.3	0.2	0.0	0.2
31	13.0	12.0	12.0	13.0	0.2	0.2	0.2	0.2
32	13.0	12.0	12.0	13.0	0.3	0.2	0.2	0.2
33	13.0	7.5	7.1	7.1	0.2	0.0	0.0	-0.1
35	13.0	12.0	8.7	7.5	0.3	0.2	0.0	0.0
37	10.2	8.7	6.6	5.7	0.2	0.0	-0.1	-0.4
38	7.5	12.0	8.7	6.6	0.0	0.2	0.0	-0.1
39	13.0	13.0	12.0	7.5	0.3	0.3	0.2	0.0
40	13.0	10.2	9.8	8.7	0.3	0.2	0.0	0.0
41	13.0	13.0	10.2	8.7	0.3	0.2	0.0	0.0
42	13.0	13.0	12.0	10.2	0.2	0.2	0.2	0.0
43	13.0	13.0	13.0	13.0	0.3	0.2	0.2	0.3
45	12.0	9.8	8.7	8.7	0.2	0.0	0.0	0.0
46	13.0	10.2	8.7	7.5	0.3	0.0	0.0	0.0
47	13.0	13.0	13.0	13.0	0.3	0.3	0.3	0.3

ID	Age [Gyr]				Z [Log(Z/Z$_\odot$)]			
	$0.1r_e$	$0.5r_e$	$1r_e$	$2r_e$	$0.1r_e$	$0.5r_e$	$1r_e$	$2r_e$
48	12.0	13.0	13.0	10.2	0.2	0.3	0.2	0.2
50	12.0	10.2	10.2	10.2	0.2	0.0	0.0	0.2
51	13.0	10.2	10.2	10.2	0.2	0.2	0.0	0.0
52	13.0	12.0	13.0	13.0	0.2	0.2	0.2	0.2
55	13.0	10.2	10.2	13.0	0.3	0.2	0.2	0.2
56	12.0	12.0	10.2	8.7	0.2	0.2	0.0	0.0
57	9.8	10.2	10.2	8.7	0.0	0.2	0.0	0.0
58	12.0	13.0	13.0	7.1	0.2	0.3	0.2	-0.1
59	13.0	9.8	7.5	7.5	0.3	0.0	0.0	0.0
61	7.5	12.0	12.0	12.0	0.0	0.2	0.2	0.2
62	13.0	12.0	10.2	7.5	0.2	0.2	0.0	0.0
63	7.5	7.5	6.6	5.4	0.0	0.0	-0.1	-0.4
64	7.1	6.6	6.6	6.6	-0.1	-0.1	-0.1	-0.1
65	9.8	8.7	7.1	6.3	0.0	0.0	-0.1	-0.4
68	13.0	10.2	10.2	12.0	0.2	0.2	0.2	0.2
69	8.7	7.5	8.7	10.2	0.0	0.0	0.0	0.0
70	7.5	7.1	7.5	12.0	0.0	-0.1	0.0	0.2
71	13.0	8.7	7.5	7.1	0.2	0.0	0.0	0.0
72	13.0	8.7	7.5	7.1	0.3	0.0	0.0	-0.1
73	13.0	7.1	7.1	7.5	0.2	0.0	-0.1	0.0
74	13.0	6.3	5.7	5.7	0.3	-0.4	-0.4	-0.4
76	13.0	12.0	10.2	9.8	0.3	0.2	0.0	0.0
77	7.1	7.5	7.5	7.5	-0.1	0.0	0.0	0.0
80	7.5	7.1	7.1	7.1	0.0	-0.1	-0.1	-0.1
81	7.5	7.5	7.5	9.8	0.0	0.0	0.0	0.0
82	13.0	7.5	7.1	7.1	0.2	0.0	0.0	-0.1
83	13.0	12.0	12.0	13.0	0.3	0.2	0.2	0.2
84	13.0	13.0	12.0	12.0	0.2	0.2	0.2	0.2
85	7.1	10.2	8.7	7.1	-0.1	0.0	0.0	-0.1
87	13.0	12.0	8.7	6.6	0.2	0.2	0.0	-0.1
88	8.7	13.0	13.0	10.2	0.0	0.2	0.2	0.0
89	12.0	10.2	8.7	7.5	0.2	0.0	0.0	0.0
90	13.0	10.2	7.5	7.1	0.2	0.0	0.0	-0.1
91	13.0	8.7	7.1	6.6	0.3	0.0	0.0	-0.1
93	13.0	13.0	10.2	7.1	0.3	0.2	0.2	-0.1
94	13.0	13.0	12.0	8.7	0.3	0.3	0.2	0.0
96	13.0	13.0	13.0	12.0	0.3	0.3	0.2	0.2
97	13.0	13.0	13.0	13.0	0.2	0.2	0.2	0.2
98	13.0	13.0	12.0	9.8	0.2	0.2	0.2	0.0

ID	Age [Gyr]				Z [Log(Z/Z$_\odot$)]			
	$0.1r_e$	$0.5r_e$	$1r_e$	$2r_e$	$0.1r_e$	$0.5r_e$	$1r_e$	$2r_e$
99	6.6	12.0	13.0	13.0	-0.4	0.2	0.2	0.3
100	13.0	12.0	10.2	8.7	0.2	0.2	0.0	0.0
101	12.0	7.5	7.5	7.1	0.2	0.0	0.0	-0.1
104	9.8	10.2	8.7	7.1	0.0	0.2	0.0	-0.1

Table C.17.: SSP results for the MACS 0416 sample in the $r_{625} - Y_{105}$ color. The first column contains the IDs of the galaxies. The ages for the populations located at the respective radii are derived by assuming a fixed solar metallicity. The metallicities are determined by fixing the age to 12 Gyr at $z = 0$.

ID	Age [Gyr]				Z [Log(Z/Z$_\odot$)]			
	$0.1r_e$	$0.5r_e$	$1r_e$	$2r_e$	$0.1r_e$	$0.5r_e$	$1r_e$	$2r_e$
21	6.3	8.7	8.7	7.1	-0.4	-0.4	-0.4	-0.4
25	8.7	13.0	12.0	7.1	-0.1	0.2	0.0	-0.4
26	12.0	13.0	12.0	7.1	0.0	0.2	0.0	-0.4
30	6.3	7.1	7.1	6.6	-0.4	-0.4	-0.4	-0.4
31	10.2	13.0	13.0	7.5	-0.1	0.2	0.0	-0.4
33	7.5	13.0	13.0	12.0	-0.4	0.0	0.2	0.0
38	7.1	9.8	9.8	7.5	-0.4	-0.1	-0.1	-0.4
43	7.5	10.2	8.7	7.1	-0.4	-0.1	-0.4	-0.4
45	7.5	10.2	8.7	7.1	-0.4	-0.1	-0.1	-0.4
50	10.2	13.0	13.0	7.5	-0.1	0.2	0.0	-0.4
53	9.8	13.0	13.0	8.7	-0.1	0.3	0.2	-0.4
54	7.5	13.0	12.0	8.7	-0.4	0.0	0.0	-0.4
55	6.6	6.3	5.7	5.7	-0.4	-0.4	-0.4	-0.4
57	12.0	13.0	12.0	8.7	0.0	0.0	0.0	-0.1
63	10.2	13.0	13.0	9.8	-0.1	0.3	0.2	-0.1
65	13.0	12.0	10.2	7.5	0.0	0.0	-0.1	-0.4
66	10.2	7.5	7.5	10.2	-0.1	-0.4	-0.4	-0.1
68	7.5	10.2	8.7	7.1	-0.4	-0.1	-0.1	-0.4
70	8.7	13.0	13.0	9.8	-0.4	0.3	0.2	-0.1
71	8.7	13.0	12.0	7.1	-0.4	0.2	0.0	-0.4
85	13.0	10.2	8.7	7.5	0.0	-0.1	-0.1	-0.4
87	10.2	12.0	8.7	6.6	-0.1	0.0	-0.4	-0.4
88	12.0	13.0	12.0	9.8	0.0	0.0	0.0	-0.1
93	7.1	12.0	10.2	6.6	-0.4	0.0	-0.1	-0.4
94	9.8	8.7	7.5	7.1	-0.1	-0.1	-0.4	-0.4
95	6.3	10.2	8.7	6.6	-0.4	-0.1	-0.1	-0.4
96	8.7	8.7	7.5	6.6	-0.4	-0.1	-0.4	-0.4
98	7.1	6.6	7.1	8.7	-0.4	-0.4	-0.4	-0.4
102	8.7	10.2	10.2	8.7	-0.4	-0.1	-0.1	-0.4
103	7.1	12.0	9.8	6.6	-0.4	0.0	-0.1	-0.4
104	10.2	10.2	8.7	7.1	-0.1	-0.1	-0.4	-0.4
105	13.0	12.0	12.0	10.2	0.2	0.0	0.0	-0.1
107	13.0	13.0	13.0	9.8	0.3	0.2	0.0	-0.1
109	9.8	9.8	8.7	7.1	-0.1	-0.1	-0.4	-0.4
113	7.5	13.0	12.0	8.7	-0.4	0.0	0.0	-0.4

ID	Age [Gyr]				Z [Log(Z/Z$_\odot$)]			
	$0.1r_e$	$0.5r_e$	$1r_e$	$2r_e$	$0.1r_e$	$0.5r_e$	$1r_e$	$2r_e$
115	6.6	7.5	7.5	7.1	-0.4	-0.4	-0.4	-0.4
133	8.7	13.0	13.0	10.2	-0.4	0.2	0.2	0.0
154	13.0	13.0	9.8	6.6	0.0	0.0	-0.1	-0.4

Table C.18.: SSP results for the MACS 0416 sample in the $Y_{105} - H_{160}$ color. The first column contains the IDs of the galaxies. The ages for the populations located at the respective radii are derived by assuming a fixed solar metallicity. The metallicities are determined by fixing the age to 12 Gyr at $z = 0$.

ID	Age [Gyr]				Z [Log(Z/Z$_\odot$)]			
	$0.1r_e$	$0.5r_e$	$1r_e$	$2r_e$	$0.1r_e$	$0.5r_e$	$1r_e$	$2r_e$
21	7.5	9.8	10.2	10.2	0.0	0.0	0.0	0.0
25	7.5	7.5	7.1	6.6	0.0	0.0	-0.1	-0.1
26	10.2	10.2	10.2	8.7	0.2	0.2	0.0	0.0
30	6.6	5.7	5.7	5.7	-0.1	-0.4	-0.4	-0.4
31	12.0	7.5	7.1	6.3	0.2	0.0	-0.1	-0.4
33	13.0	7.5	7.1	7.1	0.3	0.0	-0.1	-0.1
38	13.0	6.3	5.7	6.3	0.2	-0.4	-0.4	-0.4
43	7.5	6.6	6.6	6.6	0.0	-0.1	-0.1	-0.1
45	13.0	13.0	13.0	13.0.0	0.3	0.3	0.3	0.2
50	13.0	7.5	7.1	7.5	0.3	0.0	-0.1	0.0
53	13.0	12.0	7.5	7.1	0.3	0.2	0.0	-0.1
54	7.5	7.5	7.1	6.6	0.0	0.0	-0.1	-0.1
55	6.6	7.1	5.7	5.0	-0.1	-0.1	-0.4	-0.4
57	13.0	8.7	8.7	10.2	0.2	0.0	0.0	0.2
63	8.7	8.7	8.7	9.8	0.0	0.0	0.0	0.0
65	13.0	12.0	8.7	7.5	0.3	0.2	0.0	0.0
66	8.7	8.7	8.7	8.7	0.0	0.0	0.0	0.0
68	12.0	10.2	9.8	7.5	0.2	0.2	0.0	0.0
70	13.0	12.0	9.8	7.5	0.2	0.2	0.0	0.0
71	13.0	7.1	7.1	7.1	0.3	-0.1	-0.1	-0.1
85	8.7	7.1	7.1	10.2	0.0	-0.1	0.0	0.0
87	13.0	12.0	8.7	7.1	0.3	0.2	0.0	0.0
88	13.0	10.2	8.7	7.5	0.2	0.0	0.0	0.0
93	13.0	13.0	10.2	9.8	0.3	0.2	0.2	0.0
94	12.0	8.7	7.5	7.5	0.2	0.0	0.0	0.0
95	8.7	10.2	10.2	9.8	0.0	0.2	0.2	0.0
96	13.0	8.7	8.7	7.5	0.2	0.0	0.0	0.0
98	7.1	6.3	6.3	6.6	-0.1	-0.4	-0.4	-0.1
102	7.5	6.6	6.6	6.6	0.0	-0.1	-0.4	-0.1
103	6.3	7.5	7.5	7.1	-0.4	0.0	0.0	-0.1
104	8.7	7.5	7.1	6.6	0.0	0.0	-0.1	-0.1
105	13.0	7.1	6.6	6.6	0.3	-0.1	-0.1	-0.1
107	13.0	8.7	7.5	7.1	0.3	0.0	0.0	-0.1
109	12.0	13.0	12.0	10.2	0.2	0.2	0.2	0.0
113	13.0	13.0	13.0	13.0	0.3	0.2	0.2	0.2

ID	Age [Gyr]				Z [Log(Z/Z$_\odot$)]			
	$0.1r_e$	$0.5r_e$	$1r_e$	$2r_e$	$0.1r_e$	$0.5r_e$	$1r_e$	$2r_e$
115	13.0	8.7	7.5	8.7	0.3	0.0	0.0	0.0
133	13.0	12.0	12.0	13.0	0.3	0.2	0.2	0.3
154	13.0	12.0	10.2	8.7	0.2	0.2	0.0	0.0

Table C.19.: SSP results for the MACS 1206 sample using a color-color grid with $r_{625}-Y_{105}$ and $Y_{105}-H_{160}$. The first column contains the IDs of the galaxies. The ages and metallicities for the stellar populations at the respective radii are derived by finding the nearest grid points with their colors corresponding to modelled ages and metallicities.

ID	Age [Gyr]				Z [Log(Z/Z$_\odot$)]			
	$0.1r_e$	$0.5r_e$	$1r_e$	$2r_e$	$0.1r_e$	$0.5r_e$	$1r_e$	$2r_e$
1	12.0	12.0	13.0	13.0	0.0	0.0	-0.1	-0.1
3	13.0	13.0	13.0	13.0	0.4	0.3	0.2	0.2
4	13.0	10.2	10.2	10.2	-0.4	-0.4	-0.4	-0.4
5	8.7	12.0	9.8	9.8	0.2	0.0	0.0	0.0
6	13.0	10.2	9.8	9.8	0.2	0.2	0.2	0.2
8	13.0	13.0	13.0	13.0	-0.4	-0.1	-0.1	-0.1
10	10.2	12.0	9.8	9.8	0.3	0.2	0.2	0.2
11	13.0	12.0	7.5	7.5	-0.1	0.0	0.2	0.2
12	9.8	8.7	10.2	10.2	0.0	0.0	-0.1	-0.1
15	13.0	12.0	12.0	12.0	0.0	0.0	-0.1	-0.1
17	12.0	10.2	8.7	8.7	0.0	0.0	0.0	0.0
19	9.8	9.8	7.5	7.5	-0.1	0.0	0.0	0.0
20	7.5	7.1	6.3	6.3	-0.4	-0.4	0.0	0.0
21	12.0	7.1	6.6	6.6	-0.1	0.2	0.2	0.2
22	13.0	10.2	8.7	8.7	0.0	0.2	0.2	0.2
23	10.2	12.0	8.7	8.7	0.0	0.0	0.0	0.0
24	13.0	7.1	6.3	6.3	-0.1	0.4	0.4	0.4
25	7.5	12.0	10.2	10.2	0.4	0.0	0.0	0.0
26	7.5	10.2	12.0	12.0	0.4	0.2	0.0	0.0
28	12.0	13.0	13.0	13.0	0.2	0.2	0.0	0.0
29	9.8	13.0	10.2	10.2	0.3	0.0	0.0	0.0
30	8.7	12.0	7.5	7.5	0.3	0.0	0.2	0.2
31	9.8	7.5	7.5	7.5	0.2	0.2	0.2	0.2
32	13.0	13.0	8.7	8.7	0.2	0.0	0.2	0.2
33	9.8	13.0	12.0	12.0	0.2	-0.1	-0.1	-0.1
35	12.0	12.0	12.0	12.0	0.3	0.2	0.0	0.0
37	12.0	8.7	12.0	12.0	0.0	0.0	-0.4	-0.4
38	13.0	7.5	6.3	6.3	-0.1	0.2	0.3	0.3
39	7.1	7.5	7.5	7.5	0.4	0.3	0.2	0.2
40	13.0	12.0	10.2	10.2	0.2	0.0	0.0	0.0
41	9.8	13.0	12.0	12.0	0.3	0.0	0.0	0.0
42	13.0	13.0	13.0	13.0	0.2	0.2	0.0	0.0
43	13.0	13.0	8.7	8.7	0.2	0.0	0.2	0.2
45	12.0	13.0	9.8	9.8	0.0	-0.1	0.0	0.0
46	12.0	13.0	13.0	13.0	0.2	0.0	-0.1	-0.1
47	13.0	10.2	9.8	9.8	0.2	0.2	0.2	0.2

ID	Age [Gyr]				Z [Log(Z/Z$_\odot$)]			
	$0.1r_e$	$0.5r_e$	$1r_e$	$2r_e$	$0.1r_e$	$0.5r_e$	$1r_e$	$2r_e$
48	13.0	12.0	8.7	8.7	0.2	0.2	0.2	0.2
50	13.0	12.0	10.2	10.2	0.0	0.0	0.0	0.0
51	8.7	7.5	7.1	7.1	0.2	0.2	0.2	0.2
52	13.0	10.2	7.5	7.5	0.0	0.0	0.2	0.2
55	12.0	12.0	10.2	10.2	0.2	0.0	0.0	0.0
56	13.0	13.0	12.0	12.0	0.0	0.0	0.0	0.0
57	9.8	7.1	6.6	6.6	0.0	0.2	0.3	0.3
58	13.0	7.5	7.1	7.1	0.2	0.3	0.3	0.3
59	13.0	13.0	13.0	13.0	0.2	0.2	0.0	0.0
61	13.0	12.0	7.5	7.5	0.0	0.0	0.2	0.2
62	13.0	12.0	9.8	9.8	0.2	0.0	0.0	0.0
63	13.0	12.0	13.0	13.0	0.0	-0.1	-0.4	-0.4
64	6.6	7.5	7.1	7.1	0.2	-0.1	-0.1	-0.1
65	13.0	13.0	10.2	10.2	0.0	-0.1	-0.1	-0.1
68	13.0	10.2	7.5	7.5	0.2	0.0	0.2	0.2
69	13.0	8.7	7.1	7.1	-0.1	0.0	0.2	0.2
70	13.0	10.2	7.5	7.5	-0.1	-0.1	0.0	0.0
71	13.0	12.0	10.2	10.2	0.0	-0.1	-0.1	-0.1
72	13.0	13.0	13.0	13.0	0.3	0.2	0.0	0.0
73	13.0	7.5	8.7	8.7	0.0	0.0	-0.1	-0.1
74	9.8	13.0	13.0	13.0	0.4	0.2	-0.1	-0.1
76	10.2	13.0	12.0	12.0	0.2	0.0	0.0	0.0
77	9.8	12.0	12.0	12.0	-0.1	-0.1	-0.1	-0.1
80	12.0	13.0	9.8	9.8	-0.1	-0.4	-0.1	-0.1
81	12.0	13.0	12.0	12.0	-0.1	-0.1	-0.1	-0.1
82	13.0	13.0	13.0	13.0	0.2	0.0	-0.1	-0.1
83	13.0	13.0	13.0	13.0	0.2	0.2	0.0	0.0
84	13.0	13.0	13.0	13.0	0.2	0.2	0.0	0.0
85	13.0	9.8	7.1	7.1	-0.1	0.0	0.2	0.2
87	8.7	7.5	7.5	7.5	0.2	0.2	0.0	0.0
88	13.0	9.8	7.5	7.5	0.2	0.2	0.3	0.3
89	7.5	12.0	13.0	13.0	0.2	0.0	-0.1	-0.1
90	12.0	13.0	13.0	13.0	0.2	0.0	-0.1	-0.1
91	6.3	13.0	13.0	13.0	0.4	-0.1	-0.1	-0.1
93	12.0	8.7	9.8	9.8	0.2	0.2	0.0	0.0
94	7.1	10.2	13.0	13.0	0.4	0.3	0.2	0.2
96	8.7	13.0	13.0	13.0	0.4	0.2	0.2	0.2
97	13.0	13.0	13.0	13.0	0.2	0.2	0.0	0.0
98	13.0	12.0	13.0	13.0	0.2	0.2	0.0	0.0

ID	Age [Gyr]				Z [Log(Z/Z$_\odot$)]			
	$0.1r_e$	$0.5r_e$	$1r_e$	$2r_e$	$0.1r_e$	$0.5r_e$	$1r_e$	$2r_e$
99	13.0	13.0	7.5	7.5	-0.4	0.0	0.3	0.3
100	12.0	13.0	12.0	12.0	0.2	0.0	0.0	0.0
101	13.0	12.0	7.5	7.5	0.2	-0.1	0.0	0.0
104	13.0	13.0	13.0	13.0	0.0	0.0	-0.1	-0.1

Table C.20.: SSP results for the MACS 0416 sample using a color-color grid with $r_{625}-Y_{105}$ and $Y_{105}-H_{160}$. The first column contains the IDs of the galaxies. The ages and metallicities for the stellar populations at the respective radii are derived by finding the nearest grid points with their colors corresponding to modelled ages and metallicities.

ID	Age [Gyr]				Z [Log(Z/Z$_\odot$)]			
	$0.1r_e$	$0.5r_e$	$1r_e$	$2r_e$	$0.1r_e$	$0.5r_e$	$1r_e$	$2r_e$
21	5.7	8.7	7.5	6.3	0.4	0.0	0.2	0.3
25	8.7	13.0	13.0	7.5	0.0	-0.1	-0.1	-0.1
26	12.0	13.0	12.0	6.3	0.0	0.0	0.0	0.3
30	6.6	8.7	8.7	7.5	-0.1	-0.4	-0.4	-0.4
31	10.2	13.0	13.0	10.2	0.0	0.0	-0.1	-0.4
33	6.3	13.0	13.0	13.0	0.4	-0.1	-0.1	-0.1
38	6.3	13.0	13.0	9.8	0.3	-0.4	-0.4	-0.4
43	7.5	13.0	13.0	7.5	0.0	-0.4	-0.4	-0.1
45	6.3	7.5	7.1	6.3	0.4	0.3	0.3	0.4
50	7.1	13.0	13.0	7.5	0.4	0.0	-0.1	0.0
53	7.1	13.0	13.0	13.0	0.4	0.2	0.0	-0.4
54	7.5	13.0	13.0	13.0	0.0	-0.1	-0.1	-0.4
55	7.1	5.7	6.3	5.7	-0.1	0.3	-0.4	-0.1
57	9.8	13.0	13.0	7.5	0.2	-0.1	-0.1	0.2
63	12.0	13.0	13.0	9.8	-0.1	0.0	0.0	0.0
65	10.2	12.0	13.0	7.5	0.2	0.0	-0.1	0.0
66	9.8	7.1	7.1	10.2	0.0	0.2	0.2	0.0
68	6.6	10.2	8.7	6.3	0.3	0.0	0.0	0.3
70	7.1	13.0	13.0	12.0	0.3	0.2	0.0	-0.1
71	6.6	13.0	13.0	6.6	0.4	-0.1	-0.1	0.2
85	13.0	12.0	10.2	7.1	-0.1	-0.1	-0.1	0.2
87	7.1	12.0	8.7	6.6	0.4	0.0	0.0	0.2
88	8.7	12.0	13.0	12.0	0.2	0.0	-0.1	-0.1
93	6.3	9.8	10.2	6.3	0.4	0.2	0.0	0.3
94	10.2	8.7	7.5	7.1	0.0	0.0	0.0	0.0
95	5.7	10.2	7.5	5.7	0.4	0.0	0.2	0.4
96	7.1	8.7	7.5	6.3	0.3	0.0	0.0	0.2
98	7.1	7.5	8.7	13.0	0.0	-0.4	-0.4	-0.4
102	10.2	13.0	13.0	13.0	-0.1	-0.4	-0.4	-0.4
103	8.7	13.0	12.0	6.3	-0.4	-0.1	-0.1	0.2
104	13.0	12.0	10.2	7.5	-0.1	-0.1	-0.1	-0.1
105	8.7	13.0	13.0	13.0	0.3	-0.1	-0.4	-0.4
107	10.2	13.0	13.0	12.0	0.3	0.0	-0.1	-0.1
109	10.2	8.7	7.5	6.3	0.0	0.2	0.2	0.3
113	7.1	10.2	12.0	7.1	0.4	0.2	0.0	0.3

ID	Age [Gyr]				Z [Log(Z/Z$_\odot$)]			
	$0.1r_e$	$0.5r_e$	$1r_e$	$2r_e$	$0.1r_e$	$0.5r_e$	$1r_e$	$2r_e$
115	6.3	8.7	7.5	6.3	0.4	0.0	0.0	0.3
133	6.6	13.0	13.0	7.5	0.4	0.0	0.0	0.3
154	13.0	13.0	9.8	6.6	0.0	0.0	0.0	0.2